

# Large Hybrid High Precision MEMS Mirrors

THÈSE N° 5152 (2011)

PRÉSENTÉE LE 30 NOVEMBRE 2011

À LA FACULTÉ SCIENCES ET TECHNIQUES DE L'INGÉNIEUR  
LABORATOIRE DE CAPTEURS, ACTUATEURS ET MICROSYSTÈMES  
SECTION DE MICROTECHNIQUE

ÉCOLE POLYTECHNIQUE FÉDÉRALE DE LAUSANNE

POUR L'OBTENTION DU GRADE DE DOCTEUR ÈS SCIENCES

PAR

Dara BAYAT

acceptée sur proposition du jury:

Prof. P.-A. Farine, président du jury  
Prof. N. de Rooij, Dr W. Noell, directeurs de thèse  
Dr B. Guldemann, rapporteur  
Prof. H. Shea, rapporteur  
Dr F. Zamkotsian, rapporteur



ÉCOLE POLYTECHNIQUE  
FÉDÉRALE DE LAUSANNE

Suisse  
2011



## Abstract

This thesis presents the design and microfabrication technology of a tip-tilt, 2 degree of freedom “mirror system” made out of Silicon On Insulator (SOI) wafers with two movable mirrors that have diameter of 10 mm. The system was intended for precise beam steering applications and tracking for inter-satellite telecommunication. Implementation of two mirrors allowed one mirror to have large static mechanical scan angles ( $\pm 3.5^\circ$ ) and the other to have fast fine pointing capabilities within  $\pm 0.2^\circ$  static mechanical scan angle.

The first mirror was magnetically actuated and has a resonance frequency of 200Hz and the large rotation angle. The second mirror was designed to use either electrostatic actuation or electromagnetic actuation. The resonance frequency is 1 KHz.

The main objective of this thesis was the microfabrication of large mirrors (10 mm) and actuators. The study of upper limits of achievable resonant frequencies in combination with static deflection was another major aim of the project, as well as optimization of the flatness of the mirrors. The undertaken research presents a study of different non-contact actuation schemes for use in MOEMS devices, namely electrostatic and magnetic actuation schemes.

Determination of the best magnetic actuation scheme for use in this thesis was carried out according to the design constraints and size limitations. It was concluded that the best magnetic actuation scheme consists of a moving magnet and a microfabricated stationary coil. This scheme created high force and the stationary microfabricated coils could easily dissipate heat through conduction into a heat sink. This configuration was of great advantage in space where heat convection does not exist.

The considered electrostatic schemes included parallel plate actuators and vertical comb actuators. The vertical comb actuator was chosen to be fabricated due to its scalability that allows the microfabrication process to be easily adapted to smaller or larger devices.

The microfabrication and implementation of the magnetically actuated mirrors was proven to be very straightforward resulting in high yield and uniformity of both the high and low frequency devices. The microfabrication of the electrostatic actuator was also achieved successfully. The operation performance of the electrostatically actuated mirror was not as satisfactory as the magnetically actuated mirrors. It was concluded that electrostatic actuation might be more suited to smaller devices, rather than the devices designed in the present study.

The fabrication and actuation performance of the components of a “mirror system” that combines fast and large angle actuation was successfully demonstrated in this thesis. Very good mirror flatnesses were also obtained with RMS flatness of  $\lambda/10$  for near infrared wavelengths.

This project shows the general advantage of magnetic actuation for large MOEMS devices with large actuation ranges and proves the feasibility of their fabrication. Potential applications of these devices are robotic 3D vision, imaging LIDARs (Light Detection And Ranging), docking sensors and inter-satellite laser communications.

**Key words:** Hybrid, high precision, MOEMS, Microfabrication, large mirror, flat mirror, electrostatically actuated mirror, magnetically actuated mirror, Micro-coil, inter-satellite telecommunication.



## Résumé

Cette thèse présente la conception et la microfabrication d'un système de miroirs « tip/tilt » à deux degrés de liberté. Ce système pour satellite permettra de suivre par laser la position de satellites voisins et d'établir une communication inter-satellitaire. Il est conçu à partir de plaques de silicium de type « Silicon on Insulator » (SOI). Le système se compose de deux miroirs mobiles qui fournissent deux types de balayages: un balayage grossier du premier miroir avec un angle de balayage de  $\pm 3.5^\circ$  et un balayage fin du deuxième miroir de  $\pm 0.2^\circ$ .

Le premier miroir est conçu en utilisant une actuation magnétique avec une fréquence de résonance de 200 Hz et un grand angle de rotation. Le deuxième miroir permet aussi bien d'utiliser un actuateur électrostatique qu'un actuateur électromagnétique. Sa fréquence de résonance est de 1kHz.

L'objectif principal de cette thèse était de créer de grands micromiroirs mobiles par microfabrication (diamètre de 10 mm). Dans un second temps, l'étude des fréquences de résonance maximales atteignables a été effectuée en fonction de la déflexion statique, ainsi que l'optimisation de la planéité des miroirs. Et finalement, ce travail présente une étude des différents schémas d'actuation pour des MOEMS électrostatiques et magnétiques.

La détermination du meilleur type d'actuation a été accomplie en tenant compte des contraintes dimensionnelles du design. Le meilleur actuateur magnétique est constitué d'un aimant mobile et d'une bobine stationnaire. Ce schéma génère de grandes forces et dissipe facilement la chaleur grâce au dissipateur thermique de la bobine, cette dernière qualité est essentielle dans l'espace où la convection thermique n'a pas lieu.

Les deux schémas électrostatiques étudiés ont été celui des plaques parallèles et celui des actionneurs à peignes verticaux. Le schéma des actionneurs à peignes verticaux a été choisi en raison de sa facilité d'implémentation dans des designs de différentes tailles.

Les efforts consentis en microfabrication ont permis d'obtenir un rendement de fabrication élevé pour les différents designs d'actionneurs magnétiques (fréquences de résonance différentes). Pour les actionneurs électrostatiques la microfabrication a également été accomplie avec succès. Néanmoins leurs performances n'étaient pas aussi bonnes si on les compare avec les actionneurs magnétiques. En conclusion, ces actionneurs électrostatiques seraient mieux adaptés pour des micromiroirs ayant des tailles plus petites que celles étudiées dans cette thèse.

La fabrication et les performances d'actionneurs magnétiques à grand angle de balayage ont été démontrées dans cette étude. De bonnes planarités de miroirs ont également été obtenues avec une planarité de  $\lambda/10$  (RMS) pour des longueurs d'ondes proches de l'infrarouge.

Ces travaux démontrent également les avantages d'une actuation magnétique lorsque de grands angles de balayages sont requis. Les applications potentielles de ces systèmes se trouvent par exemple dans le domaine de la vision 3D, de l'imagerie LIDAR (Light Detection And Ranging) ou encore dans la communication laser inter-satellites.

Mots-clés: Hybride, haute précision, MOEMS, Microfabrication, grand miroir, miroir plat, miroir avec actionneurs magnétiques, miroir avec actionneurs électrostatiques, Microbobine, communication inter-satellitaire



# Table of contents

|   |           |
|---|-----------|
| <b>LIST OF FIGURES</b>  | <b>IX</b> |
| <b>1 INTRODUCTION</b>   | <b>1</b>  |
| <b>2 STATE OF THE ART</b>   | <b>5</b>  |
| 2.1 Galvo-mirrors   | 5         |
| 2.2 Microfabricated devices   | 5         |
| 2.2.1 Electrostatic actuation   | 6         |
| 2.2.2 Magnetic actuation  | 6         |
| 2.2.3 Micro-coils   | 8         |
| 2.2.4 Magnetic materials for MEMS   | 8         |
| 2.3 Steering devices for space  | 9         |
| 2.4 Summary   | 11        |
| <b>3 THEORY</b>   | <b>13</b> |
| 3.1 Electromagnetic actuation   | 14        |
| 3.2 Scaling laws of the magnetic actuation schemes                            | 16        |
| 3.2.1 Wire-wire interaction scheme  | 16        |
| 3.2.2 Wire-magnet interaction scheme  | 17        |
| 3.2.3 Wire – ferrite interaction scheme                                       | 17        |
| 3.2.4 Effect of scaling on micro-coils  | 19        |
| 3.2.5 Effect of coil scaling on the force to mass ratio                       | 20        |
| 3.2.6 Force magnitude of the different magnetic schemes                       | 21        |
| 3.2.7 Total Mass of the moving system and force to mass ratio                 | 23        |
| 3.3 Electrostatic actuation   | 23        |
| 3.3.1 Parallel plate actuator   | 24        |
| 3.3.2 Comb drive actuator   | 24        |
| 3.3.3 Scaling law for the electrostatic actuators                             | 25        |
| 3.4 Comparison of magnetic and electrostatic actuation                        | 26        |
| 3.5 Mechanical springs  | 28        |
| 3.6 Summary   | 30        |
| <b>4 CONCEPT</b>  | <b>31</b> |
| 4.1 Actuation design study  | 31        |
| 4.1.1 Magnetic actuators  | 32        |
| 4.1.2 Solenoid Actuators  | 32        |
| 4.1.3 Magnetic comb drive actuator  | 34        |
| 4.1.3.1 Achievable forces   | 34        |
| 4.1.3.2 Possible magnetic comb actuator design                                | 35        |
| 4.1.4 Possible clapper designs  | 37        |
| 4.1.5 Voice coil design   | 38        |
| 4.1.6 Moving magnet actuation   | 39        |
| 4.1.6.1 Moving coil—stationary magnet design                                  | 40        |
| 4.1.6.2 Choices of magnetic materials   | 41        |
| 4.1.7 Torque driven ferrite based design                                      | 42        |
| 4.2 Comparison of magnetic Actuators  | 43        |
| 4.2.1 Conclusion and chosen magnetic design                                   | 44        |
| 4.3 Electrostatic actuation   | 45        |
| 4.3.1 Parallel plate Actuator   | 45        |
| 4.3.2 Comb drive Actuator   | 47        |
| 4.3.3 Conclusion and chosen electrostatic design                              | 48        |
| 4.4 Core aspects of the mirror design   | 48        |
| 4.4.1 Magnetic design   | 49        |
| 4.4.1.1 Magnetic mirror concept   | 49        |
| 4.4.1.2 Dependency of the resonant frequency on the maximum static tilt angle | 50        |
| 4.4.2 Electrostatic design  | 50        |
| 4.4.2.1 Electrostatic design concept  | 50        |
| 4.4.2.2 Resonant frequency vs. maximum tilt angle                             | 51        |
| 4.4.3 Separation of the design to two mirrors                                 | 52        |
| 4.4.4 Optical beam dimensions   | 52        |
| 4.5 Fabrication and assembly  | 53        |

|            |  |            |
|------------|--|------------|
| 4.5.1      | Magnetic mirror  | 53         |
| 4.5.1.1    | Microfabrication of the mirror and moving platform                       | 54         |
| 4.5.1.2    | Bonding of the mirror and the actuation wafers                           | 54         |
| 4.5.1.3    | Assembly   | 54         |
| 4.5.1.4    | Mechanical design  | 55         |
| 4.5.2      | Electrostatic mirror   | 57         |
| 4.5.2.1    | Bonding of the mirror and the actuation wafers                           | 58         |
| 4.5.2.2    | Assembly   | 59         |
| 4.5.2.3    | Mechanical design  | 60         |
| <b>4.6</b> | <b>Combination of the magnetic and electrostatic designs</b>             | <b>61</b>  |
| <b>4.7</b> | <b>Commercially fabricated parts</b>                                     | <b>61</b>  |
| 4.7.1      | Commercially microfabricated coils                                       | 62         |
| 4.7.2      | Design of coils for magnetic actuation                                   | 62         |
| 4.7.3      | Magnets  | 64         |
| <b>5</b>   | <b>SIMULATION</b>  | <b>65</b>  |
| <b>5.1</b> | <b>Electromagnetic design</b>  | <b>65</b>  |
| 5.1.1      | Magnetic force simulations   | 65         |
| 5.1.2      | Mechanical simulations   | 67         |
| <b>5.2</b> | <b>Electrostatic design</b>  | <b>71</b>  |
| 5.2.1      | Force simulations  | 71         |
| 5.2.2      | Mechanical simulations   | 72         |
| <b>5.3</b> | <b>Heat dissipation from mirror</b>                                      | <b>75</b>  |
| <b>6</b>   | <b>MICROFABRICATION</b>  | <b>77</b>  |
| <b>6.1</b> | <b>Microfabrication of the mirror</b>                                    | <b>77</b>  |
| 6.1.1      | Mirror from SOI wafer  | 77         |
| 6.1.2      | Mirror from bulk wafer   | 80         |
| <b>6.2</b> | <b>Microfabrication of the magnetically actuated platform</b>            | <b>81</b>  |
| <b>6.3</b> | <b>Wafer bonding and finalization of the wafer etching and release</b>   | <b>84</b>  |
| 6.3.1      | Different tested bonding metal stacks                                    | 84         |
| 6.3.2      | Eutectic vs. thermo-compression bonding                                  | 85         |
| 6.3.3      | Design of the bonding mask   | 85         |
| <b>6.4</b> | <b>Finalization of the fabrication after bonding</b>                     | <b>85</b>  |
| <b>6.5</b> | <b>Microfabrication of the electrostatically actuated platform</b>       | <b>86</b>  |
| <b>6.6</b> | <b>Assembly process of the magnetically actuated mirror</b>              | <b>92</b>  |
| 6.6.1      | Assembly of the magnets on the backside of the actuation platform        | 92         |
| 6.6.2      | Assembly of the mirror chip on the coil chip                             | 93         |
| 6.6.3      | Assembly process of the electrostatically actuated mirror                | 94         |
| <b>7</b>   | <b>CHARACTERIZATION</b>  | <b>97</b>  |
| <b>7.1</b> | <b>Magnetically actuated mirror</b>                                      | <b>97</b>  |
| 7.1.1      | Coil temperature measurements  | 97         |
| 7.1.1.1    | TCR measurements in the oven   | 98         |
| 7.1.1.2    | Temperatures acquired from thermal imaging                               | 98         |
| 7.1.1.3    | Temperature increase in air and in vacuum                                | 100        |
| 7.1.1.4    | Electromigration   | 101        |
| 7.1.1.5    | Inductance   | 103        |
| 7.1.1.6    | Heat sink  | 103        |
| 7.1.2      | Force measurements   | 103        |
| 7.1.2.1    | Calculation of force   | 104        |
| 7.1.3      | Comparison of coil designs   | 106        |
| 7.1.4      | Microfabrication   | 106        |
| 7.1.5      | Resonant behavior and modes  | 108        |
| 7.1.5.1    | Slow mirror  | 108        |
| 7.1.5.2    | Fast mirror  | 111        |
| 7.1.6      | Measurement of the static angular deflection                             | 112        |
| 7.1.7      | Discussion   | 114        |
| <b>7.2</b> | <b>Mirror flatness characterization</b>                                  | <b>115</b> |
| 7.2.1      | Bonding profiles and their effect on SOI mirror curvature                | 115        |
| 7.2.2      | Bonding profiles and their effect on bulk Silicon wafer mirror curvature | 116        |
| <b>7.3</b> | <b>Electrostatic actuator</b>  | <b>117</b> |
| 7.3.1      | Microfabrication   | 117        |

|          |                                      |            |
|----------|--------------------------------------|------------|
| 7.3.2    | Resonant frequencies and mode shapes | 120        |
| 7.3.3    | Discussion and comparison            | 121        |
| <b>8</b> | <b>SUMMARY AND CONCLUSION</b>        | <b>123</b> |
| <b>9</b> | <b>OUTLOOK</b>                       | <b>129</b> |
|          | <b>REFERENCES</b>                    | <b>131</b> |
|          | <b>AKNOWLEDGMENTS</b>                | <b>137</b> |
|          | <b>CURRICULUM VITAE</b>              | <b>139</b> |



## List of figures

- Figure 1-1: Cross section view of the steering-mirror concept comprising both a magnetically and an electrostatically actuated mirror. The two mirrors are fabricated separately from their underlying actuation platforms and are thus very flat and optimized for light weight and high speed. .... 3
- Figure 2-1: The backside SEM micrograph of the fabricated device with resonant frequency of 30 kHz, S. Hsu et al [12]. The design is based on torsion hinges. The reinforcement frame keeps the mirror flat while resonating. .... 6
- Figure 2-2: Two magnetically actuated devices, realized by Yalcinkaya et al.[47] and Oliveira et al.[28]. a) The mirror of Yalcinkaya et al. is capable of 2-DOF movement. It has a fast scan axis that works at 21 KHz for a mechanical rotation of 65° and a slow scan which is operated with 60Hz for a mechanical rotation of 53°. b) The Oliveira et al mirror has only 1-DOF. It operates at 1.2 KHz for a mechanical rotation of 9°. These mirrors use a micro fabricated coil and an external magnetic field to create a Lorentz force for actuation. .... 7
- Figure 2-3: TALP1000B steering mirror from Texas Instruments [48]. This is a magnetically actuated mirror with conventional wound coils situated under the magnets. The magnets are visible on the mirror surface. Two are positioned on the inner frame and two on the outer frame of the device. .... 7
- Figure 2-4: SEM micrograph of a high aspect ratio RF inductor coil on a silicon substrate; 92 $\mu\text{m}$  thick, 20  $\mu\text{m}$  width and 14  $\mu\text{m}$  spacing, fabricated by Brunet et al [31]. .... 8
- Figure 2-5: Two examples of devices that are used for two different applications in space. a) The device made by Coppoosle et al. [Contraves] [11] has a 0.4° rotation angle and a 1 kHz closed-loop resonant frequency. It is used for inter-satellite telecommunication. b) The device made by Heneien et al. [CSEM] [15] has a rotation angle of 0.06° and a resonant frequency of 1Hz. 3 of these devices are used to help in detection of gravitational waves with linking three stationary satellites that are 5 million kilometers apart. .... 10
- Figure 3-1: a) The force in a voice coil actuator is given by Lorenz law. The current in all the wires has the same direction and the field is generally non-divergent. The direction of the force is given with right hand rule. The parallel magnetic field can be provided with a large magnet that creates a quasi-parallel field around its center. b) The force in a spiral coil is created by the divergence of the magnetic field. The direction of the force is perpendicular to the plane of the spiral coil. The diverging magnetic field can be provided with a small cylindrical magnet magnetized along its central axis. .... 14
- Figure 3-2: A magnetic circuit consisting of a copper winding a stator and a clapper that are made out of ferromagnetic materials. The magnetic field created by the coil is concentrated in the stator and clapper due to the high permeability of the ferromagnetic material. The magnetic circuit path is shown by dashed lines. The force between the stator and the clapper is directly proportional to the stator's cross section surface  $A$ . .... 16
- Figure 3-3: The simulated spiral copper coil with 10 turns is shown. The copper is inside a silicon substrate. The spiral coil has a current density of  $J \approx 10^9 \text{ A/m}^2$ . The voltage is set to 0.6V at the centre of the coil and to 0V at the outer end of the spiral coil. .... 20
- Figure 3-4: The cross section view of the temperature differences inside the 100 $\mu\text{m}$  substrate. The coil's cross section is 50x50  $\mu\text{m}^2$ . The rise in temperature is 2 °C. .... 20
- Figure 3-5: The cross section view of the temperature differences inside the 500 $\mu\text{m}$  substrate. The coil's cross-section is 50 $\mu\text{m}$  by 50 $\mu\text{m}$ . The rise in temperature is 5 °C. .... 20

- Figure 3-6: A schematic cross section view of a coil is shown. This coil has the length  $L$  the outer radius of  $r_2$  and an inner radius of  $r_1$ . The inner radius is filled with air. The coil has  $N$  wire turns. .... 21
- Figure 3-7: The magnetic field at the center of a solenoid with a volume of  $V=10^{-6} \text{ m}^3$ . The radius and length of the magnet are varied such that the total volume stays constant at  $10^{-6} \text{ m}^3$ . The wire used for this calculation has a gauge of  $90 \mu\text{m}$  in diameter with an injected current of  $I = 100\text{mA}$ . As the length of the magnet increases compared to the radius, a maximum magnetic field of  $10\text{mT}$  can be reached. The maximum magnetic fields form ferrite and magnetic materials are also shown as a comparison. .... 22
- Figure 3-8: The simplest electrostatic actuator uses parallel plates. It consists of two plates with the surface  $A$ . An applied voltage on these two plates creates the force. The force of this kind of actuator is non-linear. .... 24
- Figure 3-9: Schematics of the in-plane comb-drive and the vertical comb-drive actuators. a) in-plane comb-drive: two comb sets that are at the same height. The force in this configuration is in the direction of the length  $L$ . b) vertical comb-drive: two comb sets that are at different heights. The force in this configuration is in the direction of the thickness  $t$ . .... 25
- Figure 3-10: The magnetic system is represented by a closed magnetic loop made out of a magnetic material that also has a small air filled gap. A coil winding around the ferrite creates the magnetic field. The total length of the ferrite is denoted by  $l$ . .... 27
- Figure 3-11: A typical breakdown voltage due to Paschen's law.  $p$  is at atmospheric pressure of air  $p = 101 \text{ kPa}$ ,  $a = 43.6 \times 10^6$  and  $b = 12.8$ . According to this graph, the breakdown voltage decreases to a minimum around  $5\mu\text{m}$  separation gap and then increases. .... 27
- Figure 3-12: A comparison of the energy densities of the electrostatic and electromagnetic actuators. This simplified comparison shows that as the surfaces that define the gaps of the capacitor and magnetic loop approach towards one another, the electrostatic actuation can become advantageous. In this graph the transition occurs at around  $3\mu\text{m}$ . .... 28
- Figure 3-13: A cantilever is the simplest flexure beam. The bending value  $Y$  due to an applied load  $W$  at the free end of the cantilever is shown. .... 29
- Figure 3-14: A folded flexure beam is shown. One side of this design can be fixed and the other can move in the desired direction. Folded springs are advantageous in places where available space is an issue and folding the spring will reduce the waste of space around the design. .... 29
- Figure 4-1: The cross section of the solenoid. The coil shown in green is wrapped around the ferromagnetic material. The ferromagnetic material is shown in gray and consists of the stator that is fixed and the moving part or the clapper that is placed at a distance of  $X_0$  from the stator. The pull-in distance is at  $1/3X_0$ . .... 33
- Figure 4-2: A variation of the solenoid design that uses two stators. The clapper is placed above the two stators and is allowed to turn around the fulcrum. The forces are highly nonlinear and pull-in occurs. .... 33
- Figure 4-3: The plunger design. The stator is modified to form an opening where the clapper can be inserted. In this configuration the clapper is called the plunger. As long as the clapper is away from the corners of the opening of the stator and in the linear region shown in orange, the force is to a great extent linear and no pull-in will occur. This linear region is shown with light orange. .... 34
- Figure 4-4: The mask and the fabricated device of the magnetic comb-drive actuator as presented by Schonhardt et al [83]. The combs with the rectangular slots are fixed. The slots are used to fix external coils on the combs. The inner combs can be attracted to left and right and act as plungers. The advantage of this design is that the air gaps are not too small. This facilitates the fabrication of the device. .... 35

- Figure 4-5: Possible configuration of the magnetic comb drive. The actuator, shown in gray, will be placed under the mirror. It can be connected to the mirror through a lever that is shown in blue. This lever can not be longer than 1mm. This is due to the small available linear range of the actuator. This in turn reduces the available torque..... 36
- Figure 4-6: The schematic view of the clapper-stator actuator and the mirror. The coils are shown in green. The magnetic circuit is shown in gray, with the clapper electroplated on the mirror. The mirror is shown in blue. The mirror turns around the pivot point. The forces in this design are due to the magnetic field in the gap of the actuator and are nonlinear. .... 37
- Figure 4-7: Implementation of the voice coil design. The mirror is shown in blue. The voice coils can be put under the mirror. Either the coils or the magnets can be put on the mirror. This design has linear forces. Since the force depends on the gap  $l_e$ , the perfect alignment of the magnet and the coil are essential. .... 38
- Figure 4-8: A schematic top-view of the moving magnet—stationary coil system is shown. The microfabricated coil increases the current density that can be applied to the system. The magnetization direction is along the Z axis of the magnet. The magnet is put 1mm above the coil.. 39
- Figure 4-9: a) Schematic top-view of the moving magnet-stationary coil actuator. b) Cross-section of the FEM simulation shown in polar coordinates. The magnetization direction is along the Z axis of the magnet. The magnet is put 1mm above the coil. It has a diameter of 1mm. the coil is 4mm in diameter with wire cross section of  $50 \times 50 \mu\text{m}^2$ . The injected current in the coil is  $I=1\text{A}$ . .... 40
- Figure 4-10: The rise in the temperature of the actuation platform with a coil integrated on it. The platform thickness is  $300\mu\text{m}$  and the copper coil's cross-section is  $50\mu\text{m}$  by  $50\mu\text{m}$ . The coil extends through the  $100\mu\text{m}$  thick beam till the heat sink. The length of the beam is 8mm. A current density of  $J \approx 10^8 \text{ A/m}^2$  increases the platforms temperature by  $50^\circ\text{C}$ ..... 41
- Figure 4-11: Cross section schematic of the torque driven design. The mirror is covered with a permaloy shown in blue. The mirror is not shown. The permaloy is magnetized along the long axis of the layer, shown by the arrow. A coil is put around the mirror, shown in orange. The magnetic field of the coil, shown with dotted arrows, forces the permaloy to turn towards the magnetic field. .... 42
- Figure 4-12: The schematic configuration of the parallel plate system with a 1 cm mirror. The forces of this kind of actuator are nonlinear. The distance between the mirror and the stationary electrode should be set to 1mm in order to avoid snap-in issues if the mirror has to turn  $3.5^\circ$ ..... 46
- Figure 4-13: The variations of the force of the parallel plate actuator as the gap is changed from 13 to  $65\mu\text{m}$ . the gap distance is shown on the top axis. The corresponding actuation angle for the gap distance is shown on the bottom axis. Three different voltages are shown. 100V is shown in dotted black, 200V is shown in red dashed, and 300V is shown in green line. The forces at the  $65\mu\text{m}$  distance are minute. If the desired actuation distance is reduced the force increases nonlinearly. . 46
- Figure 4-14: Possible schematic of 1cm comb-drive actuator. The comb fingers are created at the far ends of the mirror to increase the torque. A voltage is applied between the stationary and the moving combs. It makes the moving combs move down into the stationary combs..... 47
- Figure 4-15: The force that can be created by the vertical comb design on a 1cm mirror. This figure shows the force due to voltage change from 0V to 200V. Two different gap sizes 5 and  $6 \mu\text{m}$  are shown with red line and dashed black lines respectively. Decreasing the gap increases the maximum force..... 48
- Figure 4-16: The cross section and the top and bottom views of the different parts of the magnetic mirror system including the mirror the magnets and the coils are shown. The magnets are assembled on the mirror. A spacer is put between the mirror and the coils. The coils are microfabricated in a silicon substrate to reduce heat creation. The device is put on a heat sink..... 49

- Figure 4-17: Plot of the available angles for a 1cm mirror at different resonant frequencies " $f_r$ ". The calculations of this figure are done for a 1cm mirror of 300 $\mu\text{m}$  thickness which 70% of its mass is removed by patterning. Three different magnet thicknesses are shown in brown for 100 $\mu\text{m}$ , blue for 300 $\mu\text{m}$  and purple for 500 $\mu\text{m}$ . Increasing the mass of the magnets is advantageous for the amplitude of the system and disadvantageous for the resonant frequency, especially at higher angular deflections..... 50
- Figure 4-18: General concept of the electrostatic design. The mirror is bonded to the platform. The top view of the system shows the three comb sections between the adjacent springs that make the 2D rotation possible..... 51
- Figure 4-19: The achievable angles due to variation of resonant frequencies according to the available forces. The size of the mirror is set to 1cm. The voltage is set to  $U = 150\text{ V}$  and the gap changes from 3 to 5  $\mu\text{m}$ . A gap of 4 $\mu\text{m}$  can give a rotation angle of  $\theta_{\text{mech}} \approx 0.2^\circ$  for a resonant frequency of  $f_r = 1\text{ KHz}$ . These results show that the electrostatic actuator has the same tilt angle as the magnetic actuator for higher resonant frequencies. .... 51
- Figure 4-20: Division of the system to two different mirrors. One is used as a slow moving coarse position finder with a high steering angular range and the other mirror will be a fine tuning mirror that has a fast response time but small steering angular range. .... 52
- Figure 4-21: The translation of the beam of light by " $\Delta x$ " on the second mirror as it is reflected from the first mirror. This translation is dependant on the incident angle of the beam on the first mirror, the translation angles of the mirrors and the distance between the moving mirrors and the fixed mirror. Due to the small deflection of the first mirror, the translation is  $\Delta x = 300\mu\text{m}$  for  $\theta_{\text{inc}} = 30^\circ$ . This means that an optical beam diameter of 8mm can be easily used with this system..... 53
- Figure 4-22: The schematic view of the mirror and the moving platform is shown. The mirror and the moving platform were microfabricated out of two separate wafers. The moving platform was made of a SOI wafer. The hollowed mirror is shown on the top with its frame around it. The moving platform is shown on the bottom. It is connected to the frame via the springs. The frame has holes that were used for alignment during assembly. .... 55
- Figure 4-23: The cross-section of the different parts of the design that were assembled is shown. The different steps consist of (a) assembly of the magnets on the mirror. (b) Assembly of mirror on the spacer. (c) Assembly of spacer on the coil substrate. (d) Attachment to heat sink..... 55
- Figure 4-24: Exploded views of the two actuator-mirrors (slow and fast) are shown. This figure only shows parts that are relevant to the mechanical actuation. The mirror is shown at the top. It has a thickness of 300 $\mu\text{m}$ . The mirror bonds to a platform that is shown under the mirror. The bonding spot is shown in red at the center of the platform. This platform contains four springs that are situated on the four sides of it. The magnets are assembled on the back of the platform. .... 57
- Figure 4-25: The springs of the fast and slow mirrors. The fast mirror spring is shown on top and the slow mirror spring on bottom. The total length of each spring of the fast mirror with  $\theta = 3.5^\circ$  mechanical rotation is 8mm and the total spring length of slow mirror with  $\theta = 0.2$  mechanical rotation is 2.1 mm. the fixed positions are shown with the dotted areas..... 57
- Figure 4-26: Process flow and top view of the electrostatic mirror depicting one-side DRIE for self aligned vertical comb drives. a- DRIE of the device layer. b- BOX removal using vapor phase hydrofluoric acid (HF-VPE). c- DRIE into the handle layer through the device layer. d- DRIE with a delayed mask process on the handle layer to trench out the unwanted combs. e- HF-VPE release of the unwanted combs..... 58
- Figure 4-27: The mirror and the actuation platform are made out of two separate wafers. They could be bonded together at wafer level. .... 59
- Figure 4-28: Assembly of the different parts of the electrostatic actuator mirror. (a) The schematic assembly of the alignment structure with pins on the PCB substrate where the electrical contacts

- are situated. (b) The alignment structure is used to guide the electrostatic mirror chip into its place on the contact electrodes of the PCB. .... 59
- Figure 4-29: The exploded view of the mechanical design for simulations is shown. The frame around the platform and the mirror is not shown. It consists of a moving platform shown on the top. Three "T" shaped springs are situated around the central circle. The angle between them is  $120^\circ$ . The mirror part of the actuator is shown in the lower part. The hollowed part of the mirror is visible and one part is shown with an arrow. .... 60
- Figure 4-30: The dimensions of the spring of the electrostatic actuator. The lower part is  $1000\mu\text{m}$  long and connects to the moving platform. The upper part is  $4000\mu\text{m}$  long and is fixed to the frame shown with dotted triangles. The width of both parts is  $800\mu\text{m}$ . .... 60
- Figure 4-31: The magnetic and electrostatic mirrors can both be integrated on an SOI wafer. The mirrors are fabricated from the handle layer. Electrostatic combs are formed on the device layer. The fixed combs of the electrostatic mirror are formed on the handle layer. A third fixed mirror is needed for the system to reflect the light from the first mirror on the second mirror. .... 61
- Figure 4-32: Cross section view of the coil that consists of two copper layers situated on top of each other, shown in orange. Each layer has a thickness of  $7\mu\text{m}$ . The wire width is  $50\mu\text{m}$ . the gap between two adjacent wires is  $20\mu\text{m}$ . The gaps and the two layers are separated from each other with polyimide shown in dark pink. The coils are fabricated on an Aluminum oxide layer shown in light blue. .... 63
- Figure 4-33: The spiral coils with a diameter of 4 mm. The mask of the coils and the final product are shown in a & b respectively. The magnet, shown in red, is placed on the top centre of the spiral coil as shown in b. the magnet has a diameter of 2mm. The magnetization direction "M" is normal to the surface. Figure c shows one of the spiral coils. The coil has a fill factor of over 70%. The lower layer of the coil can be seen as a darker straight wire on the right side of the figure. .... 63
- Figure 4-34: The unidirectional current coils masks and the final product are shown in a & b respectively. The magnet, shown in red, is placed on the top side but only on one side of the coil as shown in b. Therefore all the current that passes under the magnet move in the same direction. This is why this coil is called the unidirectional current coil. The magnetization direction "M" is parallel to the surface. c) Shows one of the unidirectional current coils. The coil has a fill factor of over 70%. .... 63
- Figure 5-1: The cross-section of the magnetic field of the spiral coil in the Polar coordinates. The magnet magnetization direction  $M$  is shown with a black arrow. The magnet is shown in green and the two layers of the coils are shown in dark blue and violet. The distance between the coil and magnet is 1mm. The divergence of the field is the main factor of creating the force ..... 65
- Figure 5-2: The cross-section of the magnetic field of the unidirectional current coil in the Cartesian coordinates. The magnet magnetization direction  $M$  is shown with a black arrow. The magnet is shown in green and the two layers of the coils are shown in dark blue and violet. The distance between the coil and magnet is 1mm. In this system the force mainly follows the Lorentz force. .... 66
- Figure 5-3: The linear relation between the force and injected current is shown for a coil-magnet distance of  $Z=500\mu\text{m}$ . This result is in complete accordance with the Biot-Savart law of the magnetic field of a steady line current. The result shown here is only for the spiral coil since the unidirectional coil. .... 67
- Figure 5-4: Resulting force of the unidirectional and spiral coil simulations as the coil-magnet distance is changed. The force of the spiral coil design is higher than the force of the unidirectional current coil design. Both designs show nonlinear force behavior as the distance changes. The injected current is kept constant at  $J = 1.33\text{E}9 \text{ A/m}^2$ . .... 67

- Figure 5-5: The maximum deflections of the two magnetic designs are shown. The exerted force is 6mN for the slow mirror (a) and 12mN on the fast mirror (b). The force is applied four times on the four magnets of each design. Two of forces on each design are exerted upwards and two downwards. The slow system (a) with  $\theta = 3.5^\circ$  mechanical rotation deflects to an average of 300 $\mu$ m. The fast system (b) with  $\theta = 0.2^\circ$  mechanical rotation deflects 17 $\mu$ m. .... 68
- Figure 5-6: (a) The Mises stresses of the slow mirror system is shown. (b) A close-up of the spring is shown. The maximum stress is 213MPa..... 68
- Figure 5-7: (a) The Mises stresses of the fast mirror system is shown. (b) A close-up of the spring is shown. The maximum stress is 130MPa for the fast mirror. .... 68
- Figure 5-8: The first three mode shapes of the slow mirror. The shown results are 10 times exaggerated. (a) The first mode is the piston mode at resonant frequency of  $f_r = 160$ Hz. (b) The second mode is a rotation around the diagonal of the square platform at a resonant frequency of  $f_r = 202$ Hz. (c) The third mode is a rotation around the perpendicular diagonal to the second mode, at a resonant frequency of  $f_r = 203$ Hz..... 70
- Figure 5-9: The first three mode shapes of the fast mirror with  $\theta = 0.2^\circ$  mechanical rotation is shown. The shown deflections are 50 times exaggerated. (a) The first mode is the piston mode at resonant frequency of  $f_r = 878$ Hz. (b) The second mode is a rotation around the axis passing through the center of two facing springs of the square platform at a resonant frequency of  $f_r = 1005$ Hz. (c) The third mode is a rotation around the perpendicular axis to the second mode, at a resonant frequency of  $f_r = 1011$ Hz. .... 71
- Figure 5-10: The scalar value of the electric field of one set of vertical combs. The upper comb with the thickness of 40 $\mu$ m was moved into two other combs of thickness 100 $\mu$ m that were placed under it. The width of all the combs is 5 $\mu$ m, and the gap is set to 5 $\mu$ m on each side. .... 72
- Figure 5-11: The total force of 640 combs. Two voltage values of  $U=150$ V and  $U=200$ V are shown in this figure. It can be seen that when the upper comb is completely out of the lower combs or completely plunged into them a transition of the force profile occurs. This is evident at 5 $\mu$ m and 40 $\mu$ m displacements..... 72
- Figure 5-12: The deflection due to force. The mirror is shown on the topside. The force on each electrode is set to 7mN and is shown with a white arrow. (a) The deflection due to force applied to one electrode of the actuation platform. (b) The deflection due to force applied to two electrodes of the actuation platform. Although Applying force to one electrode easily attains the  $0.2^\circ$  angle, applying two forces to two electrodes leads to a deflection of slightly less than  $0.2^\circ$ ..... 73
- Figure 5-13: Lateral forces of 30mN were applied laterally shown with white arrows. This force is three time higher than the lateral force at full deflection. The maximum lateral deflection is 0.3  $\mu$ m. This is well bellow the “one third of the total distance” snap-in criterion ..... 74
- Figure 5-14 : The Mises stress of the system when the force is applied to two electrodes is shown. The maximum Mises stress is 200 MPa. The maximum stress occurs at the corners..... 74
- Figure 5-15: The resonant frequencies of the system are shown. (a) The first mode is the piston mode at  $f_r = 563$  Hz. (b) The second is a deflection at  $f_r = 918$  H. The third mode is at  $f_r = 926$  Hz which is slightly bellow 1Khz..... 75
- Figure 5-16: The results of simulations and calculations of temperature increase on the mirror vs. the heat flux. The electrostatically actuated and the fast magnetically actuated mirrors show lower increase in temperature compared to the fast electromagnetic mirror. This is mainly related to the shorter length of the springs of these two devices compared to the spring length of the magnetically actuated slow mirror. From left to right, the simulated points show 1mW, 10mW, and 100mW of applied Heat on the mirror topside..... 76

- Figure 6-1: Two masks that are used for the delayed mask process. a) The first mask for the delayed mask process is used to create the outer edge of the round mirror as well as the frame around the mirror by DRIE etching. b) The second mask creates the inner form of the mirror as well as continuing to shape the outer edge and the frame. .... 78
- Figure 6-2: a) The SOI wafer with the patterned resist on top. b) Patterning of the SiO<sub>2</sub> layer with BHF. c) Replacement of the resist that is patterned with the first delayed mask. d) DRIE of the outer rims which is the first part of delayed mask process. e) Removal of the resist and continuation of DRIE with the SiO<sub>2</sub> as the second delayed mask. f) Removal of the excess SiO<sub>2</sub> on the surface. .... 79
- Figure 6-3: SEM micrograph of the resulting shape of the backside of the mirror. The small circles are used as bonding pads. .... 79
- Figure 6-4: The process flow of the mirror made form a bulk silicon wafer. (a) Thermal oxidation. (b) Photoresist patterning on front and back sides. (c) Opening of the SiO<sub>2</sub> in BHF. (d) DRIE on the backside. (e) 400nm thermal oxidation. (f) Spray-coating of the backside with photoresist. (g) Photoresist patterning. (h) Opening of the SiO<sub>2</sub> in BHF. (i) Metal deposition. (j) Lliftoff of excess metal. .... 81
- Figure 6-5: The result of one circular deposition. The close-up of the circle shows that the metal is deposited in the hole without touching the SiO<sub>2</sub> around it. .... 81
- Figure 6-6: a) The mask designed for the front side and that creates the springs and the platform for the magnets. b) The backside mask that creates a release structure which removes the unwanted mass of the platform leaving only the bonding and alignment structures behind. .... 82
- Figure 6-7: a) E-beam metal deposition on the wafer using the patterned negative resist. b) Resulting metal structure. c) Patterning of the photoresist with the front side mask and the subsequent DRIE of the front side. d) Patterning of photoresist on the handle layer and opening the holes and trenches in the SiO<sub>2</sub> layer using BHF. e) Partial opening of the handle layer by DRIE. . 83
- Figure 6-8: SEM micrographs of the front and backside. a) One of the springs that was etched on the front side of the SOI wafer. B) The etched backside of the wafer with the holes and trenches used for the releasing process and also the bonding and alignment structures that will remain after the release. .... 83
- Figure 6-9: Optical picture of the released backside and the remaining bonding and alignment structures. .... 84
- Figure 6-10: The bonding mask and the seven different bonding patterns that were put on the different chips. The square lines around each chip are to bond the frames of the magnetic platform chips with their corresponding frames around the mirror chips. The central part of each design (dots and rings) is the part that attaches the mirror to the actuation platform. .... 84
- Figure 6-11: a) The schematic cross section of the bonded wafer. b) Finalization of the DRIE on the handle layer of the actuation platform. c) Complete removal of the device layer of the mirror by DRIE. d) Release of the unwanted structure by HF-VPE. e) Release of the chip from the wafer. .... 86
- Figure 6-12: The masks designed for the front side and that creates the springs and the moving platform. a) The mask that creates the opening that thin down the springs. b) The mask that creates the combs around the moving platform and also shapes the springs. .... 87
- Figure 6-13: The backside masks that creates a release structure which removes the unwanted combs and mass of the platform leaving only the bonding and alignment structures behind. .... 88
- Figure 6-14: The fabrication concept that creates two pairs of combs is shown. One pair is on the device layer and one on the handle layer. The upper combs on the frame were removed in this process as well as the lower combs on the mirror. The combs remaining on the lower part of the frame and the combs remaining on the upper part of the mirror produce the vertical actuation. .... 88

- Figure 6-15: The process flow of the electrostatic actuator. (a) Cleaning of the SOI wafer. (b) Aluminum deposition. (c) Photoresist lithography and opening of the aluminum in Alu etch. (d) Removal of first photoresist and application of the second layer and photolithography. (e) First DRIE step of the combs and trenches on the front side. (f) HF-VPE of the BOX. (g) DIRE etching into handle layer. (h) Removal of photoresist and delayed mask process for thinning down the springs. (i) Removal of Al and thermal oxidation. (j) Photoresist spinning and patterning of the SiO<sub>2</sub> of the backside. (k) Removal of first photoresist and application of the second photoresist layer with patterning. (l) First DRIE and partial opening of the backside. (m) Removal of the resist and second DRIE of the backside (second delayed mask). (n) Release of the structures by HF-VPE. (o) Released mirror chip..... 90
- Figure 6-16: A closer look at the mask with comparison to the process flow. There is a trench circumventing all the combs shown with the dashed arrow. This is the release trench for one of the two sets of combs created on the chip front side. This trench is smaller than the other trenches; therefore it is etched slower than the others in DRIE etching. The combs and the trench used for releasing the chip are also shown..... 91
- Figure 6-17: A comparison of the first delayed mask process of the backside and the process flow. In this step the open trenches are partially etched. .... 91
- Figure 6-18: A comparison of the second delayed mask and the process flow. In this step all the trenches that were partially etched will be etched until the BOX. The trench above the combs is only etched until it reaches the combs. .... 91
- Figure 6-19: SEM micrograph of the backside of the actuation platform. The interdigitated combs can be observed..... 91
- Figure 6-20: The handmade device used for assembly of the magnets. It consists of a platform where the magnetic mirror is put and hold in place using a vacuum hole. The platform can rotate around the x and y axes. It is also equipped with a vacuum gripper tip to hold the magnet. This part can move with 6-DOF (X, Y, Z and rotations) to position the magnet. .... 92
- Figure 6-21: a) The backside of the actuation platform with the assembled magnets. The magnets were positioned around the four corners of the mirror and glued to their place. b) Alignment of the magnets is ensured by pushing them against the pillar at each corner..... 93
- Figure 6-22: a) The coil chip with the four holes. b) The coil chip mounted on the aluminum slab. The four pins are placed in the holes and the spacers are positioned on them. c) The mirror chip is mounted on the pins. The distance between the magnets and the coils is 550  $\mu\text{m}$ . .... 93
- Figure 6-23: The base chip made out of PCB. There are three electric pads arranged circularly that connect with the electrodes of the electrostatic actuator. The small bored square pads can be used for connecting the lower body of the actuator to ground. The circular holes that are the furthest from the centre are used to guide the alignment structure into its place..... 94
- Figure 6-24: The alignment structure glued to place on the PCB using the alignment holes and pogo pins. The pogo pins were removed after this procedure..... 94
- Figure 6-25: The electrostatic was put into the alignment structure and aligned on the electrodes. The electrode contacts can be glued to place. Pogo pins can also be used..... 95
- Figure 7-1: 4 point measurements of the voltage and the current for finding the TCR. A small current is injected in the coil that is placed in an oven. The corresponding voltage is read from the voltmeter as the oven's temperature is increased. The temperature is read from the oven. The coils resistance is calculated from the voltage and the current which in turn can be used to calculate the TCR. .... 97
- Figure 7-2: A typical result of the TCR measurements that shows the presence of hysteresis in the ensemble of the system. This can be seen in the nonlinearity of the curve as the temperature

- increases (ramp up) and another as the system is cooling down (ramp down). This hysteresis should be mainly due to temperature differences between the coil and its surrounding. .... 98
- Figure 7-3: Temperature of the spiral coil at  $I = 500\text{mA}$ . It can be seen that the areas of the highest temperature are between to adjacent copper turns. There is a temperature gradient towards the outer rim of the coil..... 99
- Figure 7-4: The temperature increase due to current injection for 18 seconds. This graph is taken on a line that is shown in Figure 7-3. The “Mean” curve shows the average temperature of this line and the “Max” curve shows the point with the highest temperature..... 99
- Figure 7-5: The temperature increase due to current injection according to thermal emission measurements performed with an infrared camera and the results of TCR based temperature measurements are shown for comparison. The  $\text{TCR}=0.0039$  is in red,  $\text{TCR}=0.00256$  is in black, the mean temperature from radiation measurements is in blue and the maximum temperature in the radiation test is in green. The TCR graphs (red and black) and the mean temperature from radiation measurements (blue line) are of the same nature. .... 100
- Figure 7-6: Results of temperature increase of the coil for a current injection of  $I = 500\text{ mA}$  in vacuum shown in black and in air shown in green. The vacuum chamber has of pressure  $P \approx 6\text{E-}2\text{ mbar}$ . When systems reach thermal equilibrium a temperature difference of  $T_{\text{vac}} - T_{\text{air}} = 95\text{ }^\circ\text{C}$  can be seen between the coil in vacuum and the coil in air. This is due to absence of convection in vacuum. .... 101
- Figure 7-7: Consecutive long duration test of the coil’s resistance variations. The system is injected with  $I = 500\text{ mA}$  and the resistance of the coil was registered as a function of time. The system is then let to cool down and the procedure is repeated again for 5 times. In total the system was operated for 85 hours. The first two measurements had a different heat sink which explains the higher maximum resistances compared to the other 3 measurements. It can be seen that after each measurement the system goes back to the same starting value of  $R = 20.16 \pm 0.1\ \Omega$  which signifies the absence of Electromigration. .... 102
- Figure 7-8: A good and a bad heat sink. a) The heat sink covers the whole backside area of the coil substrate. b) The heat sink covers the backside only partially. c) The resulting uneven heat distribution led to the fracture of the substrate and coils. .... 103
- Figure 7-9: Built force-measurement setup consisting of a cantilever with a known spring constant with a magnet attached to one end of it. The other end is fixed. The coil is placed under the magnet at a certain distance. As the current is increased the displacement of the cantilever is observed using an optical profiler..... 104
- Figure 7-10: The resulting forces versus varying distances. The simulation results are also shown for comparison. The spiral coil configuration creates a higher force than the unidirectional coil which is in accordance to the simulation results. The curve fit of the measured forces are also shown that used the proposed empirical formula ..... 104
- Figure 7-11: The results of the experiment for the spiral coil and a cantilever with  $k = 42\text{ N.m}^{-1}$ . Three different initial values of the coil magnet gap ( $500\mu\text{m}$ ,  $400\mu\text{m}$ ,  $300\mu\text{m}$ ) are shown. The corresponding curve fits are shown in solid lines. The fits represent the numerical values very well. The snap-in point is shown with black arrows..... 105
- Figure 7-12:  $\text{SiO}_2$  layer that protects the structures bellow the mirror from being etched unwontedly. The round mirror is shown at the bottom. The spring is seen under the silicon dioxide layer that protected it during DRIE etching. .... 107
- Figure 7-13: An extreme misalignment example. A perfect alignment puts the edge of the round mirror above the edge of the square actuation platform, just before the spring. In general a misalignment of several ten of micrometers was present in one or two axes of the chips..... 107

- Figure 7-14: Having too much glue could lead to misalignment of the magnet and the alignment structure as shown here. The glue does not let the magnet to be pushed to its place..... 107
- Figure 7-15: The resonant behavior of the system was measured using an impedance analyzer and a Laser Doppler Vibrometer (LDV). The impedance-meter excites the mirror at different frequencies and reads the output of the LDV..... 108
- Figure 7-16: The response of the mirror to a frequency sweep from 100 Hz to 300 Hz is shown for air in red and for vacuum in black. The vacuum pressure was  $P=0.05$  mbar. The  $Q$  factors in air and vacuum for the first peak (142 Hz) are  $Q = 38$  and  $Q = 63$  respectively..... 109
- Figure 7-17: Setup that was used to find the mode shapes of the 3 resonant frequencies. An AC voltage source sends a sinusoidal signal with a certain frequency to the mirror and to an oscilloscope with two input channels. The LDV output is also sent to another channel of the oscilloscope. A Matlab program was used to read out the oscilloscope data and calculate the amplitude and phase shift of the oscillating mirror. It could also scan the laser light on the mirror surface..... 110
- Figure 7-18: a) The second mode rotates around one of the diagonals of the mirror actuation platform at 186 Hz. b) The third mode rotates around the diagonal perpendicular to the first diagonal at 250 Hz..... 110
- Figure 7-19: The response of the mirror to a frequency sweep from 40 Hz to 1500 Hz is shown for air in red and for vacuum in black. The vacuum pressure was  $P=0.05$  mbar. The  $Q$  factors in air and vacuum for the first peak (770 Hz) are  $Q = 32$  and  $Q = 110$  respectively..... 111
- Figure 7-20: The second mode rotates nearly around a pair of the springs that face each other. b) The third mode rotates around the pair of springs that are perpendicular to the first pair as predicted by simulations. .... 112
- Figure 7-21: Setup for static angular deflection measurements of the mirror. It used a beam splitter and a laser. The laser beam was directed towards the mirror surface through the beam splitter. The reflected light was shone on a screen positioned at a known distance from the beam splitter. Therefore as the mirror deflects by  $\theta$  degrees the laser beam would deflect by  $2*\theta$  degrees. .... 112
- Figure 7-22: The resulting rotation angles for the X and Y directions. According to this graph the mirror can be mechanically deflected to 3.5 degrees with a 350 mA current injected in each coil. These results show that the mirror works within the specifications and is quite symmetrical. .... 113
- Figure 7-23: If the distance between the coil and the magnet is increased to  $850\mu\text{m}$ , the total deflection drops due to the decrease of force by the inverse square law. But the force profile becomes quasi-linear (small non-linear variation). The mirror deflects  $2^\circ$  with a current injection of  $I = 500\text{mA}$  in each coil..... 113
- Figure 7-24: The rotation angle of the fast mirror is shown. The shown mirror has a quasi linear response to the applied current. It reaches the desired rotation of  $0.2^\circ$  and has a symmetrical response as can be seen from the linear fits of the measurements in X and Y directions..... 114
- Figure 7-25: The surface properties of the mirrors were measured after bonding with a WYKO optical profiler from VEECO. Four different typical results of the mirror curvature due to the bonding profile are shown. The best results are from the mirrors that are connected closer to the centre (a and b). .... 116
- Figure 7-26: The surface properties of the mirrors made with a bulk silicon wafer are shown for two different mirrors. a) The mirror is from the center of the wafer and has an RMS curvature of  $R_q = 67\text{nm}$ . b) The mirror is from the corner of the wafer and has an RMS curvature of  $R_q = 114\text{nm}$ . A comparison bulk and SOI wafers shows a slightly better mirror flatness quality for the mirror fabricated from the bulk silicon wafer. .... 117

- Figure 7-27: From right to left, the ensemble of the moving platform, the combs, the trench that defines the electrode and the spring are seen. .... 118
- Figure 7-28: Two backside close-ups of the released combs are shown. The combs on the left are the fixed combs and the combs on the right side are situated on the moving platform. b) The combs on the right side are under-etched due to notching effect of the DRIE as the combs were etched from the front side. The roughness on the bottom of the combs on the left side is due to un-optimized DIRE process on the front side of the mirror..... 118
- Figure 7-29: The oxide layer provides complete protection for the combs. This figure shows the backside before the combs on the right side are released with HF-VPE. All the trenches between the combs are completely closed with oxide except the opening between the combs and the spring. The silicon grasses that can be seen here were removed by an additional Oxidation and during HF-VPE. .... 119
- Figure 7-30: a) The original gap between the combs on the top of the actuator has increased from  $6\mu\text{m}$  to  $8\mu\text{m}$  during processing. The thickness of the combs has decreased from  $15\mu\text{m}$  to  $13\mu\text{m}$ . b) The gap at the bottom after  $80\mu\text{m}$  of etching increased to more than  $9\mu\text{m}$  and combs width decreased to  $7.5\mu\text{m}$ . This shows a  $4^\circ$  deviation from vertical etching in the DRIE process. .... 119
- Figure 7-31: a) The rough surface of the spring after DRIE. b) The springs were thinned down  $23\mu\text{m}$  instead of  $20\mu\text{m}$ . the mean surface roughness of the sample shown on top-right side of the graph is  $150\text{nm}$ . The maximum peak to valley height is around  $700\text{nm}$ ..... 120
- Figure 7-32: The response of two different actuators to a frequency sweep from  $40\text{ Hz}$  to  $1200\text{ Hz}$  is shown There are two resonant peaks at  $367\text{Hz}$  and  $526\text{Hz}$  for the first mirror (shown in black) and  $360\text{Hz}$  and  $520\text{Hz}$  for the second mirror (shown in red). .... 121
- Figure 7-33: a) The first mode corresponds with the piston movement of the mirror. b) The second mode corresponds with a rotation around one spring of the actuator. .... 121



# 1 Introduction

Micro Electro Mechanical Systems (MEMS) have been used more and more extensively in the past decades. The reason lies in their small size leading to advantages that can not be achieved with larger-scale devices. They are usually lighter, faster, more precise, and have lower power consumption.

MEMS-based optical-beam steering scanners are a major part of MEMS devices. They are presently in use in various systems, including fiber optic telecommunication, scanning mirrors for displays and LIDARS, microscopy, endoscopy, tomography, optical attenuators, etc. The dimensions of these mirrors vary from  $10\mu\text{m}$  to  $1\text{mm}$ . They are usually used in scanning mode (resonance and static) or in the “on – off” state [1-5].

In this project we were interested in mirror systems for potential use in LIDAR and inter-satellite laser telecommunications. Inter-satellite laser telecommunication links mainly consist of steering mirrors, and optical components. Adaptive optics is also sometimes used to help in reduction of atmospheric, thermal drift, and misalignment aberrations. Operating with laser beams at distances of a kilometer and further requires laser beam diameters of several millimeters, thus they need mirrors of the same diameter. These diameters are in the range of tens of millimeters to more than 100 millimeters [6-21]. The steering angular ranges of these mirrors [6-21], are in the order of 1 mrad to 100 mrad. The angular resolution of these devices is of great importance since a slight rotation at the origin translates to huge translations at distances of several thousand kilometers. therefore The angular resolution of these mirrors is usually in the range of  $1\mu\text{rad}$  with the best value of  $0.1\mu\text{rad}$  [15]. If the effects of other parts of the telecommunication system are not considered, the angular resolution of the moving mirrors of these systems is mostly dependant on the accuracy of the feedback system.

Devices currently used in space are usually made with conventional technologies and are bulky. Inter-satellite communication and LIDAR applications require lightweight, fast steering and scanning mirrors. These qualities are all present in MOEMS devices. However use of MEMS devices, in general, has been limited in space. The reason lies in the maturity of the conventional technologies which have proven to be accurate and reliable. However, as it was the case of accepting MEMS devices in consumable products, space application are also slowly becoming comfortable with using MEMS.

The present project aims at developing a compact microfabricated steering mirror system of relatively large size (10 mm mirror diameter).

The system presented here is a two-mirror system that is based on microfabrication of large mirrors of 10mm in diameter that can be steered over a wide steering angular range. The system is designed to be reliable and space compatible [22] including resistance to thermal effects, fatigue, stiction, frictionless, and, to the extent possible, shock resistance. The two-mirror system consists of an electrostatically actuated high resonant frequency mirror with a small mechanical actuation range ( $f_r = 1\text{ kHz}$ ,  $\theta = \pm 0.2^\circ = 3\text{ mrad}$ ) and a magnetically actuated mirror with low resonant frequency and larger mechanical actuation range ( $f_r = 200\text{ Hz}$ ,  $\theta = \pm 3.5^\circ = 61\text{ mrad}$ ). Another magnetically actuated mirror with high frequency and low actuation range was also fabricated in this thesis ( $f_r = 1\text{ kHz}$ ,  $\theta = \pm 0.2^\circ = 3\text{ mrad}$ ) and it can replace the electrostatically actuated mirror. The

electrostatic mirror is actuated by an integrated vertical comb-drive. The electromagnetic mirror comprises magnets that are mounted on the backside of the mirror platform and planar coils that are positioned under the magnets to create the magnetic actuation force as shown in Figure 1-1. The angular resolution of these mirrors is also dependant on the feedback system and should also be in the  $1\mu\text{rad}$  range.

The sizes of the mirrors fabricated in this thesis are sufficiently large to be used in LIDAR systems. However, they are small in comparison with the mirrors that are used for inter-satellite telecommunications that have diameters of around 100 mm (e.g. Baister et. al. [9]; mirror diameter 7cm). In comparison, this means that the divergence angle of a Gaussian beam is seven times larger for the 10mm mirror fabricated in this thesis, since this angle is inversely dependant on the beam waist diameter of a Gaussian beam. However, even the use of simple beam-expander optics in front of the outgoing laser beam can increase the beam waist; thus decreasing the divergence angle. This means that the angular resolution of the system can also be improved using a beam expander setup, since any angular rotation of the laser before the beam expander will be scaled down by the expansion ration after the beam expander.

The reason why the system is divided into two mirrors is that the non-resonant scan angle of a single mirror decreases if its resonant frequency is increased (faster response time). This is due to the inverse relation of these two system attributes. This problem can be surmounted by the use of two mirrors. Analogously, this principle is used in many adaptive-optics systems for telescopes and imaging systems, and to our best knowledge this principle has not been implemented using micro-machining.

The designs should also be complemented with a very flat mirror capable of supplementing the maximum actuation range attainable. Thus, the choice of microfabrication as method is advantageous due to the use of crystalline silicon and the ease of fabrication. It has been shown that micro fabricated mirror devices are capable of withstanding billions of working cycles with nearly no wear [2]. The ease of batch production is also an advantage of microfabrication. It can tremendously reduce the cost per piece of the final device. Therefore it was decided to use microfabrication of silicon wafers for making the micromechanical part of the device.

A schematic cross section of the complete system is shown in Figure 1-1. The device is based on a 3-mirror configuration, with two movable mirrors. This system consists of an electrostatically actuated mirror, shown on the left part of Figure 1-1 that acts as a fine tuning position finder that has a small range in the order of  $\pm 0.2^\circ$  mechanical and a short response time in the order of 1ms this mirror acts as a fine tuning position finder. The other mirror that is magnetically actuated, shown on the right part, acts as a coarse position finder with a large deflection angle in the order of  $\pm 3.5^\circ$  mechanical and a long response time in the order of 10ms. The fixed mirror that is positioned above the two moving mirrors reflects the light reflected from the electrostatically actuated mirror on to the magnetically actuated mirror. As it was mentioned before, the electrostatically actuated mirror can be replaced with a magnetically actuated mirror which has the same rotation angle and response time. All of the mirrors shown in Figure 1-1 are capable of 2 dimensional "2D" movements.

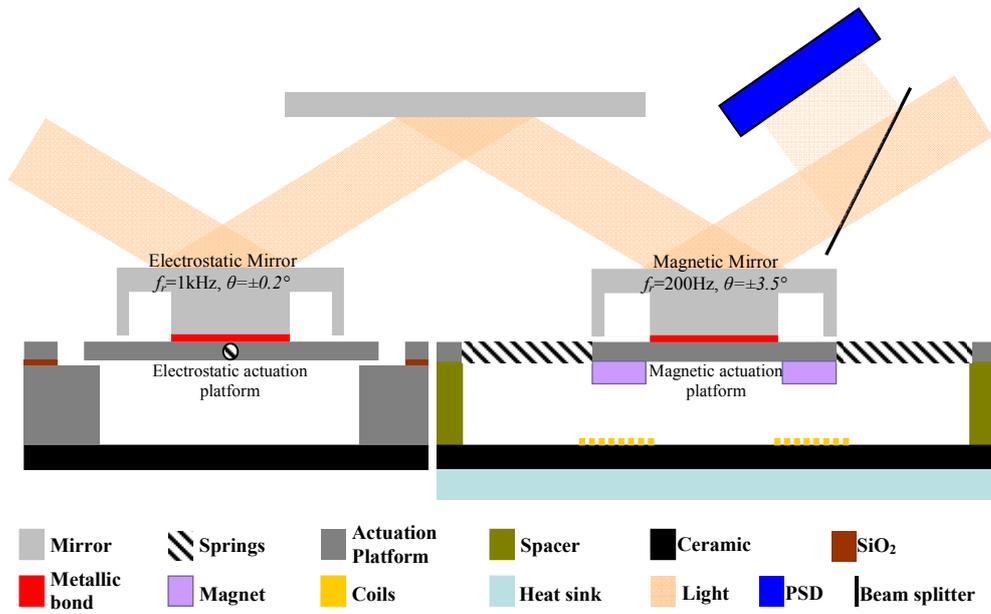


**Figure 1-1:** Cross section view of the steering-mirror concept comprising both a magnetically and an electrostatically actuated mirror. The two mirrors are fabricated separately from their underlying actuation platforms and are thus very flat and optimized for light weight and high speed.



## 2 State of the art

Several different devices are available that use beam steering scanners [2-4]. They can be divided to three main categories of interest:

- 1) Galvo-mirrors: These devices created with conventional technologies are used for laser scanners. These devices usually utilize conventional electric servo motors.
- 2) Microfabricated devices: This category is mainly used in optical systems for earthbound telecommunications.
- 3) The category of the devices that are created with conventional technologies have been constructed to be used in space

There are many different actuation methods of these devices, consisting of electrostatic, magnetic, piezoelectric, thermal actuators, etc. In this project only the two non-contact actuation methods, electrostatic and magnetic, were considered. In the following the Galvo-mirrors and the microfabricated devices using these two actuation methods will be discussed followed by the category of devices used nowadays in space telecommunications.

### 2.1 Galvo-mirrors

Galvo-mirrors are the most widely used mirrors for laser scanning and steering. They are usually mirrors capable of one dimensional “1D” actuation since they are mounted on a rotating servo motor. For 2D actuation two of them are combined together. By using a servo motor for actuation their rotation angle has no limit. They usually have diameters of a few millimeters to over 10mm. Their resonant frequency also ranges from 1Hz to more than 10kHz. Their disadvantage can be in their total mass and 1D actuation.

### 2.2 Microfabricated devices

There are several different classes of microfabricated mirrors. However, the methods of suspension and pivots used in these devices can be categorized in three different design groups: Gimbal design (either 1-DOF or 2-DOF) [25-29], tip-tilt designs capable of converting in-plane movements to a movement in 3D [23-28] and bending flexure design [9-11]. The dimensions of these devices vary from a few hundred micrometers to about millimeters [10, 14]. Their mechanical tilting angles vary between a few degrees up to several tens of degrees. Three main categories of Microfabricated mirrors are in use nowadays:

Scanning mirrors [21, 29-40]: Scanning mirrors are largely used in projectors. There are several different companies and groups working on these devices.

ON-OFF mirrors [2, 28-31]: ON-OFF mirrors are used in fiber optics [25-27], projectors [2] as well as space applications [41].

Steering mirrors [5, 29-36]: Steering mirrors that are of interest in this project are used in optical links and LIDARS.

### 2.2.1 Electrostatic actuation

Many of the scanners use electrostatic actuation (parallel-plate actuation [5, 22, 51] and comb-drive actuation [32, 40-50, 55, 56, 58]). Electrostatic actuation has been the preferred method of actuation for MOEMS. This is mainly due their ease of fabrication and compatibility with the microfabrication processes as well as very low power consumption and the straightforward actuation physics.

Very high resonant frequencies and high tilt angles are some of the notable achievements for the electrostatic actuators. Three interesting examples with resonant frequencies above 10 kHz are given [13, 18, 37], with the prominent result of 30 kHz, S. Hsu et al [30] as shown in Figure 2-1 that was fabricated in the Fraunhofer Institute for photonic Microsystems. This device has a mechanical tilt angle of  $\pm 10^\circ$ . It should be mentioned that all of these devices are operated in resonant scanning mode.

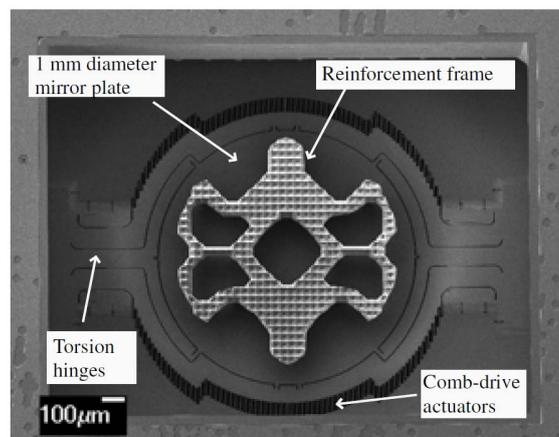


*Figure 2-1: The backside SEM micrograph of the fabricated device with resonant frequency of 30 kHz, S. Hsu et al [12]. The design is based on torsion hinges. The reinforcement frame keeps the mirror flat while resonating.*

### 2.2.2 Magnetic actuation

There are several different classes of magnetic actuators and many of them are used for fabricating magnetically actuated micro-mirrors. Any magnetic actuator can consist of three main components: coils, magnets and ferrites. Magnetic actuators can be classified into two main groups. In the first group the moving part of the actuator is the coil [34, 35, 54, 57, 61]. In the second group the moving part is the magnet [11, 41-43] or the ferrite [42-44].

The necessity of having coils or magnets that have to be integrated on the device has made magnetic actuation less favorable and less utilized until recent years. However the advantage of magnetic actuation comes from the higher created forces [45, 46]. In general the electromagnetic work can be up to  $10^4$  times bigger than the work done by an electrostatic counterpart [46]. There are other advantages in electromagnetic actuation; namely a higher adaptability in transport of the magnetic energy, comparable resonant frequencies to the electrostatic actuators while attaining higher rotation angles and the viability of finer continuous rotation and translation movements [45]. Two examples of magnetically actuated devices which are closer to the tilt angle and size realm of this project are realized by Yalcinkaya et al.[47] and Oliveira et al.[28]. They are shown in figure 3a&b. The mirror of Yalcinkaya et al. is capable of 2-DOF movements. It has a fast scan axis that works at 21 kHz for a mechanical rotation of  $65^\circ$  and a slow scan axis that has a natural frequency

of 400Hz but it is operated with 60Hz for a mechanical rotation of  $53^\circ$ . The Oliveira et al mirror has only 1-DOF. It operated at 1.2 kHz for a mechanical rotation of  $9^\circ$ . Both of these mirrors use a micro fabricated coil and an external magnetic field to create a Lorentz force. These examples show devices that have the dimensions close to those needed in the present project, therefore confirming the possibility of making 1cm devices out of silicon.

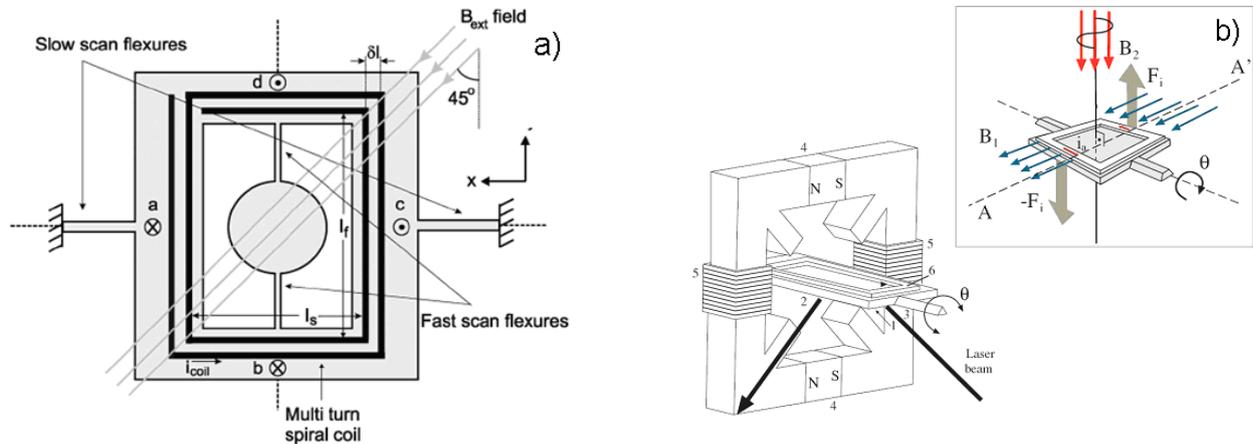


**Figure 2-2:** Two magnetically actuated devices, realized by Yalcinkaya et al.[47] and Oliveira et al.[28]. a) The mirror of Yalcinkaya et al. is capable of 2-DOF movement. It has a fast scan axis that works at 21 KHz for a mechanical rotation of  $65^\circ$  and a slow scan which is operated with 60Hz for a mechanical rotation of  $53^\circ$ . b) The Oliveira et al mirror has only 1-DOF. It operates at 1.2 KHz for a mechanical rotation of  $9^\circ$ . These mirrors use a micro fabricated coil and an external magnetic field to create a Lorentz force for actuation.

Another design that is very close to the design developed in this thesis is the steering mirror from Texas Instruments Inc. shown in Figure 2-3 named TALP1000B [48]. This is a magnetically actuated mirror with conventional wound coils situated under the magnets. The magnets are visible in Figure 2-3. Two are positioned on the inner frame and two on the outer frame of the device. The mirror is 3.2mm x 3.6mm with a resonant frequency of  $f_r = 130\text{Hz}$ . The mechanical rotation angle is  $\pm 5^\circ$ .

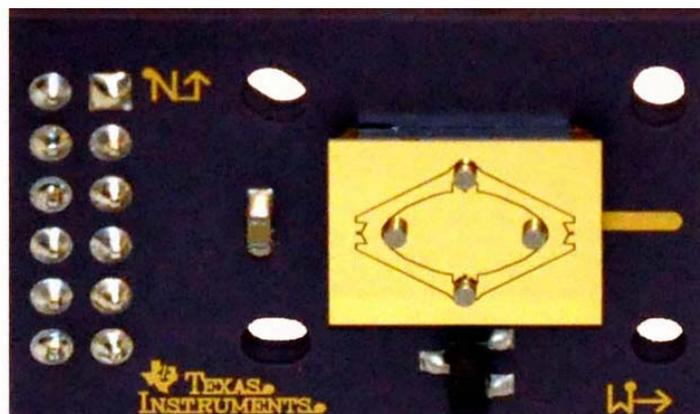


**Figure 2-3:** TALP1000B steering mirror from Texas Instruments [48]. This is a magnetically actuated mirror with conventional wound coils situated under the magnets. The magnets are visible on the mirror surface. Two are positioned on the inner frame and two on the outer frame of the device.

### 2.2.3 Micro-coils

An important part of the magnetic actuators used in MOEMS is the microfabricated coil. These coils are also used in micro pumps and very commonly as micro antennas. Electroplating and lithography are used to create the coils on silicon [44-51]. Very high thickness and aspect ratios can be achieved with these techniques [49, 50]. Brunet et al [49] demonstrates the high aspect ratio microfabricated coils fabricated. An SEM micrograph of the high aspect ratio RF inductor coil on a silicon substrate is shown in Figure 2-4. This coil is 92  $\mu\text{m}$  thick, 20  $\mu\text{m}$  wide and it has 14  $\mu\text{m}$  spacing between adjacent copper wires.



*Figure 2-4: SEM micrograph of a high aspect ratio RF inductor coil on a silicon substrate; 92 $\mu\text{m}$  thick, 20  $\mu\text{m}$  width and 14  $\mu\text{m}$  spacing, fabricated by Brunet et al [31].*

Usually a coil is positioned on a heat sink if very high current densities are supposed to be injected into it. The heat sink helps in evacuating the created heat by the coil. The problem with putting the coil on the moving parts of a microfabricated device is the effect of the created heat on those parts. This could be problematic for space application since there is no heat convection in space. A solution to this problem is to encapsulate the system in a gas filled environment if it is supposed to work in space. However this is not a big problem for devices that work in resonance in air, such as the example in Figure 2-2. Nevertheless, the use of microfabricated coils that are positioned on a heat sink can greatly increase the maximum current density that is injected into them [76, 78]. This is due to the increasing surface to volume ratio that increases heat dissipation. Current densities of  $J=10^9 \text{ A.m}^{-2}$  can easily be obtained from these micro-coils.

### 2.2.4 Magnetic materials for MEMS

There are four parameters that are important in defining the properties of a magnetic material and where and how it can be used:

Remnant magnetic field  $B_r$ , is the magnetic induction corresponding to zero magnetizing force in a magnetic material after saturation in a closed magnetic circuit.

Saturation is the state reached when an increase in applied external magnetizing field  $H$  cannot increase the magnetization of the material further. This is represented with  $B_s$ ; the saturation magnetic field.

Coercivity  $H_c$ , is the intensity of the applied magnetic field required to reduce the magnetization of that material to zero after the magnetization of the sample has been driven to saturation.

Maximum energy product  $(BH)_{max}$ , is the maximum product of  $B$  and  $H$  which can be obtained on the demagnetization curve. This value is a good indicator of the magnets' strength.

Both soft magnetic materials and permanent magnetic materials are used in MEMS. Soft magnetic materials such as NiFe are used more often due to their ease of deposition [44, 51-58]. They are usually deposited using electroplating. However these materials usually have a low  $(BH)_{max}$  and  $H_c$  and they demagnetize very easily. However their  $B_r$  can be higher than permanent magnets. That is why they are usually used in anisotropic configurations to reduce the demagnetizing effects [9, 30, 36, 52-54]. They are also used to create the magnetic circuits that concentrate the magnetic flux to a certain position. This reduces the loss and increases the magnetic field at the desired position, therefore increasing the magnetic force.

Bulk hard magnetic materials have a very high  $(BH)_{max}$  and  $H_c$  compared to the soft magnetic materials. However their integration to MEMS is a challenge that is yet to be overcome. Great advances have been made in recent years towards this goal. There are several techniques to integrate magnetic materials onto MEMS [[81-83] *and references therein*]. Bulk magnetic materials are usually fabricated from compressed powders. Therefore one solution for use in MEMS is to bond a magnetic wafer on the Si wafer and selectively etch the magnetic material [59]. The drawback would be that all the subsequent fabrication steps should be compatible with the magnetic material.

Some laboratories have used resins containing the magnetic powder and curing them on the wafer [[59] *and references therein*]. Results usually show significant variations in magnetization. Deposition methods, such as PLD, sputtering, and electroplating have also been tested. These deposition techniques usually create very thin layers of magnetic materials. Both the deposition and resin based techniques have  $(BH)_{max}$  that are lower than their bulk counterparts [81-83]. However recent developments manage to increase both the thickness and  $(BH)_{max}$  [60]. This is a field that will continue to mature in the upcoming years. Therefore regarding the current stage of the technology the end users must choose the suitable technology for their application.

### 2.3 Steering devices for space

The mirrors that are nowadays in use for satellite telecommunication are not MEMS devices. They are usually much bigger mirrors with diameters of tens of millimeters as shown in Table 2-1. These mirrors are usually used for satellite-satellite or earth-satellite telecommunication [19] and also for alignment of several satellites [15]. A comparison of several different mirrors used by ESA is given by [4, 62, 64]. The weight of these devices is usually several hundred grams. Their rotation angle varies from 0.06 degrees [15] to 9 degrees [18]. And the resonant frequencies vary from 100 Hz to 2.5 kHz. Most of these devices use electromagnetic actuation [7, 11, 13, 61], while the best results in

terms of speed and rotation are obtained by the piezoelectric actuation of [8], although it has hysteresis and a nonlinear force, thus a more complicated control scheme. The electromagnetic actuator used is always a Lorenz actuator due to the linearity of the created force. The electrostatic actuator has the lowest power consumption.

**Table 2-1: Comparison of different mirrors used for satellite telecommunication. They usually have diameters of tens of millimeters. They are used for satellite-satellite or earth-satellite telecommunication**

| mirror                                   | diameter [mm]      | rotation angle [°]                  | frequency [Hz]                        | actuation                       | power [W]                            | mass [g] | resolution [ $\mu$ rad] | RMS flatness |
|--|--------------------|-------------------------------------|---------------------------------------|---------------------------------|--------------------------------------|----------|-------------------------|--------------|
| Coppoole (contraves) [6]                 | 28 - 27<br>usefull | 0.4                                 | 100 (open loop)<br>1000 (closed loop) | magnetic-voice coil<br>(Lorenz) | 25                                   | 150      | < 1 p-p                 | lambda/50    |
| Suhonen [21]                             | 23                 | 0.2                                 | 140-180                               | electrostatic<br>paralel plate  | 1-mean                               | ?        | 0.4                     | lambda/50    |
| Hafez [13]                               | 30 x 40            | 3                                   | ~100                                  | magnetic-voice coil<br>(Lorenz) | 17                                   | 90       | ?                       | ?            |
| Kazuhiko Aoki [7]                        | 40                 | 4(open loop)<br>0.002 (closed loop) | 50 (open loop)<br>300 (closed loop)   | magnetic-voice coil<br>(Lorenz) | 2.5                                  | 250      | < 1                     | ?            |
| SILEX fine<br>positioning Assembly [8]   | 60                 | 9.2                                 | 2500                                  | piezoelectric                   | 1.5 (tracking)<br>16.5 (acquisition) | 400      | < 5                     | lambda/50    |
| SILEX coarse<br>positioning Assembly [8] | 250                | 180                                 | ~2                                    | conventional motor              | 30                                   | 14000    | 100                     | ?            |
| Henien [15]                              | 50 ?               | 0.06                                | ~1                                    | piezoelectric                   | 0.001                                | 160      | 0.1                     | ?            |

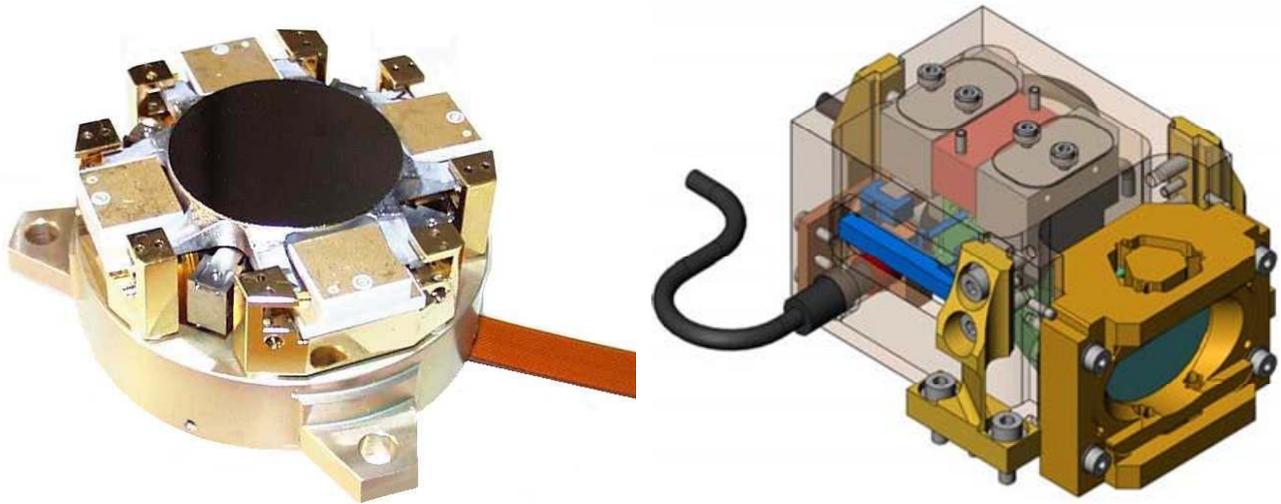


**Figure 2-5: Two examples of devices that are used for two different applications in space. a) The device made by Coppoosle et al. [Contraves] [11] has a  $0.4^\circ$  rotation angle and a 1 kHz closed-loop resonant frequency. It is used for inter-satellite telecommunication. b) The device made by Heneien et al. [CSEM] [15] has a rotation angle of  $0.06^\circ$  and a resonant frequency of 1Hz. 3 of these devices are used to help in detection of gravitational waves with linking three stationary satellites that are 5 million kilometers apart.**

Two examples of these devices are shown in Figure 2-5 [11, 15] that are used for two different applications in space. The device in [11] made by Coppoosle et al. [Contraves] has a  $0.4^\circ$  rotation angle and a 1 kHz closed-loop resonant frequency. The open loop frequency is at 100 Hz the actuation method is electromagnetic and the mirror size is 28mm in diameter useful area. It is used for inter-satellite telecommunication. The device in [15] made by Heneien et al. [CSEM] has a rotation angle of  $0.06^\circ$  and a resonant frequency of 1Hz. The mirror size is 50mm in diameter. It

---

uses piezoelectric actuators. 3 of these devices are used to help in detection of gravitational waves with linking three stationary satellites that are 5 million kilometers apart.

## 2.4 Summary

There are two commonly used non-contact actuators used in MOEMS: electrostatic and electromagnetic. Electrostatic actuators are more commonly used in MOEMS due to the integrity with microfabrication techniques. The progresses made in recent years towards integrating magnetic components such as magnets and micro-coils in to MEMS devices, has lead to a growing interest in magnetic actuators mainly due to the higher forces they can provide.

Our interest was in making a MEMS device for space applications. MEMS devices however are optimized for earth bound use. The majority of systems used in space are not currently MEMS based. This thesis explores the possibility of using non-contact force MOEMS actuators in space. Relatively large mirrors (1 cm diameter) were microfabricated while focusing on increasing the resonant frequencies, reducing power consumption, and increasing fracture reliability with the use of the two non-contact actuation methods. The final system consists of two mirrors that work together to steer the light beam. One of the mirrors is used for small rotations  $\theta = \pm 0.2^\circ$  but with a fast response  $f_r = 1\text{kHz}$  (magnetic or electrostatic actuation) and the other mirror is used for larger rotations  $\theta = \pm 3.5^\circ$  but with a slower response  $f_r = 200\text{Hz}$  (magnetic actuation). A third mirror is also present to reflect the beam from the first mirror to the second one as shown in Figure 1-1. A configuration where the third mirror is not used can be envisaged. However the configuration presented here, with the third mirror, can be beneficial in the future, if the two different mirrors are fabricated and situated on the same wafer.



### 3 Theory

As it was mentioned in the state of the art, this thesis examines the fabrication of mirrors capable of steering actuation using non-contact actuation forces. Three major parts in the project needed to be optimized. The electrostatic actuation, the magnetic actuation and the actuation springs. In order to make a system capable of non-resonant steering while maintaining a high resonant frequency (fast response time), two major aspects should be studied:

- 1-maximum material strength
- 2-maximum available force

The maximum strength of the material is defined by its hardness and maximum stress it can handle before fracture. The mechanical design should consider this criterion to avoid mechanical failure of the design, especially for the mechanical springs, while maintaining the design parameters for other requirements of the system such as resonant frequency and mechanical translations.

The force in combination with the spring constant of the springs defines the resonant frequency and the maximum mechanical translation of the device. The resonant frequency  $f$  and the force  $F$  of a mechanical actuator can be given by the following formulas:

$$f = 1/2\pi\sqrt{k/M} \quad \text{Eq. 3-1}$$

$$F = kx \quad \text{Eq. 3-2}$$

In Eq. 3-1  $f$  is the resonant frequency,  $M$  is the mass and  $k$  is the spring constant. Eq. 3-2 is the hook's law of elasticity and  $x$  is translation. The same formulas can apply to rotation if  $F$  is replaced with torque,  $T$ ,  $M$  replaced by moment of inertia  $I$ ,  $x$  by rotation  $\theta$ , and  $k$  by rotational spring constant.

Combining Eq. 3-1 and Eq. 3-2 shows that the maximum resonant frequency achievable with an actuator is proportional to:

$$f \propto \sqrt{1/x} \sqrt{F/M} \quad \text{Eq. 3-3}$$

The resonant frequency will decrease with  $\sqrt{1/x}$  as the maximum needed translation increases. In the case of rotational movement,  $x$  is replaced by  $r * \theta$ , where  $\theta$  is the rotation angle and  $r$  is the radius to the rotation center.

The  $\sqrt{F/M}$  term is of particular importance. It shows that the resonant frequency is proportional to the force to mass (force to volume) ratio. This factor shows the evolution of resonant frequency as the force to mass ratio of the actuator is scaled. Therefore this factor demonstrates the benefit of an increase or decrease in the dimensions of the system on the resonant frequency.

Dimensional factors,  $x$ ,  $r$ , and  $\theta$  are essentially dictated by the configuration of the actuator and the limits of fabrication technologies. The force to mass (F/M) ratio is directly related to the type and configuration of the actuator that is used. However these two are not independent of each other. In many cases the dimension constraints of the desired design could make an actuator with an inferior F/M ratio more desirable to one with a higher F/M ratio.

The introduction of the F/M ratio necessitates a comparison of the different actuation schemes and the respective scale reduction laws. In this thesis the two most commonly used non-contact actuation schemes, electrostatic and electromagnetic, will be discussed.

### 3.1 Electromagnetic actuation

There is a range of different magnetic actuators. In general they can be divided to three main actuation categories [62, 63]:

1) Wire-wire interaction scheme: In this case two different wires conducting currents will interact to create the magnetic force. The force can be calculated using the Biot-Savart law.

2) Wire magnet interaction scheme: In this case the interaction between the magnet's magnetic field and the current in the wire creates the magnetic force. Two important categories of actuators are possible using this scheme:

a) Voice-coil type actuators: voice coils are very commonly used in loudspeakers. Figure 3-1a shows the general concept of the voice-coil that consists of a large magnet and parallel wires. The current in all the wires has the same direction and the field is generally kept non-divergent. The direction of the force is given with right hand rule and is parallel to the plane of the wires and perpendicular to their direction. The parallel magnetic field can be provided with a large magnet that creates a quasi-parallel field around its center. The value of the force is given by the Lorentz force law:

$$\vec{F} = N L \vec{I} \times \vec{B} \quad \text{Eq. 3-4}$$

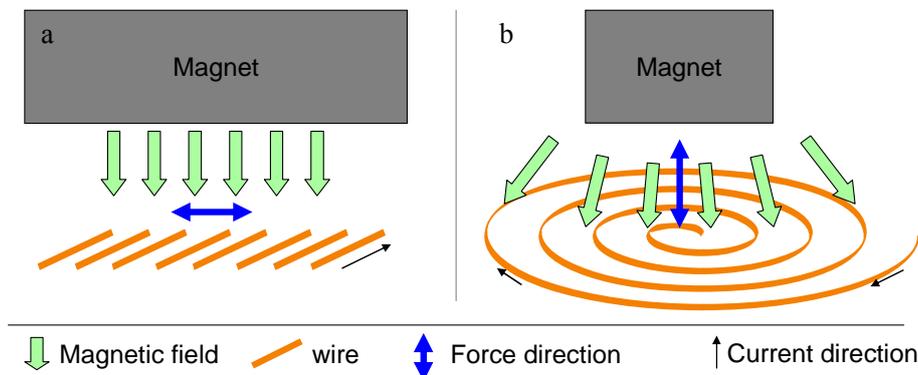


**Figure 3-1:** a) The force in a voice coil actuator is given by Lorentz law. The current in all the wires has the same direction and the field is generally non-divergent. The direction of the force is given with right hand rule. The parallel magnetic field can be provided with a large magnet that creates a quasi-parallel field around its center. b) The force in a spiral coil is created by the divergence of the magnetic field. The direction of the force is perpendicular to the plane of the spiral coil. The diverging magnetic field can be provided with a small cylindrical magnet magnetized along its central axis.

$N$  is the number of wire turns in the magnetic field;  $L$  is the length of each wire,  $I$  the injected current in the wire, and  $B$  the magnet's magnetic field.

b) Coil – magnet actuators in which the gradient of the magnetic field creates the magnetic force:

$$\vec{F} \approx \nabla(\vec{m} \cdot \vec{B}) \quad \text{Eq. 3-5}$$

This formula is an approximation for small magnets [64, 65],  $m$  is the magnetic moment. More accurate calculations can be found in [66-69]. Figure 3-1b shows the general schematics of this configuration. The force in a spiral coil is created by the divergence of the magnetic field. The diverging magnetic field can be provided with a small cylindrical magnet magnetized along its central axis. The direction of the force is perpendicular to the plane of the spiral coil; this is the main differences between these two configurations.

3) Wire – Ferrite interaction scheme: in this case the induced field in the ferrite creates the force. The field is usually created by a coil. This type of actuation is generally used in many conventional magnetic actuators. They are known as reluctance actuators. The reluctance method can be used to calculate the force of these actuators using the Ampere's law:

$$\int H \cdot dl = V_{MMF} = NI \quad \text{Eq. 3-6}$$

$V_{MMF}$  is the magnetomotive force,  $H$  is the magnetization field,  $N$  is the wire number of turns,  $I$  is the injected current in the wire and,  $l$  is the length of the magnetic circuit. A typical magnetic circuit is shown in Figure 3-2. This special circuit is called a clapper design. A magnetic circuit consists of a winding (copper coil) a stationary part (stator) and a moving part (clapper). The stator and clapper are made out of ferromagnetic materials. The magnetic field created by the coil is concentrated in the stator and clapper due to the high permeability of the ferromagnetic material used in their fabrication. The force between the stator and the clapper is directly proportional to the stator's cross section surface  $A$ .

The wire-wire, wire-magnet, and wire-ferrite are the three categories of magnetic actuators. They can also be combined together to create different actuations schemes that can be more suitable for different needs of different projects.

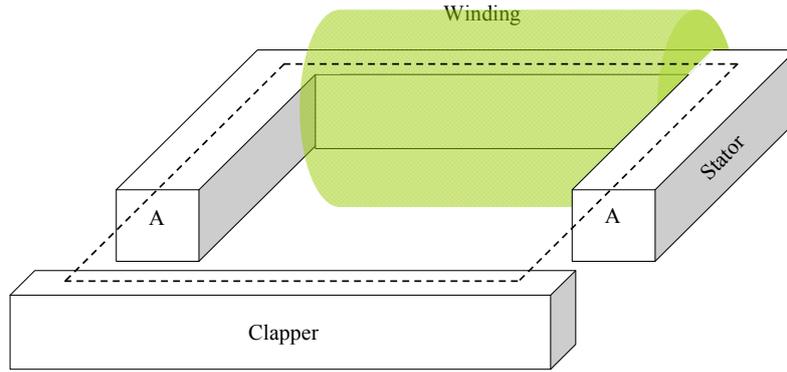


**Figure 3-2:** A magnetic circuit consisting of a copper winding a stator and a clapper that are made out of ferromagnetic materials. The magnetic field created by the coil is concentrated in the stator and clapper due to the high permeability of the ferromagnetic material. The magnetic circuit path is shown by dashed lines. The force between the stator and the clapper is directly proportional to the stator's cross section surface  $A$ .

### 3.2 Scaling laws of the magnetic actuation schemes

The force of each of the magnetic actuators mentioned in the previous section scales differently as its dimensions is reduced. A good indicator of this behavior is the F/M ratio discussed in Eq. 3-3. This comparison of different scaling laws for many different magnetic interactions has been developed in [62, 63]. An excerpt of the scaling-laws calculations that are relevant to this project will be given in the following. In this discussion each dimension  $L$  will be reduced by a factor of  $K$ . The reduced dimension will be indicated by a prime.  $V$  is the volume of the magnetic element.

$$L' = L / K \Rightarrow V' = V / K^3 \quad \text{Eq. 3-7}$$

#### 3.2.1 Wire-wire interaction scheme

The wire-wire interaction is the effect of one wire on the other wires adjacent to it. The interaction force between two wires can be calculated with the Biot-Savart's law [70].

$$dB = \frac{\mu_0}{4\pi} \frac{(J_1 \cdot A_1) * \hat{r}}{|r|^3} dl_1 \quad \text{Eq. 3-8}$$

$$d\vec{F} = \frac{\mu_0}{4\pi} \frac{(J_1 \cdot A_1)(J_2 \cdot A_2) * \hat{r}}{|r|^3} dl_1 \cdot dl_2 \quad \text{Eq. 3-9}$$

$\mu_0$  is the permeability of space.  $J$  is the current density,  $dl_1$  and  $dl_2$  are the infinitesimal lengths of the wires and  $r$  is the distance between the wires. Using the scaling factor  $K$  to reduce all the dimensions in Eq. 3-9 we will have  $B' = B / K$  and  $F' = F / K^4$ . Dividing the resulting equation by the scaled mass  $M' = M / K^3$ , we can write:

$$\frac{F'}{M'} = \frac{1}{K} \frac{F}{M}$$

Eq. 3-10

According to this formula reducing the dimensions of this system is disadvantageous since the F/M ratio will be divided by K.

### 3.2.2 Wire-magnet interaction scheme

In the case of the wire-magnet interaction there are two different possible categories of actuators as was discussed in the beginning of chapter 3.1.

- 1- The wire-magnet interaction as shown in Figure 3-1 a, which obeys Eq. 3-4.
- 2- The coil-magnet interaction as shown in Figure 3-1 b, which obeys the Eq. 3-5.

The magnetic field of a magnet can be found using the magnetic scalar potential  $V^*$ :

$$\vec{B}_{mag} = -\mu_0 \nabla V^* = -\mu_0 \int \vec{M} \cdot \frac{\hat{r}}{r^3} dV$$

Eq. 3-11

Here  $\vec{M}$  is the magnetization of the magnetic material and  $V$  is the Volume of the magnet. According to Eq. 3-11 the magnetic field of a magnet does not change by scaling. Therefore the force to mass ratio according to any of the equations Eq. 3-4 or Eq. 3-5 is given by:

$$\frac{F'}{M'} = \frac{F}{M}$$

Eq. 3-12

This shows that scaling has no effect on the force to mass ratio of the system. The reason to differentiate between these two systems becomes evident when the configuration in which they are used comes into discussion. This will be seen in chapter 7.1.2 where they are used in our configuration.

### 3.2.3 Wire – ferrite interaction scheme

Before deriving the F/M ratio of the wire-ferrite interaction, a brief introduction to the reluctance method will be given since it is used in many different magnetic actuators.

The reluctance method can be used in situations where a closed magnetic circuit can be placed around the system. An example was given in Figure 3-2. The magnetic system is represented by a closed magnetic loop made out of a magnetic material that also has a small gap. The reluctance method is usually used to calculate the magnetic forces of these systems [46, 71] using the

Ampere's law shown in Eq. 3-6. As an example the magnetic field of the system shown in Figure 3-2 will be calculated as follows:

$$\int H \cdot dl = \frac{B_F l_F}{\mu_F} + \frac{2B_g l_g}{\mu_g} = NI = NJ A_{wire} \quad \text{Eq. 3-13}$$

$B_F$  is the magnetic field in the ferrite,  $l_f$  is the total length of the ferrite circuit,  $\mu_F$  is the permeability of the ferrite, consisting of the stator and the clapper.  $B_g$  is the magnetic field in the gap,  $l_g$  is the length of the gap,  $\mu_g$  is the permeability of the gap.

If the losses in the ferrite and the gap are omitted and the cross section of the air gap and ferrite are considered to be equal, the magnetic field in the gap and ferrite can be shown to be equal by using the law of conservation of magnetic flux  $\Phi$ :

$$\Phi_F = \Phi_g \Rightarrow B_F A_F = B_g A_g \Rightarrow B_F = B_g \quad \text{Eq. 3-14}$$

The energy density that is stored in the gaps is given by [72]:

$$u_m = B_g^2 / 2\mu_0 \quad \text{Eq. 3-15}$$

The force is given by

$$F = \partial U_m / \partial z = \partial(u_m V) / \partial z \quad \text{Eq. 3-16}$$

$z$  is the direction of the induced force and  $U_m = u_m \cdot V$  is the total energy. Using Eq. 3-13 and Eq. 3-16 the force to mass ratio can be written as:

$$\frac{F'}{M'} = \frac{1}{K} \frac{F}{M} \quad \text{Eq. 3-17}$$

Therefore reducing the size of these systems is disadvantageous. It should be mentioned that the maximum field in the ferrite can not be more than the saturation value ( $B_s \approx 2.2$  T for steel and FeCo alloys [Vacoflux]) [73].

### 3.2.4 Effect of scaling on micro-coils

Micro-coils are becoming more and more widely used in magnetic MEMS devices as was discussed in chapter 2.2.3. Their advantage lies in the high current densities that can run through them. This is partly due to the increasing surface to volume ratio as the coil wire dimensions shrink [62, 74, 75].

$$\frac{S'}{V'} = K \frac{S}{V} \quad \text{Eq. 3-18}$$

This leads to a thermal conductivity that increases as the coils are scaled down. Therefore as the amount of created heat remains constant, the current density can increase  $J' = K_j J$ .

However microfabricated planar coils are usually placed on substrates that have high thermal conductivity. These substrates are also usually very thin and in contact with a heat sink as discussed in chapter 2.2.3. This allows the planar micro coils to take full advantage of the scaling law. This is not the case for winded coils as they can be very thick. This somewhat reduces their overall conductivity. Therefore this relation should be used with caution. Therefore the scaling factor  $K$  is replaced with  $K_j$  for the current density.

Simulations of the planar one layer coils are shown in Figure 3-3, Figure 3-4, and Figure 3-5. These simulations show the temperature rise in coils embedded in silicon substrates that are in contact with a heat sink at a constant temperature. There is no heat convection in these simulations to simulate the conditions in space.

Simulations were done on a coil inside two silicon substrates; one 100 $\mu\text{m}$  and the other 500 $\mu\text{m}$  thick. The copper coil has a cross section of 50 by 50  $\mu\text{m}^2$  and is placed inside the silicon substrate. It has 10 turns with a fill factor of 50%. The voltage on the coil is 0.6V and the backside of the substrate is put to 0 °C for steady state simulations. The current density  $J \approx 10^9$  A/m<sup>2</sup> can be seen in Figure 3-3.

The cross section view of the temperature rise in different parts of the 100 $\mu\text{m}$  and 500 $\mu\text{m}$  silicon substrates can be seen in Figure 3-4, and Figure 3-5. The rise in temperature for the 100 $\mu\text{m}$  device is only 2 °C while the temperature rises to 5 °C for the 500 $\mu\text{m}$  device. Since no air convection is present in these simulations, as is the case in space, these results are ideal for space application provided that there is a heat sink that is attached to the substrate.

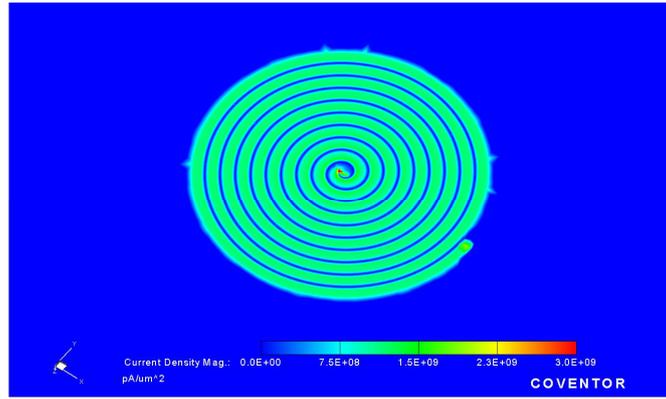


Figure 3-3: The simulated spiral copper coil with 10 turns is shown. The copper is inside a silicon substrate. The spiral coil has a current density of  $J \approx 10^9 \text{ A/m}^2$ . The voltage is set to 0.6V at the centre of the coil and to 0V at the outer end of the spiral coil.

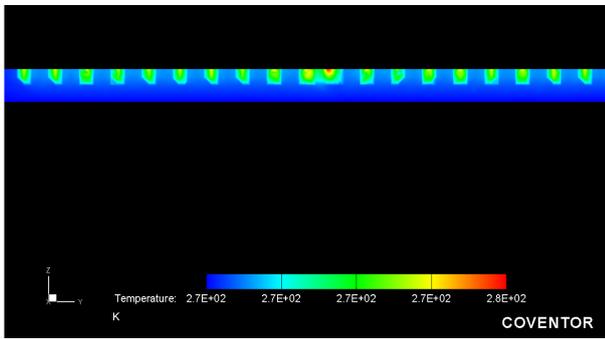


Figure 3-4: The cross section view of the temperature differences inside the 100µm substrate. The coil's cross section is 50x50 µm<sup>2</sup>. The rise in temperature is 2 °C.

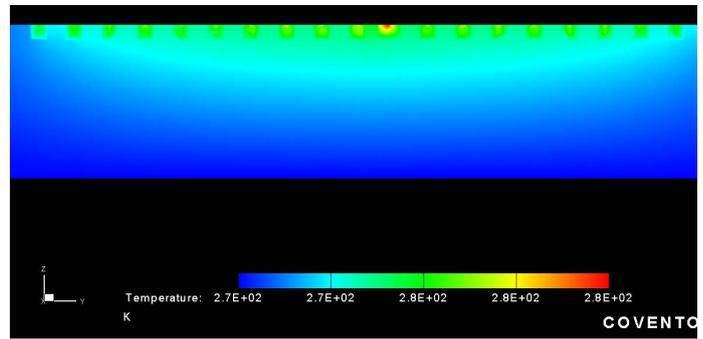


Figure 3-5: The cross section view of the temperature differences inside the 500µm substrate. The coil's cross-section is 50µm by 50µm. The rise in temperature is 5 °C.

### 3.2.5 Effect of coil scaling on the force to mass ratio

As it was show in the previous section, scaling of the coil dimensions introduces a new scaling factor  $K_J$ . Inserting this scaling factor into the force to mass ratio of the magnetic actuation schemes will multiply all of the abovementioned scaling relations with  $K_J$ . The resulting laws are shown in Table 3-1. As mentioned before, the applicability of the scaling factor of the current density shall always be considered before the following scaling factors are implemented.

The wire-wire scheme is multiplied by  $K_{J1}$  and  $K_{J2}$  since there are two interacting wires in the system. This table shows that potentially wire-wire and wire-magnet schemes are the preferred choices.

Table 3-1: Comparison of different magnetic actuation systems with regards to the scaling of their F/M ratio. The effect of scaling of the current density is also included.

| Interaction | Wire-ferrite                                | Wire-wire   | Wire-magnet                       |
|-------------|---|---|-----------------------------------|
| Scaling law | $\frac{F'}{M'} = \frac{K_J}{K} \frac{F}{M}$ | $\frac{F'}{M'} = \frac{K_{J1} * K_{J2}}{K} \frac{F}{M}$ | $\frac{F'}{M'} = K_J \frac{F}{M}$ |

### 3.2.6 Force magnitude of the different magnetic schemes

Having established the scaling laws, one question still remains: having the same dimensions, which of the mentioned schemes has a higher value of F/M ratio to begin with?

There is no straightforward answer to this question. In general the answer depends on the specific requirements of the project. The best result could be obtained by using one of the mentioned schemes, for example coil only, or by combining several aspects, such as “magnets + coil + ferrite”. However a very basic energy comparison between the main components of the magnetic system i.e. magnets coil, and ferrite, is possible. The mass densities of all of these components are more or less the same. Therefore mass can be omitted in the following comparison.

The energy stored in the unit volume of a magnetic component is given by Eq. 3-15. The force is given by Eq. 3-16. According to this equation the force of the system is proportional to  $B^2$ . Therefore the maximum field of the three main magnetic components should suffice for a comparison.

The magnetic field of the magnet and ferrite are easy to find as shown bellow:

- 1- Ferrite: the Maximum field is given by the saturation magnetic field  $B_s$ . the highest found value to date is around  $B_s = 2.2$  [T] for some kinds of steel and FeCo alloys (Vacoflux) [73].
- 2- Magnet: the Maximum field is given by the remnant magnetic field  $B_r$ . the highest found value to date is around  $B_r = 1.2$  [T] for NdFeB magnets [73].

The maximum energy is then calculated by inserting these values in Eq. 3-15.

3- Coil: The case of a coil is somewhat different. The magnetic field of a coil depends on its radius and length. The magnetic field of a finite coil is given by [76-78]. A schematic cross section view of a coil is shown in Figure 3-6. This coil has the length  $L$  the outer radius of  $r_2$  and an inner radius of  $r_1$ . The coil has  $N$  wire turns. The field of the coil on its central axis can be given by a simplified formula:

$$B_{center-axial} = \frac{\mu_0 N I L \ln(2r_2 + \sqrt{L^2 + 4r_2^2})}{2r_2^2}$$

Eq. 3-19

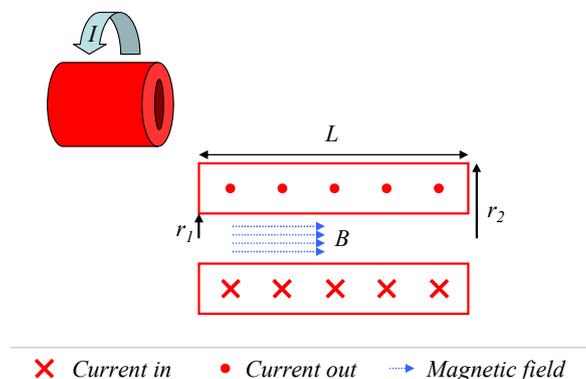
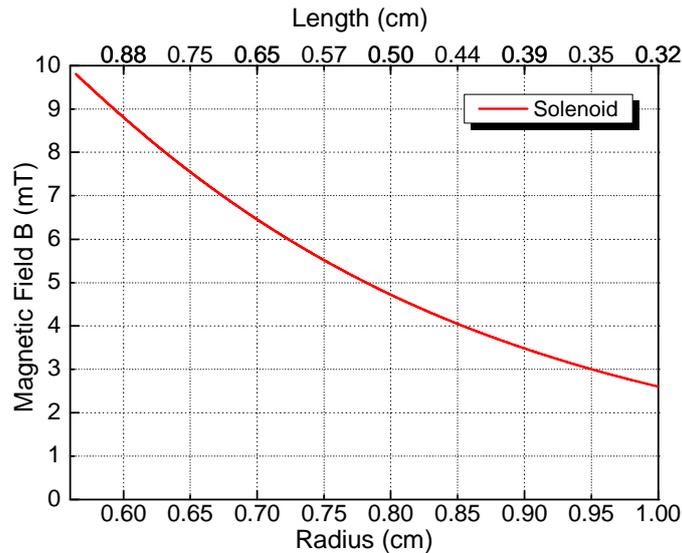


Figure 3-6: A schematic cross section view of a coil is shown. This coil has the length  $L$  the outer radius of  $r_2$  and an inner radius of  $r_1$ . The inner radius is filled with air. The coil has  $N$  wire turns.



**Figure 3-7:** The magnetic field at the center of a solenoid with a volume of  $V=10^{-6} \text{ m}^3$ . The radius and length of the magnet are varied such that the total volume stays constant at  $10^{-6} \text{ m}^3$ . The wire used for this calculation has a gauge of  $90 \mu\text{m}$  in diameter with an injected current of  $I = 100\text{mA}$ . As the length of the magnet increases compared to the radius, a maximum magnetic field of  $10\text{mT}$  can be reached. The maximum magnetic fields form ferrite and magnetic materials are also shown as a comparison.

$N$  is the number of wire turns,  $I$  is the injected current,  $L$  is the length of the coil, and  $r_2$  is the outer radius, as shown in Figure 3-6. In Eq. 3-19, the inner radius  $r_1$  is set to zero and the field is at the center of the solenoid where it has the maximum value. Although the field varies in strength and direction as we move away from the central axis, it can nonetheless give us a first approximation of the stored energy in the system.

The magnetic field at the center of a solenoid with a volume of  $V=10^{-6} \text{ m}^3$  is shown in Figure 3-7. This figure shows the resulting magnetic field as the radius and the length of the magnet are varied synchronously. The radius and length of the magnet are varied such that the total volume stays constant at  $V=10^{-6} \text{ m}^3$ . The wire used for this calculation has a gauge of  $90 \mu\text{m}$  in diameter with an injected current of  $I = 100\text{mA}$  which is in accordance with the American Wire Gauge (AWG) standard for maximum currents. As the length of the magnet increases compared to the radius, a maximum magnetic field of  $10\text{mT}$  can be reached. The energy density of the system can be found by Eq. 3-15. It can be seen that the maximum magnetic field of a Solenoid is much lower than the maximum magnetic field of a magnet or a ferrite.

However the maximum usable magnetic field of the magnet depends on how it is implemented and the maximum field of a ferrite should be created using a coil. Therefore, a magnetic system designs try to implement all the possible magnetic components in order to take advantage of their individual magnetic energies.

A system consisting of only a coil is analogous to the wire-wire Scheme. This is the case of the coil shown in Figure 3-7 (wire-wire scheme).

In Figure 3-7 the magnetic field of the ferrite should be created by a coil. Therefore Ferrite is already a multi component system (wire-ferrite scheme).

On the other hand, the magnetic field of the magnet is an intrinsic property. However, in order to be able to actuate the magnet a coil is needed. Therefore the total magnetic field of the coil-magnet system is a combination of the magnetic fields of these two components (wire-magnet scheme).

The “force to mass” ratios of these schemes were summarized in Table 3-1. However the scaling laws should be used with regard to the field (energy) values shown in Figure 3-7, since different criterions such as the dimensions, temperature, mechanical constraints, etc, could make one system more advantageous than the other. The total energy is the combination of the energies of the different magnetic component used in the system.

### 3.2.7 Total Mass of the moving system and force to mass ratio

Until now only the mass of the actuator was considered in the F/M ratio calculations. If the mass of the whole actuation system (including the mirror, springs, etc) is considered the force to mass ratio can be written by Eq. 3-20. In this formula the mass of the system  $M$  (the mechanical and mirror parts, only) remains constant. The mass and force of the actuators are the only parts that are scaled.

$$\frac{F'_{tot}}{M'_{tot}} = \frac{F'_{tot}}{m' + M} = \frac{i K^{3-\gamma} F}{(i + n K^3) m} \quad \text{Eq. 3-20}$$

All the characters shown with a prime on top are properties after being scaled. In this formula the mass of the magnetic actuator is shown with  $m$ . The total mass of the system after scaling is shown with  $M'_{tot} = m' + M$ .  $i$  is the number of actuators that can be fitted on the mechanical part.  $F'_{tot}$  is the total force of these actuators. The mass of the mirror part  $M$  does not have a prime since it remains constant, as discussed above. The other characters are defined as follows:

$n$ : The mass of one actuator ( $m$ ) and the mirror part ( $M$ ) are related with  $M = n m$ .

$\gamma$ : integer related to the scaling factor of the force depending on what actuation scheme is used. According to Table 3-1 the value of  $\gamma$  can be 4, 3, and 2.

The right side of Eq. 3-20 shows that increasing the number of actuators “ $i$ ” is advantageous, regardless of the scaling laws. The initial mass of the actuator is also important. Increasing the initial mass  $m$  of the actuator (decreasing  $n$ ) increases the force to mass ratio. Likewise, scaling the actuator to bigger volumes (decreasing  $K$ ) also increases the force to mass ratio of the system for all values of  $\gamma$ . Therefore although the force to mass ratio of the actuator is important, it is better to keep the size of the actuator comparable to the size of the moving platform

## 3.3 Electrostatic actuation

Electrostatic force arises from the interaction between electrically charged particles. The most common device that creates this effect is the capacitor. The force is proportional to the cross-

sectional area of a capacitor. Therefore it follows a different scaling law compared to the magnetic forces where the force is volume dependant.

The electrostatic actuation usually utilizes electrostatic comb drives. Parallel plate actuators have also been used although they can show snap-in issues. The main hindrance of the electrostatic actuator is the lower achievable force for long-range actuations. However they have the advantage of having the actuator integrated in to the silicon MEMS. This means that the mass of the system can be lower than the magnetically actuated mirror.

### 3.3.1 Parallel plate actuator

The simplest electrostatic actuator uses parallel plates as shown in Figure 3-8. It consists of two plates with the surface  $A$ . An applied voltage on these two plates creates the force. The force of this kind of actuator is non-linear. This force non-linearity in combination with linear springs that obey Hook's law result in a snap-in point where the two plates of the actuator are pulled towards each other without control. This point is usually one third of the total distance between the plates [79]. The force between the plates is given by:

$$F = \frac{1}{2} \frac{\partial C}{\partial x} U^2 = \epsilon_0 \frac{U^2 A}{2 \text{gap}^2} \quad \text{Eq. 3-21}$$

$U$  is the voltage,  $A$  is the surface of the plates,  $\epsilon_0$  is the vacuum permittivity,  $C$  is the capacitance and  $\text{gap}$  is the distance between the two plates. Here the direction of the force  $x$ , is perpendicular to the plane of the plates.

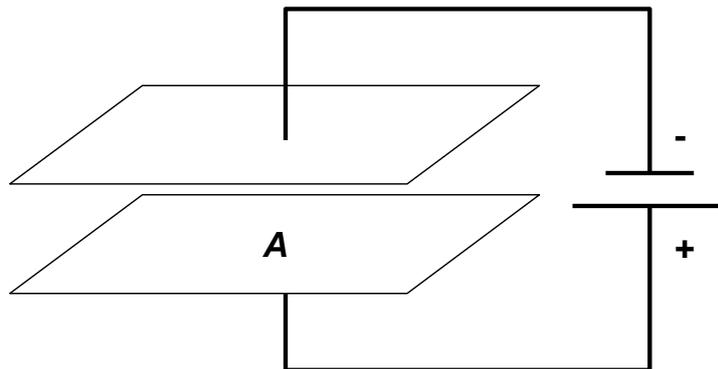


*Figure 3-8: The simplest electrostatic actuator uses parallel plates. It consists of two plates with the surface  $A$ . An applied voltage on these two plates creates the force. The force of this kind of actuator is non-linear.*

### 3.3.2 Comb drive actuator

Most of the electrostatic actuators use comb actuators. These comb actuators either move in plane or out of plane according to their configuration. These two configurations are shown Figure 3-9. Figure 3-9a shows two comb-sets that are at the same height. The force in this configuration is in the direction of the length  $L$  of the combs;  $F_L \propto \partial C / \partial L$ . Figure 3-9b shows two comb sets that are at different heights. The force in this configuration is in the direction of the thickness  $t$  of the

combs;  $F_t \propto \partial C / \partial t$ . This kind of actuator is called the vertical comb-drive actuator. In this project only the vertical comb is used. The force can be given by:

$$F = \varepsilon_0 \frac{n U^2 L}{2 \text{ gap}}$$

Eq. 3-22

Here  $n$  is the number of the comb fingers and  $\text{gap}$  is the distance between two adjacent combs as shown in Figure 3-9 b. This formula shows that this system is linear for the most of its actuation length since it has no displacement dependence in the out of plane direction. However this is not true in reality due to the fringing fields of the combs. There is also an unwanted lateral force in the comb-drive actuator between the adjacent comb fingers. Their force is given by Eq. 3-21. Since these forces are non-linear they can create unwanted lateral snap-in behavior if the combs are not mutually centralized. Therefore the design of a comb-drive actuator should always compensate for this behavior by having very stiff springs that limit the actuator's movement in the unwanted direction.

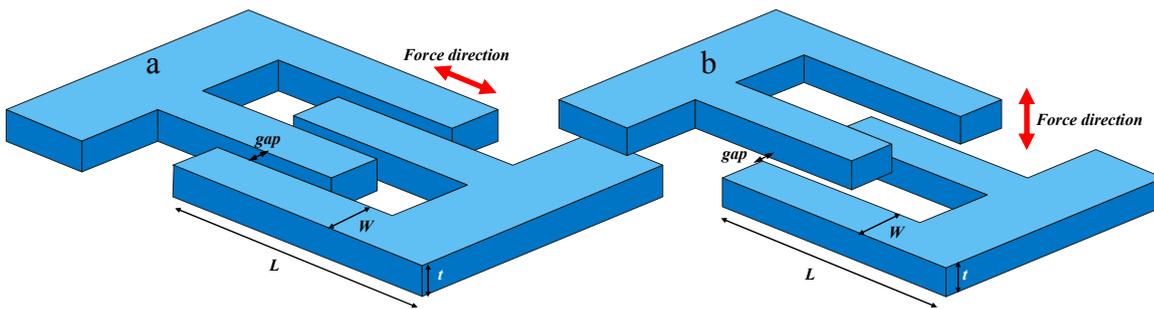


**Figure 3-9: Schematics of the in-plane comb-drive and the vertical comb-drive actuators. a) in-plane comb-drive: two comb sets that are at the same height. The force in this configuration is in the direction of the length  $L$ . b) vertical comb-drive: two comb sets that are at different heights. The force in this configuration is in the direction of the thickness  $t$ .**

### 3.3.3 Scaling law for the electrostatic actuators

The forces of the electrostatic actuators shown in Eq. 3-21 and Eq. 3-22 do not scale if the voltage  $U$  remains constant. However the maximum voltage that can be applied to an electrode is given by the Paschen's law of breakdown voltage:

$$U = \frac{a(p \text{ gap})}{\ln(p \text{ gap}) + b}$$

Eq. 3-23

Here  $p$  is the pressure,  $a$  and  $b$  are constants dependant on the gas, and  $\text{gap}$  is the distance between the combs in SI units. If  $V$  is scaled by  $K$  it can be written as:

$$U' = \frac{ap(\text{gap}/K)}{\ln(p \text{ gap}) + b - \ln(K)} \approx \frac{U}{K} \quad \text{Eq. 3-24}$$

In Eq. 3-24 as  $K$  is increased, “ $-\ln(K)$ ” will decrease. Therefore it can be omitted. Care should be taken in the use of this relation since this form of Paschen’s law is limited to large gap sizes. As the gap size is decreased to values lower than  $5\mu\text{m}$  this relation should be replaced by the Modified Paschen’s law of breakdown voltage [80-83]. However based on this equation the force to mass ratio for both of the electrostatic actuators can be written as:

$$\frac{F'}{M'} = K \frac{F}{M} \quad \text{Eq. 3-25}$$

### 3.4 Comparison of magnetic and electrostatic actuation

A common assessment is usually made by comparing the magnetic and electrostatic energy densities:

$$u_e = 1/2 CU^2 \quad \text{Eq. 3-26}$$

$u_e$  is the electrostatic energy density,  $C$  is the capacitance and  $U$  is the voltage. The magnetic energy density  $u_m$  is given by Eq. 3-15. Two simple systems can be envisaged for a comparison between  $u_e$  and  $u_m$ . The electrostatic system is represented by a circuit consisting of a capacitor and a voltage source as shown in Figure 3-8.

The magnetic system is represented by a closed magnetic loop made out of a magnetic material that also has a small air filled gap. A cross section view of this magnetic circuit is shown in Figure 3-10. It consists of a ferrite with a coil winding around it. The total length of the ferrite is denoted by  $l$ . according to Figure 3-7 this system might not be the most advantageous magnetic system. However, it is the most commonly used. It is also easier to analyze due to its known maximum energy density. It also resembles the parallel plate electrostatic actuator and therefore suited for comparison.

The energy density that is stored in these two gaps can be compared as follows. The magnetic field  $B$  can be considered to have the maximum value  $B_s$ , the saturation magnetic field, that can be up to  $B = 2.2$  Teslas as discussed in section 3.2.3. The magnetic energy density in the gap of the magnetic circuit has a constant value. The maximum value for  $U$  in the electrostatic actuator is defined by Paschen's law for breakdown voltage, Eq. 3-23.

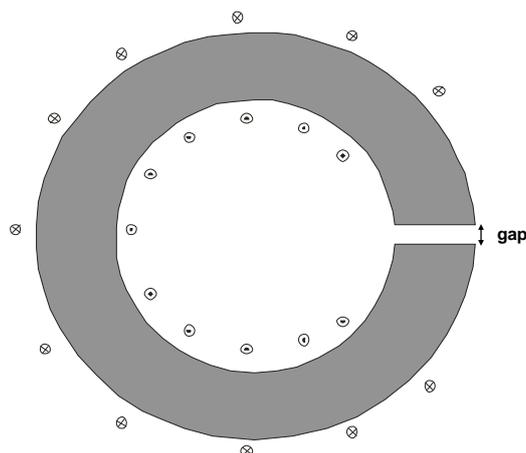


**Figure 3-10:** The magnetic system is represented by a closed magnetic loop made out of a magnetic material that also has a small air filled gap. A coil winding around the ferrite creates the magnetic field. The total length of the ferrite is denoted by  $l$ .

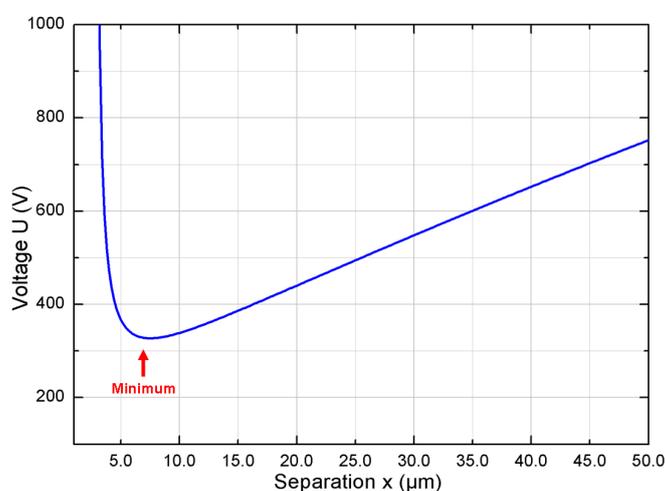


**Figure 3-11:** A typical breakdown voltage due to Paschen's law.  $p$  is at atmospheric pressure of air  $p = 101 \text{ kPa}$ ,  $a = 43.6 \times 10^6$  and  $b = 12.8$ . According to this graph, the breakdown voltage decreases to a minimum around  $5 \mu\text{m}$  separation gap and then increases.

Figure 3-11 shows a typical breakdown voltage due to Paschen's law. In this figure  $p$  is at atmospheric pressure of air  $p = 101 \text{ kPa}$ ,  $a = 43.6 \times 10^6$  and  $b = 12.8$ . According to this graph, the breakdown voltage decreases to a minimum around  $5 \mu\text{m}$  separation gap and then increases. By introducing the Paschen's law into Eq. 3-26 the maximum energy density of the electrostatic actuator can be found.

Figure 3-12 shows a comparison of the two energy densities. This simplified comparison shows that as the surfaces that define the gaps of the capacitor and magnetic loop approach towards one another, the electrostatic actuation can become advantageous. The transition occurs at around  $3 \mu\text{m}$  in Figure 3-12. This value is close to  $2 \mu\text{m}$  according to [84]. The resulting breakdown voltage is around  $V=270 \text{ Volts}$ .

However several publications show that the value of breakdown voltage decreases rapidly when the minimum of the Paschen's curve shown in Figure 3-11 is reached. In smaller distances breakdown depends on the electrostatic field. Therefore it also depends on comb roughness and edges and at

field strengths above 100 V/ $\mu\text{m}$ , electron field emission can occur [85-88]. Therefore gaps smaller than 5 $\mu\text{m}$  are not practical for actuation purposes, unless they are used with lower voltages.

According to this analysis it is theoretically unlikely for an electrostatic actuator to surpass any magnetic actuator. However, in practical cases the electrostatic actuator can be more advantageous due to limitations in microfabrication of magnetic materials and the higher temperatures and power consumption of the coils if compared to the integrability of electrostatic actuators into silicon wafers and their very low power consumption.

It should be mentioned that for actuators that use dielectric materials with much higher dielectric constants electrostatic actuation can become more advantageous than magnetic actuation, in addition to keeping their low consumption characteristics.

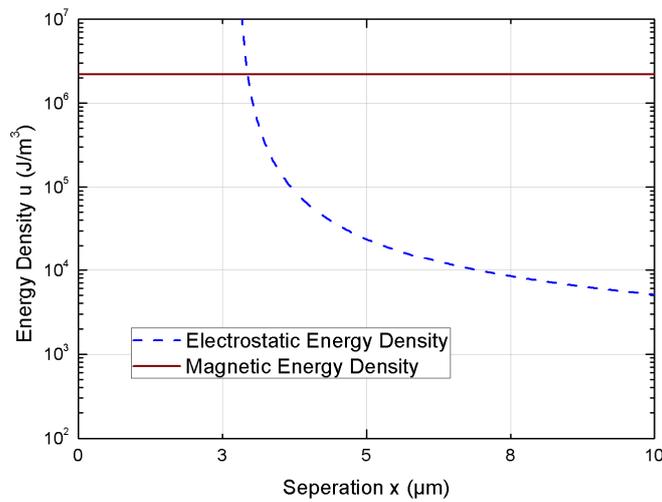


**Figure 3-12:** A comparison of the energy densities of the electrostatic and electromagnetic actuators. This simplified comparison shows that as the surfaces that define the gaps of the capacitor and magnetic loop approach towards one another, the electrostatic actuation can become advantageous. In this graph the transition occurs at around 3 $\mu\text{m}$ .

### 3.5 Mechanical springs

Many MEMS devices use springs to suspend their moving parts and to provide a counter force to the attractive or repulsive force of the actuators. In many cases like thermal and piezoelectric actuators they can also be used as actuators of the system [89, 90].

There are two main categories of springs; torsion springs and flexure springs. Torsion springs are widely used in MEMS devices [25, 29, 30]. The rotation angle  $\theta$  of these springs is given by [91]:

$$\theta = \frac{Tl}{KG} \quad \text{Eq. 3-27}$$

$T$  is the twisting moment,  $l$  is the length of the spring,  $G$  is the modulus of rigidity, and  $K$  is a factor dependant on form and dimensions of the cross section. This kind of spring has the advantage of limiting the movement in any other direction except in the desired rotational direction.

Flexure springs are also widely used in MEMS devices. The simplest flexure beam is a cantilever as shown in Figure 3-13. The bending value  $Y$  due to an applied load  $W$  is given by:

$$Y = \frac{W}{3EI} l^3 \quad \text{Eq. 3-28}$$

$E$  is the Young's modulus of the material.  $I$  is the second moment of inertia, and  $l$  is the length of the beam.  $I$  is proportional to the thickness  $t$  and the width  $w$  of the cantilever, according to the shape of its cross section [91].

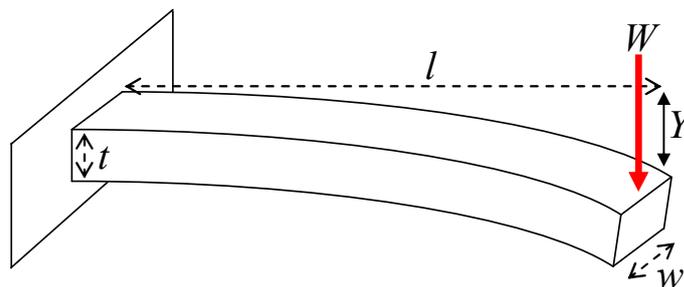


**Figure 3-13:** A cantilever is the simplest flexure beam. The bending value  $Y$  due to an applied load  $W$  at the free end of the cantilever is shown.

Another variation of the flexure beams that is widely used in MEMS is the folded flexure beam shown in Figure 3-14. One side of this design can be fixed and the other can move in the desired direction. This spring can also be cascaded to create even longer and softer springs. In general the flexure beam is more prone to movement in the unwanted directions. However since it is usually longer than the torsion springs it is less prone to fracture. Therefore it is used even in cases where only rotation is needed [92, 93]. Folded springs are also advantageous in places where space is an issue or the length of the spring exceeds the boundaries of the actuating device. Folding the spring will reduce the waste of space around the design.

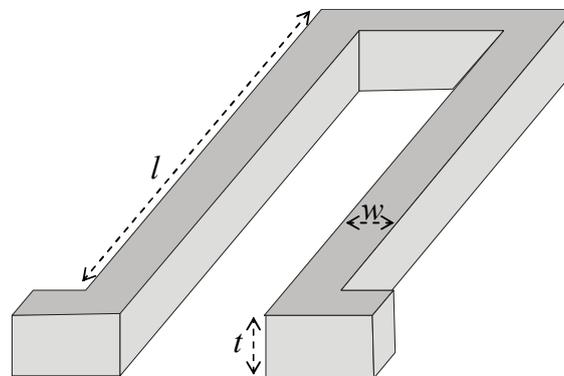


**Figure 3-14:** A folded flexure beam is shown. One side of this design can be fixed and the other can move in the desired direction. Folded springs are advantageous in places where available space is an issue and folding the spring will reduce the waste of space around the design.

### 3.6 Summary

In this chapter the scaling laws for the magnetic and electrostatic actuators were presented, including wire-wire, wire-ferrite and wire-magnet actuation schemes. A brief introduction to different mechanical springs used in microfabrication was also given.

It was shown that the coil-magnet interactions are the most advantageous in terms of reducing the system dimensions (scaling down). Furthermore the energy densities of the different magnetic schemes were compared. It was shown that magnet and ferrite have limiting intrinsic magnetic fields. The coil can create the highest magnetic fields. However, a coil is limited by the heat that it creates. In practical applications these systems are combined together to merge their energies and especially take advantage of the intrinsic fields. In terms of the scaling law however, the wire-magnet actuation scheme has the upper hand.

In the next step the total mass of the system was considered. It was shown that if the actuators are integrated on a moving platform (e.g. mirror) that is heavier than them increasing the size of the actuator (within reasonable values) is advantageous for the force to mass ratio. Therefore although the force to mass ratio of the actuator is important, it is better to keep the size of the actuator comparable to the size of the moving platform.

The electrostatic parallel plate and vertical comb actuators were also shown. It was shown that the down scaling these two actuators is beneficial. The electrostatic and electromagnetic actuators were compared with each other. Theoretically by considering the energy density and the scaling factors, the magnetic actuator is better than the electrostatic one. However practical issues such as limitations in microfabrication of magnetic materials and the higher temperatures and power consumption of the coils compared to the integrability of electrostatic actuators into silicon wafers and their very low power consumption can make (and in many cases does make) the electrostatic actuation more advantageous.

## 4 Concept

In this chapter different magnetic and electrostatic actuator schemes will be presented and adapted to the needs of the current project. They will be compared and the best magnetic and electrostatic actuators for our application will be chosen.

These design concepts will be brought together to form the selected design. In order to do so the design of the moving magnet actuator is further developed and the achievable resonant frequencies and angles will be derived. This will also be done for the electrostatic actuator. From these results it will be shown that the high steering angular range and short response time are problems that are mutually exclusive. Therefore the best solution for this problem is to have two 2D mirrors, one of which is used as a slow moving coarse position finder with a high steering angular range and the other mirror will be a fine tuning mirror that has a short response time but small steering angular range. The large steering angular range was set to  $3.5^\circ$  and the small steering angular range was set to  $0.2^\circ$ . However before showing the final concept, a comparison of the magnetic and electrostatic actuators is given in the following that depicts the approach to the final design.

Table 4-1 summarizes the specifications of the actuator schemes and different 2D mirrors that were fabricated in this thesis.

*Table 4-1: summary of the specifications of the actuators and 2D mirrors that were fabricated during this thesis*

|                           | <b>Resonant frequency</b> | <b>Tilt angle</b> | <b>Actuator</b>                             |
|---------------------------|---------------------------|-------------------|---|
| slow magnetic mirror      | <b>200 Hz</b>             | $\pm 3.5^\circ$   | <b>Moving magnet-stationary planar coil</b> |
| Fast magnetic mirror      | <b>1kHz</b>               | $\pm 0.2^\circ$   | <b>Moving magnet-stationary planar coil</b> |
| Fast electrostatic mirror | <b>1kHz</b>               | $\pm 0.2^\circ$   | <b>Electrostatic comb drive actuator</b>    |

### 4.1 Actuation design study

Several different magnetic and electrostatic actuator schemes were discussed and compared in chapter 3.2. It was shown in section 3.2.7 that these systems need to be optimized for a specific application where they have to be used. Therefore several different actuators were studied for our specific application considering the correct dimensions based on the fabrication possibilities and limitations. Microfabrication compatibility and compactness were the two central preferred characteristics of all the studied designs. Several aspects of these systems were compared including force over mass F/M ratio, power consumption, actuation method, range, and response times of the different systems. The most suitable design was accordingly chosen based on these criterions.

### 4.1.1 Magnetic actuators

In this chapter different magnetic actuator designs will be presented. They will be categorized in the following groups:

- 1- Voice coils design
- 2- Solenoid designs
- 3- Torque driven ferrite based design
- 4- Coil-magnet design

Both the voice coil and solenoid behaviors can be modeled with reluctance method, briefly discussed in chapter 3.1. The major difference between solenoids and voice coils is having “current” dependant forces for the voice coil and “distance and current” dependant forces for the solenoid. The torque driven ferrite based design however generates torque using the directional demagnetization factor that will be discussed later in chapter 4.1.7 [23-28, 47, 52, 58, 94-98]. The coil magnet force is dependant on the field divergence as shown in 3.2.2.

In the following a discussion of the different advantages and disadvantages of each of these devices will be provided and the best design for this project will be chosen accordingly. It should be noted that the calculated values given in the following sections are not exact values of the different calculated parameters. They are however accurate enough for comparison between the different designs.

### 4.1.2 Solenoid Actuators

A general overview of the solenoid actuators is given here with some useful formulas to be used in the next sections. Different solenoid designs have been realized that have linear and non-linear force profiles. They are investigated by Nemirovsky et al [45] which compares two different methods of flux control and magnetomotive force (MMF) control. A summary of the MMF control of the different designs will be given here since controlling the flux can be much more complicated. The solenoid actuators can be separated to two groups. The first is the group that has a nonlinear force curve and a second group who has a sufficiently linear force in a certain range of their total stroke.

The clapper actuator was shown in Figure 3-2. A cross section view of the same clapper actuator is shown in Figure 4-1 for convenience. The clapper is attached to a spring that is fixed on the other end. At rest, the clapper is at a distance of  $X_0$  away from the stator. The following two formulas can be derived from the magnetic energy [45]:

$$\frac{\partial U_M}{\partial x} - \frac{V_{MMF}^2}{2} \left( \frac{\partial}{\partial x} \left( \frac{1}{R(x)} \right) \right)_{V_{MMF}} = 0$$

$$\frac{\partial^2 U_M}{\partial x^2} - \frac{V_{MMF}^2}{2} \left( \frac{\partial^2}{\partial x^2} \left( \frac{1}{R(x)} \right) \right)_{V_{MMF}} = 0$$

Eq. 4-1

$V_{MMF}$  is the magnetomotive force,  $U_M$  is the magnetic potential and  $R(x)$  is the reluctance. Using these formulas it can be shown if a linear spring is attached to the clapper as shown in Figure 4-1 the systems will have a pull-in point where the clapper will snap into the stator without any control. This behavior is analogous to the electrostatic parallel plate actuator and happens after one third of the total gap distance  $x_{PI} = 1/3X_0$ .

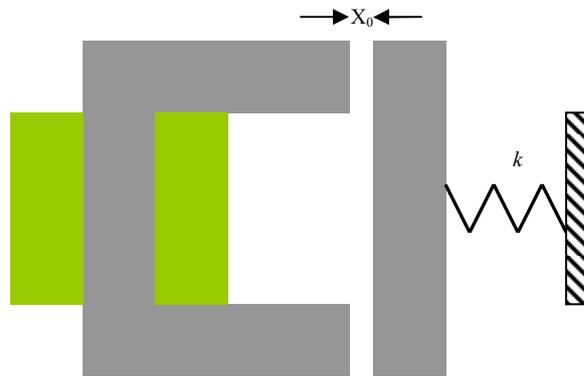


*Figure 4-1: The cross section of the solenoid. The coil shown in green is wrapped around the ferromagnetic material. The ferromagnetic material is shown in gray and consists of the stator that is fixed and the moving part or the clapper that is placed at a distance of  $X_0$  from the stator. The pull-in distance is at  $1/3X_0$ .*

The second variation, shown in Figure 4-2, uses two stators like the one shown in Figure 4-1. The clapper however is placed above the two stators and allowed to turn around a fulcrum. The system response is quite complex and dependent on several factors. The system is usually solved numerically. However it can be shown that this system also exhibits pull-in behavior[45].

The last design is shown in Figure 4-3. This design is called the plunger design. Using the same formulas as above it can be shown that as long as the clapper is away from the corners of the opening of the stator, the force is to a great extent linear. Therefore no pull-in will occur. This region is shown with light orange in Figure 4-3. These three designs are the most common reluctant actuators. They had to be adapted to our dimensions for a correct comparison. This will be shown in the following.

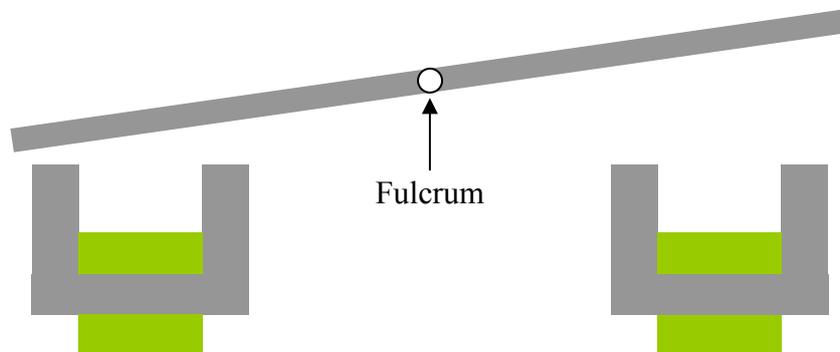


*Figure 4-2: A variation of the solenoid design that uses two stators. The clapper is placed above the two stators and is allowed to turn around the fulcrum. The forces are highly nonlinear and pull-in occurs.*

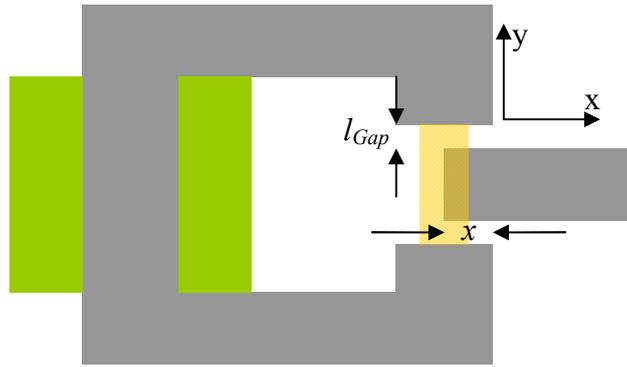


**Figure 4-3: The plunger design.** The stator is modified to form an opening where the clapper can be inserted. In this configuration the clapper is called the plunger. As long as the clapper is away from the corners of the opening of the stator and in the linear region shown in orange, the force is to a great extent linear and no pull-in will occur. This linear region is shown with light orange.

### 4.1.3 Magnetic comb drive actuator

A very interesting example using the plunger design is fabricated by Schonhardt et al [99] that creates a magnetic comb-drive actuator as shown in Figure 4-4. In this figure the combs with the coil slots are fixed and the inner combs can be attracted to left and right. The force of the system can be derived from Eq. 4-1 to be:

$$F = -\frac{1}{2} i^2 \frac{\partial}{\partial x} \left( \frac{N^2}{R_{Core} + R_{Gap}(x)} \right) \quad \text{Eq. 4-2}$$

$R_{Core}$  is the reluctance of the ferrite stator and the ferrite clapper combined together.  $R_{Gap}$  is the reluctance of the gap between the clapper and the stator.  $R_{Gap} = l_{Gap} / (\mu_0 A)$ ; where  $l_{Gap}$  is the distance between the stator and clapper and  $A$  is the surface of the clapper in the gap where its normal is parallel to  $l_{Gap}$ . This relation shows that decreasing  $l_{Gap}$  will increase the force. However this task can not always be easy. Schonhardt et al. have used ferrite combs to overcome this problem by adding more combs and achieving higher forces while keeping the fabrication relatively simple; since the gap should not necessarily be very small in this design. The increase of comb numbers also helps in linearization of the force profile [99].

#### 4.1.3.1 Achievable forces

The force created by the solenoid is directly related to the surface of flux exchange between the clapper/plunger and the stator that closes the magnetic flux loop. If the surface that creates the force is set to be  $A = W \times x$ , where  $W$  is the width of the actuator and  $x$  is the length of the part of the plunger that moves inside the opening, as shown in Figure 4-3, then Eq. 4-2 can be written as [46]:

$$F(x) = -n \frac{1}{4} N^2 i^2 \left( \frac{\mu_0 W}{l_{Gap}} \right) \quad \text{Eq. 4-3}$$

In this formula  $R_{Core}$  is set to zero.  $n$  is the number of the combs on the actuator as shown in Figure 4-4.  $N$  is the number of coil winding turns. However there is also a lateral force in the  $y$  direction on the fingers of the comb and it is given by:

$$F(y) = -\frac{1}{4} N^2 i^2 \left( \frac{\mu_0 W x}{l_{Gap}^2} \right) \quad \text{Eq. 4-4}$$

Since this equation depends on the  $l_{Gap}^2$ , the springs should be designed to be very stiff in the  $y$  direction and the alignment of the plunger and the core should be very precise to avoid lateral snap-in. these design considerations are quite similar to the electrostatic comb drive as discussed in chapter 3.3.2

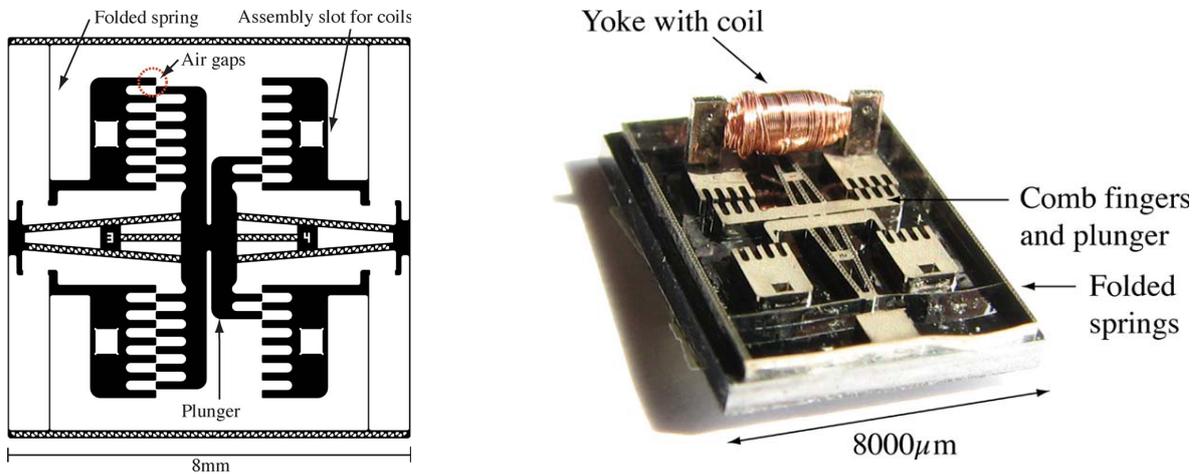


*Figure 4-4: The mask and the fabricated device of the magnetic comb-drive actuator as presented by Schonhardt et al [83]. The combs with the rectangular slots are fixed. The slots are used to fix external coils on the combs. The inner combs can be attracted to left and right and act as plungers. The advantage of this design is that the air gaps are not too small. This facilitates the fabrication of the device.*

To calculate the forces and accelerations of the device several factors should be considered. They include the mass of the plunger, the saturation field of the ferrite ( $B_s$ ), and the maximum stroke of the device. Some empirical result show the maximum stroke range of an 8mm device to be around  $500\mu\text{m}$ [99], while the linear range is only  $150\mu\text{m}$ . However our 1cm mirror with  $3.5^\circ$  of deflection will have a  $\pm 400\mu\text{m}$  stroke range at its far ends. This means that the actuator should be arranged in a way to achieve the full actuation range of the mirror within its linear range, as presented in the following.

#### 4.1.3.2 Possible magnetic comb actuator design

The system shown by Schonhardt et al [99] could have been used in the current project with a configuration that is shown in Figure 4-5 which consist of a mirror that pivots in the middle with a lever that is attached to the actuator. Considering the 1 cm mirror size of this project, using a 1mm

lever can reduce the maximum displacement needed to  $70\mu\text{m}$  which is well within the linear region of the actuator's stroke. The major drawback of this design is the short lever. The force of rotation is given by  $F = I \alpha / r$ , where  $I$  is the moment of inertia,  $\alpha$  is the angular acceleration and  $r$  is the distance from the pivot point; in this case the  $1\text{mm}$  lever. Therefore if  $\alpha$  is fixed, the system needs more force as  $r$  gets closer to the pivot point.

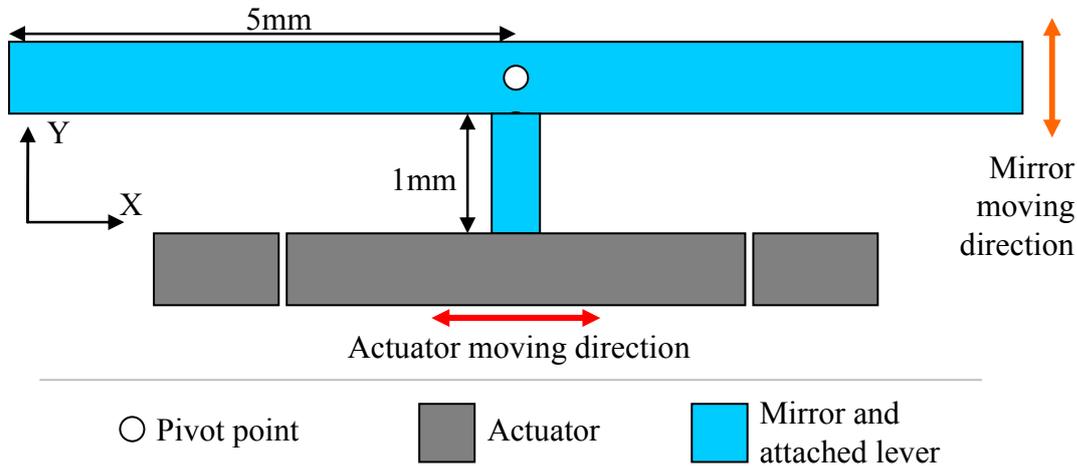


**Figure 4-5: Possible configuration of the magnetic comb drive. The actuator, shown in gray, will be placed under the mirror. It can be connected to the mirror through a lever that is shown in blue. This lever can not be longer than  $1\text{mm}$ . This is due to the small available linear range of the actuator. This in turn reduces the available torque.**

Choosing the dimensions as given by Schonhardt et al, for the dimensions of the device, the following values can be found. The value for the force with  $n=8$  fingers is  $F \approx 20\text{mN}$ . This value is obtained with  $N=300$  coil winding turns, air gap width of  $25\mu\text{m}$ , and actuator thickness of  $W=400\mu\text{m}$ , finger length of  $500\mu\text{m}$ , finger width of  $150\mu\text{m}$  and a current of  $I=70\text{mA}$ . These values with a relative permeability of  $\mu_r=40000\text{H/m}$  for the ferrite lead to an inductance of  $L=0.1\text{Wb/A}$ . This is based on an inductance of a ferrite circuit as shown in Figure 3-10 and calculated as follows [70]:

$$L = \frac{\mu_r \mu_0 N^2 A}{l}$$

Eq. 4-5

Eq. 4-5 omits the air gap in Figure 3-10. The rise time of a RL circuit can be found by  $T = L / R$ .  $R$  is the resistance of the coil. This corresponds to a rise time of  $\tau=0.1\text{S}$  for the RL circuit of the winding. This value is too large for the speeds that are desirable in this project. However the power consumption  $W=R I^2=6\text{mW}$  is quite low in this system.

The mass of this actuator is around  $m \approx 5\text{mg}$ . The hysteresis in the ferrite should also be considered. Although the hysteresis loop in ferrites is small it can be a source of complication of the operation and control of the device.

#### 4.1.4 Possible clapper designs

The solenoid design shown in Figure 4-2 can be considered as the stator-clapper design shown in Figure 4-1. These designs all have a nonlinear force profile. The force can again be found from Eq. 4-1 to be:

$$F(y) = -\frac{1}{4} N^2 i^2 \left( \frac{\mu_0 A}{l_{Gap}^2} \right) \quad \text{Eq. 4-6}$$

$A$  is the surface of the stator in the gap between the stator and clapper as shown in Figure 3-2. The schematic view of the clapper-stator actuator on the mirror can be seen in Figure 4-6. The coils are shown in green. The magnetic circuit is shown in gray, with the clapper part put on the mirror. The mirror is shown in blue. The mirror turns around the pivot point. The clapper could be deposited on the mirror by electroplating. The cross section view shows two actuators at each end of the mirror which is advantageous regarding the average speed of the system due to higher torque. However the gap between the clapper and the stator should be 3 times larger than the needed value of the desired rotation angle. This is due to the snap-in issue discussed in chapter 4.1.2 and it greatly reduces the force since the force is inversely proportional to  $l_{gap}^2$ , as shown in Eq. 4-6. The gap length should be around 1mm for a  $3.5^\circ$  deflection range of a 1cm mirror.

In order to achieve a reasonable force that is comparable with the magnetic-comb actuator the maximum number of coil turns are used  $N=6300$ . The achievable force at maximum distance is  $F=3\text{mN}$ . The injected current is  $I=100\text{mA}$ . This is equivalent to a power consumption of  $4\text{W}$ . The mass of the clapper's moving part is in the order of  $m \approx 6\text{mg}$ . The device has also a high inductance due to presence of the ferrite, which is comparable with the previous example and therefore a rise time of  $\tau \approx 0.01\text{S}$ . The hysteresis in the ferrite should also be considered.

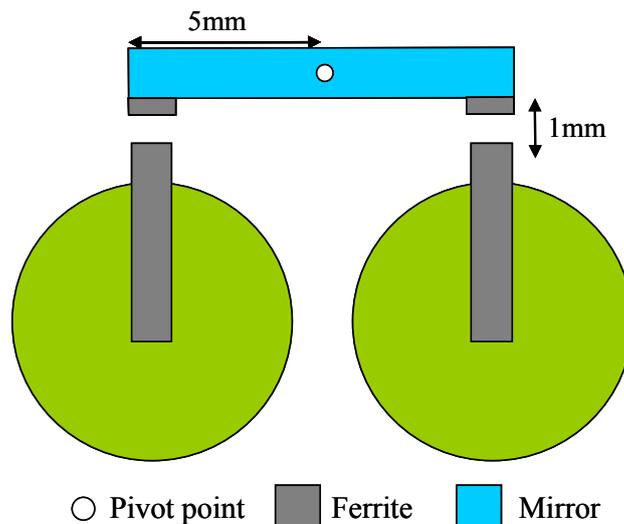


**Figure 4-6:** The schematic view of the clapper-stator actuator and the mirror. The coils are shown in green. The magnetic circuit is shown in gray, with the clapper electroplated on the mirror. The mirror is shown in blue. The mirror turns around the pivot point. The forces in this design are due to the magnetic field in the gap of the actuator and are nonlinear.

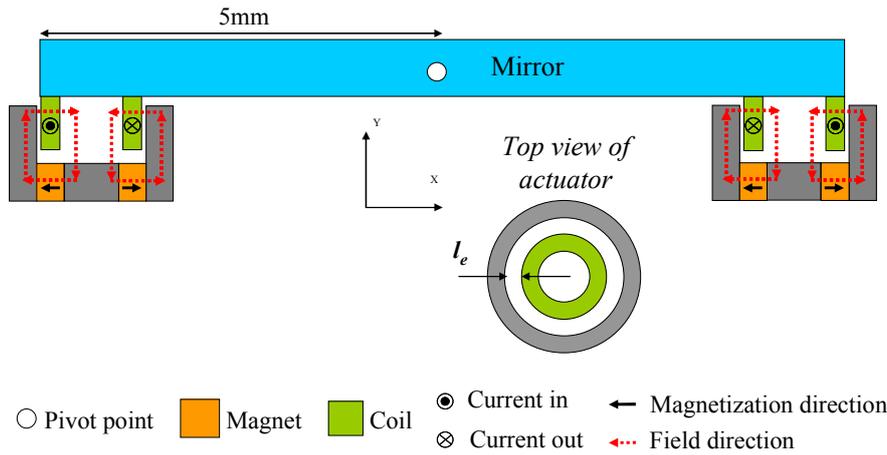


**Figure 4-7: Implementation of the voice coil design.** The mirror is shown in blue. The voice coils can be put under the mirror. Either the coils or the magnets can be put on the mirror. This design has linear forces. Since the force depends on the gap  $l_e$ , the perfect alignment of the magnet and the coil are essential.

A question might arise is why not using a permanent magnet in the solenoid design. The reason is that the magnet imposes a permanent force on the ferrite. This increases the chance of pull-in which then requires a huge reverse force in order to separate the two parts. Permanent magnet solenoid designs are usually used for switches, relays and pumps and they are not suitable for fine positioning.

#### 4.1.5 Voice coil design

The voice coil design is shown in Figure 4-7. The voice coil uses the Lorentz law to create the actuation force and it can benefit from permanent magnet forces due to its configuration. It has no pull-in, a linear force profile and the ability of the force to push and pull. The possible implementation of the voice coil is shown in Figure 4-7. The magnetic field is created by permanent magnets with a radial magnetization direction. The magnetic field  $B_{gap}$ , which is exerted on the coil inside the gap, depends on the magnet that is used in the system and the gap dimensions. This field can be calculated simply by the reluctance method. The magnetic circuit is shown in dotted red lines in Figure 4-7. The simplified formula for the magnetic field in the gap can be given as:

$$B_{gap} = \frac{B_r}{1 + \frac{l_e}{l_m} \mu_{rm}} \quad \text{Eq. 4-7}$$

$B_r$  is the remnant magnetic field of the permanent magnet,  $l_m$  is the length of the magnet and  $l_e$  is the length of the gap. In order to increase  $B_{gap}$ ,  $l_m$  should increase and  $l_e$  should decrease. In this formula the demagnetization effects of the magnet and ferrite are neglected.

Voice coils of 3mm in diameter can be envisaged to be built. In the following calculations the coil width is 1 mm and the number of wire turns is  $N=300$ , the wire diameter is set to  $D_{wire}=100\mu\text{m}$  and the injected current is  $I=100\text{mA}$ . The length of the gap between the magnet and coil is considered to be  $500\mu\text{m}$ . The force of the moving coil voice coil can be up to  $F=50\text{mN}$ . This force is based on the actuator design shown in Figure 4-7 where the coil has no ferrite in its central circle. If a central

ferrite pillar were present in this design the force would increase up to 4 times. However this would also increase the rise time of the circuit much more considerably. Therefore the presented design is sufficient for comparison purposes. The inductance of a coil is given by [100]. For the present coil  $L=65\text{mH}$ . The rise time of this system is  $\tau \approx 10\mu\text{S}$ . The power consumption of this configuration is around  $0.1\text{W}$ . The mass of the coil is  $m=200\text{ mg}$ .

The limiting factor of the force in the moving-coil voice coil design is the integration of the coils on a moving platform and the heat created by the current. This limit comes from the inability of the conventional coils to dissipate energy, which results in the failure of the protecting cover of the wire. Also putting a heat-creating device on a moving platform is not suitable for vacuum applications. This is due to the absence of convection in space which will lead to heat accumulation and failure of the device. Another important hindrance in this design is the alignment of the coil with the magnet in these dimensions, since the magnetic circuit and the coils are two separate parts that should be put inside each other and aligned perfectly to avoid touching each other.

#### 4.1.6 Moving magnet actuation

As it was said before some scanning MOEMS devices use moving-magnet configurations. There are many different configurations that can be thought of. The design that is represented here has an important feature for use in space. It uses microfabricated coils that rest on a heat sink and dissipate heat via conduction. The magnet is situated on the moving part of the design; hence the name of the design “moving magnet – stationary coil”.

A schematic implementation of this configuration is shown on the 1cm mirror in Figure 4-8. A schematic top-view of the moving magnet-stationary coil actuator and a cross-section of the FEM magnetic field simulation of this actuator are shown in Figure 4-9. The FEM cross-section is shown in polar coordinates and shows the magnetic field of the system. The magnetization direction is along the Z-axis of the magnet. The mirror is put  $500\mu\text{m}$  above the coils and the magnets have a maximum gap of  $1\text{mm}$  when the mirror is tilted. The magnet has a diameter of  $1\text{mm}$ . the coil is  $4\text{mm}$  in diameter with wire cross section of  $50*50\mu\text{m}^2$ . The injected current in the coil is  $I=1\text{A}$ . The power consumption of this configuration is around  $1\text{W}$ . The inductance of a microfabricated coil can be calculated by the formulas in [100-103].  $L$  is calculated to be around  $L=1\mu\text{H}$ . The rise time of the system can be calculated around  $\tau=0.1\mu\text{s}$ .

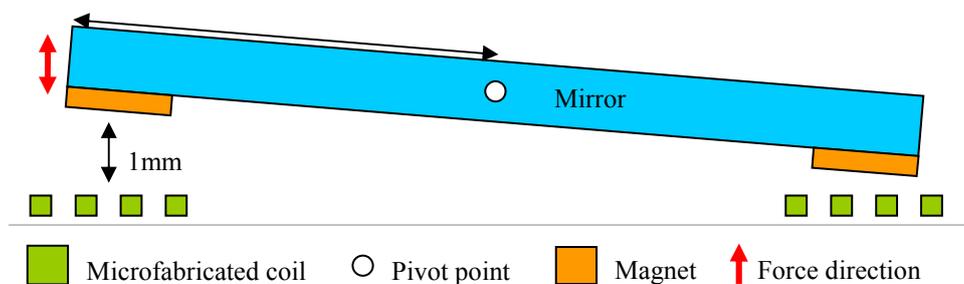


**Figure 4-8:** A schematic top-view of the moving magnet—stationary coil system is shown. The microfabricated coil increases the current density that can be applied to the system. The magnetization direction is along the Z axis of the magnet. The magnet is put  $1\text{mm}$  above the coil

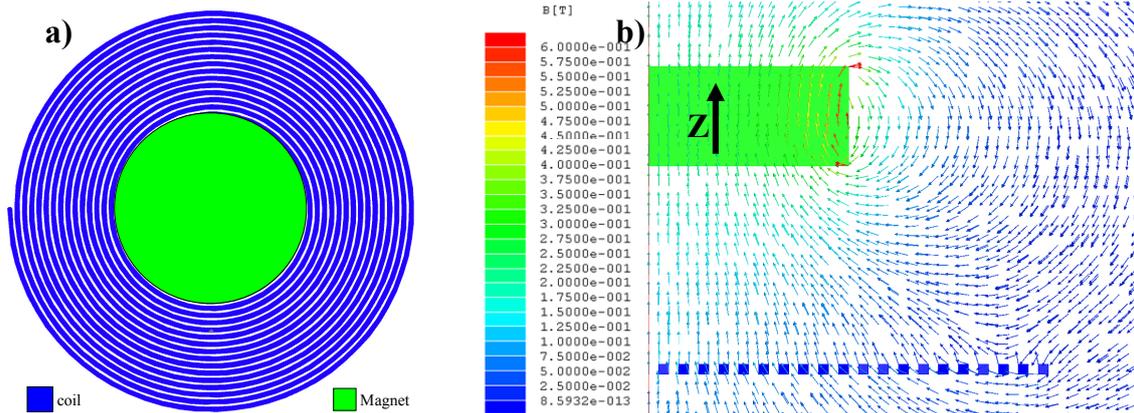


**Figure 4-9:** a) Schematic top-view of the moving magnet-stationary coil actuator. b) Cross-section of the FEM simulation shown in polar coordinates. The magnetization direction is along the Z axis of the magnet. The magnet is put 1mm above the coil. It has a diameter of 1mm. the coil is 4mm in diameter with wire cross section of  $50 \times 50 \mu\text{m}^2$ . The injected current in the coil is  $I=1\text{A}$ .

The force between the magnet and the coil is shown by simulations to be around 5mN at a 1mm distance, using NdFeB magnets. According to the scaling law shown in Table 3-1, if the dimension of the coil remains constant, the  $F/M$  ratio does not change by decreasing the magnet size. This was verified by FEM simulations.

#### 4.1.6.1 Moving coil—stationary magnet design

The moving magnet design discussed above in section 4.1.6 uses microfabricated coils. One strong reason for using microfabricated coils is the high current density that can be put in them [104, 105]; it can be as high as  $10^9 \text{ A/m}^2$ . This fact is directly related to the law of scalability as discussed in chapter 3.2.4. However another approach could place the coils on the moving platform and put the magnets in stationary position. This could be advantageous due to the lower mass of the coils compared to the magnets.

As discussed in chapter 3.2.4, planar coils are usually in contact with a good heat sink that usually covers the entire backside of the coil substrate that takes the heat away. If the coil is put on the actuation platform this condition is not satisfied anymore. The simulation shown in Figure 4-10, shows the inconvenience of putting the coil on the actuation platform in absence of air convection. There is no heat convection in these simulations to simulate the condition in space.

In Figure 4-10 the platform shown on the lower right part has a thickness of  $300\mu\text{m}$  and the copper coil's cross section is  $50\mu\text{m}$  by  $50\mu\text{m}$  buried into the platform for better heat conduction. The coil extends through the beam till the heat sink shown on the top left of Figure 4-10. The platform is attached to a heat sink through the 8mm long beam of a  $100\mu\text{m}$  width. All parts, except the coil, are made of silicon and the coil is made of copper. It was shown that with a current density of  $J \approx 10^9 \text{ A/m}^2$  injected into the coil, the temperature rises to higher than  $2000 \text{ }^\circ\text{C}$  which is completely unrealistic. This shows that the springs do not have a big enough cross section to dissipate the heat. Although optimizations can be done to reduce these temperatures, it was decided to avoid the dire consequences of this approach altogether. The maximum working temperature of the magnetic materials is a good example. For NdFeB magnets this temperature can be as low as  $80 \text{ }^\circ\text{C}$ . Simple

accidental touch of the magnet and the coil could result in loss of magnetization during a long time period.

Reducing the maximum temperature of the device to 50 °C will decrease the current density to  $J \approx 10^8 \text{ A/m}^2$  as can be seen in Figure 4-10. The one order of magnitude decrease in  $J$ , from  $10^9$  to  $10^8 \text{ A/m}^2$ , will correspond to the same amount of decrease in the force magnitude. Also the integrated coils have to be connected to the electronics through the beams. Therefore using a “moving magnet-stationary coil” configuration is advantageous to the “moving coil-stationary magnet” configuration in space applications since heat complications can be avoided.

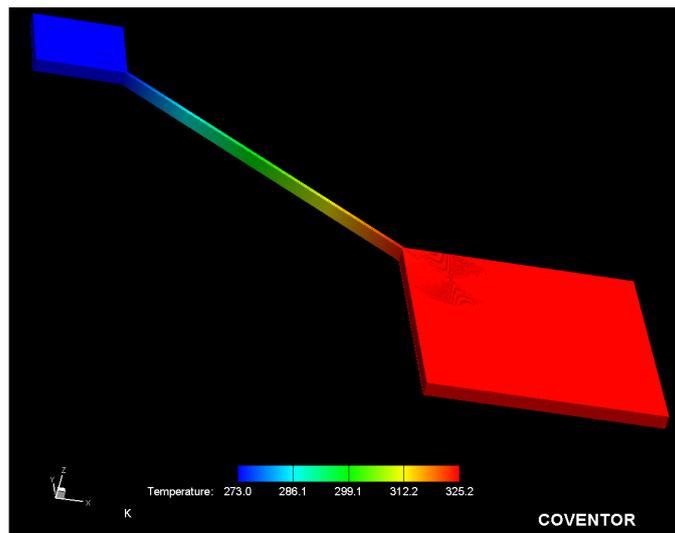


*Figure 4-10: The rise in the temperature of the actuation platform with a coil integrated on it. The platform thickness is 300 $\mu\text{m}$  and the copper coil’s cross-section is 50 $\mu\text{m}$  by 50 $\mu\text{m}$ . The coil extends through the 100 $\mu\text{m}$  thick beam till the heat sink. The length of the beam is 8mm. A current density of  $J \approx 10^8 \text{ A/m}^2$  increases the platforms temperature by 50 °C.*

#### 4.1.6.2 Choices of magnetic materials

In general there was the possibility of choosing between permanent magnet materials such as SmCo, NdFeB and AlNiCo and a magnetizable material such as NiFe. The choice of the magnetic material is limited by the offer from the providers. Different providers propose cylindrical NdFeB magnets (Supermagnete SA, Audemars SA) with a diameter of 2mm, or Cuboid 2\*2mm SmCo magnets (Audemars SA). The thickness of these magnets could vary between 100 to 500 $\mu\text{m}$ . The NdFeB magnet is the better choice because of its higher Maximum energy product  $(BH)_{\text{max}}$ , as shown in Table 4-2, compared to SmCo. It also has a lower mass density  $\rho_{\text{NdFeB}} \approx 7500 \text{ kg/m}^3$  compared to  $\rho_{\text{SmCo}} \approx 8500 \text{ kg/m}^3$ . This table shows that NdFeB is the preferred choice due to its lesser mass and higher  $(BH)_{\text{max}}$ . AlNiCo magnets have much lower  $(BH)_{\text{max}}$  and comparable densities  $\rho_{\text{AlNiCo}} \approx 7100 \text{ kg/m}^3$ . While a magnetizable material such as NiFe is the least appreciable due to very low  $(BH)_{\text{max}}$ . it should be noted that the values in Table 4-2 are typical values for each family of the magnets. These values can vary significantly in each of the mentioned families. An advantage of the SmCo family of magnets is in their very high Curie temperature. Some variants can have Curie temperatures around 250 °C.

*Table 4-2: Comparison of the available magnetic and magnetizable materials. It can be seen that NdFeB is the best choice due to its high BH product and lower mass density, while NiFe is the worst choice.*

| material      | Magnetization | $B_r$ [T] | $H_c$ [kA/m] | $(BH)_{max}$ [KJ/m <sup>3</sup> ] | Mass density [Kg/m <sup>3</sup> ] |
|---------------|---------------|-----------|--------------|-----------------------------------|-----------------------------------|
| <i>NdFeB</i>  | Permanent     | 1.2       | 950          | 300                               | 7500                              |
| <i>SmCo</i>   | Permanent     | 1.1       | 800          | 230                               | 8500                              |
| <i>AlNiCo</i> | permanent     | 1.2       | 80           | 44                                | 7100                              |
| <i>NiFe</i>   | Magnetizable  | 0.8       | 0.1          | 7                                 | 7500                              |

#### 4.1.7 Torque driven ferrite based design

This design uses permalloy layers and printed/microfabricated coils [44, 51-56, 84]. The principle of operation and the cross section of the device are shown in Figure 4-11. The mirror is covered with a permalloy. The permalloy is magnetized along the long axis of the layer. The dimensions of the permalloy are chosen in a way to have the thickness quite smaller than the length. This shape creates a high directional anisotropy in the magnetization of the permalloy [55]. This means that if the magnetization tries to change direction it will lose its strength and therefore it will resist this change [53, 55, 73]. This effect is known as the demagnetization factor [73].

If a coil is put around the mirror the magnetic field of the coil forces the permalloy magnetization to change direction towards the magnetic field. The demagnetization factor however will try to resist this change and therefore it will exert an equal force in the opposite direction of the change on the permalloy [53, 55]. The permalloy will then turn towards the magnetic field due to this effect.

Simulations of this device show that if a microfabricated coil of 10 turns is put around the permalloy with a thickness of 50 $\mu$ m and length of 10mm a force of 2mN can be expected. Permalloy thicknesses higher than 50 $\mu$ m are hard to obtain and do not significantly increase the force in comparison to the added mass. The current injected in the coil is set to  $I=1A$ . The cross section of the coil wire is 50 x 50  $\mu$ m<sup>2</sup>. The power consumption is around 1.5Watts. The inductance is around  $L = 2mH$  and the rise time of the coil is around  $\tau = 0.1\mu s$ . the mass of the moving part is around  $m = 40mg$ .

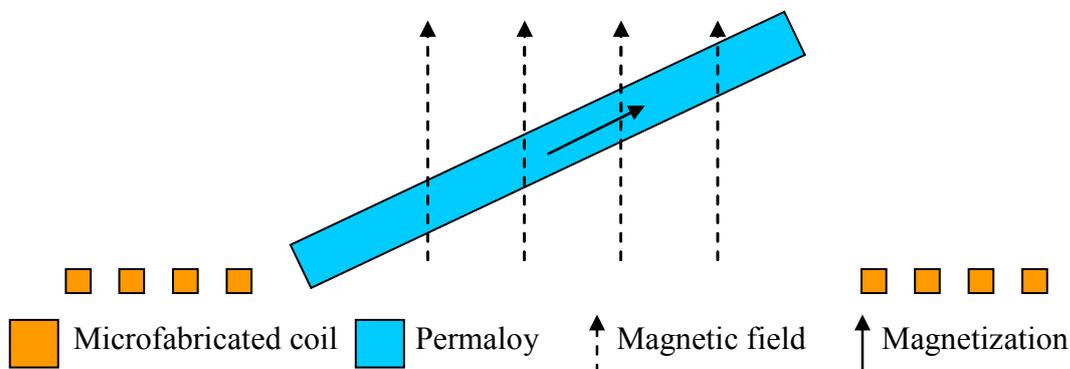


*Figure 4-11: Cross section schematic of the torque driven design. The mirror is covered with a permalloy shown in blue. The mirror is not shown. The permalloy is magnetized along the long axis of the layer, shown by the arrow. A coil is put around the mirror, shown in orange. The magnetic field of the coil, shown with dotted arrows, forces the permalloy to turn towards the magnetic field.*

## 4.2 Comparison of magnetic Actuators

Several different magnetic designs have been discussed in the previous sections. Table 4-3 shows the different aspects of the different magnetic designs. In this table the favorable aspects are shown in blue. The disadvantages are shown in red and the average aspects are shown in orange. A comparison of the different aspects will follow and show the advantage of the moving magnet design over the other designs.

- a) The first important factor for comparison is the force to mass (F/M) ratio of the actuator part of the system. The plunger (magnetic comb) design has the highest value. The clapper, the voice coil and moving magnet—stationary coil designs have average values that are much lower than the plunger design. The torque driven ferrite based design has the lowest value.
- b) The number of actuators that can be put on a moving platform of  $1\text{cm}^2$  is shown in this row of Table 4-3.
- c) The next important factor for comparison is the force to mass ratio of the whole system, including the mass of the mirror, etc. In these calculations the force to mass ratio F/M is replaced by torque to moment of inertia ratio T/I, since all of the systems are used for rotation. The ratio thus becomes:

$$\frac{T}{I_{tot}} = \frac{nT}{nI_{actuator} + I_{mirror}} \quad \text{Eq. 4-8}$$

$T$  is the torque of one actuator.  $I_{actuator}$  is the actuator's moment of inertia.  $I_{mirror}$  is the moment of inertia of the  $1\text{ cm}^2$  mirror, and  $n$  is the number of actuators. The mass of the mirror is set to 30mg in the following calculations. The plunger (magnetic comb) actuator has the worst T/I ratio although it has the best F/M ratio as shown in row (a). This is because of the short attachment pillar to the mirror shown in Figure 4-5. The torque driven design also has a low T/I value. The clapper and voice-coil designs have much better T/I values and the moving magnet—stationary coil design shows the highest T/I ratio.

- d) The power consumption of the plunger and voice coil are the lowest of all the designs. The others all have a few watts of consumption. However microfabricated coils can dissipate the power more easily and avoid heating complications.
- e) The rise time  $\tau$  of the coil used in each design is also important. Even with a very good F/M ratio, the system's response can not be faster than the response of the electronic circuit of the system. The voice coil, the torque driven, and the moving magnet—stationary coil design have the lowest rise times.
- f) Rise time is inversely proportional to resistance in an RL circuit and power consumption is directly proportional to resistance. Therefore if the power consumption is increased to the maximum value on the list (4 Watts for the clapper design) the rise time will be more comparable between the different designs. This can be done by adding a series resistance to the

RL circuit;  $\tau = L/(R_0 + R_{add})$ .  $R_0$  is the intrinsic resistance of the RL circuit and  $R_{add}$  is the added series resistance. This is shown in (f) as “*Compensated  $\tau$* ”.

- g) Another advantage of the voice coil, torque driven and moving magnet designs is the ability to exert force in two directions.
- h) The displacement range of the different designs is either small or medium. Very large displacement range is very hard to obtain without significantly reducing the force.
- i) The linearity of the force is the factor that affects the ease of the feedback control of the system. The voice coil and the plunger Designs are the only designs that fulfill this criterion. However implementation of a feedback controls are capable of compensating for the force nonlinearities and therefore the impact of the force nonlinearity is considered to be moderate on the final decision.
- j) Hysteresis can also complicate the control of the system. The voice coil and the moving magnet designs are advantageous in this regard.
- k) As mentioned before, heat dissipation is done by conduction in space, if no gas encapsulation is envisaged. The torque driven and moving magnet design have the advantage of using stationary microfabricated coils that have high heat dissipation capabilities.
- l) Last but not least is the difficulty of the fabrication process is shown. The torque driven and clapper designs do very well in this regard. These two designs do not need any manual manipulation and all parts can be microfabricated. The plunger has a difficult fabrication process while the voice coil design has a complicated assembly process as previously discussed. The moving magnet—stationary coil design uses magnets that are assembled on the mirror.

This is due to the fact that the deposition of magnetic materials on MEMS is a new and progressing field that has yet to mature, as discussed in chapter 2.2.4. The best magnets available are fabricated in bulk and have very high  $(BH)_{max}$  values. In order to take advantage of this property and keep the fabrication simple, the magnets should be manually positioned on the moving platform. This however is not a very precise procedure.

#### 4.2.1 Conclusion and chosen magnetic design

Having the advantages and disadvantages of the different magnetic designs, the moving magnet design is preferable. This design has the highest T/I ratio, the fabrication process is not too hard, there is no hysteresis in this design and the nonlinearity of the force can be handled with the feedback system. The two important factors of heat dissipation and electronic rise time are also quite acceptable for this design. These factors lead to the conclusion that the moving magnet design is convenient for this project and was used for actuation.

**Table 4-3: Achievable forces, advantages, and disadvantages of the different design concepts. According to this table the moving magnet design is the most advantageous design since overall, it has the best characteristics.**

|                             | (1) Plunger<br>(magnetic comb)        | (2) Clapper                     | (3) Voice coil                                   | (4) Torque driven                             | (5) Moving magnet   |
|-----------------------------|---------------------------------------|---------------------------------|--|---|---|
| a) F/M                      | 20mN/5mg<br>=4000                     | 3mN/6mg<br>=500                 | 50mN/200mg<br>=250                               | 2mN/40mg<br>=50                               | 5mN/10mg<br>=500  |
| b) No. of actuators         | 1                                     | 2                               | 4  | 1   | 4   |
| c) T/I ratio                | 2800                                  | 30500                           | 48000  | 6000  | 60000   |
| d) Power                    | 6mW                                   | 4W                              | 0.1W   | 1.5 W   | 1W  |
| e) Rise time $\tau$         | 100ms                                 | 10mS                            | 10 $\mu$ s                                       | 100 ns  | 100 ns  |
| f) Compensated $\tau$       | 150 $\mu$ s                           | 10ms                            | 1 $\mu$ s  | 40 ns   | 25 ns   |
| g) Push-pull                | No                                    | No                              | Yes  | Yes   | Yes   |
| h) Range                    | Medium                                | Small                           | Medium   | Medium  | Medium  |
| i) Linear force             | Yes                                   | No                              | Yes  | No  | No  |
| j) Hysteresis               | High                                  | High                            | Low  | Medium  | Non   |
| k) Heat dissipation         | Low                                   | Very Low                        | Low  | High  | High  |
| l) Fabrication<br>/assembly | Hard                                  | Easy/integrated                 | Hard   | Easy/integrated                               | Easy/manipulation   |
| Limiting factor             | Low F/M,<br>Cumbersome<br>fabrication | Slow rise time,<br>Hysteresis   | Heat dissipation,<br>fabrication                 | Low F/M and high<br>moving mass               | Force<br>nonlinearity<br>and moving<br>mass                   |
| Advantages                  | linear response                       | High force, easy<br>fabrication | Push-pull, fast<br>rise time, linear<br>response | High heat<br>dissipation, easy<br>fabrication | High heat<br>dissipation, no<br>hysteresis, fast<br>rise time |

### 4.3 Electrostatic actuation

Two different electrostatic designs were presented in chapter 3.3. These two designs were examined to find the preferred design for our application.

#### 4.3.1 Parallel plate Actuator

Figure 4-12 shows the schematic configuration of the possible system with a 1 cm mirror. The forces of this kind of actuator are nonlinear and can be found by Eq. 3-21. If the mirror size is fixed at 1cm and the desirable actuation angle is  $\pm 3.5^\circ$ , the distance needed for actuation is around 350 $\mu$ m. As it was discussed in chapter 3.3.1, the parallel plate actuator exhibits snap-in behavior after 1/3 of the total gap distance. Therefore the gap between the plates in Figure 4-12 should be 3 times as large and around 1mm.

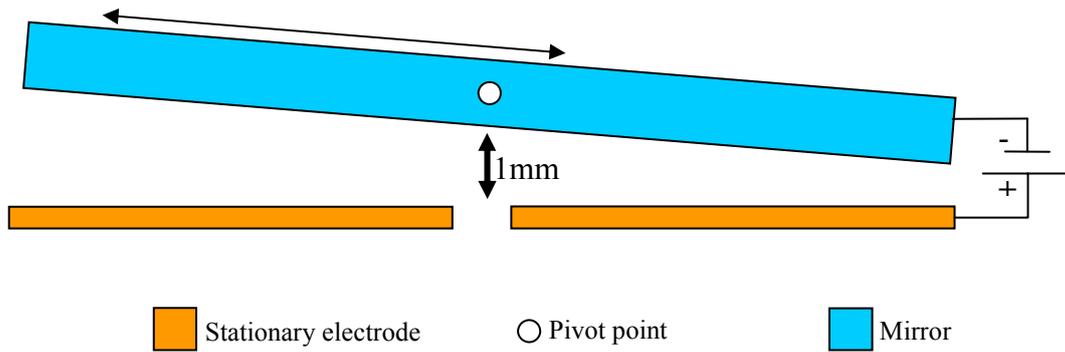


**Figure 4-12:** The schematic configuration of the parallel plate system with a 1 cm mirror. The forces of this kind of actuator are nonlinear. The distance between the mirror and the stationary electrode should be set to 1mm in order to avoid snap-in issues if the mirror has to turn  $3.5^\circ$ .

Figure 4-13 shows the variation of the force as the gap is changed from 13 to  $65\mu\text{m}$  for three different voltages on the top axis of the figure. Figure 4-13 shows that the force at a gap of  $65\mu\text{m}$  is already minute. However if the desired actuation angle is reduced the force increases nonlinearly. If the total distance is reduced to  $25\mu\text{m}$ , the force at  $U=200\text{V}$  would be  $F=3\text{mN}$  and for  $U=300\text{V}$  it would be  $F=6\text{mN}$ .

However the snap-in behavior of the actuator should also be considered, since only one third of the initial distance is usable before snap-in occurs. The corresponding actuation angle for the gap distance is shown on the bottom axis of Figure 4-13. The corresponding actuation angle for a  $25\mu\text{m}$  gap is around  $\theta = 0.2^\circ$ .

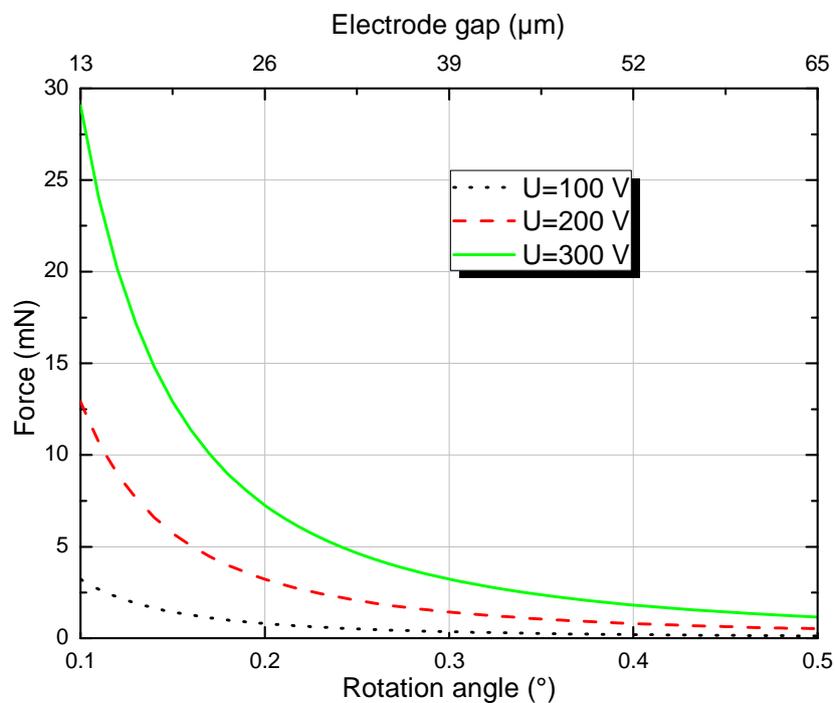


**Figure 4-13:** The variations of the force of the parallel plate actuator as the gap is changed from 13 to  $65\mu\text{m}$ . the gap distance is shown on the top axis. The corresponding actuation angle for the gap distance is shown on the bottom axis. Three different voltages are shown.  $100\text{V}$  is shown in dotted black,  $200\text{V}$  is shown in red dashed, and  $300\text{V}$  is shown in green line. The forces at the  $65\mu\text{m}$  distance are minute. If the desired actuation distance is reduced the force increases nonlinearly.

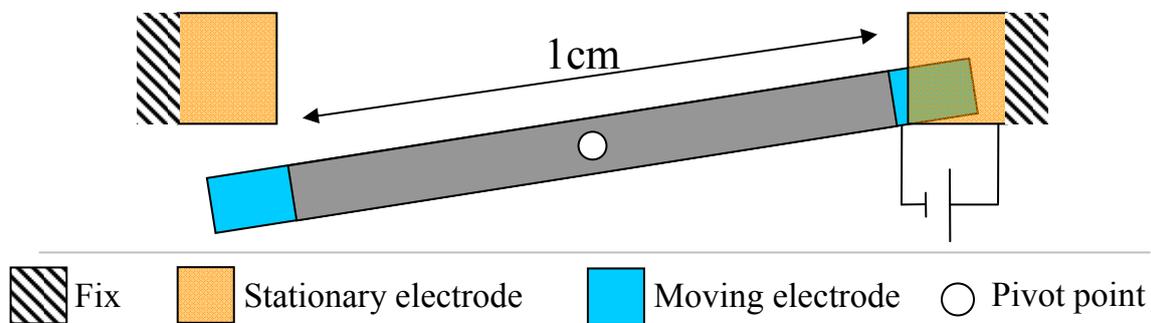
### 4.3.2 Comb drive Actuator

Figure 4-14 is the possible schematic of 1cm comb-drive actuator. The comb fingers are created at the far ends of the mirror to increase the torque. A voltage is applied between the stationary and the moving combs. It makes the moving combs move down into the stationary combs. The force of the system is given by Eq. 3-22.

If the mirror width of the 1cm is patterned to a comb actuator, about 500 and more fingers can be formed on each side of the 1cm square mirror depending on the gap between the combs. If the desirable actuation angle is set to  $\pm 0.2^\circ$ , the attainable force is shown in Figure 4-15. This figure shows the force due to voltage change. The minimum gap size should be set to  $5\mu\text{m}$  to avoid any chance of breakdown as discussed in chapter 3.4. The length of the combs is considered to be  $200\mu\text{m}$ .

This configuration can create large forces just like the parallel plate electrostatic actuator. For a gap of  $5\mu\text{m}$ , and a voltage of  $U=200\text{V}$  the force is around  $F=5\text{mN}$ .

The  $0.2^\circ$  rotation angle is chosen since it creates an out of plane displacement of around  $40\mu\text{m}$  for this mirror size. This is an acceptable displacement value for a vertical comb actuator that is also comparable to the parallel plate actuator of the previous section. An inconvenience of this design lies in the nonlinearity of the lateral forces that can be approximated by Eq. 3-21. This force can be very problematic due to its nonlinear nature which can increase rapidly and cause lateral snap-in.



**Figure 4-14:** Possible schematic of 1cm comb-drive actuator. The comb fingers are created at the far ends of the mirror to increase the torque. A voltage is applied between the stationary and the moving combs. It makes the moving combs move down into the stationary combs.

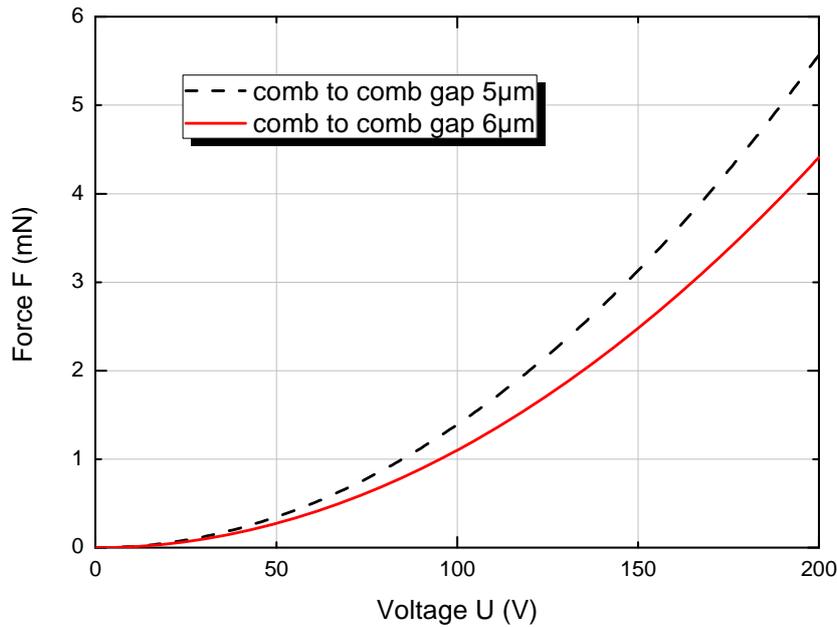


*Figure 4-15: The force that can be created by the vertical comb design on a 1cm mirror. This figure shows the force due to voltage change from 0V to 200V. Two different gap sizes 5 and 6  $\mu\text{m}$  are shown with red line and dashed black lines respectively. Decreasing the gap increases the maximum force.*

### 4.3.3 Conclusion and chosen electrostatic design

As it was shown above both of the electrostatic actuators can generate forces of the same order of magnitude if the rotation angle is small. The parallel plate actuator, on the other hand, is much easier to fabricate. However, these actuators can only have small rotation angles with a mirror size of 1cm. Therefore their implementation needs to be combined with other means if larger rotation angles are needed.

The chosen design for this thesis was a vertical comb electrostatic mirror. A novel method of fabrication of the electrostatic actuator was proposed that will be shown in the following chapters. In order to test the fabrication feasibility of this process, the vertical comb actuator design was chosen.

This decision was based on the fact that the vertical comb actuator is easily scalable; therefore the fabrication design can also be used for smaller electrostatic vertical comb actuators.

## 4.4 Core aspects of the mirror design

In the previous sections the general aspects of the different types of actuators were examined and compared and the most adapted design concepts for this project were found.

In this section a representation of the magnetic and electrostatic actuators with the correct dimensions and forces will be shown. The achievable resonant frequencies and rotation angles will be presented for both of the actuators and compared. The final concept of the design will be presented based on this comparison. The key properties and implementation guidelines of the design will also be shown.

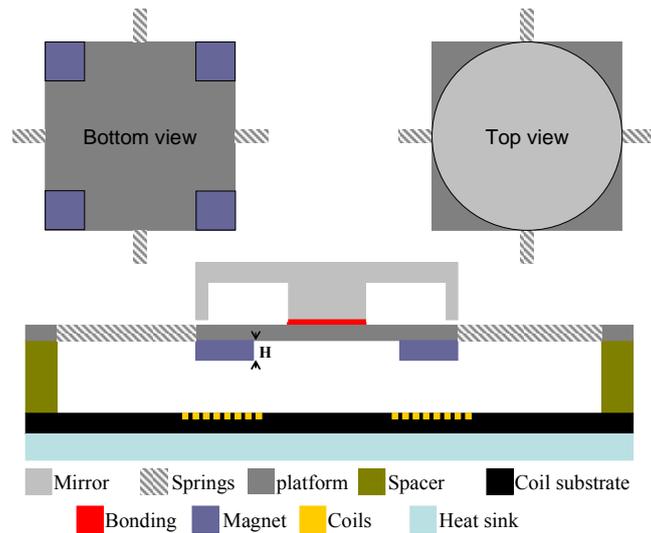


*Figure 4-16: The cross section and the top and bottom views of the different parts of the magnetic mirror system including the mirror the magnets and the coils are shown. The magnets are assembled on the mirror. A spacer is put between the mirror and the coils. The coils are microfabricated in a silicon substrate to reduce heat creation. The device is put on a heat sink.*

#### 4.4.1 Magnetic design

The design of the magnetic mirror will be presented here. The inverse relation between the maximum rotation angle and resonant frequency will be presented, that leads to dividing the system into two actuator-mirrors.

##### 4.4.1.1 Magnetic mirror concept

The general concept of the scanner system is presented in Figure 4-16. It uses moving magnet-stationary coil actuators as discussed in chapter 4.1.6. Figure 4-16 shows the cross section of the design and the top and bottom views. The major parts of the device can be described as follows: a) the moving platform where the springs are also situated around it. The magnets are attached on the backside of this moving platform. b) The mirror bonded to the front side of this platform. c) This platform is placed on the driving coils with a spacer that creates the needed separation distance between the magnet and the coils. f) The assembled system is put on a heat sink that keeps the coil temperature under control. The mirror and the moving platform were made from two separate wafers in order to ease their fabrication. This gave a great extent of freedom in shaping the mirror and hollowing it to reduce its mass.

This design has 4 magnets. Each magnet is put on one corner of the mirror. 3 magnets are sufficient for 2D movements. However in this case having more magnets is more advantageous in terms of F/M ratio as discussed in 3.2.7.

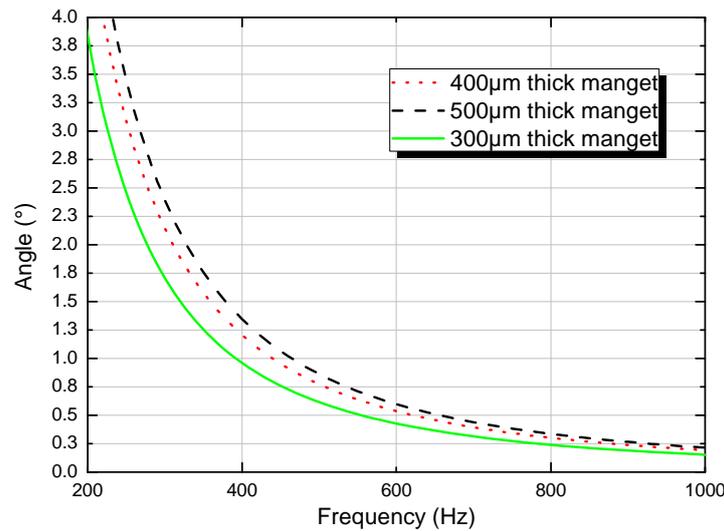


*Figure 4-17: Plot of the available angles for a 1cm mirror at different resonant frequencies “ $f_r$ ”. The calculations of this figure are done for a 1cm mirror of 300µm thickness which 70% of its mass is removed by patterning. Three different magnet thicknesses are shown in brown for 100µm, blue for 300µm and purple for 500µm. Increasing the mass of the magnets is advantageous for the amplitude of the system and disadvantageous for the resonant frequency, especially at higher angular deflections.*

#### 4.4.1.2 Dependency of the resonant frequency on the maximum static tilt angle

Using Eq. 3-1 and Eq. 3-2, the maximum resonant frequency of the device with regard to the maximum desired static tilt angle of the design can be plotted. According to these equations, the frequency of the design depends on the mass and the spring constant and the deflection angle is dependant on the force and spring constant. A plot of the available resonant frequencies “ $f_r$ ” for a 1cm mirror at different static deflection angles can be obtained. This plot is shown in Figure 4-17. The calculations of this figure are done for a mirror with 1cm diameter and 100µm thickness. The force is approximated by the interaction of the axial magnetic field of a cylindrical magnet and a spiral coil [70]. Three different magnet thicknesses are shown in Figure 4-16 (300µm, 400µm, 500µm), which mainly show the effect of changing the magnet thickness on the system’s amplitude. This shows that increasing the thickness of the magnets is advantageous for the amplitude of the system, especially at lower frequencies. The angular deflection drops to  $\theta \approx 0.2^\circ$  at  $f_r = 1$  kHz.

#### 4.4.2 Electrostatic design

It was shown that high forces can be obtained from the electrostatic and magnetic actuators if the actuation range is small. Another advantage of the electrostatic design is that its mass is much smaller than the magnetic design.

##### 4.4.2.1 Electrostatic design concept

The general concept of the electrostatic vertical comb design is shown in Figure 4-18. The mirror is made out of one wafer and the moving platform containing the springs and combs are made from another wafer. The mirror is created separately. It is then bonded to the actuation platform. The Top view of the electrostatic system is also shown in Figure 4-18. The actuation platform was designed to be round with 3 springs around it. The combs are around the rim of the circular moving platform.

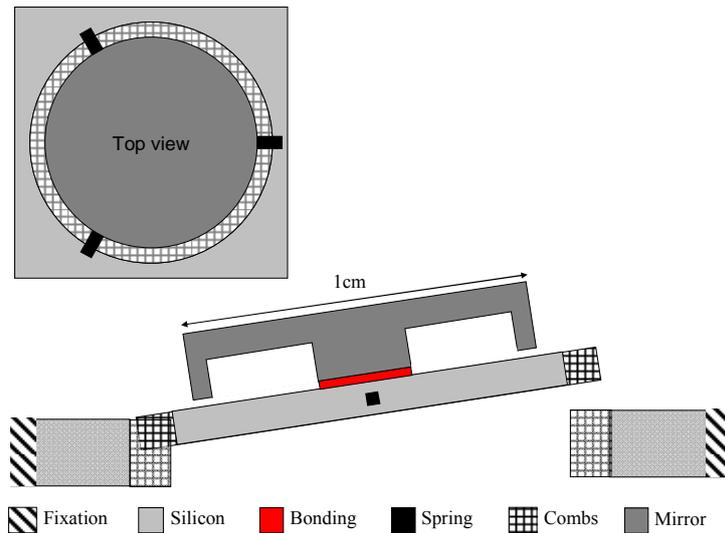


**Figure 4-18:** General concept of the electrostatic design. The mirror is bonded to the platform. The top view of the system shows the three comb sections between the adjacent springs that make the 2D rotation possible.

Therefore if each comb is set to be  $10\mu\text{m}$  wide and the gap to be  $5\mu\text{m}$ , each section between the two adjacent springs can have 640 combs. These three comb sections between the adjacent springs make the 2D rotation possible.

#### 4.4.2.2 Resonant frequency vs. maximum tilt angle

The achievable angles due to variation of the resonant frequencies according to the available forces derived in chapter 4.3.2 are shown in Figure 4-19. The size of the mirror is set to 1cm as usual. In this figure the voltage is set to  $U = 200\text{V}$  and the gap between the combs is  $5\mu\text{m}$  and  $6\mu\text{m}$ . as it was shown in chapter 4.3 the electrostatic force is only effective in small gap sizes. However as the resonant frequency approaches  $f_r = 1\text{ kHz}$  the tilt angle becomes comparable with that of the magnetic actuator  $\theta \approx 0.2^\circ$ .

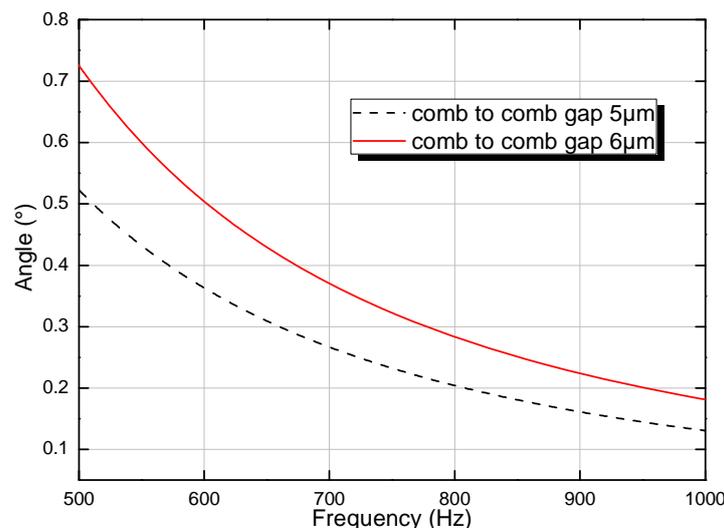


**Figure 4-19:** The achievable angles due to variation of resonant frequencies according to the available forces. The size of the mirror is set to 1cm. The voltage is set to  $U = 150\text{ V}$  and the gap changes from 3 to  $5\mu\text{m}$ . A gap of  $4\mu\text{m}$  can give a rotation angle of  $\theta_{\text{mech}} \approx 0.2^\circ$  for a resonant frequency of  $f_r = 1\text{ kHz}$ . These results show that the electrostatic actuator has the same tilt angle as the magnetic actuator for higher resonant frequencies.

#### 4.4.3 Separation of the design to two mirrors

The comparisons of the resonant frequencies vs. the tilt angle of the electrostatic and magnetic devices show the incompatibility of having high angles and high resonant frequencies at the same time due to the available forces. In order to achieve large actuation range and high resonant frequency, the system is divided to two mirrors. One of these mirrors is used as a slow moving coarse position finder with a high steering angular range ( $f_r = 200$  Hz,  $\theta = \pm 3.5^\circ = 61$  mrad) and long response time and the other mirror is a fine tuning mirror that has a short response time and a small steering angular range ( $f_r = 1$  kHz,  $\theta = \pm 0.2^\circ = 3$  mrad). This principle is used in many adaptive-optics systems and the examples used in satellite telecommunications were given in chapter 2.3. In the rest of this thesis these two mirrors will be called the slow and fast mirrors respectively. This concept is shown in Figure 4-20. To our knowledge this principle has not been implemented using micro-machining. A fixed mirror is also added to the system in order to be able to position both of the moving mirrors on the same level.

These two mirrors are capable of moving independently. Their sum of two independent angles gives the final beam tilt angle.

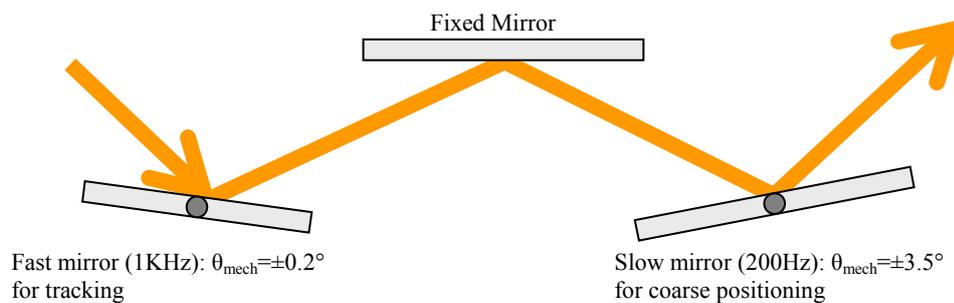


**Figure 4-20: Division of the system to two different mirrors. One is used as a slow moving coarse position finder with a high steering angular range and the other mirror will be a fine tuning mirror that has a fast response time but small steering angular range.**

#### 4.4.4 Optical beam dimensions

The diameter of the optical beam that can be manipulated by these mirrors should be smaller than the diameter of the mirrors. This is due to the illumination method and the arrangement of the system as shown in Figure 4-21. Due to this configuration, the incident beam on the first mirror will be reflected on a fixed mirror and then to the second mirror. This leads to a translation of the optical beam “ $\Delta x$ ” on the second mirror as shown in Figure 4-21. This translation is dependant on the incident angle of the beam on the first mirror, the translation angles of the mirrors and the distance between the moving mirrors and the fixed mirror.

This translation angle can be calculated using simple ray optics although the incident beam on the mirrors is Gaussian. This is possible since the mirror diameter is 10 mm large and the wavelengths that are normally used for inter-satellite telecommunications are in the 1  $\mu\text{m}$  range [19]. These values result in a very long Rayleigh range ( $z_0 = 50$  m) for the laser beam, which results in a very small divergence angle of less than 80  $\mu\text{rad}$ .

The angle of incidence on the 1<sup>st</sup> mirror is the first factor that reduces the optical beam's width. The higher this angle, the smaller the optical beam's width should be. Otherwise some part of the incident beam will surpass the borders of the moving mirror. An incident angle of  $\theta_{inc} = 30^\circ$  will allow a beam width of 9mm to be shone on the first 1cm mirror. The mirror translation angles in these calculations are as discussed in the previous chapters and shown in Figure 4-21.

Increasing the distance between the moving mirrors and the fixed mirror will also lead to higher optical beam translations  $\Delta x$ , on the second moving mirror. If the moving mirrors and the fixed mirror are 5mm apart, the optical beam's translation value is  $\Delta x = 300\mu\text{m}$ . This value reduces with the reduction of this distance. Therefore the beam's width should still decrease a further  $2 \cdot \Delta x$  in value if the 2<sup>nd</sup> mirror's size is also kept at 1cm.

As a whole, each mirror should reserve 1mm of its width to compensate for the optical beam translations. This value is calculated for a fixed mirror that is 5mm away from the moving mirrors. Therefore a light beam with a diameter of at least 8mm can be easily obtained from this system.

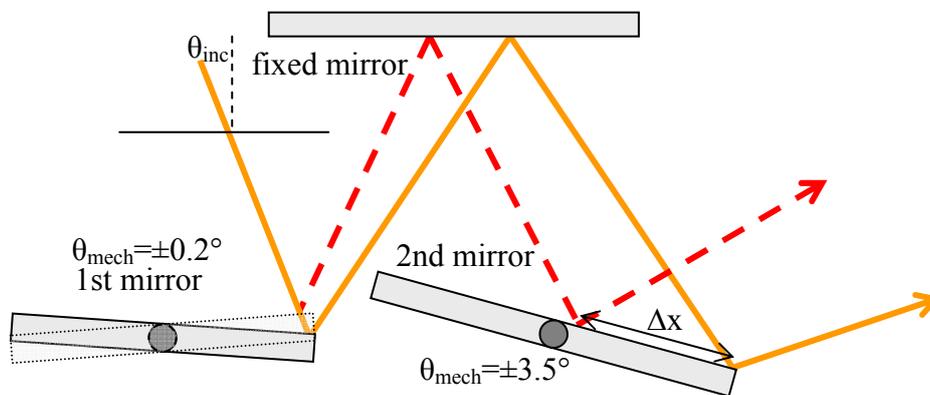


**Figure 4-21:** The translation of the beam of light by “ $\Delta x$ ” on the second mirror as it is reflected from the first mirror. This translation is dependant on the incident angle of the beam on the first mirror, the translation angles of the mirrors and the distance between the moving mirrors and the fixed mirror. Due to the small deflection of the first mirror, the translation is  $\Delta x = 300\mu\text{m}$  for  $\theta_{inc} = 30^\circ$ . This means that an optical beam diameter of 8mm can be easily used with this system.

## 4.5 Fabrication and assembly

The fabrication and assembly concepts of the magnetically and electrostatically actuated mirrors will be presented in the following. This chapter does not strictly deal with the process flow of the fabrication, but rather with the decisions that were made on how each part should be fabricated and how it should be assembled.

### 4.5.1 Magnetic mirror

Different fabrication and assembly procedures will be discussed here: 1) Microfabrication of the actuation platforms, 2) microfabrication of the mirror, 3) bonding of the actuator platform and the mirror, d) assembly of the magnets on the moving platform, e) assembly of the actuating system on the coils and the heat sink

#### 4.5.1.1 Microfabrication of the mirror and moving platform

The mirror and the moving platform were microfabricated out of two separate wafers. The moving platform was made of a “Silicon On Insulator” SOI wafer. Two different processes were used for microfabricating the mirror, one method used a SOI wafer and another method used a simple silicon wafer.

The schematic view of the mirror and the moving platform is shown in Figure 4-22. The hollowed mirror is shown on the top with its own frame around it. The moving platform is shown on the bottom. It is connected to the frame via the springs. The springs on the moving platform were made on the front side or the device layer of the SOI wafer. The frame of the moving platform has holes that were used for alignment during assembly as can be seen in Figure 4-22. These holes were fabricated on the backside or the handle layer of the mirror.

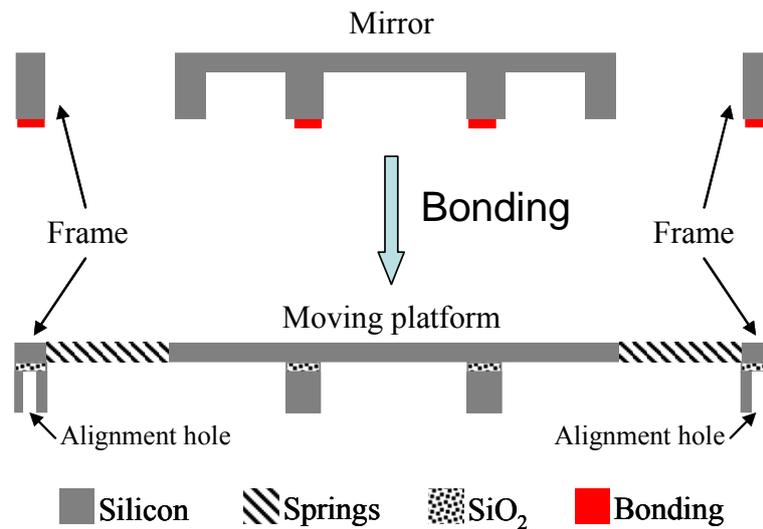
#### 4.5.1.2 Bonding of the mirror and the actuation wafers

The mirror and the actuation platform are bonded together at wafer level. This minimizes the misalignment of the actuation platform and the mirror as shown in Figure 4-22. This process granted us the freedom of forming the mirror to our desired shape. By this method the mirror could be easily hollowed to have the least possible weight. On the other hand bonding profile of these two parts could be optimized to make the mirror as flat as possible.

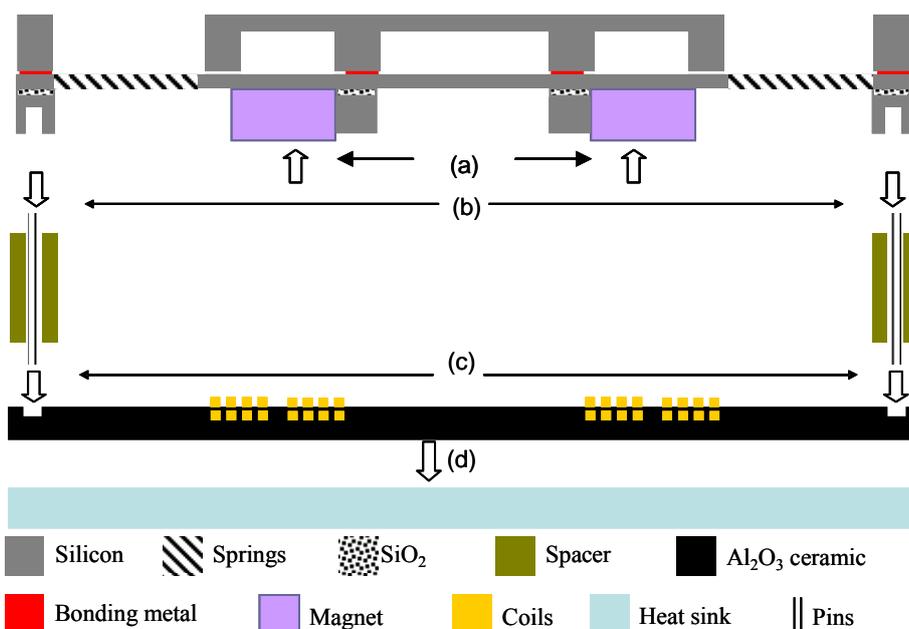
#### 4.5.1.3 Assembly

Figure 4-23 shows the assembly of the different parts of the magnetic actuator mirror. Figure 4-23a, shows the schematic assembly of the magnets on the backside of the actuation platform. The magnets were positioned around the four corners of the backside and glued to their place. Alignment of the magnets is ensured by pushing them against alignment structures at each corner that are shown in Figure 4-22 and Figure 4-23. These alignment structures force the magnets to their correct positions.

The mirror and coil chips both have holes on the outer corners that allow pins to go through them as shown schematically in Figure 4-23b & c. The pins were glued in the holes. They allow direct alignment of the two chips. Silicon spacers were placed on the pins to create the needed distance between the mirror and the coils. Since these spacers are made out of one silicon wafer they have very good thickness uniformity. The system is then put on an aluminum heat sink as shown in Figure 4-23d.



*Figure 4-22: The schematic view of the mirror and the moving platform is shown. The mirror and the moving platform were microfabricated out of two separate wafers. The moving platform was made of a SOI wafer. The hollowed mirror is shown on the top with its frame around it. The moving platform is shown on the bottom. It is connected to the frame via the springs. The frame has holes that were used for alignment during assembly.*



*Figure 4-23: The cross-section of the different parts of the design that were assembled is shown. The different steps consist of (a) assembly of the magnets on the mirror. (b) Assembly of mirror on the spacer. (c) Assembly of spacer on the coil substrate. (d) Attachment to heat sink.*

#### 4.5.1.4 Mechanical design

The important factors for the mechanical part are the spring constant  $k$  and the maximum stress  $\sigma_{max}$  at maximum deflection. The spring constant is a function of bending and force. Therefore the force must be known to calculate  $k$  according to the needed deflection. The force in the following simulations was set to  $F = 6\text{mN}$  for the  $\theta = 3.5^\circ$  deflection and  $F = 12\text{mN}$  for the  $\theta = 0.2^\circ$ . For a 10mm mirror rotating around its center, this is equivalent to a displacement of  $z = 300\mu\text{m}$  and  $z = 20\mu\text{m}$  for the rotation angles  $\theta = 3.5^\circ$  and the  $\theta = 0.2^\circ$  respectively. These force values were chosen from the simulation results shown in Figure 5-4 in chapter 5.1.1. According to Figure 5-4 are

chosen force values were somewhat conservatively chosen. They were for coil-gap distances that were at least 2 times bigger than the values needed for displacement. This was done at the earlier stages of the project in order to compensate for the unknown force values of the real magnets and the unknown displacement values before snap-in occurred.

The maximum stress in a mechanical spring is exerted at its extremities. The maximum stress of a bending spring is given by  $\sigma_{\max} = Wl/I$ , where  $W$  is the load,  $l$  is the distance from the fixed side of the spring to where the load is applied, and  $I$  is the second moment of inertia. The maximum stress that can be applied to crystalline silicon depends on its crystallographic orientation. However, as a general rule of thumb, if the stress is kept under 200MPa it should be sufficient for any practical application.

Two different magnetic mirrors based on bending beams were designed. One with  $\theta = 3.5^\circ$  mechanical rotation and the other with  $\theta = 0.2$  mechanical rotation. An exploded view of the two actuator-mirrors is shown in Figure 4-24. This figure only shows parts that are relevant to the mechanical actuation. The frame, the coils and the heat sink are not shown in this figure.

The mirror is shown at the top. It has a thickness of  $300\mu\text{m}$  and is hollowed from underneath to reduce its mass. The mirror bonds to a platform that is shown under the mirror in Figure 4-24. The bonding spot is shown in red at the center of the platform. This platform contains four springs that are situated on the four sides of it. The springs are bending springs that are more flexible than torsion springs and therefore less prone to fracture due to the heavy weight of the system, as discussed in chapter 3.5. The platform and the springs have a thickness of  $40\mu\text{m}$ . the width of the springs is  $150\mu\text{m}$ . The total length of each spring of the mirror with  $\theta = 3.5^\circ$  mechanical rotation is 8mm and the total length of the other spring with  $\theta = 0.2$  mechanical rotation is 2.1 mm. The rectangular extrusions at the outer extremity of the springs are the places that attach to the outer frame and do not move (not shown). The magnets are situated under the platform. They have a  $2 \times 2 \text{ mm}^2$  surface. This design has a total of four magnets that allows it to rotate in the X and Y direction. Movement in the Z direction is also possible. Since the magnets can be pushed and pulled by the coils, if two magnets are pulled and two magnets pushed the system will rotate around the desired X or Y direction. Therefore there is a coil dedicated to each magnet, as shown in Figure 4-33 and Figure 4-34 in chapter 4.7.2.

A close-up view of the junction of the platform and springs are also shown in Figure 4-25. The curved connection between spring and the platform help in reducing the maximum stress.

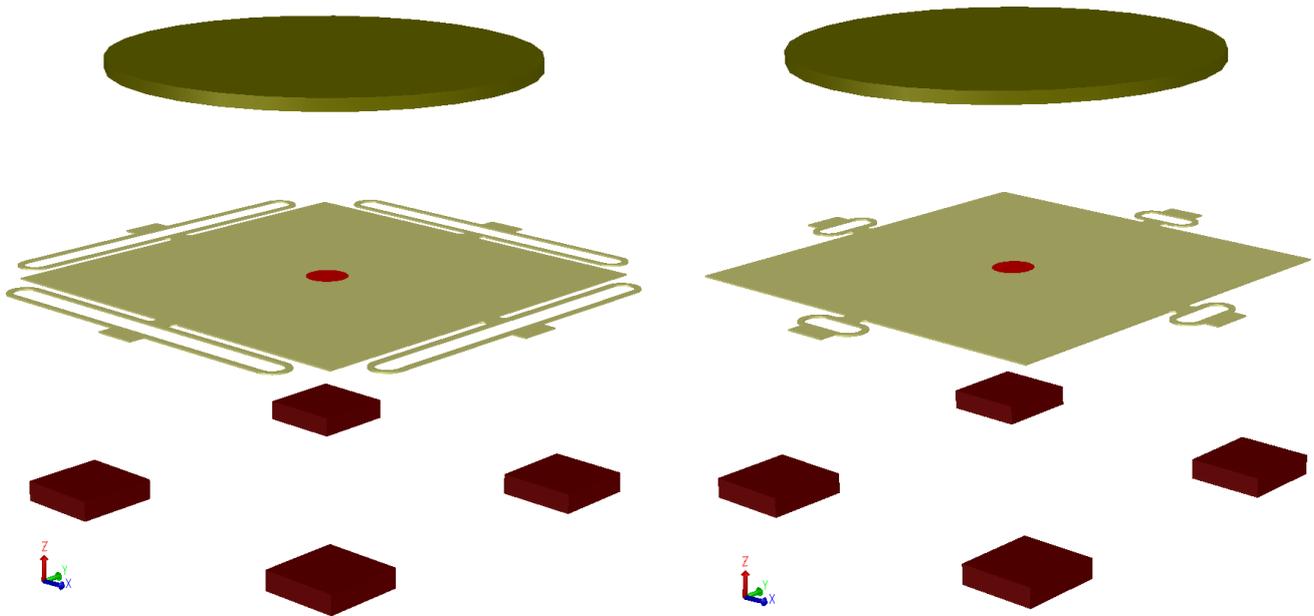


**Figure 4-24:** Exploded views of the two actuator-mirrors (slow and fast) are shown. This figure only shows parts that are relevant to the mechanical actuation. The mirror is shown at the top. It has a thickness of  $300\mu\text{m}$ . The mirror bonds to a platform that is shown under the mirror. The bonding spot is shown in red at the center of the platform. This platform contains four springs that are situated on the four sides of it. The magnets are assembled on the back of the platform.

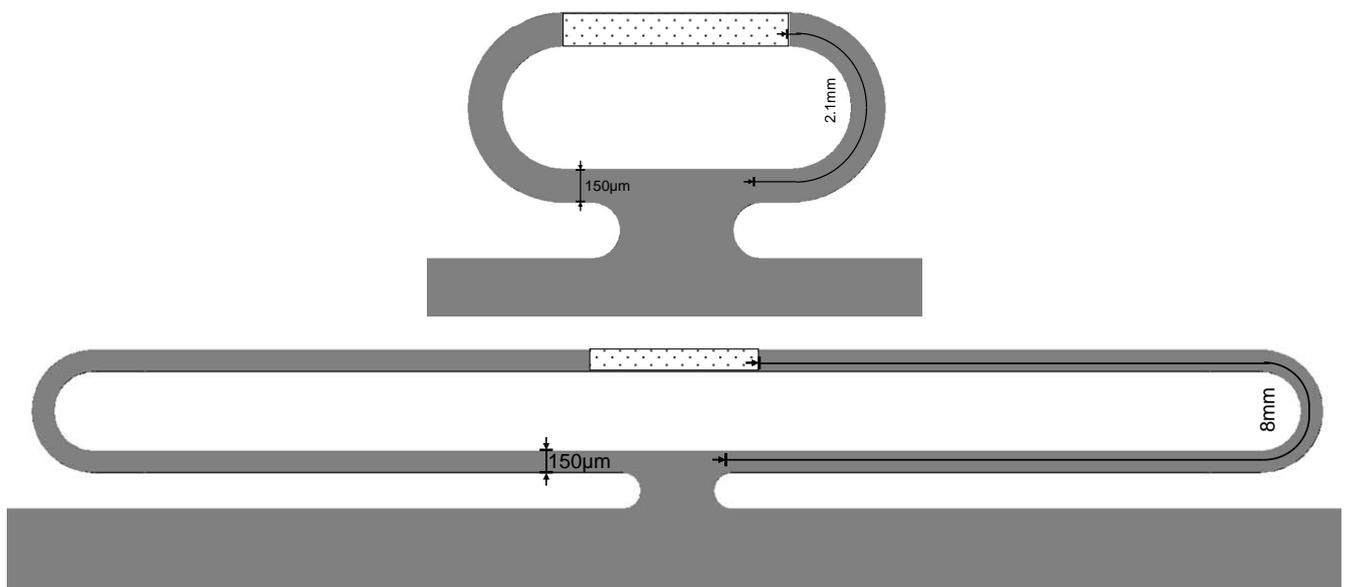


**Figure 4-25:** The springs of the fast and slow mirrors. The fast mirror spring is shown on top and the slow mirror spring on bottom. The total length of each spring of the fast mirror with  $\theta = 3.5^\circ$  mechanical rotation is 8mm and the total spring length of slow mirror with  $\theta = 0.2$  mechanical rotation is 2.1 mm. the fixed positions are shown with the dotted areas.

#### 4.5.2 Electrostatic mirror

The fabrication concept and assembly procedures of the electrostatically actuated mirror will be discussed here: 1) Microfabrication of the actuation platforms, 2) microfabrication of the mirror, 3) bonding of the actuator platform and the mirror, 4) assembly of the magnets on the moving platform, 5) assembly of the actuating system on the coils and the heat sink.

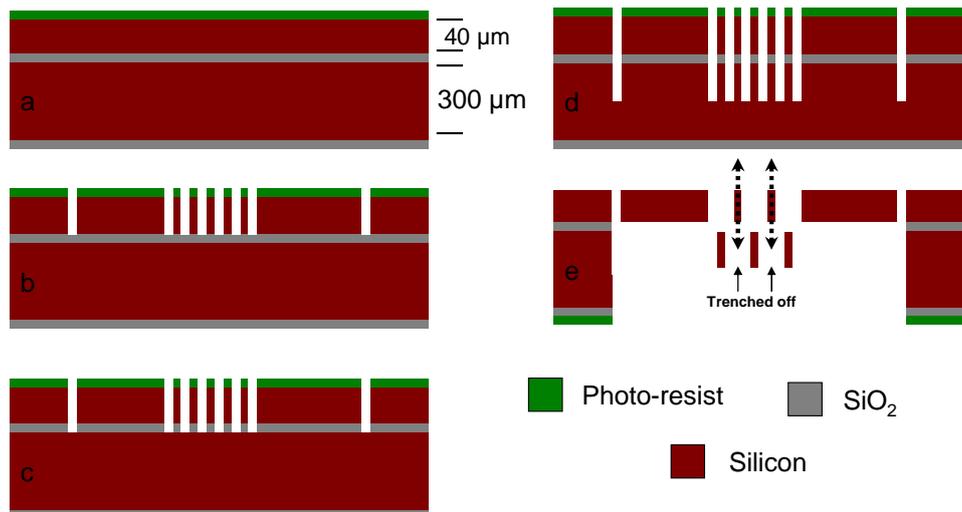


*Figure 4-26: Process flow and top view of the electrostatic mirror depicting one-side DRIE for self aligned vertical comb drives. a- DRIE of the device layer. b- BOX removal using vapor phase hydrofluoric acid (HF-VPE). c- DRIE into the handle layer through the device layer. d- DRIE with a delayed mask process on the handle layer to trench out the unwanted combs. e- HF-VPE release of the unwanted combs.*

At first the proposed microfabrication concept that creates self aligned combs will be presented. The mirror and the moving platform were also microfabricated out of two separate wafers. The moving platform was made of a SOI wafer. The same mirrors used in the magnetic design could be reused for the electrostatic design.

The microfabrication concept of the electrostatic mirror is introduced here. A process that could potentially create self aligned vertical combs was proposed and tested in this project. There are many groups that have proposed different methods for fabrication of self aligning vertical comb-drives [25, 29-39, 41, 106, 107]. In our approach the most important part of the process is forming the vertical combs by etching them on the device layer of an SOI wafer and continuing the etching into the handle layer. This implies the removal of every other comb on the backside, i.e. handle layer and front side i.e. device layer, to enable the movement of the vertical combs. This was simply done by releasing the unwanted combs with etching of the buried  $\text{SiO}_2$  layer of the SOI wafer that was holding the unwanted combs in place. This process creates two set of combs that are completely self-aligned and allow the vertical movement. The major fabrication steps are as follows, shown in Figure 4-26.

a- Deep Reactive Ion Etching (DRIE) of the device layer. b- Buried Oxide (BOX) removal using vapor phase hydrofluoric acid (HF-VPE). c- DRIE into the handle layer through the device layer. d- DRIE with a delayed mask process on the handle layer to trench out the unwanted combs. e- HF-VPE release of the unwanted combs.

Having established the basic process flow of the electrostatic actuator, the following steps that include the mirror bonding and assembly are described below.

#### 4.5.2.1 Bonding of the mirror and the actuation wafers

Similar to the magnetically actuated mirror, the mirror and the actuation platform are made out of two separate wafers. The mirror and the actuation platform could be bonded together at wafer level

as shown in Figure 4-27. The reason is the same as why it was done for the magnetic mirror; it helps in reducing the mass of the mirror, thus the mass of the whole system.

#### 4.5.2.2 Assembly

Figure 4-28 shows the assembly of the different parts of the electrostatic actuator mirror. Figure 4-28a, shows the schematic assembly of the alignment structure with pins on the PCB substrate where the electrical contacts are situated. The alignment structure is used to guide the electrostatic mirror chip into its place on the contact electrodes of the PCB as shown in Figure 4-28b. The contact between the electrostatic mirror chip and the PCB is ensured by either having Pogo pins or gluing the two parts using conductive glue.

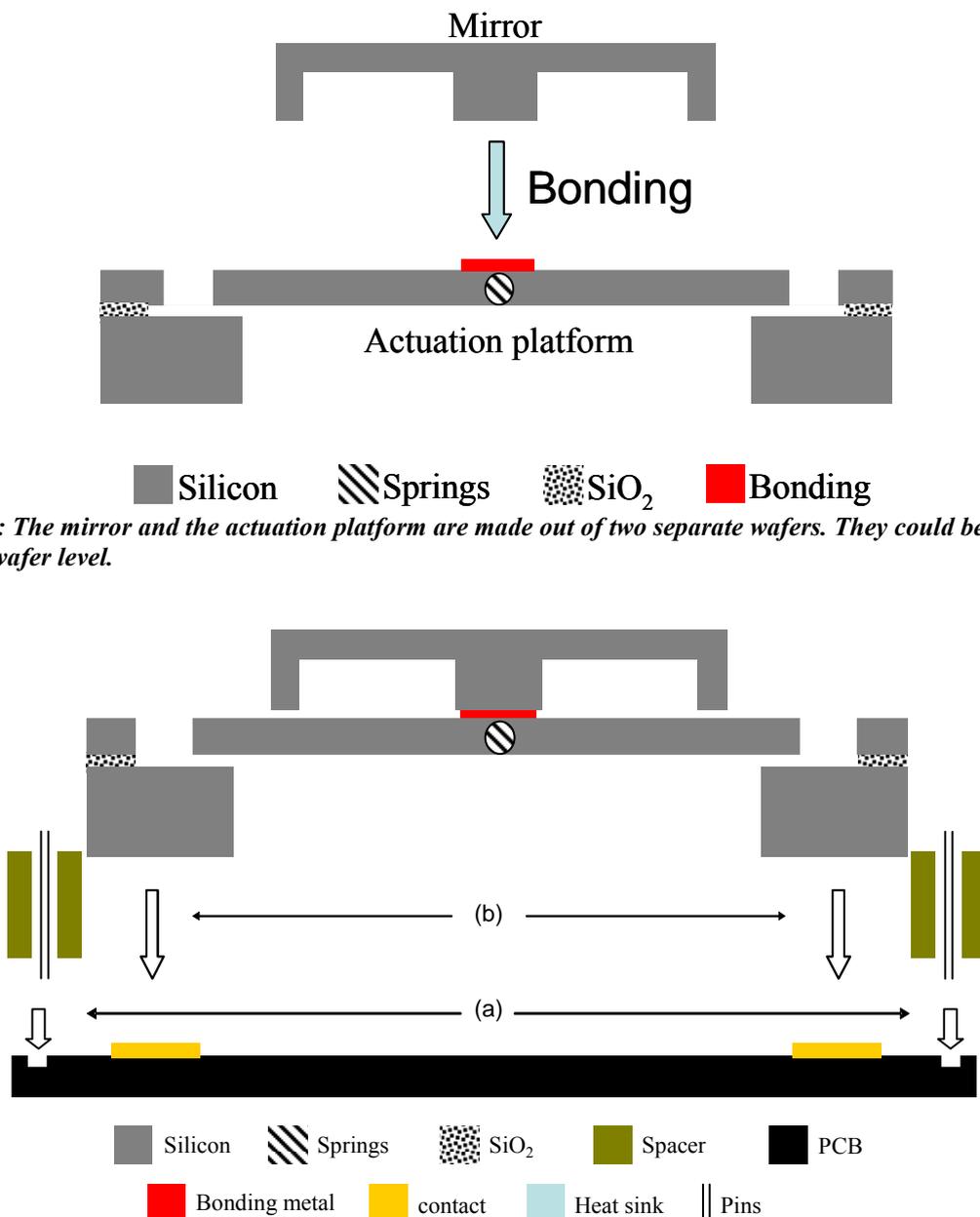


**Figure 4-28:** Assembly of the different parts of the electrostatic actuator mirror. (a) The schematic assembly of the alignment structure with pins on the PCB substrate where the electrical contacts are situated. (b) The alignment structure is used to guide the electrostatic mirror chip into its place on the contact electrodes of the PCB.

### 4.5.2.3 Mechanical design

The exploded view of the mechanical design is shown in Figure 4-29. This design was also used for simulations and the frame around the platform and the mirror is not shown. It consists of a moving platform shown on the top. Three “T” shaped springs are situated around the central circle. The angle between them is  $120^\circ$ . The combs that should be around the platform are not present in the model. The force is directly applied to the rim of the circle. A close-up view of the spring attachment to the moving platform is also shown in Figure 4-29. The moving platform has a thickness of  $40\mu\text{m}$ , the spring however, is thinned down to  $20\mu\text{m}$ . This allows the spring to have the correct spring constant. The dimensions of the “T” spring are given in Figure 4-30. The lower part is  $1000\mu\text{m}$  long and connects to the moving platform. The upper part is  $4000\mu\text{m}$  long and is fixed to the frame shown with dotted triangles. The width of both parts is  $800\mu\text{m}$ . This shape has the advantage of having a very stiff lateral movement while allowing the desired up-down movement.

The mirror part of the actuator is shown in the lower part of the Figure 4-29. The hollowed part of the mirror is visible in this figure. However, in the real device the mirror is on top of the platform.

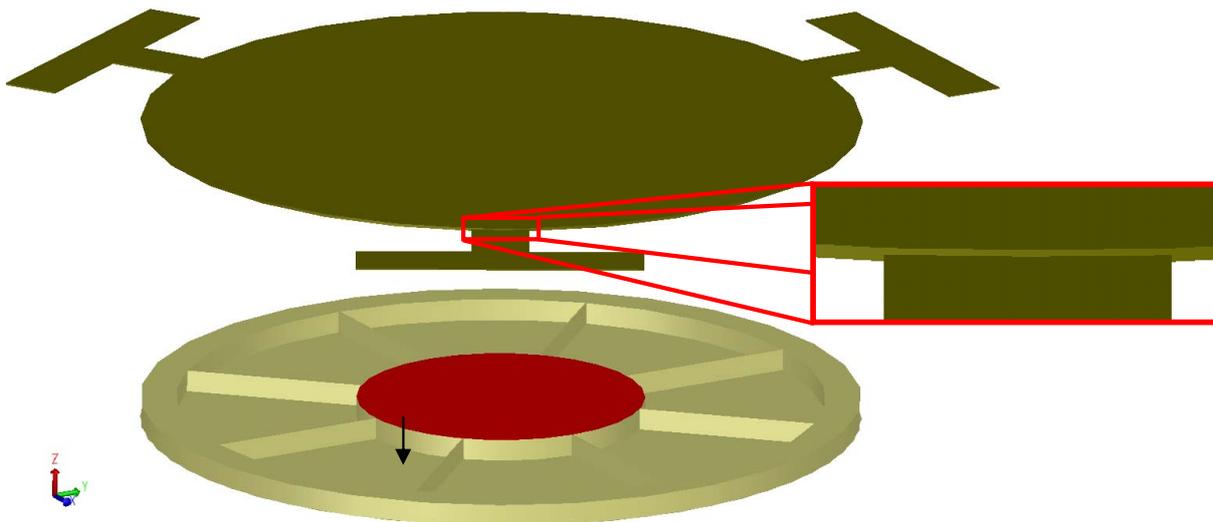


*Figure 4-29: The exploded view of the mechanical design for simulations is shown. The frame around the platform and the mirror is not shown. It consists of a moving platform shown on the top. Three “T” shaped springs are situated around the central circle. The angle between them is  $120^\circ$ . The mirror part of the actuator is shown in the lower part. The hollowed part of the mirror is visible and one part is shown with an arrow.*

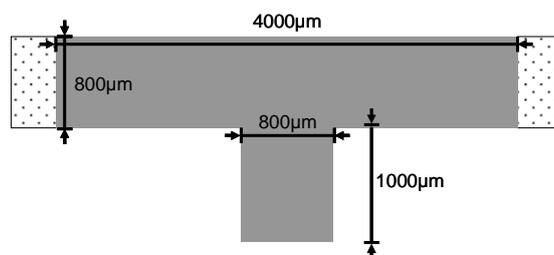


*Figure 4-30: The dimensions of the spring of the electrostatic actuator. The lower part is  $1000\mu\text{m}$  long and connects to the moving platform. The upper part is  $4000\mu\text{m}$  long and is fixed to the frame shown with dotted triangles. The width of both parts is  $800\mu\text{m}$ .*

This does not change the mechanical properties of the moving platform in the simulations. It is only shown in this manner for a better view of the hollow part. The mirror has a total thickness of  $300\mu\text{m}$ . The thickness of the hollowed region is  $250\mu\text{m}$ . The central part shown in red is attached to the centre of the moving platform. The central attachment is larger than the attachment of the magnetic actuator platform and mirror shown in Figure 4-24. This is necessary to keep the  $40\mu\text{m}$  moving platform relatively flat since its deformation could lead to snap-in behavior.

#### 4.6 Combination of the magnetic and electrostatic designs

The previous chapters showed that the system should be divided into two parts consisting of two mirrors in order to have fast response on one mirror (fast mirror) and a large rotation angle on the other (slow mirror). The general overview of this system was shown in Figure 4-21. The light is first reflected on the fast mirror and then on the slow mirror. This increases the usable surface of the mirrors. The system needs a third mirror to reflect the light from the fast mirror on the slow mirror. The magnetic design can be used both for the fast and for the slow mirrors. The electrostatic design is suitable for the fast mirror. The integrated magnetic and electrostatic mirrors are shown together in Figure 4-31. The different parts of these two designs are already discussed in chapter 4.4.1.1 and 4.4.2.1. The main idea was to fabricate the mirror and the actuation parts separately and bond these parts together. The assembly of the different parts such as the magnets and the alignment structures followed suit.

#### 4.7 Commercially fabricated parts

The magnets and the coils of the magnetic actuator were fabricated from the designs that we provided to different manufacturers. The designs are based on their technologies. They are presented in the following paragraph.

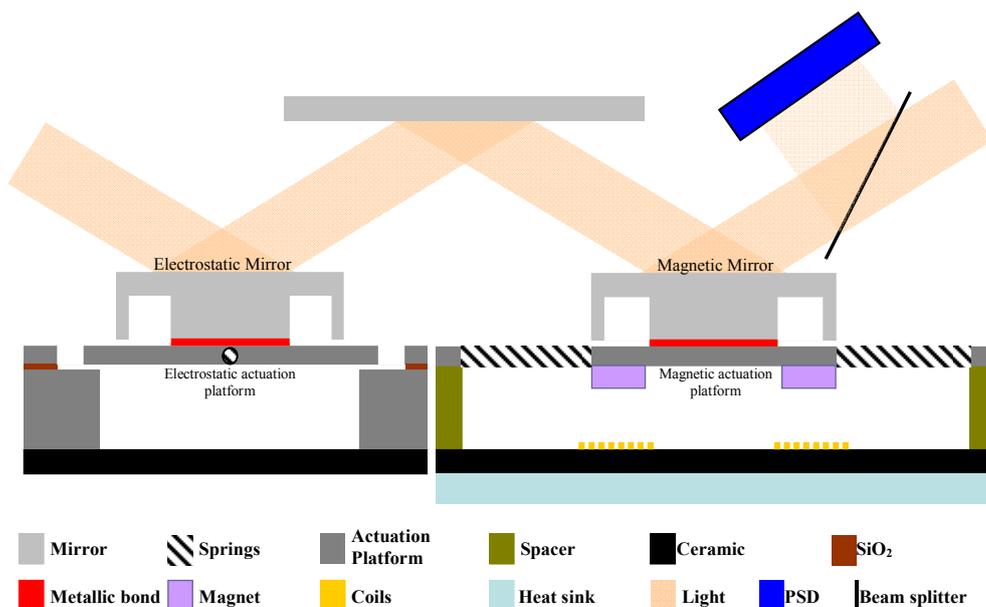


*Figure 4-31: The magnetic and electrostatic mirrors can both be integrated on an SOI wafer. The mirrors are fabricated from the handle layer. Electrostatic combs are formed on the device layer. The fixed combs of the electrostatic mirror are formed on the handle layer. A third fixed mirror is needed for the system to reflect the light from the first mirror on the second mirror.*

#### 4.7.1 Commercially microfabricated coils

The fabrication of the Silicon coils is relatively complex. Therefore, it was decided to order ceramic or polymer PCB-based coils that can be provided by different companies. Some of these companies are the GS Swiss PCB AG, Photochemie AG, or the HIGHTEC MC AG, all located in Switzerland, or the Micro Systems Engineering GmbH, a company specialized in LTCC-based devices in Germany. There are different types of PCB substrates providing different thermal conductivities:

- a) FR4, the most common polymer used for electronic boards with a low thermal conductivity. It has a thermal conductivity of about  $k=0.25\text{W/mK}$ , which is much lower than the thermal conductivity of intrinsic silicon  $k=129\text{W/mK}$ .
- b) Flex prints based on polymers such as polyimide or kapton, which can be glued to ceramic plates of high thermal conductivity.
- c) Sintered and polished ceramics such as Aluminum Oxide or  $\text{Al}_2\text{O}_3$  that provide a moderate thermal conductivity  $k=30\text{W/mK}$ .

In this project the coils were ordered from HIGHTEC MC AG, in Switzerland. They are made by copper electroplating and the substrate is  $\text{Al}_2\text{O}_3$  that has a medium thermal conductivity in comparison with Silicon. The design of these coils is presented in the following section.

#### 4.7.2 Design of coils for magnetic actuation

The coils were ordered from Hightec MC AG, Switzerland. The cross section view of the coil is shown in Figure 4-32. The coils consist of two copper layers situated on top of each other shown in orange. Each layer has a thickness of  $7\mu\text{m}$ . The wire width is  $50\mu\text{m}$ . the gap between two adjacent wires is  $20\mu\text{m}$ . The two layers consist of “2 x 28” turns. The gaps and the two layers are separated from each other with polyimide shown in dark pink. The coils are fabricated on an Aluminum oxide layer shown in light blue. The coils can be connected to the outside electronics through ZIF connectors.

Two different designs were fabricated as shown in Figure 4-33 and Figure 4-34. We call them the spiral coil and the unidirectional current coil.

The spiral coils have a diameter of 4 mm as shown in Figure 4-33. This figure shows both the mask of the coils and the final product in Figure 4-33a & b respectively. The magnet, shown in red, is placed on the top centre of the spiral coil as shown in Figure 4-33b. the magnet has a diameter of 2mm.

The unidirectional current coils are shown in Figure 4-34. This figure also shows both the mask of the coils and the final product in Figure 4-34 a & b respectively. The magnet, shown in red, is placed on the topside but only on one side of the coil as shown in Figure 4-34 b. Therefore all the current that passes under the magnet moves in the same direction. This is why the coil is called the unidirectional coil.

Another difference between these two designs is the direction of the Magnetization of the magnets. The spiral coil design uses magnets with a magnetization that is normal to the coil's top surface.

The unidirectional current coil uses magnets with a magnetization that is parallel to the top surface of the coils.

The achievable magnetic forces of the coils were evaluated by experiments. This was needed for the fine tuning of the magnetic forces and allows the correct evaluation of the mechanical springs of the system. The maximum force is directly related to the maximum current. The current is limited by the temperature increase in the coils. Therefore an investigation of the temperature increase in the coils was also carried out. These characterization steps are shown in chapter 6.

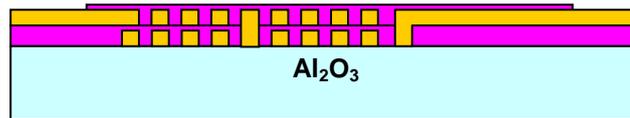


**Figure 4-32:** Cross section view of the coil that consists of two copper layers situated on top of each other, shown in orange. Each layer has a thickness of  $7\mu\text{m}$ . The wire width is  $50\mu\text{m}$ . the gap between two adjacent wires is  $20\mu\text{m}$ . The gaps and the two layers are separated from each other with polyimide shown in dark pink. The coils are fabricated on an Aluminum oxide layer shown in light blue.

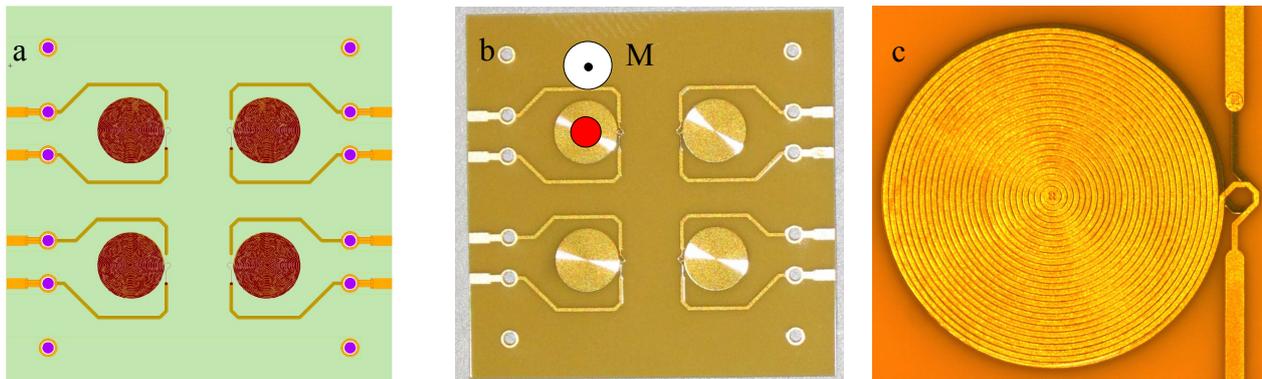


**Figure 4-33:** The spiral coils with a diameter of 4 mm. The mask of the coils and the final product are shown in a & b respectively. The magnet, shown in red, is placed on the top centre of the spiral coil as shown in b. the magnet has a diameter of 2mm. The magnetization direction "M" is normal to the surface. Figure c shows one of the spiral coils. The coil has a fill factor of over 70%. The lower layer of the coil can be seen as a darker straight wire on the right side of the figure.

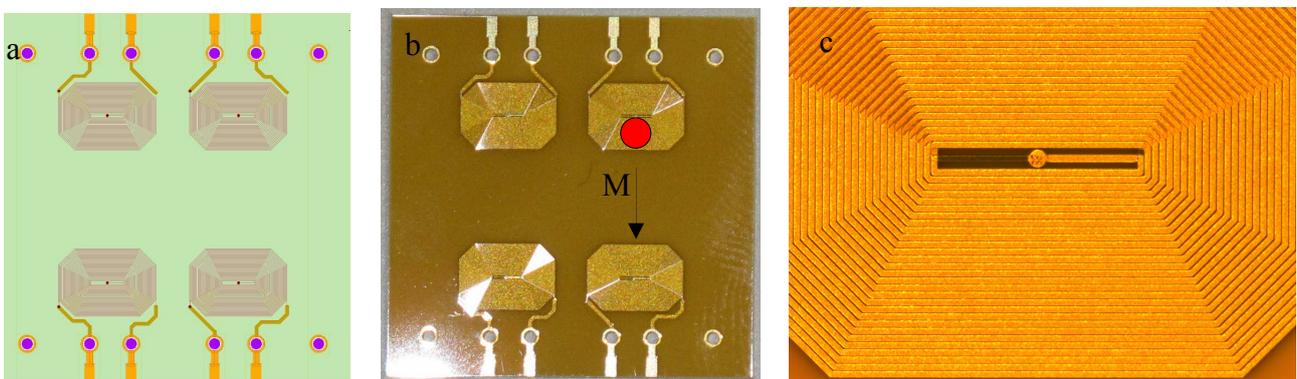


**Figure 4-34:** The unidirectional current coils masks and the final product are shown in a & b respectively. The magnet, shown in red, is placed on the top side but only on one side of the coil as shown in b. Therefore all the current that passes under the magnet move in the same direction. This is why this coil is called the unidirectional current coil. The magnetization direction "M" is parallel to the surface. c) Shows one of the unidirectional current coils. The coil has a fill factor of over 70%.

### 4.7.3 Magnets

The magnets used in this project have the diameter of 2mm. These cylindrical magnets were provided by SuperMagnet SA, Germany. Two different magnets were fabricated. The first was a 2mm magnet with 400 $\mu$ m thickness. This magnet was used in the configuration shown in Figure 4-33. Therefore it was magnetized parallel to its central axis as shown in Figure 4-33. The second was a 2mm magnet with 500 $\mu$ m thickness. This magnet was used in the configuration shown in Figure 4-34. It was magnetized perpendicular to the central axis as shown in Figure 4-34. These two magnets were compared to find the best configuration with the highest force.

## 5 Simulation

This chapter shows the simulation of the forces and mechanical actuation of the magnetically and electrostatically actuated mirrors. It starts with the electromagnetic simulation of the forces followed by the simulation of the resonant frequencies and deflection of the system due to the applied forces.

The electrostatic actuator will also be presented. The force obtainable from the combs will be simulated and applied to the mechanical system to extract the resonant frequencies and the deflection of the system due to the applied forces.

### 5.1 Electromagnetic design

This chapter shows the simulations of the magnetic force and the mechanical design. It starts with the simulation of the coils. The reason for this is that the design of the mechanical part is dependant on the forces available from the magnet-coil interaction. The obtained forces are then applied to the mechanical design.

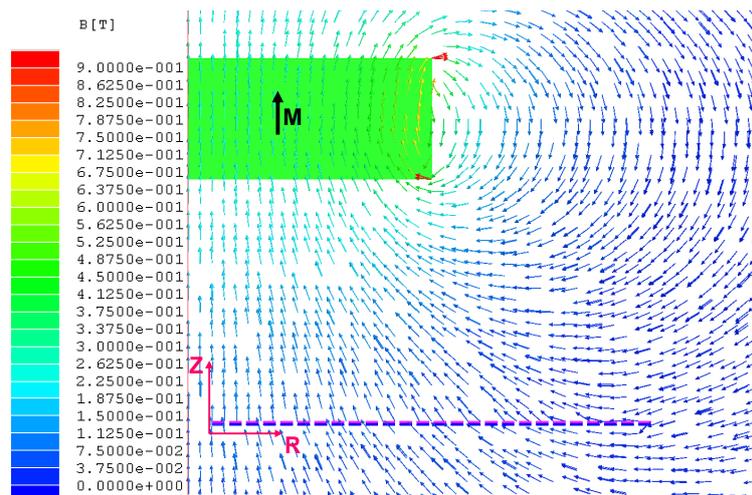


*Figure 5-1: The cross-section of the magnetic field of the spiral coil in the Polar coordinates. The magnet magnetization direction  $M$  is shown with a black arrow. The magnet is shown in green and the two layers of the coils are shown in dark blue and violet. The distance between the coil and magnet is 1mm. The divergence of the field is the main factor of creating the force*

#### 5.1.1 Magnetic force simulations

The two magnets discussed in 4.7.3 are the examples of force creation with a diverging magnetic field Eq. 3-43.1 and the Lorenz force law Eq. 3-5 as discussed in chapters 3.1 and 3.2.2. The magnetic system with the axially magnetized magnet was simulated by MAXWELL SV from Ansoft Corporation. The cross-section of the magnetic field is shown in Figure 5-1. This is a 2D simulation in the Polar coordinates. The magnet magnetization direction  $M$  is shown with a black arrow. The magnet is shown in green and the two layers of the coils fabricated by HighTec SA, discussed in section 4.7.2, are shown in dark blue and violet. The distance between the coil and

magnet is 1mm in Figure 5-1. The divergence of the field is the main factor of creating the force; i.e. the field divergence in the R-Z plane creates the force in Z direction.

The magnetic system with the magnet that was magnetized perpendicular to the central axis was also simulated by MAXWELL SV. The cross-section of the magnetic field is shown in Figure 5-2. This is a 2D simulation in Cartesian coordinates. The magnet magnetization direction  $M$  is shown with a black arrow. The magnet is shown in green and the two layers of the coils fabricated by HighTec SA, discussed in section 4.7.2, are shown in dark blue and violet. The distance between the coil and magnet is 1mm in Figure 5-2. In this system the force mainly follows the Lorentz force; i.e. the field component that is in the X direction creates the force in Z direction.

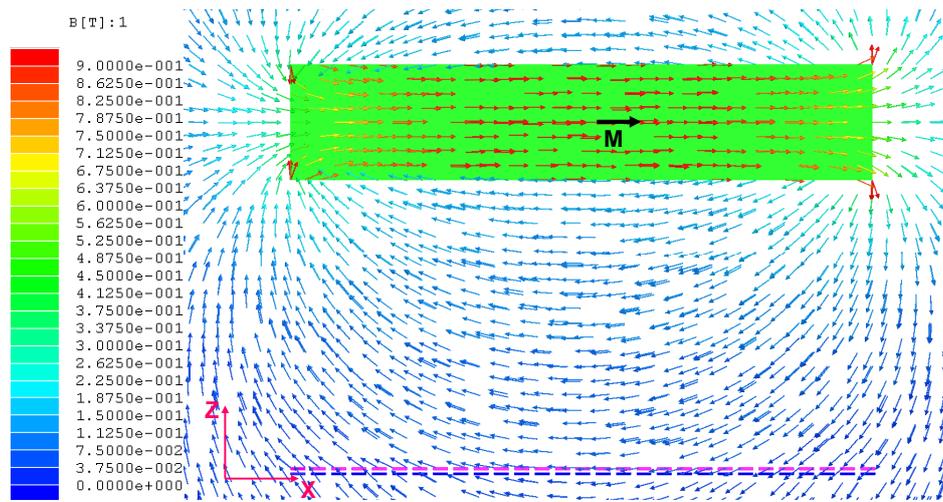


**Figure 5-2:** The cross-section of the magnetic field of the unidirectional current coil in the Cartesian coordinates. The magnet magnetization direction  $M$  is shown with a black arrow. The magnet is shown in green and the two layers of the coils are shown in dark blue and violet. The distance between the coil and magnet is 1mm. In this system the force mainly follows the Lorentz force.

The most critical variables of our system are the dependence of the force on the injected current and the distance between the coil and the magnet. At first the distance between the coil and the magnet is kept constant. Simulations show a linear relation between the force and injected current as shown in

Figure 5-3, for a coil-magnet distance of  $Z=500\mu\text{m}$ . This result is in complete accordance with the Biot-Savart law of the magnetic field of a steady line current. The result shown here is only for the spiral coil since the unidirectional coil has the same behaviour and only different values.

In the next step the injected current is kept constant at  $J = 1.33 \times 10^9 \text{ A/m}^2$  (or  $I = 500 \text{ mA}$ ) and the gap between the magnet and the coil is reduced from 1mm to 0.1mm, as shown in Figure 5-4. This figure shows a nonlinear relation between distance and force. The results shown here are for both the spiral coil and the unidirectional coil. The spiral coil creates a higher force according to these simulations.

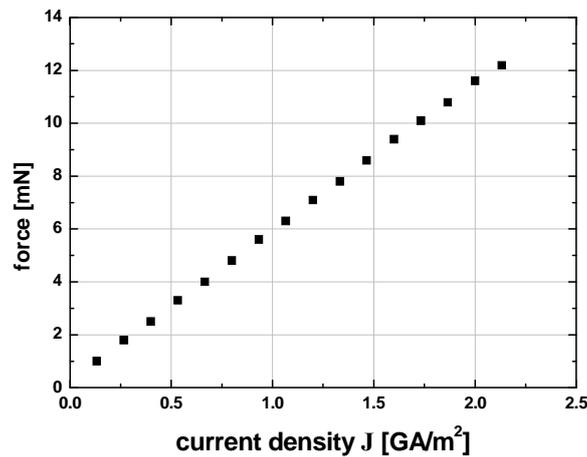


Figure 5-3: The linear relation between the force and injected current is shown for a coil-magnet distance of  $Z=500\mu\text{m}$ . This result is in complete accordance with the Biot-Savart law of the magnetic field of a steady line current. The result shown here is only for the spiral coil since the unidirectional coil.

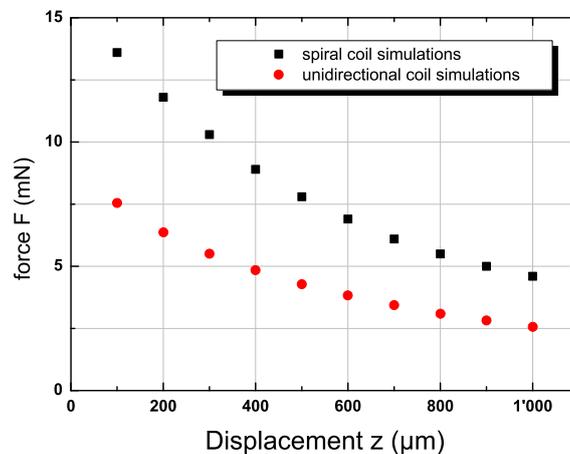
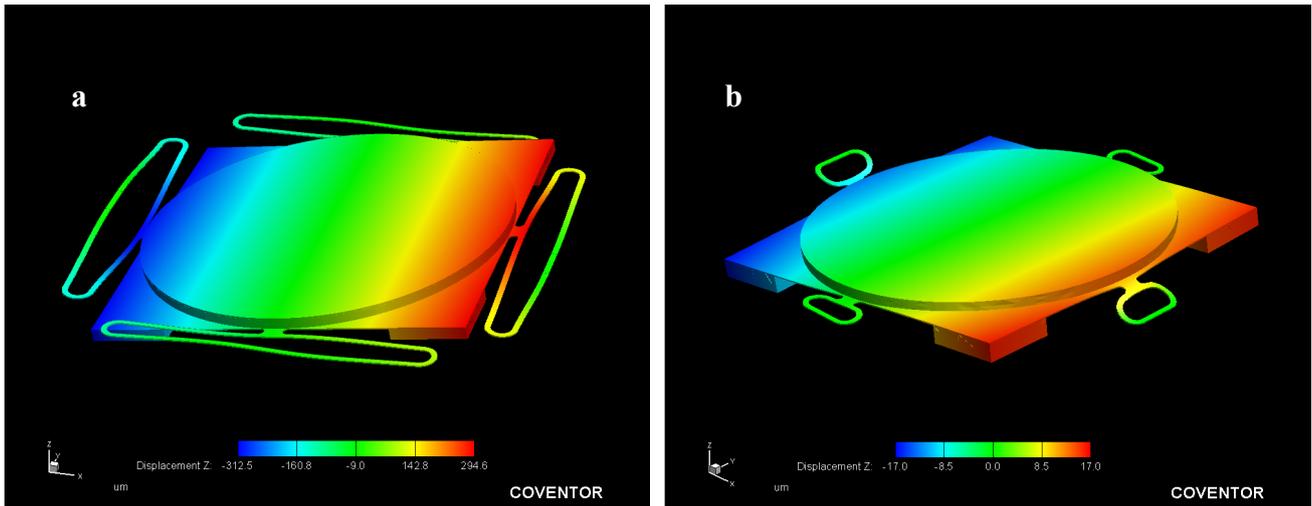


Figure 5-4: Resulting force of the unidirectional and spiral coil simulations as the coil-magnet distance is changed. The force of the spiral coil design is higher than the force of the unidirectional current coil design. Both designs show nonlinear force behavior as the distance changes. The injected current is kept constant at  $J = 1.33E9 \text{ A/m}^2$ .

### 5.1.2 Mechanical simulations

Both of the mechanical designs for the small and large angle rotations were simulated using Coventorware by Coventor, Inc. The maximum deflections of the two magnetic designs are shown in Figure 5-5 “a” & “b”. The exerted force is 6mN for the slow mirror and 12mN on the fast mirror. The force is applied on all of the four magnets of each design. Two of forces on each design are exerted upwards and two downwards. The system with  $\theta = 3.5^\circ$  mechanical rotation deflects to an average of  $300\mu\text{m}$  as shown in Figure 5-5a. The system with  $\theta = 0.2^\circ$  mechanical rotation deflects  $17\mu\text{m}$ , as shown in Figure 5-5b. The extrusions shown in Figure 4-24 are not shown in these figures. These extrusion where the fixed points in the simulations and did not move. They were fixed only from underneath. All of the deflections in these figures are 10 times exaggerated.

The Mises stresses in the designs are shown in Figure 5-5a & b and Figure 5-6a & b. It can be seen that the maximum stress is 213MPa for the slow mirror design shown in Figure 5-5a & b and 130MPa for the fast mirror shown in Figure 5-6a & b. Two close-ups of the spring are also shown in Figure 5-5b and Figure 5-6b that show the junction of the platform and the spring. The curved connection between the platform and the spring ensures a low stress at this junction.



**Figure 5-5:** The maximum deflections of the two magnetic designs are shown. The exerted force is 6mN for the slow mirror (a) and 12mN on the fast mirror (b). The force is applied four times on the four magnets of each design. Two of forces on each design are exerted upwards and two downwards. The slow system (a) with  $\theta = 3.5^\circ$  mechanical rotation deflects to an average of  $300\mu\text{m}$ . The fast system (b) with  $\theta = 0.2^\circ$  mechanical rotation deflects  $17\mu\text{m}$ .

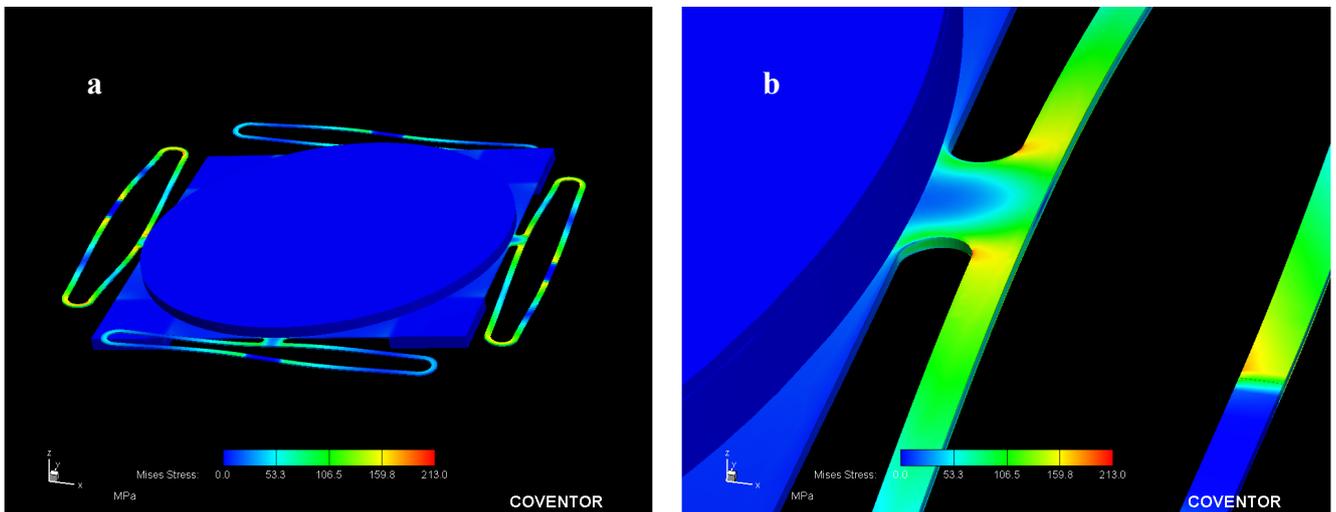


**Figure 5-6:** (a) The Mises stresses of the slow mirror system is shown. (b) A close-up of the spring is shown. The maximum stress is 213MPa.

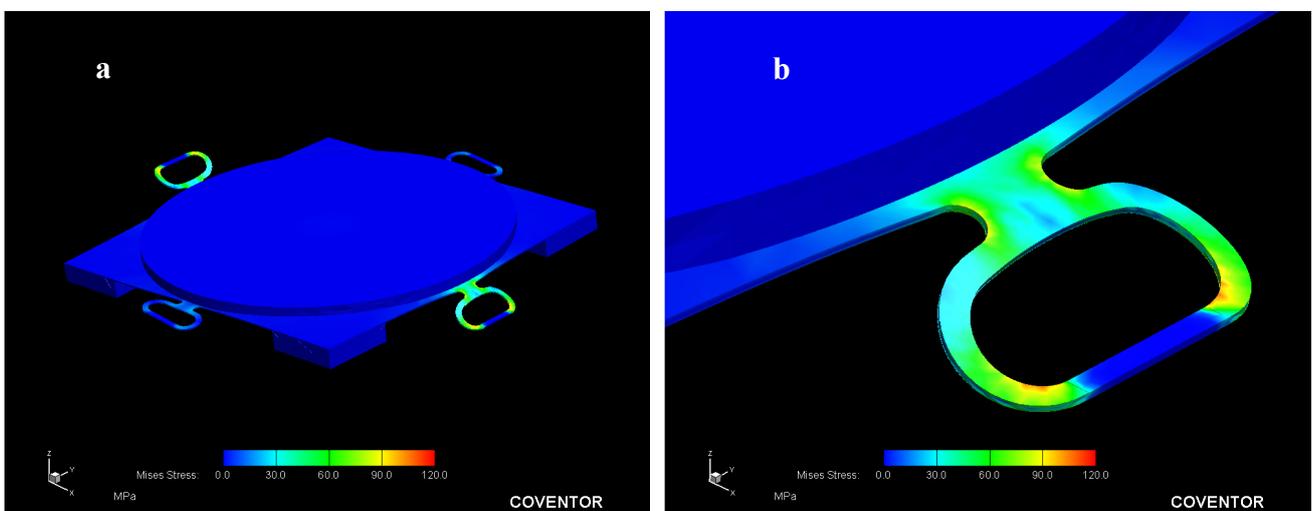


**Figure 5-7:** (a) The Mises stresses of the fast mirror system is shown. (b) A close-up of the spring is shown. The maximum stress is 130MPa for the fast mirror.

The first three mode shapes of the slow mirror with  $\theta = 3.5^\circ$  mechanical rotation is shown in Figure 5-8. The shown results are 10 times exaggerated. The first mode is the piston mode at resonant frequency of  $f_r = 160\text{Hz}$  shown in Figure 5-8a. The second mode is a rotation around the diagonal of the square platform at a resonant frequency of  $f_r = 202\text{Hz}$  shown in Figure 5-8 b. The third mode is a rotation around the perpendicular diagonal to the second mode, at a resonant frequency of  $f_r = 203\text{Hz}$  shown in Figure 5-8c. The second and the third mode have practically the same resonant frequency since the design is symmetrical.

The first three mode shapes of the fast mirror with  $\theta = 0.2^\circ$  mechanical rotation is shown in Figure 5-9. The shown deflections are 50 times exaggerated. The first mode is the piston mode at resonant frequency of  $f_r = 878\text{Hz}$  is shown in Figure 5-9a. The second mode is a rotation around the axis passing through the center of two facing springs of the square platform at a resonant frequency of  $f_r = 1005\text{Hz}$  as shown in Figure 5-9b. The third mode is a rotation around the perpendicular axis to the second mode, at a resonant frequency of  $f_r = 1011\text{Hz}$  and is shown in Figure 5-9c. Here again the second and the third modes have practically the same resonant frequency since the design is symmetrical.

The long springs of the slow mirror shown in Figure 5-8 favor a rotation along the diagonals of the moving platform. The shorter springs of the fast mirror in Figure 5-9 favor a rotation along the axis between the two facing springs. The direction of rotation is however not very important since this design rotates in 2D and is not supposed to work in resonance.

The first resonant mode of the mirror part was at 10 kHz, far from the resonant modes of the actuation platform.

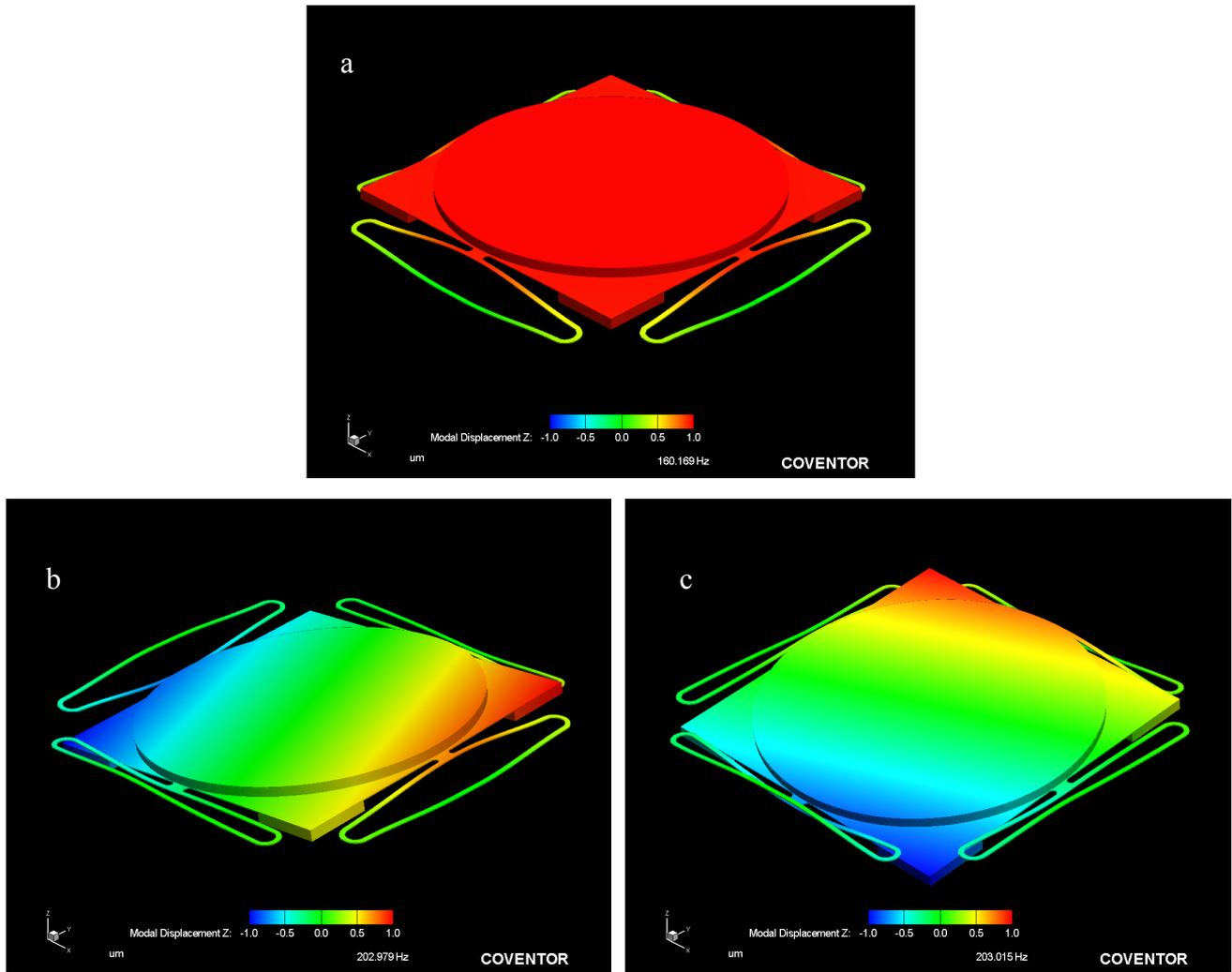


**Figure 5-8:** The first three mode shapes of the slow mirror. The shown results are 10 times exaggerated. (a) The first mode is the piston mode at resonant frequency of  $f_r = 160 \text{ Hz}$ . (b) The second mode is a rotation around the diagonal of the square platform at a resonant frequency of  $f_r = 202 \text{ Hz}$ . (c) The third mode is a rotation around the perpendicular diagonal to the second mode, at a resonant frequency of  $f_r = 203 \text{ Hz}$ .

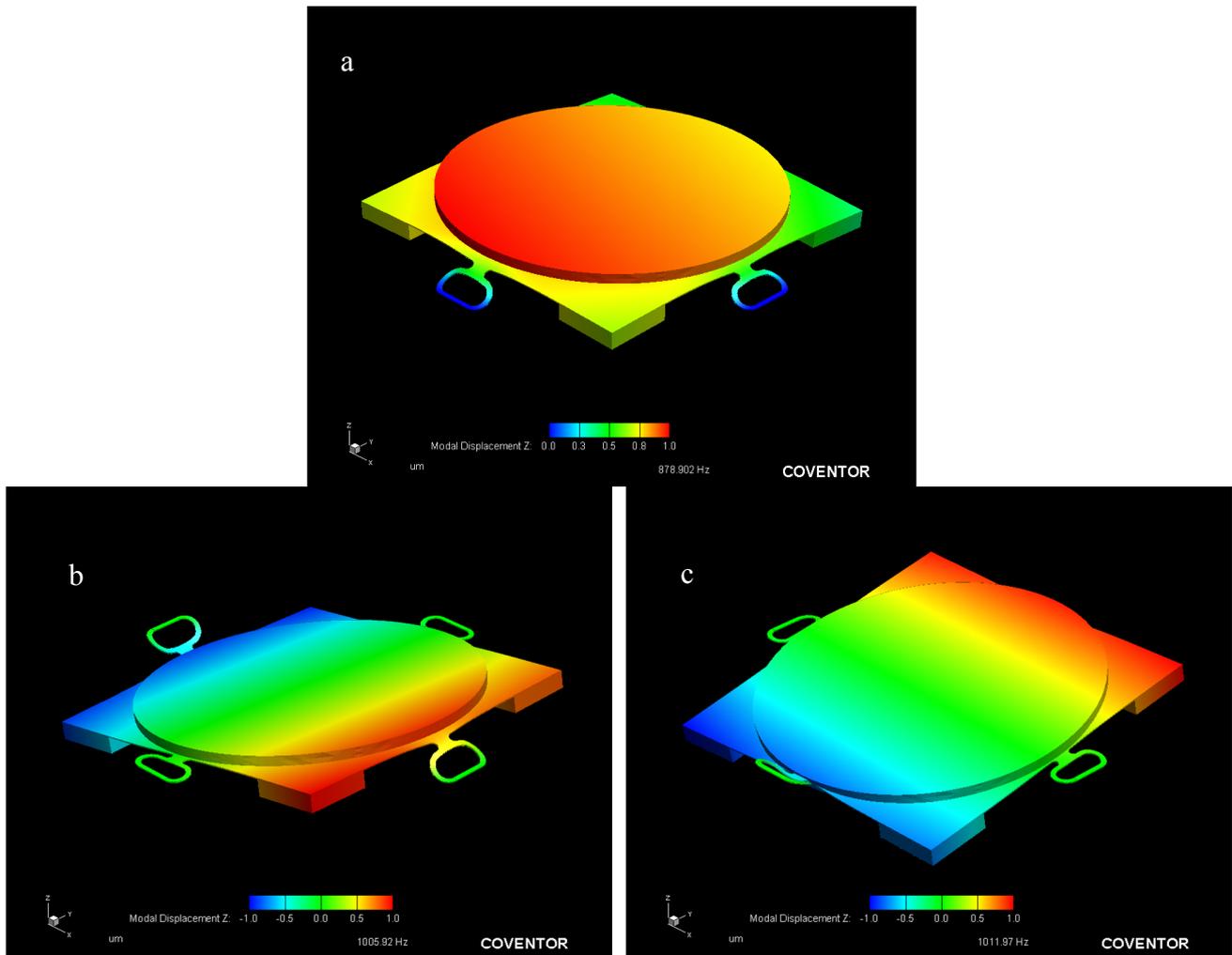


**Figure 5-9:** The first three mode shapes of the fast mirror with  $\theta = 0.2^\circ$  mechanical rotation is shown. The shown deflections are 50 times exaggerated. (a) The first mode is the piston mode at resonant frequency of  $f_r = 878\text{Hz}$ . (b) The second mode is a rotation around the axis passing through the center of two facing springs of the square platform at a resonant frequency of  $f_r = 1005\text{Hz}$ . (c) The third mode is a rotation around the perpendicular axis to the second mode, at a resonant frequency of  $f_r = 1011\text{Hz}$ .

## 5.2 Electrostatic design

The electrostatic design that was used for simulations is shown here. The mechanical design does not include the combs. The force was calculated separately and applied to the mechanical design.

### 5.2.1 Force simulations

The force of the vertical comb actuator was simulated with Maxwell SV; Ansoft Inc. as shown in Figure 5-10. This figure shows the scalar value of the electric field of one set of vertical combs. One comb with a total thickness of  $40\mu\text{m}$  was moved into two other combs of thickness  $100\mu\text{m}$ . this combs is shown on the top of the other two combs. The length of the comb is  $200\mu\text{m}$  and  $300\mu\text{m}$  for the comb-comb gaps of  $5\mu\text{m}$  and  $6\mu\text{m}$  respectively. The widths of all combs were set to  $5\mu\text{m}$ . The resulting force as the upper comb was moved inside the lower combs is shown in Figure 5-11. Figure 5-11 shows the total force of 640 set of combs. Two voltage values of  $U=150\text{V}$  and  $U=200\text{V}$  are shown in this figure. It can be seen that when the upper comb is completely out of the lower combs or completely plunged into them a transition of the force profile occurs. This is evident at

5 $\mu\text{m}$  and 40 $\mu\text{m}$  displacement. This behavior is consistent with the behavior theoretically described by Yeh et al [108].

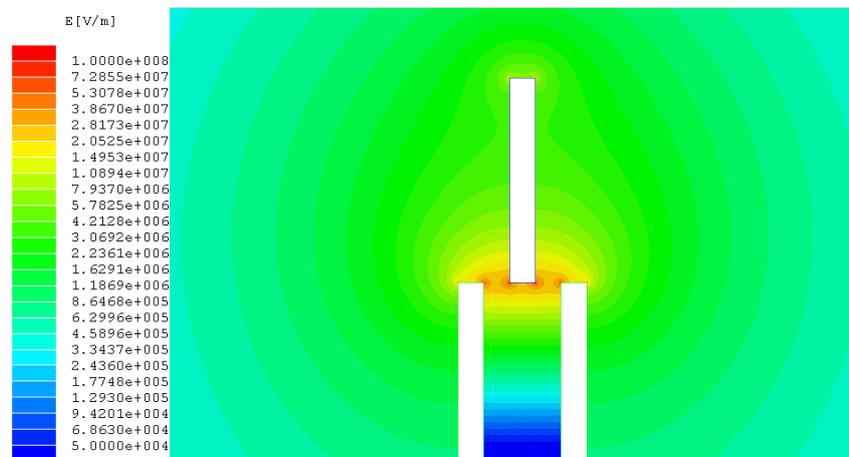


**Figure 5-10:** The scalar value of the electric field of one set of vertical combs. The upper comb with the thickness of 40 $\mu\text{m}$  was moved into two other combs of thickness 100 $\mu\text{m}$  that were placed under it. The width of all the combs is 5 $\mu\text{m}$ , and the gap is set to 5 $\mu\text{m}$  on each side.

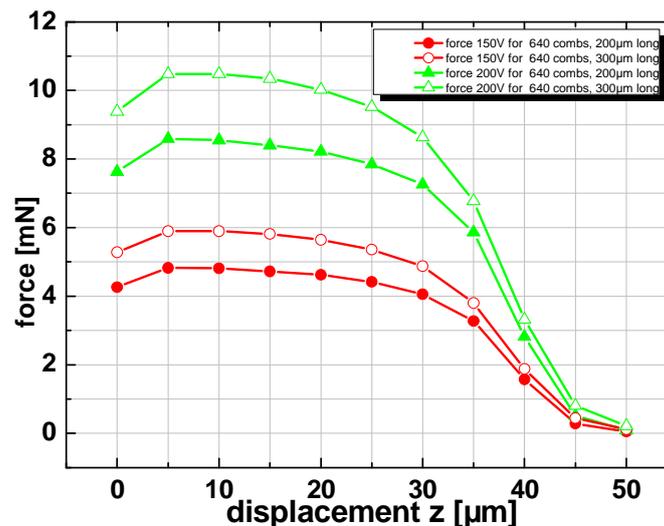


**Figure 5-11:** The total force of 640 combs. Two voltage values of  $U=150\text{V}$  and  $U=200\text{V}$  are shown in this figure. It can be seen that when the upper comb is completely out of the lower combs or completely plunged into them a transition of the force profile occurs. This is evident at 5 $\mu\text{m}$  and 40 $\mu\text{m}$  displacements.

According to the graphs shown in Figure 5-11, an attainable average force of 6 to 7mN was envisaged from the 640 combs for a displacement of 35 $\mu\text{m}$ . Another important force is the unwanted lateral force of the comb-drive actuator. As the upper comb plunges into the lower combs it tilts until the maximum angle of 0.2 $^\circ$  is reached. This creates lateral forces of up to 10mN. The design of the actuator springs should compensate for this force.

### 5.2.2 Mechanical simulations

The mechanical design was simulated with Coventorware; Coventor Inc. Figure 5-12a & b shows the deflection due to force. The mirror is shown on the topside. The moving platform is separated to

3 parts or electrodes that sit between the two neighboring springs, as discussed above in chapter 4.5.2.3. The value of force on each electrode is set to 7mN as discussed in 5.2.1. Figure 5-12a, shows the deflection due to force applied to one electrode of the actuation platform as shown by the white arrow. Figure 5-12b, shows the deflection due to force applied to two electrodes of the actuation platform as shown by the white arrows. Although applying force to one electrode easily attains the  $0.2^\circ$  angle, applying two forces to two electrodes leads to a deflection of slightly less than  $0.2^\circ$ .

As discussed in section 5.2.1, another force is also applied laterally at the same time as the 7mN force. The value of the applied lateral force of was  $F_{lat} = 30\text{mN}$ . This is three times higher than the lateral force at full deflection as discussed in 5.2.1. The total lateral movements when this force is applied to one and two electrodes are shown in Figure 5-13a & b. These figures are shown with the moving platform side-up. The maximum lateral deflection is  $0.3\ \mu\text{m}$ . This is well bellow the “one third of the total distance” snap-in criterion discussed in section 3.3.1.

The Mises stress of the system when the force is applied to two electrodes is shown in Figure 5-14. The maximum Mises stress is 200Mpa which is within the safe region as discussed in 4.5.1.4. The maximum stress occurs at the corners. This implies the importance of rounding all the corners of the final device to reduce the stress to the minimum.

The resonant frequencies of the system are shown in Figure 5-15. The first mode is the piston mode at  $f_r = 563\ \text{Hz}$ . The second and the third modes are deflections at  $f_r = 918\ \text{Hz}$  and  $f_r = 926\ \text{Hz}$  which is slightly bellow 1Khz.

The first resonant mode of the mirror part was at 10 kHz, far from the resonant modes of the actuation platform.

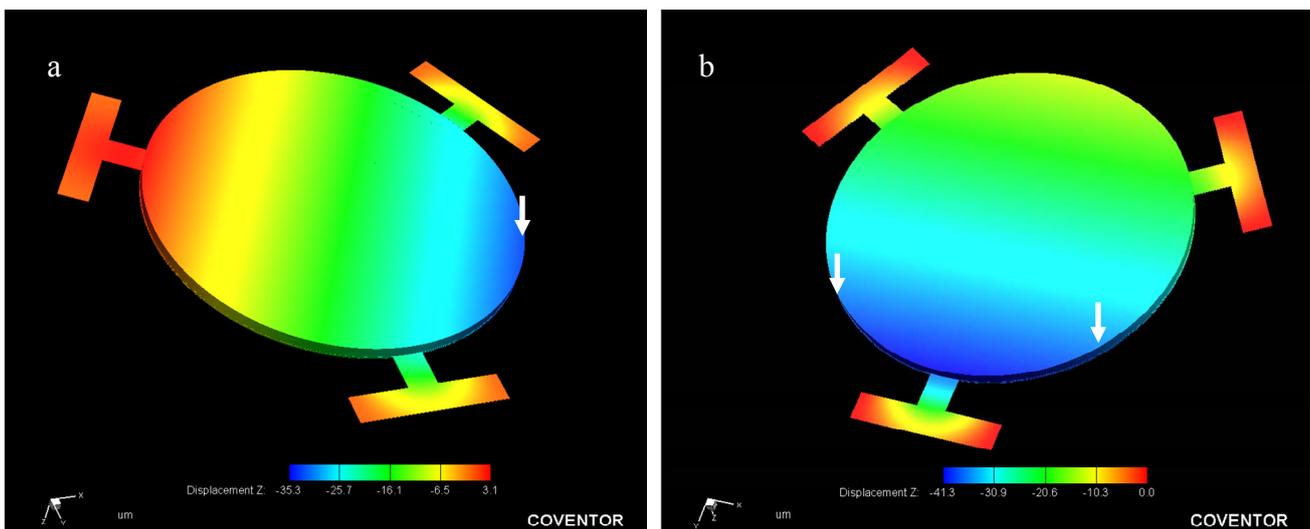


**Figure 5-12: The deflection due to force. The mirror is shown on the topside. The force on each electrode is set to 7mN and is shown with a white arrow. (a) The deflection due to force applied to one electrode of the actuation platform. (b) The deflection due to force applied to two electrodes of the actuation platform. Although Applying force to one electrode easily attains the  $0.2^\circ$  angle, applying two forces to two electrodes leads to a deflection of slightly less than  $0.2^\circ$ .**

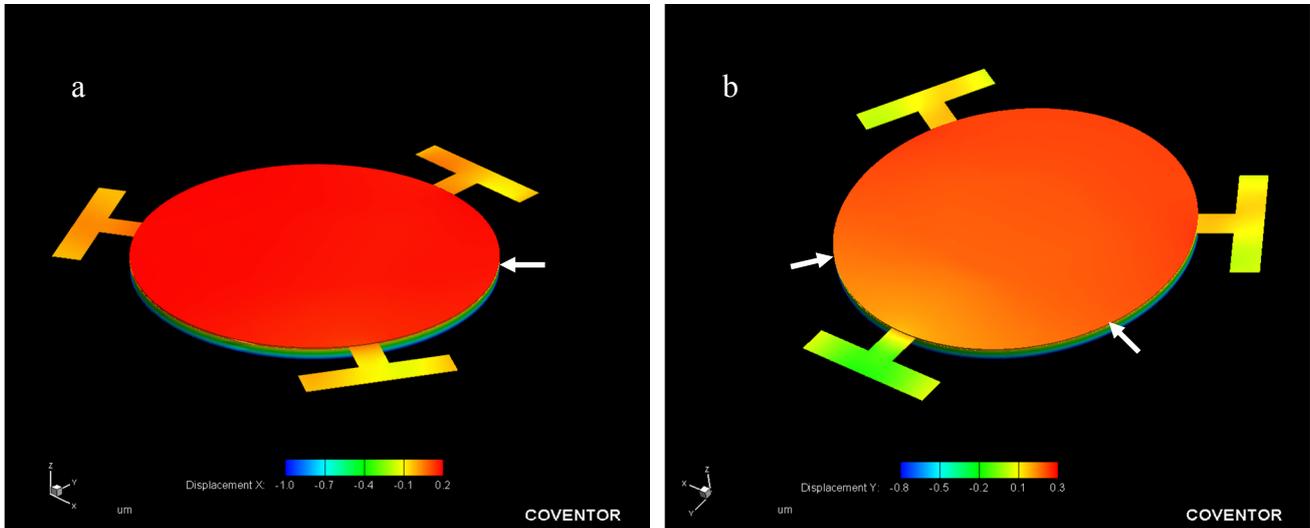


*Figure 5-13: Lateral forces of 30mN were applied laterally shown with white arrows. This force is three time higher than the lateral force at full deflection. The maximum lateral deflection is 0.3  $\mu\text{m}$ . This is well bellow the “one third of the total distance” snap-in criterion*

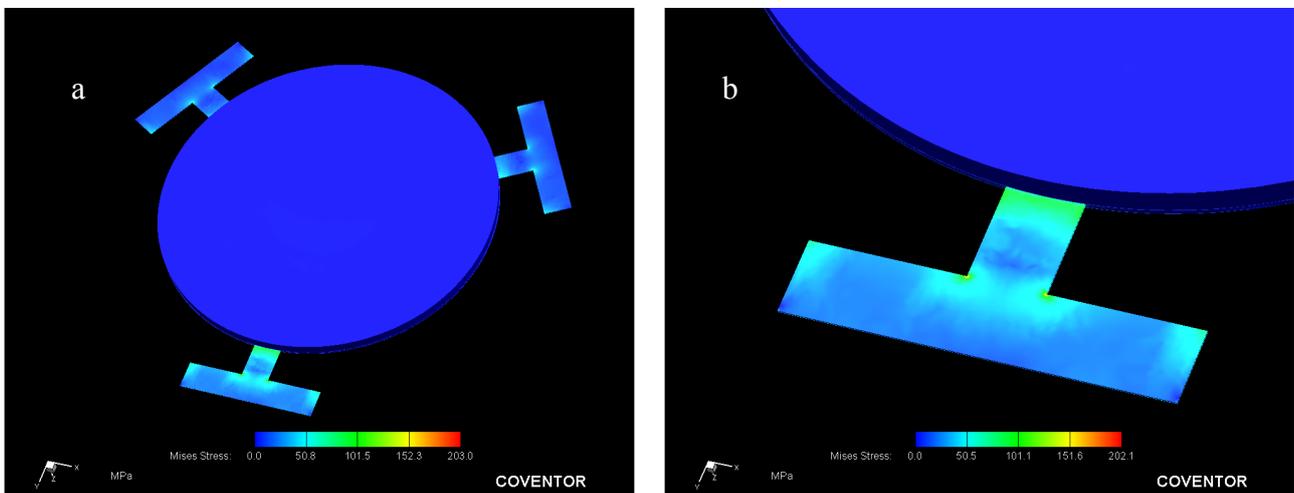


*Figure 5-14 : The Mises stress of the system when the force is applied to two electrodes is shown. The maximum Mises stress is 200 MPa. The maximum stress occurs at the corners*

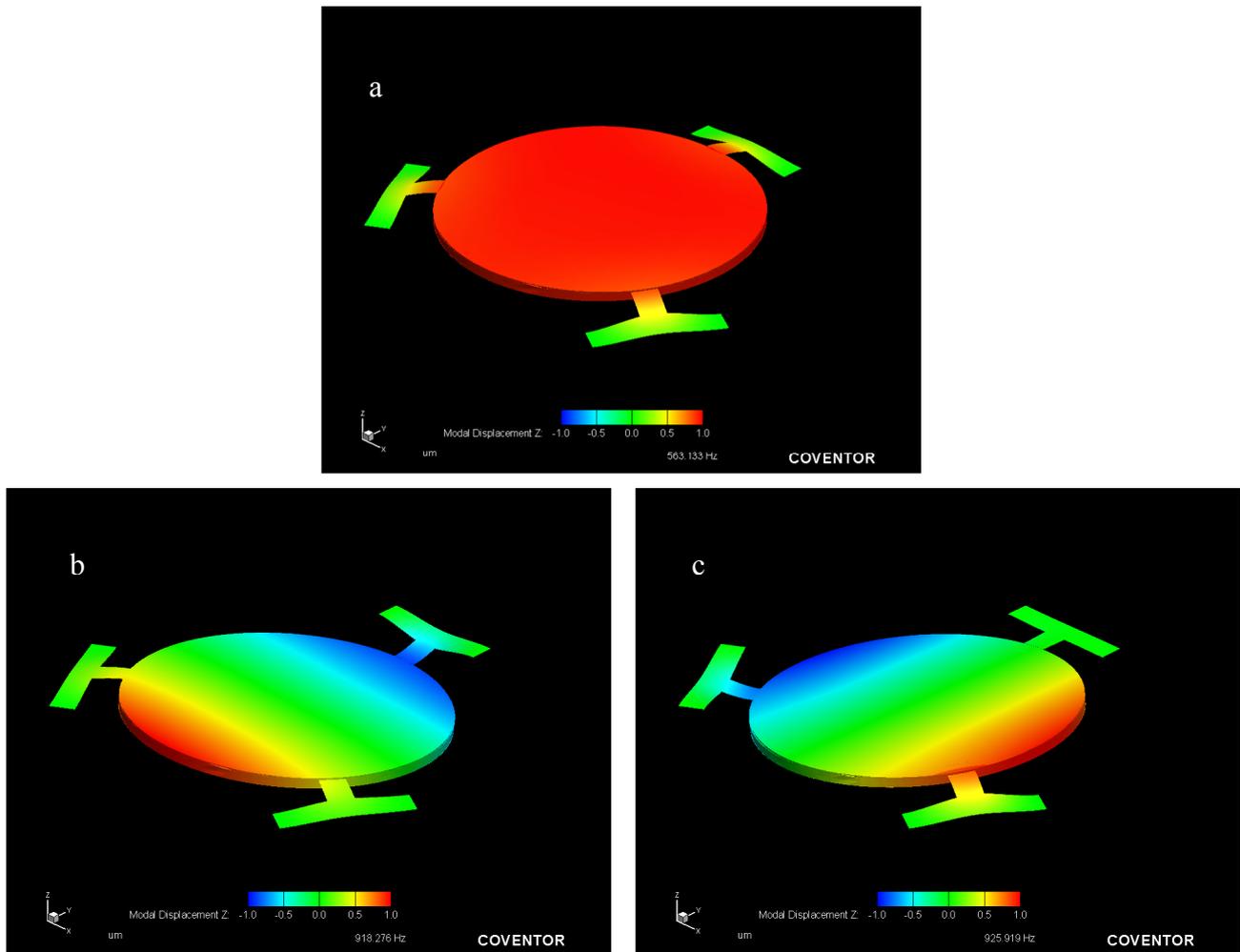


**Figure 5-15:** The resonant frequencies of the system are shown. (a) The first mode is the piston mode at  $f_r = 563$  Hz. (b) The second is a deflection at  $f_r = 918$  H. The third mode is at  $f_r = 926$  Hz which is slightly below 1Khz.

### 5.3 Heat dissipation from mirror

As the mirrors are operated in space the incident energy from the light source heats them up. The absorbed amount of heat on the mirror depends on the mirror coating and the wavelength of the beam. The amount of absorbed energy is usually less than 5%. However, in lack of heat convection the heat can only be dissipated from the springs of the actuation platforms. The amount of temperature increase on the mirror and the moving platform can be given by the simple formula for heat conduction:

$$\frac{dQ}{Adt} = q = -\frac{k(T_2 - T_1)}{l} \quad \text{Eq. 5-1}$$

There are a heat sources and a drain source in this formula. The heat source is at temperature  $T_2$  [K] and the drain source is at a lower temperature  $T_1$  [K]. The heat flux  $q$  [ $\text{W}\cdot\text{m}^2$ ] is transferred through the connection between these two sources.  $k$  is the coefficient of heat conductivity of the material used for connection between the two heat sources,  $A$  is the cross-section of this connection and  $Q$  [J] is the total heat.

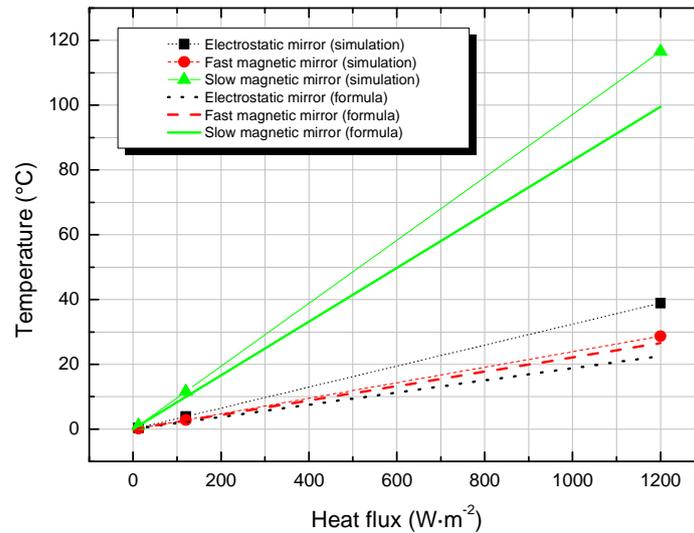


**Figure 5-16:** The results of simulations and calculations of temperature increase on the mirror vs. the heat flux. The electrostatically actuated and the fast magnetically actuated mirrors show lower increase in temperature compared to the fast electromagnetic mirror. This is mainly related to the shorter length of the springs of these two devices compared to the spring length of the magnetically actuated slow mirror. From left to right, the simulated points show 1mW, 10mW, and 100mW of applied Heat on the mirror topside.

Since there is a constant heat flux arriving on the mirror of our device and since the springs are attached to the substrate that can be considered as a second source at a lower temperature; this formula can be applied.

FEM simulations were also done on the magnetically and electrostatically actuated mirrors. The results of simulations and calculations done on these mirrors are shown in Figure 5-16 that shows a linear increase in temperature on the mirror ( $T_l$ ) as the heat flux is increased. It can be seen that the temperature increases obtained from simulations have larger gradients compared to the calculations. This is due to the fact that calculations with Eq. 5-1 only considered the length of the springs. However, in the simulations a heat flux was applied to the mirror topside, therefore the effective length is longer than the length of the springs. This resulted in an increase in the gradient of the lines from simulations.

The electrostatically actuated and the fast magnetically actuated mirrors show lower increase in temperature compared to the fast electromagnetic mirror. This is mainly related to the shorter length of the springs of these two devices compared to the spring length of the magnetically actuated slow mirror. From left to right, the simulated points shown in Figure 5-16 are 1mW, 10mW, and 100mW of applied Heat on the mirror topside.

## 6 Microfabrication

In this chapter the design of the masks for photolithography and microfabrication of the electrostatically and magnetically actuated mirrors will be shown. As discussed before in chapter 1, each system is made of two separate parts; the mirror and the actuation platform that are later bonded together. The fabrication of these two parts will be demonstrated, starting with design and fabrication of the mirror chips followed by design and microfabrication of the actuation platform. In the next step bonding will be discussed including the different bonding profiles that were used. Some final fabrication steps will be illustrated that are done after the bonding of the mirror and actuator wafers and at the end the assembly process of both the electrostatically and magnetically actuated mirrors will be shown.

The lists of different wafers used in the microfabrication of different parts are shown below in Table 6-1 and Table 6-2.

*Table 6-1: Specifications of the wafer types used for mirror fabrication*

| Wafer type          | Thickness ( $\mu\text{m}$ ) | Silicon dioxide ( $\text{SiO}_2$ ) layer on the surface ( $\mu\text{m}$ ) | Buried silicon dioxide layer (BOX) ( $\mu\text{m}$ ) | Device layer thickness ( $\mu\text{m}$ ) | Type of doping |
|---------------------|-----------------------------|---|--|--|----------------|
| SOI wafers          | 300 (handle layer)          | 3 (on top of handle layer)  | 3  | 50                                       | p-type boron   |
| Bulk silicon wafers | 525                         | 2 (formed by thermally oxidizing the wafer)                               | NA   | NA                                       | p-type boron   |

*Table 6-2: Specifications of the wafer types used for fabrication of actuator platforms*

| Type of actuator                    | Wafer type | Thickness ( $\mu\text{m}$ ) | Silicon dioxide layer ( $\text{SiO}_2$ ) ( $\mu\text{m}$ ) | Buried silicon dioxide layer (BOX) ( $\mu\text{m}$ ) | Device layer ( $\mu\text{m}$ ) | Doping       |
|-------------------------------------|------------|-----------------------------|--|--|--------------------------------|--------------|
| magnetically actuated platform      | SOI wafer  | 300                         | 2 (on top of handle layer)                                 | 2  | 40                             | p-type boron |
| electrostatically actuated platform | SOI wafer  | 300                         | 2 (on top of handle layer)                                 | 2  | 40                             | p-type boron |

### 6.1 Microfabrication of the mirror

The mirror is the first part that will be discussed. Two different wafer types were used for the fabrication of the mirror. SOI wafers and bulk silicon wafers. This was done in order to compare the flatness of the mirrors fabricated from these two different types of wafers. Both methods are discussed below.

#### 6.1.1 Mirror from SOI wafer

As mentioned before, all the mirrors are 1cm in diameter. The mirrors that are made out of an SOI wafer are formed on the handle layer of the wafer. It is fabricated with two masks using a delayed mask process. Figure 6-1 shows the designed masks for the mirror. The mask shown in Figure 6-1a, is the first mask for the delayed mask process. The second mask is shown in Figure 6-1b. The first mask is used to create the outer edge of the circular mirror as well as the frame around the mirror by DRIE etching. The second mask creates the inner form of the mirror as well as continuing to shape the outer edge and the frame. The inner form of the mirror seen in Figure 6-1b is designed to accommodate different bonding profiles, as will be discussed later on. The delayed mask technique creates outer edges that are deeper than the inner parts of the mirror. The four holes seen on the four corners of the frame are later used for alignment during assembly.

The SOI wafers used in this production run have the characteristics summarized in Table 6-1.

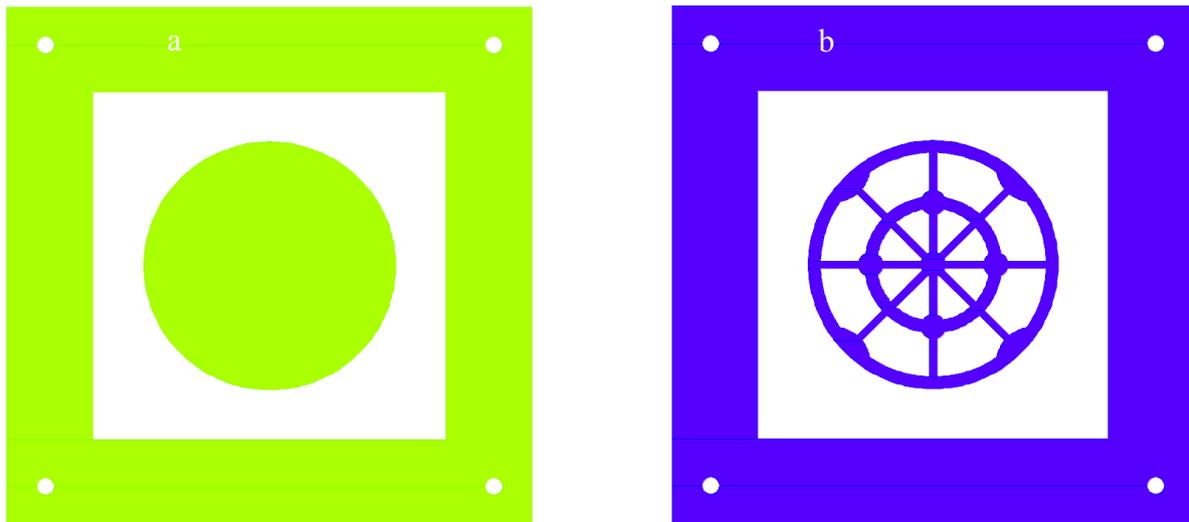


**Figure 6-1:** Two masks that are used for the delayed mask process. a) The first mask for the delayed mask process is used to create the outer edge of the round mirror as well as the frame around the mirror by DRIE etching. b) The second mask creates the inner form of the mirror as well as continuing to shape the outer edge and the frame.

a) The process flow of the mirror is shown in Figure 6-2. Figure 6-2a, shows the SOI wafer with the handle layer on top. In this figure the handle layer is already coated with a patterned resist. The photoresist used in this step for photolithography was AZ 9260 and was spin coated on the wafer using a SÜSS Micro Tech spinner machine using the mask shown in Figure 6-1b

b) The second processing step starts with etching the  $\text{SiO}_2$  layer on top of the handle layer as shown in

Figure 6-2b. This is done in Buffered hydrofluoric acid (BHF).

c) The third step, shown in Figure 6-2c, replaces the first photoresist layer with a new one. This photoresist is then patterned using the mask shown in Figure 6-1a. The photoresist used in this step was also AZ 9260 and was spin coated on the wafer using the same machine. The thickness of the resist in both cases was  $6\mu\text{m}$ .

d) The fourth step is etching the outer part of the mirror as shown in Figure 6-2d. this is done with a STS systems Deep Reactive Ion Etcher (DRIE). The etch depth depends on the machine and the height difference that is desired between the inner and outer parts of the mirror.

e) In the fifth step, shown in Figure 6-2e the photoresist is removed and DRIE etching is continued with  $\text{SiO}_2$  as the delayed mask. The etching is continued until the first opening reaches the BOX. In our case the depths were chosen in a way that when the first opening reaches the BOX the second one has a  $50\mu\text{m}$  height difference with it.

f) The last step is to remove the excess  $\text{SiO}_2$  on the surface by BHF, as shown in Figure 6-2f.

A scanning electron microscope (SEM) micrograph of the resulting shape is shown in Figure 6-3. Figure 6-2 only shows the processing done on the handle layer of the wafer. The processing on the device layer is postponed until after the bonding process that will be discussed in chapter 6.3.

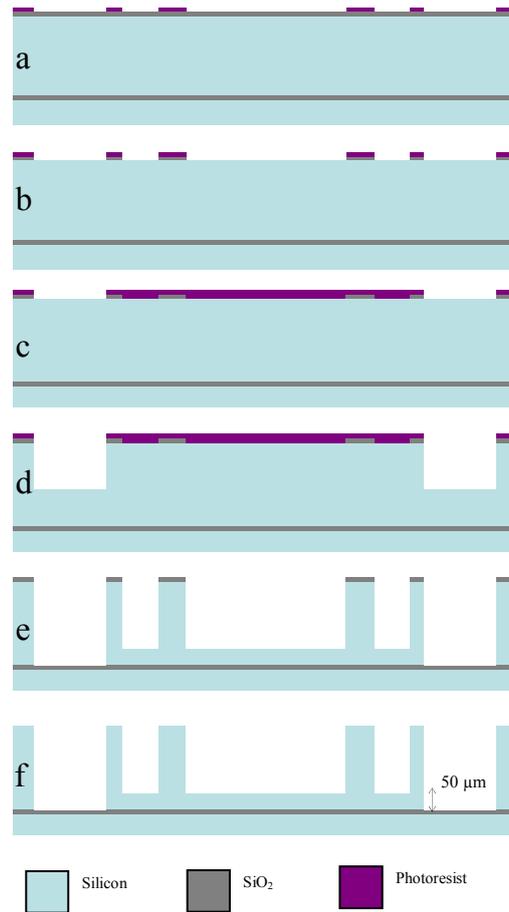


**Figure 6-2:** a) The SOI wafer with the patterned resist on top. b) Patterning of the  $\text{SiO}_2$  layer with BHF. c) Replacement of the resist that is patterned with the first delayed mask. d) DRIE of the outer rims which is the first part of delayed mask process. e) Removal of the resist and continuation of DRIE with the  $\text{SiO}_2$  as the second delayed mask. f) Removal of the excess  $\text{SiO}_2$  on the surface.

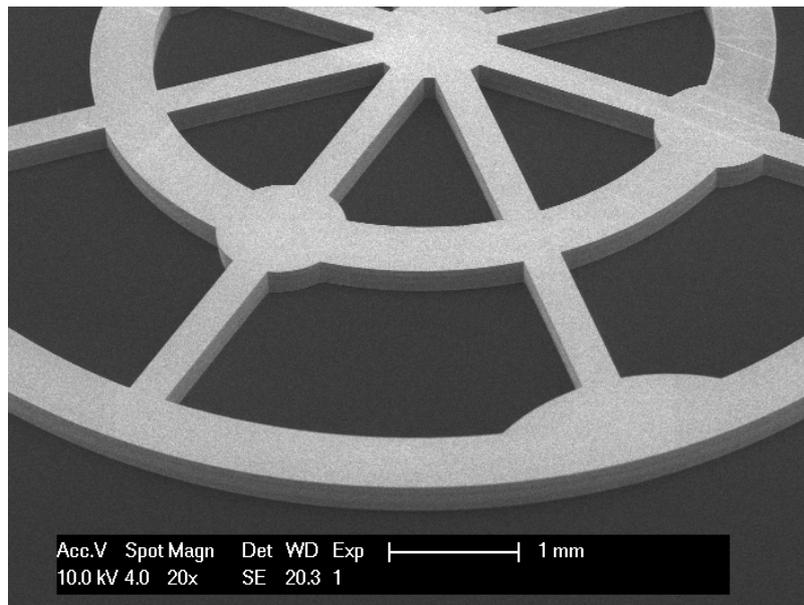


**Figure 6-3:** SEM micrograph of the resulting shape of the backside of the mirror. The small circles are used as bonding pads.

### 6.1.2 Mirror from bulk wafer

The second fabrication process of the mirror used a bulk silicon wafer with specifications given in Table 6-1. There are two main differences between the fabrication process of the SOI and bulk wafers. The SOI wafer has the BOX layer that acts as the etch stop. This layer is used to avoid unwanted etching in the following steps and is necessary. The bulk wafer lacks this layer. This layer should be created during the processing. Another difference in the processing is the deposition of the bonding metal on the bulk wafer that was not done for the mirrors made by SOI wafers. This process is more advantageous since it reduces the number of processing steps on the actuation platforms, thus reducing the chance of having contamination and dirt on the more sensitive parts of the actuators.

The masks used in this process are the same masks shown in Figure 6-1. The process flow is shown in Figure 6-4.

- a) the process starts with thermally oxidizing the wafer surface up to  $2\mu\text{m}$  thick as shown in Figure 6-4a.
- b) In the second step the wafer was patterned on both sides with photolithography as shown in Figure 6-4b. The used photoresist was AZ 9260.
- c) In the third step the silicon dioxide is patterned using BHF as shown in Figure 6-4c.
- d) The pillars of the mirror were etched by the STS systems DRIE down to  $300\mu\text{m}$  deep as shown in Figure 6-4d.
- e) The next step consists of cleaning the wafer and thermally re-oxidizing it. The oxidization thickness was  $400\text{nm}$  thick. This is shown in Figure 6-4e.
- f) In-order to deposit the bonding metal on the mirror backside, spray coating was used as shown in Figure 6-4f. The resist used was AZ 5214 negative tone photoresist.
- g) The wafer was then exposed and developed as shown in Figure 6-4g
- h) The oxide was opened using BHF as shown in Figure 6-4h. these openings are the places where metal will be deposited. If the metal is directly deposited on the  $\text{SiO}_2$  it will be peeled off when HF acid is used to remove the  $\text{SiO}_2$  in later steps.
- i) The metal was deposited using an E-beam evaporation chamber as shown Figure 6-4i.
- j) A lift-off process in Acetone removed the excess parts of the deposited metal leaving gold in the desired places as shown in Figure 6-4j.

The result of one circular deposition is shown in Figure 6-5. As it was discussed in the process flow and shown in Figure 6-4j, the metal should only be deposited in places where there is no oxide. The close-up of the circle in Figure 6-5 shows that the metal is deposited in the hole without touching the  $\text{SiO}_2$  around it.

The front side of the mirror is etched after the bonding process, as was done for the mirrors made from the SOI wafer.

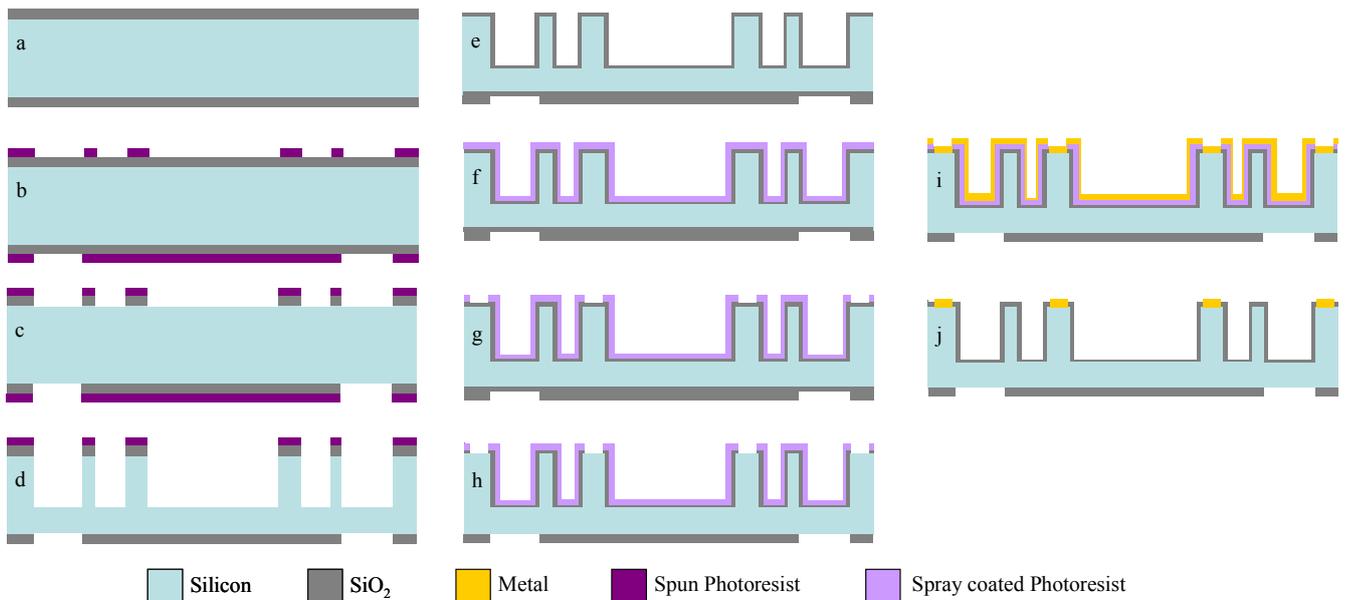


**Figure 6-4:** The process flow of the mirror made from a bulk silicon wafer. (a) Thermal oxidation. (b) Photoresist patterning on front and back sides. (c) Opening of the  $\text{SiO}_2$  in BHF. (d) DRIE on the backside. (e) 400nm thermal oxidation. (f) Spray-coating of the backside with photoresist. (g) Photoresist patterning. (h) Opening of the  $\text{SiO}_2$  in BHF. (i) Metal deposition. (j) Liftoff of excess metal

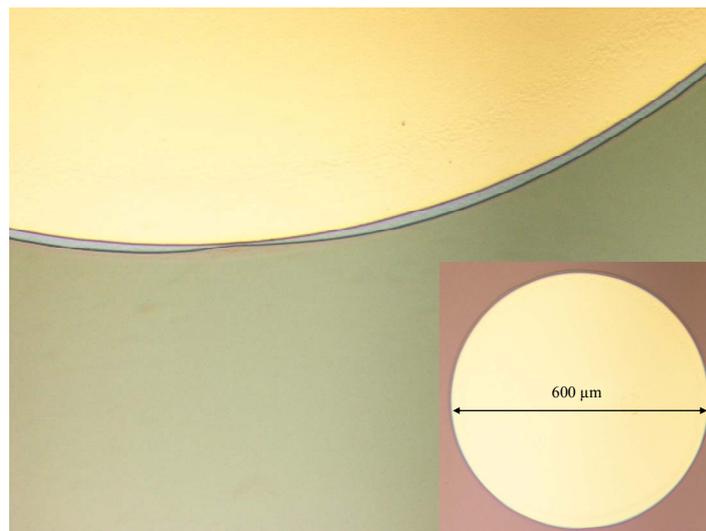


**Figure 6-5:** The result of one circular deposition. The close-up of the circle shows that the metal is deposited in the hole without touching the  $\text{SiO}_2$  around it.

## 6.2 Microfabrication of the magnetically actuated platform

The magnetically actuated platform is made out of an SOI wafer with the specifications shown in Table 6-2. One mask was designed for the front side and another for the back side etching of the wafer as shown in Figure 6-6. The front side mask shown in Figure 6-6a, creates the springs and the platform for the magnets. The backside mask shown in Figure 6-6b creates a release structure that removes the unwanted mass of the platform leaving only the bonding and alignment structures behind, as shown in Figure 6-9. The process flow is shown in Figure 6-7:

a) The first step, shown in Figure 6-7a, is to deposit the metallic layer on the front side of the SOI. This is done using a negative resist (AZ 5214) to pattern the wanted deposition shapes on the wafer. The deposition is done using an E-beam evaporation chamber.

b) A liftoff process in acetone is used in order to remove the excess metallic depositions as shown in Figure 6-7b.

It should be mentioned that these two steps could be omitted if the metal layer is formed on the mirror wafer, as was the case for the bulk wafer discussed above in chapter 6.1.2.

c) The next step is to pattern the springs on the front side of the wafer using the mask shown in Figure 6-6a. This was done with the AZ 9260 resist mask that was 6  $\mu\text{m}$  thick as shown in Figure 6-7c.

d) The next step is to pattern the handle layer using the mask shown in Figure 6-6b. the used resist was again a 6  $\mu\text{m}$  thick AZ 9260 resist. The  $\text{SiO}_2$  layer on the handle layer had to be opened in BHF. This is shown in Figure 6-7d.

e) The wafer was partially etched 220  $\mu\text{m}$  deep with the DRIE as shown in Figure 6-7e. By doing so the wafer remains robust and bonding can be done with a lower risk of breaking the wafer.

After this step the remaining photoresist on the back side can be removed. The oxide is used to finish the partially opened handle layer after the bonding is done. These steps will be shown in the following subchapters.

The SEM micrographs of the front and backside are shown in Figure 6-8. Figure 6-8a shows one part of one of the springs that were etched on the front side. The silicon part seen in the middle of the spring was released at the end of the process. Figure 6-8b shows the etched backside of the wafer with the holes and trenches used for the releasing process and also the bonding and alignment structures that will remain after the release. The remaining structures after the release process are shown in Figure 6-9.

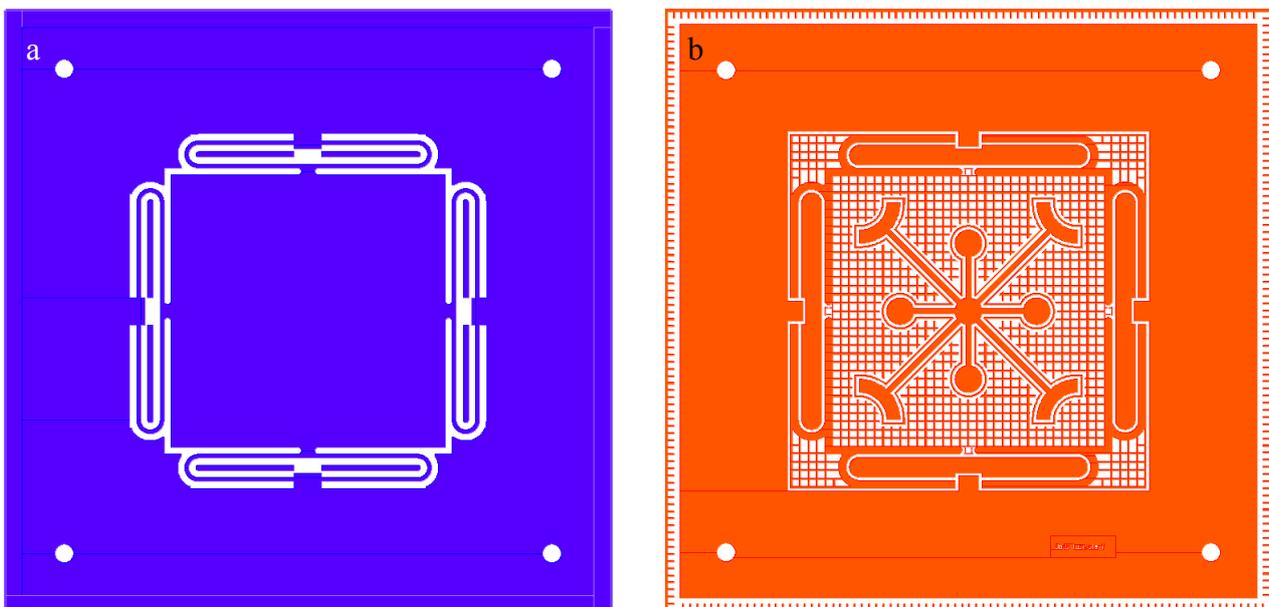


**Figure 6-6:** a) The mask designed for the front side and that creates the springs and the platform for the magnets. b) The backside mask that creates a release structure which removes the unwanted mass of the platform leaving only the bonding and alignment structures behind.

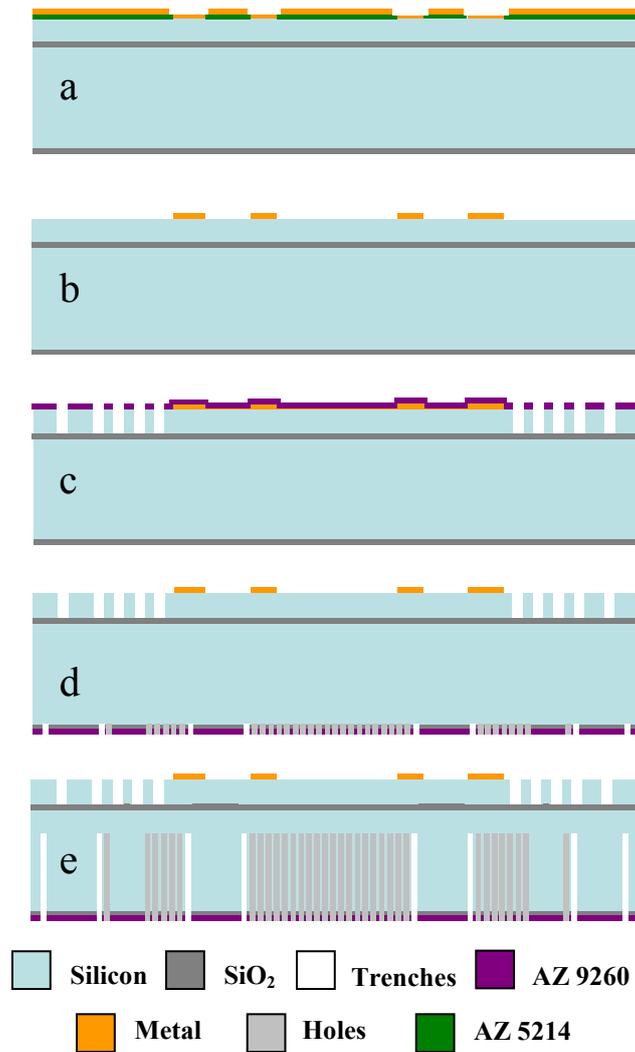


**Figure 6-7:** a) E-beam metal deposition on the wafer using the patterned negative resist. b) Resulting metal structure. c) Patterning of the photoresist with the front side mask and the subsequent DRIE of the front side. d) Patterning of photoresist on the handle layer and opening the holes and trenches in the  $\text{SiO}_2$  layer using BHF. e) Partial opening of the handle layer by DRIE.

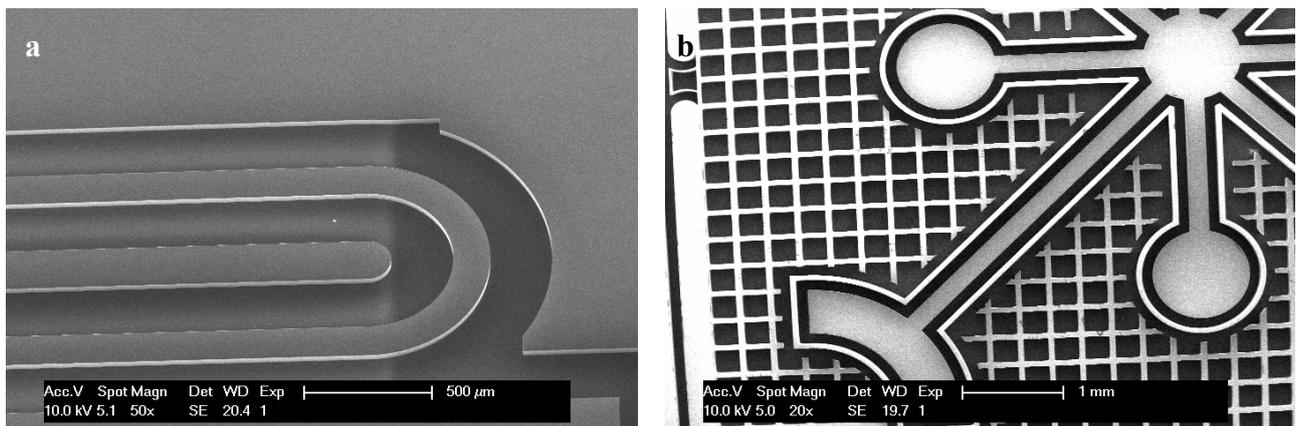


**Figure 6-8:** SEM micrographs of the front and backside. a) One of the springs that was etched on the front side of the SOI wafer. b) The etched backside of the wafer with the holes and trenches used for the releasing process and also the bonding and alignment structures that will remain after the release.

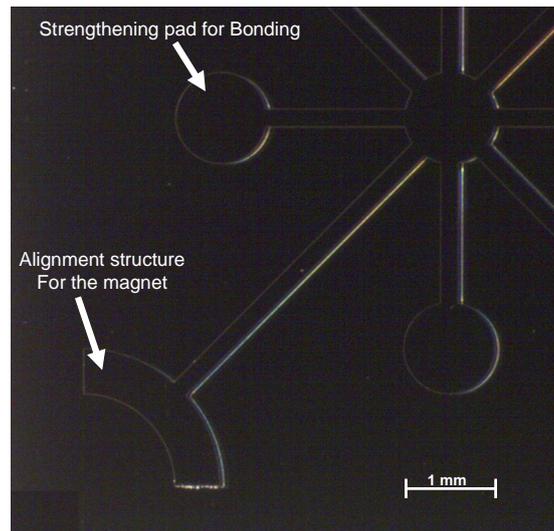


*Figure 6-9: Optical picture of the released backside and the remaining bonding and alignment structures*

### 6.3 Wafer bonding and finalization of the wafer etching and release

In this chapter the different wafer bonding processes that were used are discussed and the finalization of the microfabrication and release of the mirrors will be demonstrated.

#### 6.3.1 Different tested bonding metal stacks

Two sets of metallic stacks were used for these processes. The first used stack consisted of “Ta: 20 nm / Pt: 30 nm / Au: 800 nm”. The second used stack consisted of “Cr: 20nm / Au: 650 nm”. The first stack was abandoned because of very bad resistance of Ta in vapor phase HF etcher (HF-VPE) that is used for the release process to etch the BOX. The Cr / Au stack however was shown to resist the HF-VPE very well. In the following only the second metallic stack (Cr / Au) is used.

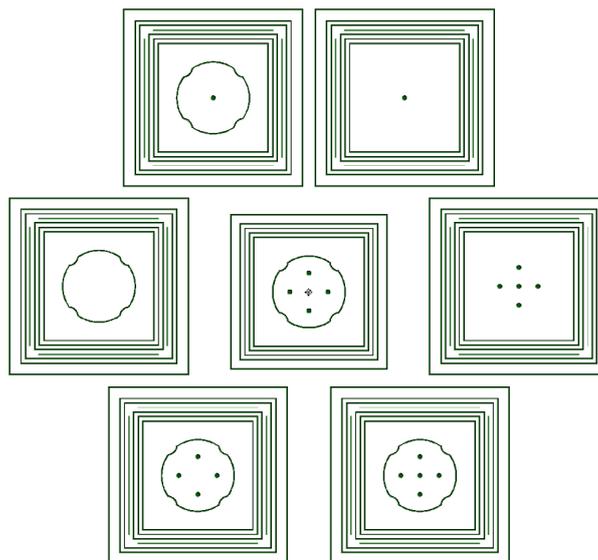


*Figure 6-10: The bonding mask and the seven different bonding patterns that were put on the different chips. The square lines around each chip are to bond the frames of the magnetic platform chips with their corresponding frames around the mirror chips. The central part of each design (dots and rings) is the part that attaches the mirror to the actuation platform.*

### 6.3.2 Eutectic vs. thermo-compression bonding

Two different bonding methods were tested; eutectic bonding and thermo-compression. Thermo-compression bonding involves two metallic layers that are compressed together to form the bond (in our case the pressure used was  $P = 8$  bars). Metal was deposited not only on the front side of the actuation part but also on the backside of mirror and then pressed together in the bonding machine. This method involves high pressures and broke some parts of the wafers that were bonded. The layers were further damaged when they were put in the DRIE. We think that the wafers broke because of several reasons; the pressure exerted during bonding, the bow of the SOI wafers and the thick BOX layer of the mirror wafer.

Eutectic bonding was used as a second bonding method. Eutectic bonding uses high temperatures that make two different layers diffuse into each other to create the bond (in our case gold and silicon). Therefore lower pressures are needed ( $P = 800$  mbars at  $300$  °C), thus reducing the chance of fracture.

### 6.3.3 Design of the bonding mask

The bonding mask used in the fabrication process is shown in Figure 6-10. There are seven chips on each wafer as can be seen in Figure 6-10. Seven different bonding patterns were put on the different chips. The squares around each chip attach the frame around the mirror (Figure 6-1) to the frame around the actuation platform (Figure 6-6). The central part of each design (dots and rings) is the part that attaches the mirror to the actuation platform. These different bonding profiles allow us to investigate the best bonding pattern for keeping the mirror as flat as possible. The first design shown on the top left of Figure 6-10 shows a ring that would be bonded to the rim of the mirror and a dot that bonds to the centre. There are other designs with more than one dot these dots are situated at half the distance between the rim and centre of the mirror.

## 6.4 Finalization of the fabrication after bonding

As it was discussed in chapters 6.1, 6.1.2 and 6.2, the last fabrication steps were carried out after bonding of the two wafers. Here the finalization of the microfabrication process will be shown. The process steps for the silicon wafer mirror after bonding are exactly the same as the steps for the SOI wafer. Therefore only the process steps of the SOI wafer are described.

The schematic cross section of the bonded wafer is presented in Figure 6-11a. Only the SOI mirror is shown in this figure. The mirror is shown on the top and the actuation platform on the bottom. They are separated by the metallic bond that is shown in yellow. It can be seen that the pillars of the mirror are exactly on top of the pillars that were formed on the actuation part (Figure 6-9) where metal was deposited. This means that in no time during bonding, pressure is applied on a membrane or a thin structure. This reduces the chances of fracture. The processing steps after bonding are described in the following:

- a) The bonded mirror and actuation platforms are shown in Figure 6-11b
- b) The first step in order to finish the microfabrication process is to etch the holes that were partially opened on the backside of the actuation platform. This is done in the DRIE with the SiO<sub>2</sub> on the

surface of the handle layer as the etch mask. This is shown in Figure 6-11b. The holes and trenches are etched until they reach the BOX.

c) In the next step, the front side of the mirror platform is completely removed using DRIE as shown in Figure 6-11c.

d) The next step is to release the unwanted parts by HF-VPE that etches all the oxide layers of the two wafers. By under-etching the BOX the unwanted parts get released as shown in Figure 6-11d.

e) The released structure is shown in Figure 6-11e. There are also trenches around each chip that define the frame around it. They are also released as shown in Figure 6-11e. Therefore no dicing is needed to release the chips.

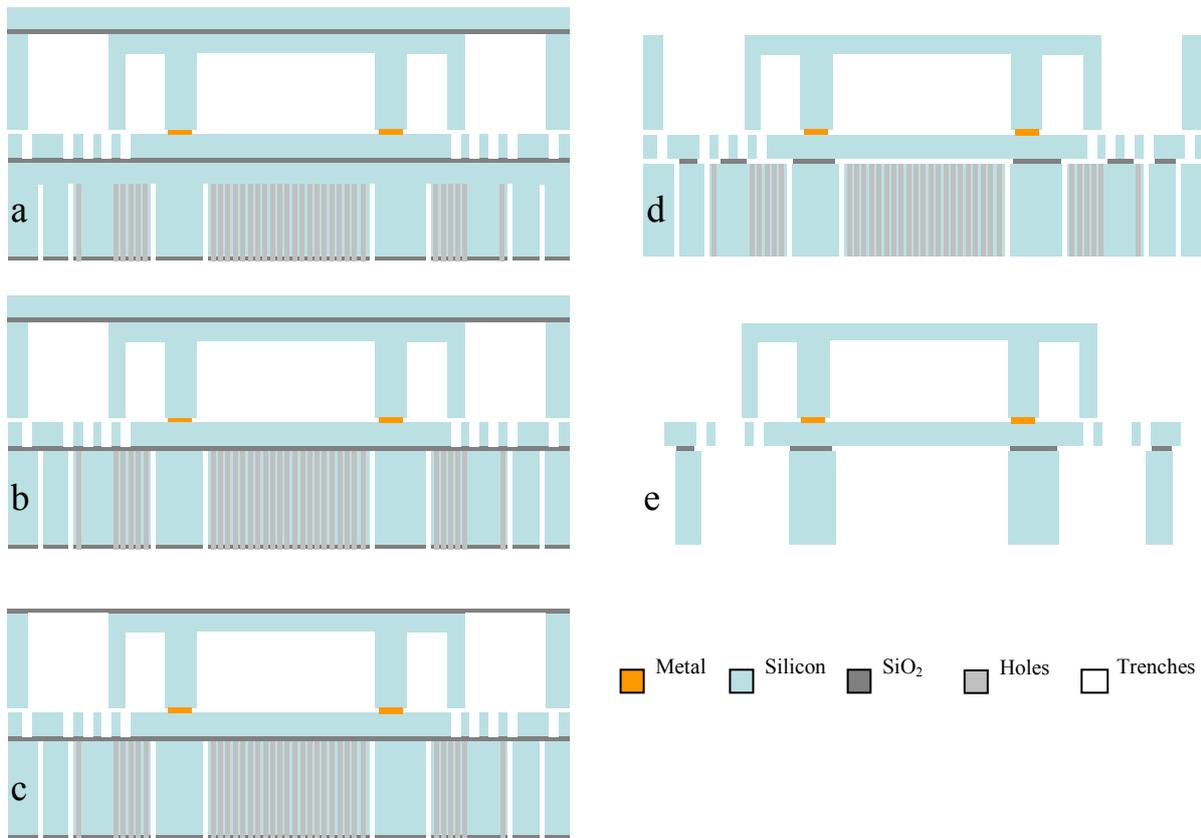


**Figure 6-11:** a) The schematic cross section of the bonded wafer. b) Finalization of the DRIE on the handle layer of the actuation platform. c) Complete removal of the device layer of the mirror by DRIE. d) Release of the unwanted structure by HF-VPE. e) Release of the chip from the wafer

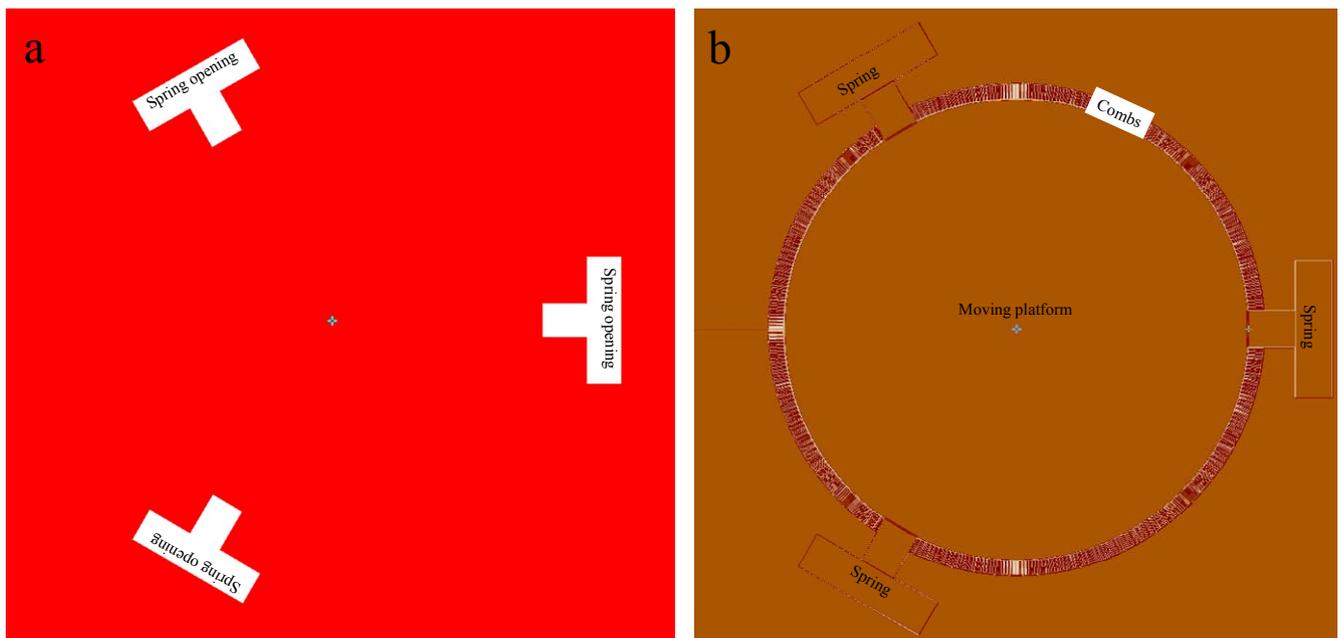
## 6.5 Microfabrication of the electrostatically actuated platform

The general concept of the fabrication of the electrostatically actuated mirror was discussed in 4.5.2. The main idea is to etch the combs on the device layer of the SOI wafer and continue to etch them into the handle layer of the SOI. There are 4 set of combs created by this process; two of which on the device layer and two in the handle layer. Two of these four sets are eventually released and removed by use of HF-VPE. This process will be shown in the following. The used SOI wafers had the specifications summarized in Table 6-2.

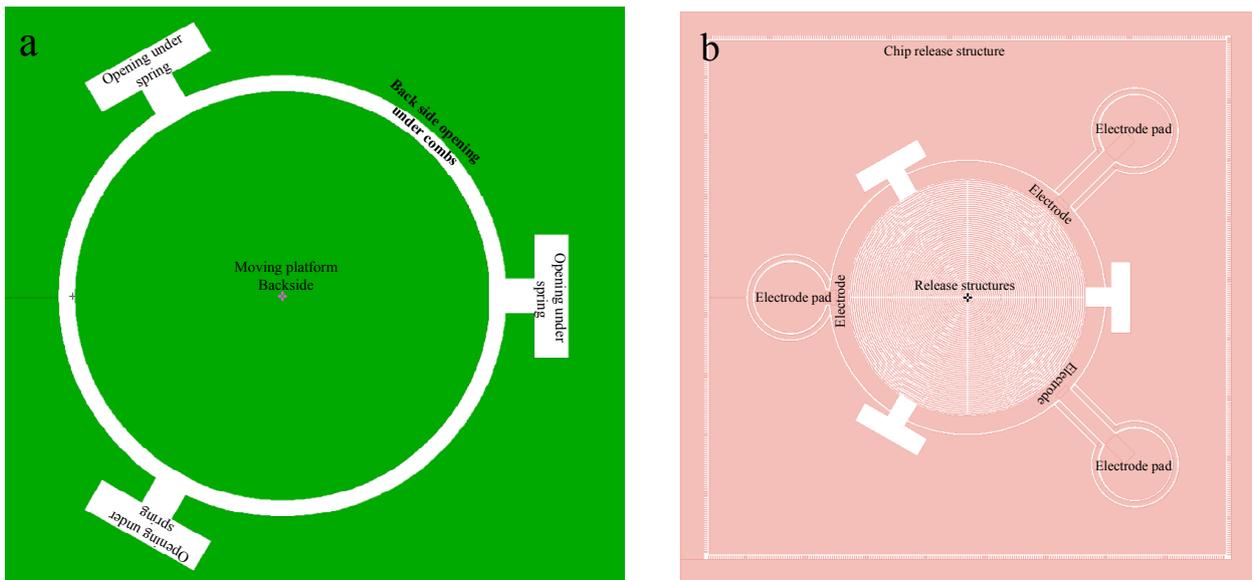
There were 4 masks involved in making the electrostatic actuator. Two masks were designed for the front side and another two for the back side etching of the wafer. The front side masks shown in

Figure 6-12a & b, present the scheme used to create the springs and the vertical combs using a delayed mask process. The mask shown in Figure 6-12a is the second mask in the delayed mask process and creates the opening that thins down the springs. The mask shown in Figure 6-12b creates the combs around the moving platform and also shapes the springs. It is the first mask in the delayed mask process and is layered on top of the second mask. It also has trenches that remove the some combs from the front side and also trenches for the release of the chips from the wafer, as shown more clearly in Figure 6-16.

The backside masks shown in Figure 6-13a & b, create release structures that remove the unwanted mass of the platform and also release the combs from the backside. The mask shown in Figure 6-13b also creates the three electrodes pads on the backside of the actuation platform. The circular structures at the centre of the mask, shown in Figure 6-13b, fall off at the end of the fabrication process leaving only the circular membrane that is formed by the device layer. These two mask shown in Figure 6-13a & b are also used in a delayed mask processes. Figure 6-13a is the second delayed mask in the fabrication process and Figure 6-13b is the first mask that is layered on top of the second mask.



**Figure 6-12:** The masks designed for the front side and that creates the springs and the moving platform. a) The mask that creates the opening that thin down the springs. b) The mask that creates the combs around the moving platform and also shapes the springs



**Figure 6-13:** The backside masks that creates a release structure which removes the unwanted combs and mass of the platform leaving only the bonding and alignment structures behind.

Before going through the process steps, a reminder about the fabrication concept seems appropriate. The process creates two pairs of combs. One pair is on the device layer and one on the handle layer as shown schematically in Figure 6-14. The upper combs on the frame were removed in this process as well as the lower combs on the mirror. The combs remaining on the lower part of the frame and the combs remaining on the upper part of the mirror produce the vertical actuation.

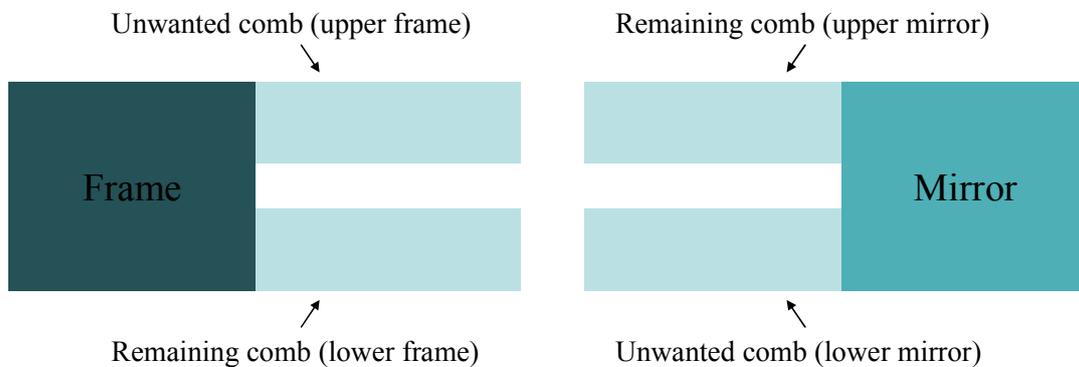


**Figure 6-14:** The fabrication concept that creates two pairs of combs is shown. One pair is on the device layer and one on the handle layer. The upper combs on the frame were removed in this process as well as the lower combs on the mirror. The combs remaining on the lower part of the frame and the combs remaining on the upper part of the mirror produce the vertical actuation.

The processing is described in the following:

- The process starts with cleaning the SOI wafer as shown in Figure 6-15a.
- The first step was to deposit aluminum on the SOI front-side, as shown in Figure 6-15b. This aluminum layer was used as the second mask for the delayed-mask process of the front side shown in Figure 6-12a. It was deposited using E-beam deposition.

c) The second step was to pattern the aluminum using photolithography as shown in Figure 6-15c. The resist used was AZ 9260. The aluminum was then etched using an Alu Etch solution. The mask is shown in Figure 6-12a.

d) The third step was to removing the first photoresist and applying a new one for the creation of the combs as shown in Figure 6-15d. The wafer is again etched with the Alu Etch solution. This will create the opening for the combs

e) The combs and release structures are etched with DRIE as shown in Figure 6-15e.

A closer look at this step with a comparison to the mask is given in Figure 6-16. This figure helps in relating different trenches with their respective positions on the mask. There is a trench circumventing all the combs shown with the dashed arrow in Figure 6-16. This is the release trench for one of the two pairs of combs created on the chip front side. This trench is smaller than the other trenches; therefore it is etched slower than the others in DRIE etching. The reason will become apparent in the next step. The combs and the trench used for releasing the chip are also shown in Figure 6-16.

f) In Figure 6-15f the BOX is etched using HF-VPE.

g) The next step is to continue etching the combs and trenches into the Handle layer of the SOI wafer as shown in Figure 6-15g. as it can be seen in Figure 6-15g, the trench that circumvents the combs stops at the BOX layer. This prevents it from going into the handle layer, because if it did it would reduce the strength of the attachment between the “lower frame” combs and the frame itself.

h) In the next step the photoresist is removed and the springs are thinned down to the desired value using Aluminum as delayed-mask. This is shown in Figure 6-15h. This step is necessary to achieve the correct value for the spring constant.

i) The aluminum is then etched completely using Alu Etch solution and the wafer is thermally oxidized as shown in Figure 6-15i. this silicon oxide layer will prevent damage to the combs when the backside is being etched.

j) Next step is to do photolithography on the handle of the wafer and pattern the silicon dioxide on the backside as shown in Figure 6-15j. The used photoresist was AZ 1518. This step creates the first step of the delayed- mask process on the backside.

k) The next step creates the second delayed-mask using photolithography as shown in Figure 6-15k. The photoresist used was AZ 9260.

l) Figure 6-15l shows the first DRIE on the backside. Figure 6-17 shows a comparison of the first mask and this step. In this step the open trenches are partially etched.

m) Figure 6-15m shows the second DRIE on the backside after the removal of the photoresist. Figure 6-18 shows a comparison of the second mask and this step. In this step all the trenches that were partially etched in the previous step will reach the BOX, while the trench above the combs is only etched until it reaches the combs.

n) The next step is to release the unwanted combs and structure as shown in Figure 6-15n. The trench behind the “lower-mirror” set of combs releases them and they get removed. The same thing happens to the “upper-frame” combs that were circumvented.

o) This creates two sets of combs at different heights that create the vertical comb movement of the combs and the mirror as shown in Figure 6-15o.

A SEM micrograph of the combs is shown in Figure 6-19. The picture shows the backside of the actuation platform. The interdigitated combs can be seen in this picture.

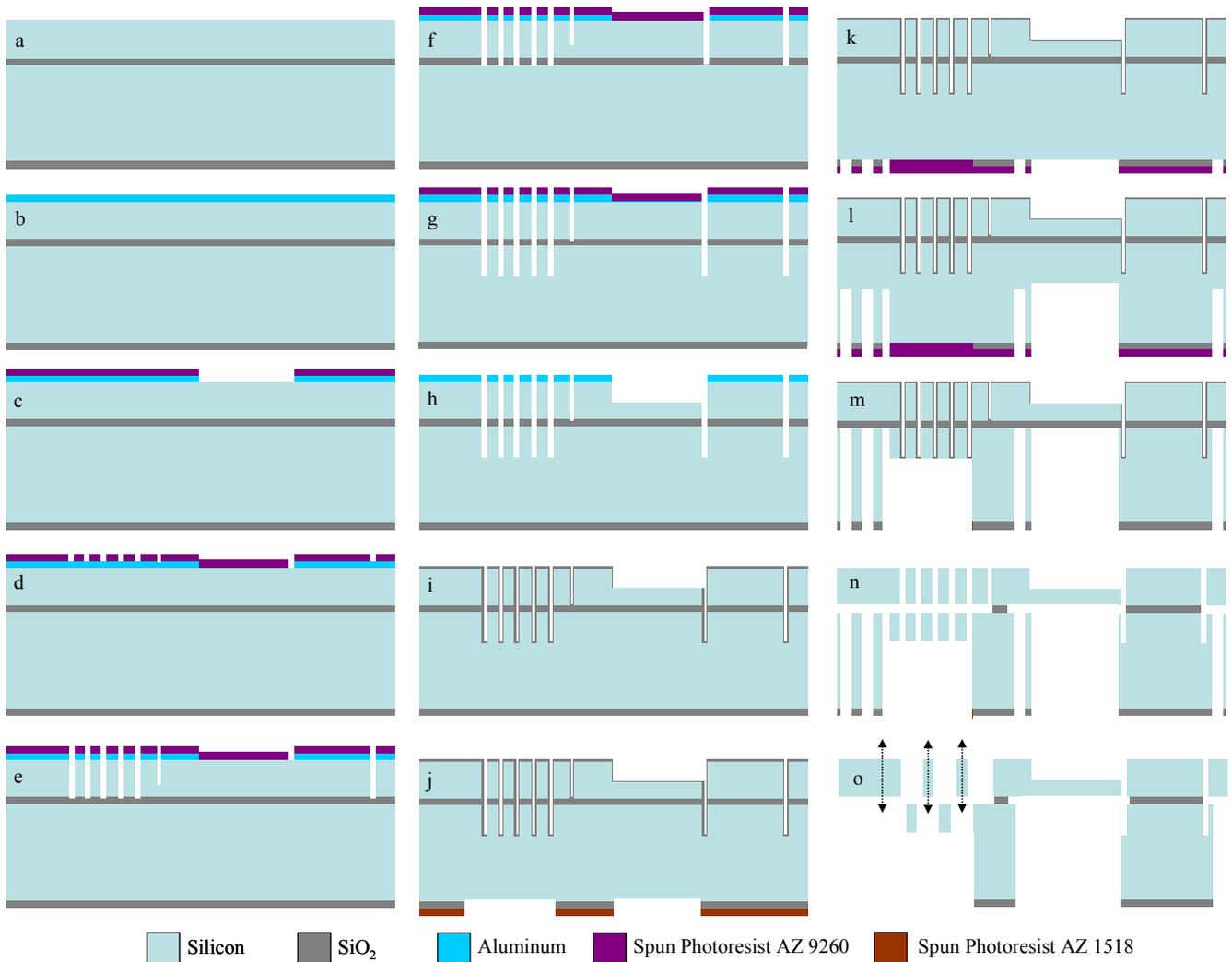


**Figure 6-15: The process flow of the electrostatic actuator. (a) Cleaning of the SOI wafer. (b) Aluminum deposition. (c) Photoresist lithography and opening of the aluminum in Alu etch. (d) Removal of first photoresist and application of the second layer and photolithography. (e) First DRIE step of the combs and trenches on the front side. (f) HF-VPE of the BOX. (g) DIRE etching into handle layer. (h) Removal of photoresist and delayed mask process for thinning down the springs. (i) Removal of Al and thermal oxidation. (j) Photoresist spinning and patterning of the SiO<sub>2</sub> of the backside. (k) Removal of first photoresist and application of the second photoresist layer with patterning. (l) First DRIE and partial opening of the backside. (m) Removal of the resist and second DRIE of the backside (second delayed mask). (n) Release of the structures by HF-VPE. (o) Released mirror chip.**

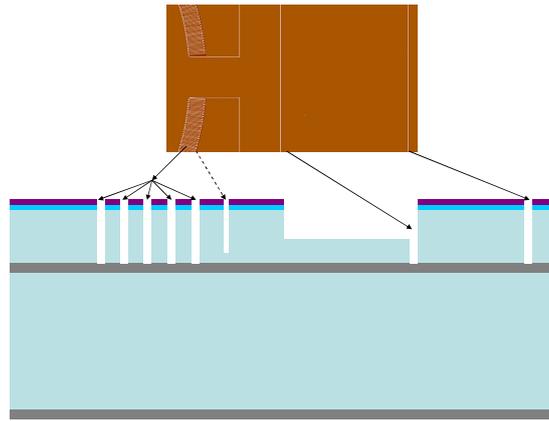


**Figure 6-16:** A closer look at the mask with comparison to the process flow. There is a trench circumventing all the combs shown with the dashed arrow. This is the release trench for one of the two sets of combs created on the chip front side. This trench is smaller than the other trenches; therefore it is etched slower than the others in DRIE etching. The combs and the trench used for releasing the chip are also shown.

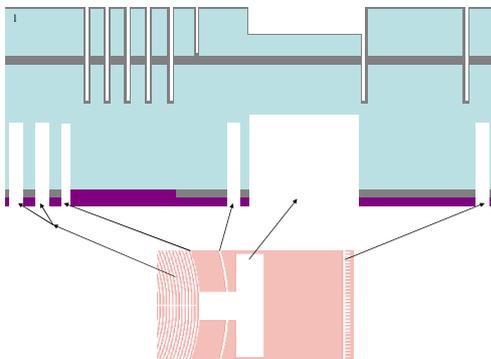


**Figure 6-17:** A comparison of the first delayed mask process of the backside and the process flow. In this step the open trenches are partially etched.

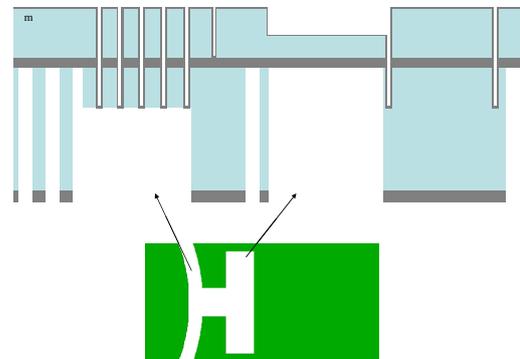


**Figure 6-18:** A comparison of the second delayed mask and the process flow. In this step all the trenches that were partially etched will be etched until the BOX. The trench above the combs is only etched until it reaches the combs.

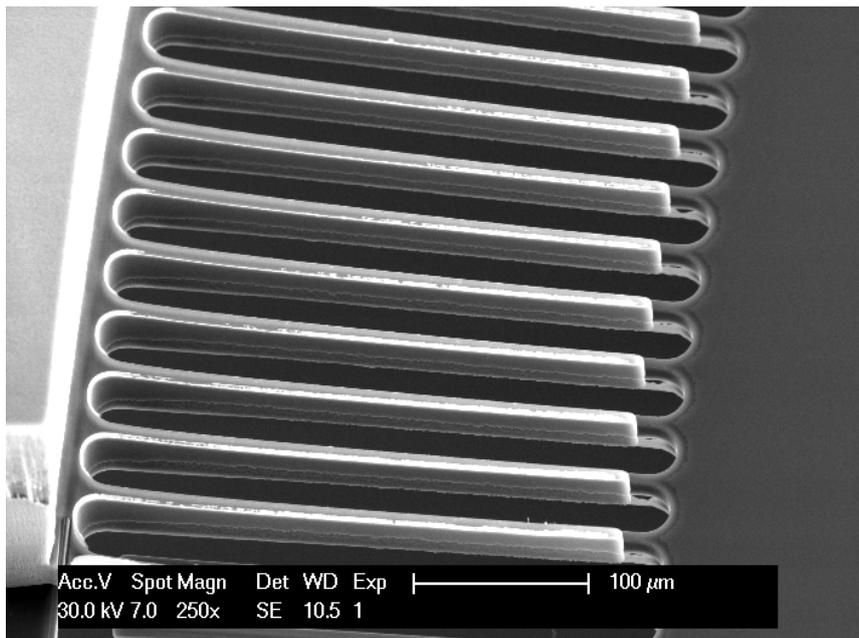


**Figure 6-19:** SEM micrograph of the backside of the actuation platform. The interdigitated combs can be observed.

## 6.6 Assembly process of the magnetically actuated mirror

In this chapter the assembling process of the magnetically actuated mirror is shown. The general concept of the assembly was shown in 4.5.2. The different tools and the assembled devices will be shown here.

### 6.6.1 Assembly of the magnets on the backside of the actuation platform

Assembly of the magnets is done using a handmade device in EPFL, NE, SAMLAB, shown in Figure 6-20. This device consists of two parts; a platform where the magnetic mirror is put and a vacuum gripper that can position the magnet on the mirror. The platform can rotate around the x and y axes. This platform can keep samples fixed in their place by air suction using a vacuum hole that is constructed in this platform. The gripper uses a vacuum suction tip to hold the magnet. This part can move with 6-DOF (X, Y, Z and rotations) to position the magnet.

The backside of the mirror's actuation platform with the assembled magnets is shown in Figure 6-21a. The magnets were positioned around the four corners of the backside and glued to their place. Alignment of the magnets is ensured by pushing them against the circular pillar at each corner shown in Figure 6-21b.

The glue used was an Ethyl cyanoacrylate compound (super glue). This glue has a very low viscosity. This property is ideal for our application since the gluing layer is very thin and uniform. Therefore all of the magnets will have the same height after gluing. This setup was also used for chip level bonding of mirrors on the actuating platform.

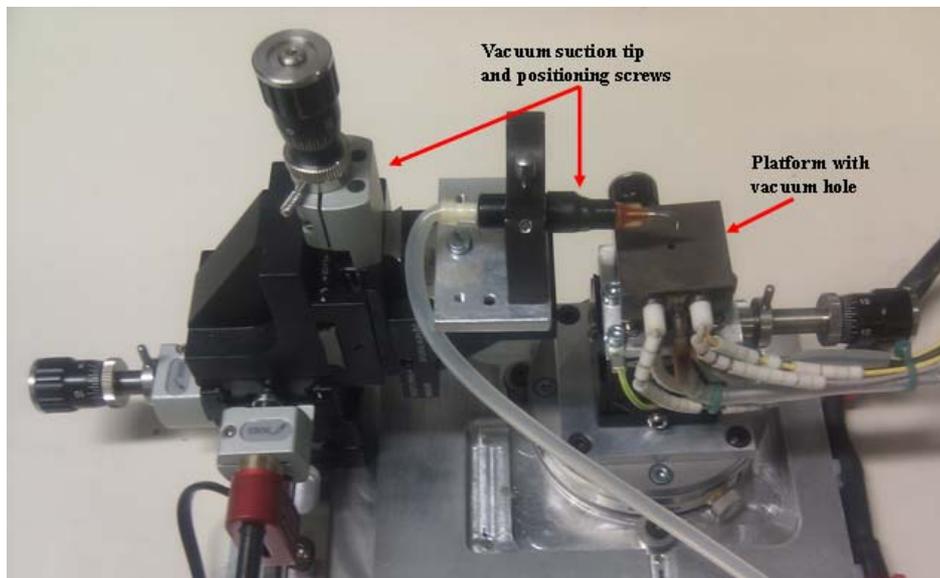


*Figure 6-20: The handmade device used for assembly of the magnets. It consists of a platform where the magnetic mirror is put and hold in place using a vacuum hole. The platform can rotate around the x and y axes. It is also equipped with a vacuum gripper tip to hold the magnet. This part can move with 6-DOF (X, Y, Z and rotations) to position the magnet.*

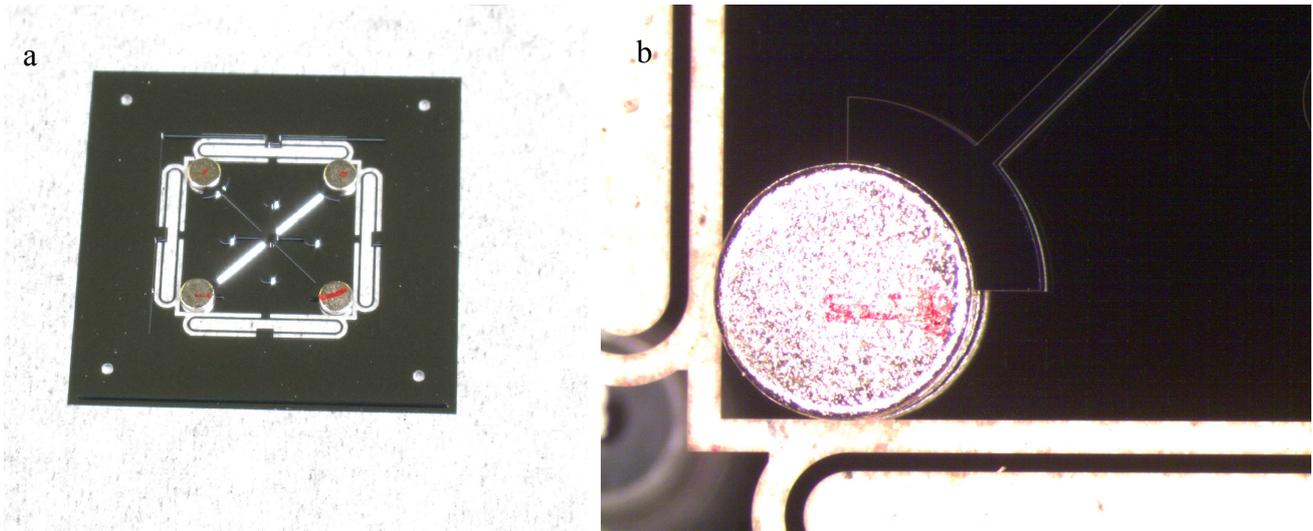


**Figure 6-21:** a) The backside of the actuation platform with the assembled magnets. The magnets were positioned around the four corners of the mirror and glued to their place. b) Alignment of the magnets is ensured by pushing them against the pillar at each corner.

### 6.6.2 Assembly of the mirror chip on the coil chip

Figure 6-22a, shows the fabricated coil chip. The mirror and coil chips both have holes on the outer corners that allow pins to go through them as shown in Figure 6-22a, and Figure 6-21a. These pins were glued in the holes as shown in Figure 6-22b. They allow direct alignment of the two chips. Silicon spacers with a thickness of  $650\ \mu\text{m}$  were placed on the pins to create the needed distance between the mirror and the coils. Since these spacers are made out of one silicon wafer they have very good thickness uniformity. These spacers are visible in Figure 6-22b. The final distance between the coils and the magnets was  $550\ \mu\text{m}$  since the magnet is  $400\ \mu\text{m}$  thick and the handle layer of the silicon wafer only  $300\ \mu\text{m}$ . the final distance is  $50\ \mu\text{m}$  more than the needed separation distance. The assembled mirror and coil chips are shown in Figure 6-22c. The aluminum slab under the device is used as a heat sink.

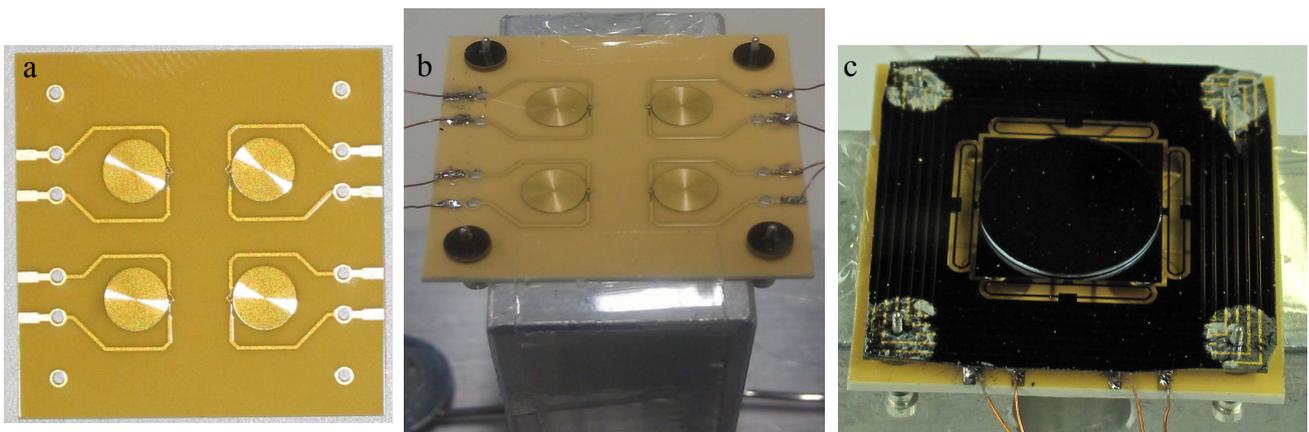
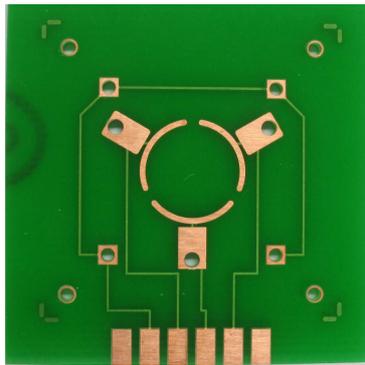


**Figure 6-22:** a) The coil chip with the four holes. b) The coil chip mounted on the aluminum slab. The four pins are placed in the holes and the spacers are positioned on them. c) The mirror chip is mounted on the pins. The distance between the magnets and the coils is  $550\ \mu\text{m}$ .

### 6.6.3 Assembly process of the electrostatically actuated mirror

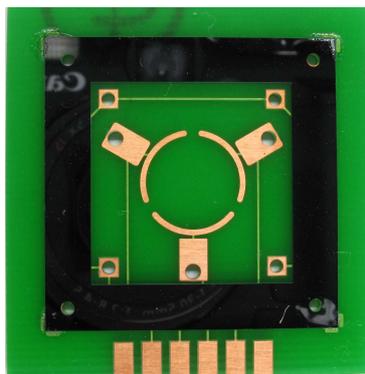
In this chapter the assembling process of the electrostatically actuated mirrors are shown. The assembly of the electrostatic chip is simpler than the electromagnetic chip and does not need any special tools. If the mirror is needed to be chip-wise bonded the setup shown in Figure 6-20 can be used. Three different parts of the electrostatic actuator are shown here.

Figure 6-23 shows the base chip made out of PCB. There are three pads arranged circularly that connect with the electrodes of the electrostatic actuator. The contacts are made either by gluing or by pogo pins. The small bored square pads can be used for connecting the lower body (handle layer) of the actuator to ground. The circular holes that are the furthest from the centre are used to guide the alignment structure into its place.



*Figure 6-23: The base chip made out of PCB. There are three electric pads arranged circularly that connect with the electrodes of the electrostatic actuator. The small bored square pads can be used for connecting the lower body of the actuator to ground. The circular holes that are the furthest from the centre are used to guide the alignment structure into its place*

The circular holes that can be seen in Figure 6-23 are the furthest from the centre and are used to guide the alignment structure into its place. This is shown in Figure 6-24. The alignment is made of Silicon and is a 250 $\mu\text{m}$  thick. It is guided to its place using pins that are put in the holes of the circular pads. The alignment structure is then glued to its place and the pins can be removed.



*Figure 6-24: The alignment structure glued to place on the PCB using the alignment holes and pogo pins. The pogo pins were removed after this procedure*

The electrostatic chip can then be easily aligned on the electrodes as shown in Figure 6-25. The electrode contacts can either be glued to place or pogo pins can be inserted in the holes of the electrodes as shown in Figure 6-24. The unused electrodes shown at the left and right of the four

central electrodes can be used to contact the upper part of the actuator. This is not shown in Figure 6-25.

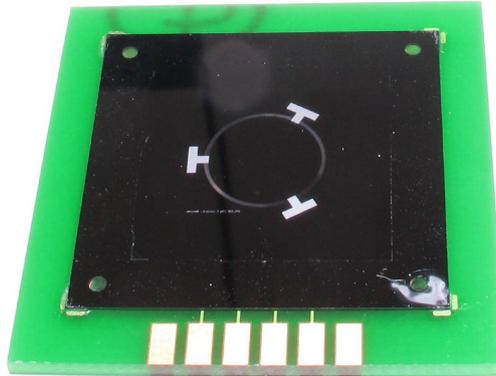


*Figure 6-25: The electrostatic was put into the alignment structure and aligned on the electrodes. The electrode contacts can be glued to place. Pogo pins can also be used.*



## 7 Characterization

The characterization of the coils, magnetic forces, microfabrication of the electrostatic and magnetic actuators, the resonant frequencies and the rotation angles will be discussed in this chapter. These results will be compared with simulations

### 7.1 Magnetically actuated mirror

The magnetically actuated mirror consists of the actuator, the mirror, and the coils. The mirror part will be characterized in a different section. The other parts are characterized in the following starting with the coils. The maximum current in the coils was investigated. This value defined the maximum force that we could extract from the system.

#### 7.1.1 Coil temperature measurements

In order to calculate the rise in the coil's temperature, the temperature coefficient of resistance (TCR) of the coils should be found. The following formula can be used to find the TCR:

$$\frac{R - R_0}{R_0} = \alpha (T - T_0) \quad \text{Eq. 7-1}$$

$R_0$  and  $R$  are the resistances before and after heating the specimen respectively.  $T$  and  $T_0$  are the specimen's temperature before and after heating respectively and  $\alpha$  is the TCR. This formula shows a linear relationship between  $R$  and  $T$ . By knowing the TCR the same formula can later be used to find the temperature increase in the coils. In the following we describe the measurement procedure for finding the TCR.

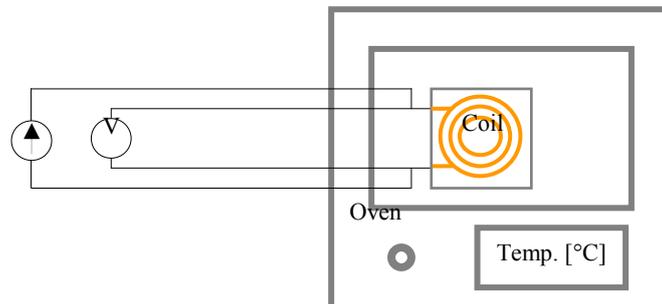


**Figure 7-1:** 4 point measurements of the voltage and the current for finding the TCR. A small current is injected in the coil that is placed in an oven. The corresponding voltage is read from the voltmeter as the oven's temperature is increased. The temperature is read from the oven. The coils resistance is calculated from the voltage and the current which in turn can be used to calculate the TCR.

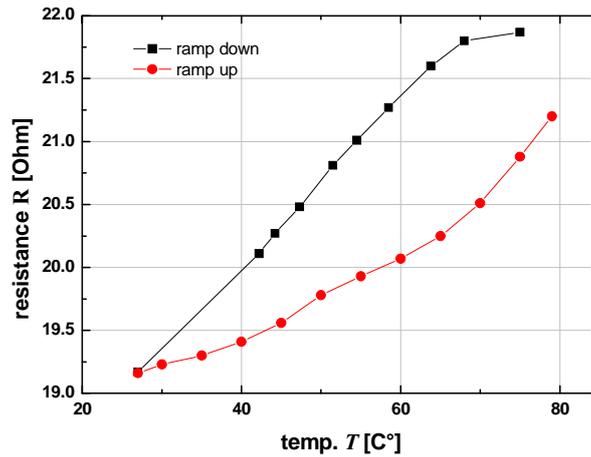


*Figure 7-2: A typical result of the TCR measurements that shows the presence of hysteresis in the ensemble of the system. This can be seen in the nonlinearity of the curve as the temperature increases (ramp up) and another as the system is cooling down (ramp down). This hysteresis should be mainly due to temperature differences between the coil and its surrounding.*

### 7.1.1.1 TCR measurements in the oven

In order to find the TCR, 4 wires were connected to a coil that was placed in an oven. The temperature of the oven was changed from ambient to 80 °C. The wires were used for “4 point measurement” of voltage and current as shown in Figure 7-1. A small current is injected in the coil and the corresponding voltage is read from the voltmeter as the oven’s temperature is increased. The temperature is read from the oven. The coil’s resistance is calculated from the voltage and the current. Having the resistance and the temperature enables us to calculate the TCR of the coil from Eq. 7-1.

A typical result of the TCR measurements is shown in Figure 7-2 . The results of these experiments show that the ensemble of the system has temperature hysteresis. This can be seen in Figure 7-2 since the resistance follows a nonlinear curve as the temperature increases (ramp up) and another as the system is cooling down (ramp down). This hysteresis should be mainly due to temperature differences between the coil and its surrounding. This problem should be eliminable by increasing the time interval of the entire measurement. This will result in a more uniform temperature of the experiment’s environment. However this problem could not be eliminated in our system. Further tests in a much more controllable environment are needed to find the reasons of this hysteretic behavior. However an average value of  $TCR = 0.00256$  is extracted from these measurements. This value is lower than the value reported in literature for copper  $TCR \approx 0.0039$  [109, 110].

### 7.1.1.2 Temperatures acquired from thermal imaging

In order to better define the temperatures in our devices, thermal imaging of the coils were carried out using an infrared camera, Cedip Jade III MW, in the EMPA laboratories, Duebendorf. For this technique to work, the emissivity of the sample should be found. To do so the coil was heated up to a certain temperature using a thermoelectric cooler (TEC) and the corresponding thermal image was taken with the infrared camera. Comparing several images at different temperatures gives the emissivity according to the following relation:

$$P = \varepsilon \sigma A T^4$$

Eq. 7-2

Where  $P$  is the radiated power,  $\varepsilon$  is the emissivity,  $\sigma$  is the Stefan–Boltzmann constant,  $A$  is the area of the sample and  $T$  is the temperature. The emissivity of the coil was found to be  $\varepsilon = 0.17$ .

Knowing the emissivity, different current densities were injected in the coil and the system's temperature was calculated using the same relation mentioned in Eq. 7-2. The results of  $I = 500\text{mA}$  current injection are shown in Figure 7-3. It can be seen that the areas of the highest temperature are between two adjacent copper turns. There is a temperature gradient towards the outer rim of the coil. The current was injected in the coil for 18 seconds. The temperature increase is shown in Figure 7-4. This graph is taken on a line, shown in Figure 7-3, near the centre of the coil. The average temperature (Mean) and the maximum temperature (Max) are shown in this graph. The “Mean” curve shows the average temperature of the rectangular area shown in Figure 7-3. and “Max” curve shows the temperature of the point with the highest temperature. It can be seen that after the current source is turned on two seconds after the start of temperature measurements, the temperature increases very fast at the beginning and then continues slowly towards thermal equilibrium.

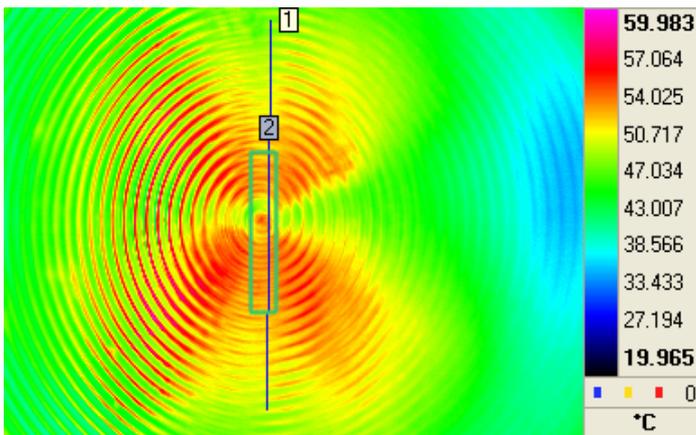


Figure 7-3: Temperature of the spiral coil at  $I = 500\text{mA}$ . It can be seen that the areas of the highest temperature are between to adjacent copper turns. There is a temperature gradient towards the outer rim of the coil.

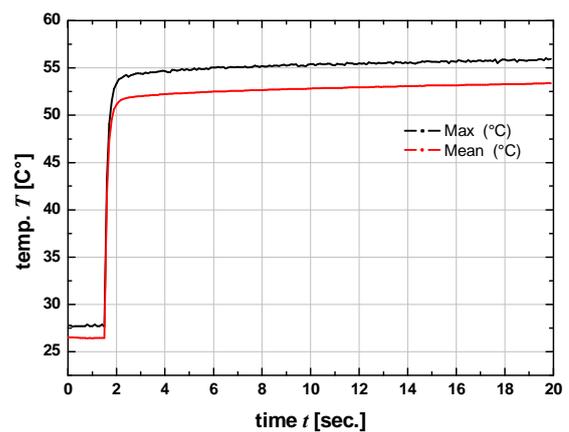


Figure 7-4: The temperature increase due to current injection for 18 seconds. This graph is taken on a line that is shown in Figure 7-3. The “Mean” curve shows the average temperature of this line and the “Max” curve shows the point with the highest temperature.

Figure 7-5 shows the results of Figure 7-4 and includes the result of TCR based temperature measurements for comparison. This figure show that the radiation temperature measurements and the TCR measurements are in excellent agreement. In Figure 7-5, the TCR graphs (red and black) and the mean temperature from radiation measurements (blue line) are of the same nature since they all show an average of the temperature. The average temperature of the mean value of these three lines is  $T = 53\text{ °C}$  with a standard error of  $\pm 3\text{ °C}$ . The mean value of the maximum temperature in the radiation test (green line) is  $55\text{ °C}$ . Comparing the two values ( $53\text{ °C}$  and  $55\text{ °C}$ ) while considering the calculated standard error shows that the maximum radiation value is an appropriate and safe

estimation of the coil's temperature. The TCR value that corresponds to the maximum temperature curve is  $TCR \approx 0.003$  which was the value used in the following calculations.

### 7.1.1.3 Temperature increase in air and in vacuum

The temperature increase of the coils can now be calculated using the TCR value. The coils were tested in air and in vacuum. These tests are only performed on the spiral coils. The unidirectional coils have a resistance that is two times higher than that of the spiral coils;  $R_{unidirect.} = 40 \Omega$ ,  $R_{spiral} = 20 \Omega$ . Therefore they create more heat and less current can be injected in them.

For measurements in air the coils are placed on an aluminum slab which acts as a heat sink. For measurements in vacuum the coil and the aluminum slab were placed in a vacuum chamber in a way that the slab would be in direct contact with the wall of the chamber. This will ensure the presence of an infinite heat sink for the coil. In both cases the system is allowed to reach thermal equilibrium. Since there is no convection possible in vacuum the only method of heat transfer is by heat conduction. This fact represents itself in a temperature difference of  $T_{vac} - T_{air} = 95 \text{ }^\circ\text{C}$  as can be seen in Figure 7-6; the injected current is  $I = 500 \text{ mA}$  in both cases. The coil temperature increases from  $23 \text{ }^\circ\text{C}$  to  $57 \text{ }^\circ\text{C}$  in air. In a vacuum chamber of pressure  $P \approx 6\text{E-}2 \text{ mbar}$ , this increase is from  $23 \text{ }^\circ\text{C}$  to  $152 \text{ }^\circ\text{C}$ .

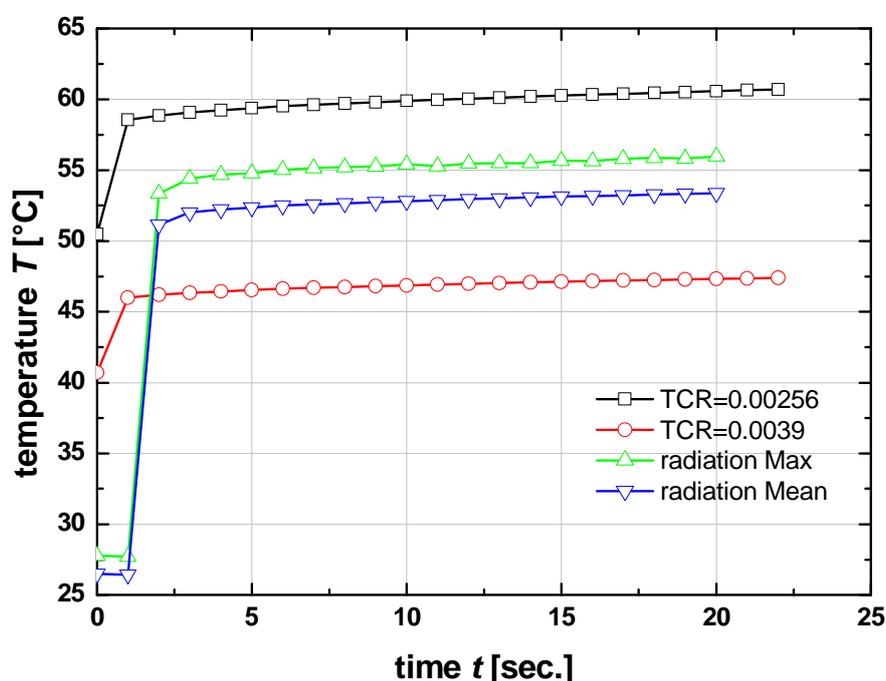
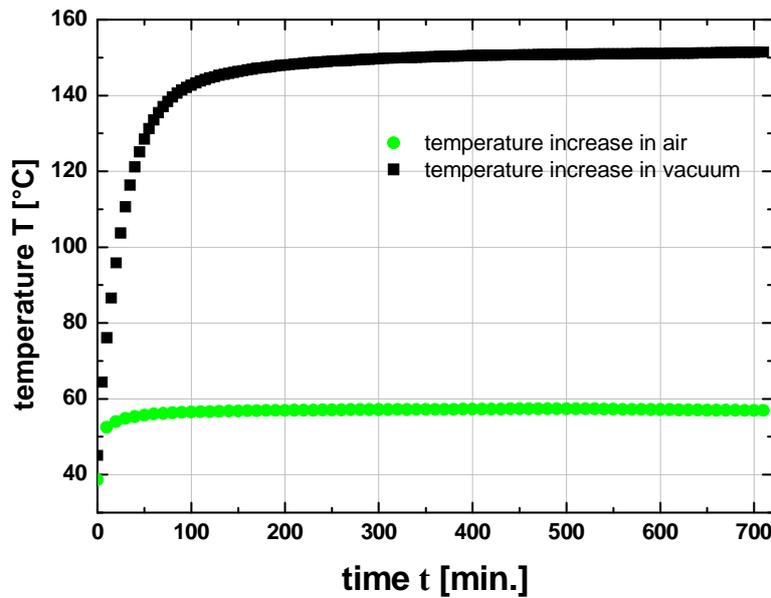


Figure 7-5: The temperature increase due to current injection according to thermal emission measurements performed with an infrared camera and the results of TCR based temperature measurements are shown for comparison. The  $TCR=0.0039$  is in red,  $TCR=0.00256$  is in black, the mean temperature from radiation measurements is in blue and the maximum temperature in the radiation test is in green. The TCR graphs (red and black) and the mean temperature from radiation measurements (blue line) are of the same nature.



*Figure 7-6: Results of temperature increase of the coil for a current injection of  $I = 500$  mA in vacuum shown in black and in air shown in green. The vacuum chamber has of pressure  $P \approx 6E-2$  mbar. When systems reach thermal equilibrium a temperature difference of  $T_{vac} - T_{air} = 95$  °C can be seen between the coil in vacuum and the coil in air. This is due to absence of convection in vacuum.*

Since heat conduction is linearly dependant on the temperature difference, it can be concluded that the temperature difference in vacuum is always around 130 °C for  $I = 500$  mA if an infinite heat sink is provided for the coils. Considering that this system will be used in space and knowing that low orbit satellites have a cool side (not facing the sun) that has temperatures around -50 °C, a current injection of  $I = 500$ mA is feasible. The final temperature will be around 80 °C which is around the maximum operational temperature of the magnets. Since the polyimide that is used in the coils is also unaffected by temperatures up to 200 °C, this system can safely be injected by a current of  $I = 500$ mA.

It should be mentioned that using coil fabricated on a silicon substrate reduces the maximum temperature considerably, due to the higher heat conduction coefficient of silicon. As an example if the coil thickness is increased to 50 $\mu$ m the resistance would drop to  $R_{spiral} = 5$   $\Omega$  which translates to 4 times lower power consumption.

#### 7.1.1.4 Electromigration

An important factor to be considered for the coils is electromigration. This effect can cause failure by creating voids in the coil and disrupting the circuit. Electromigration is the transport of material caused by the gradual movement of the ions in the conductor due to the momentum transfer between electrons and metal atoms. A simple representation of this effect can be given by the Black's law. This law gives the mean time to failure (MTTF) of a wire as follows [111]:

$$MTTF = A (J^{-n}) \exp\left(\frac{E_a}{k T}\right)$$

Eq. 7-3

A is a constant related to the cross-sectional area, J is the current density, n is the scaling factor,  $E_a$  is the activation energy of the metal, k is the Boltzmann constant and T is the temperature. According to this formula an increase in both the temperature T and current density J will decrease the MTTF. However according to Moulin et al [112] the electromigration effect is only significant after a certain temperature and current density is reached. An empirical formula based on several different coils formed on different substrates is proposed by Moulin et al:

$$J_{\text{det}}^{\text{(MA cm}^{-2}\text{)}} \cong 1.4 - 3.6 \times 10^{-3} T_{\text{det}}^{\text{(}^\circ\text{C)}} \quad \text{Eq. 7-4}$$

$J_{\text{det}}$  and  $T_{\text{det}}$  are the current density and the temperature that represent the threshold of deterioration. As an example if the coil's temperature is kept constant at 100 °C any value of  $J < 1.04 \text{ MA cm}^{-2}$  will cause no deterioration in the coil.

According to Eq. 7-4 and given the large cross-section of our coils, the deterioration threshold of the coils are at  $T=350^\circ\text{C}$  for  $I = 500 \text{ mA}$ . This is confirmed by several long duration operations of the coils; the coils were injected with current for long time durations and then the system was left to cool down. No significant or conclusive difference in the value of the resistance was found after cooling down. This was repeated on 3 different coils for several times. A typical result of such measurements is shown in Figure 7-7. This figure shows several consecutive measurements of the same coil. Each time the coil was injected with  $I = 500 \text{ mA}$  and the resistance of the coils was registered as a function of time. As it can be seen from Figure 7-7, the resistance of the coil increases as the temperature is increased due to current injection. After each measurement the system was let to cool down before the next measurement was taken. However, Figure 7-7 shows only the operation hours of the coil and not the cooling times. In total the system was operated for 85 hours.

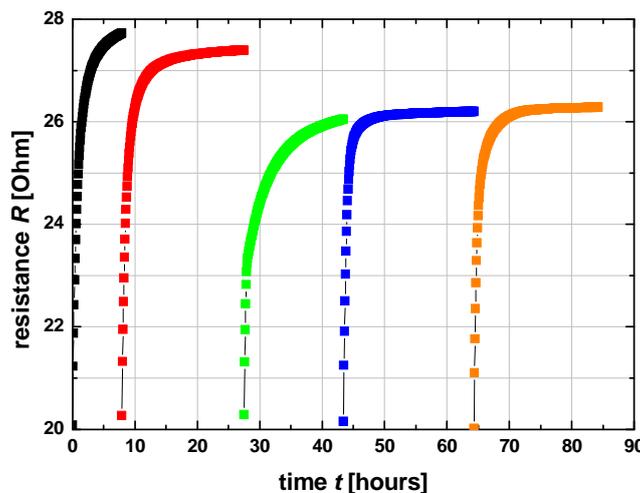


**Figure 7-7: Consecutive long duration test of the coil's resistance variations. The system is injected with  $I = 500 \text{ mA}$  and the resistance of the coil was registered as a function of time. The system is then let to cool down and the procedure is repeated again for 5 times. In total the system was operated for 85 hours. The first two measurements had a different heat sink which explains the higher maximum resistances compared to the other 3 measurements. It can be seen that after each measurement the system goes back to the same starting value of  $R = 20.16 \pm 0.1 \Omega$  which signifies the absence of Electromigration.**

The first two measurements had a different heat sink which explains the higher maximum resistances compared to the other 3 measurements. It can be seen that after each measurement the system goes back to the same starting value of  $R = 20.16 \pm 0.1 \Omega$ . The fixed value of the resistance when the coils were re-measured at room temperature also signifies the absence of Electromigration (formation of voids). Therefore, the calculations and measurements confirm, that electromigration is most likely not a failure mode for our current coil design and mode of operation.

#### 7.1.1.5 Inductance

The inductances of the two coils were measured with a RLC meter. The spiral coil and the unidirectional coil have inductances of  $L=3.5 \mu\text{H}$  and  $L=8.5 \mu\text{H}$  respectively. This is within range of the calculated values in chapter 4.1.6 based on the formulas from Wheeler et al. [100]

#### 7.1.1.6 Heat sink

An important observation was the importance of having a heat sink that completely covers the backside of the coils. Whenever this condition was not satisfied it led to cracking of the coil substrate and destruction of the coils. Two examples are given below in Figure 7-8. In Figure 7-8 a, the heat sink covers the whole backside. In Figure 7-8 b this is not the case. This resulted in fracture of the substrate on the coils as shown Figure 7-8 c.

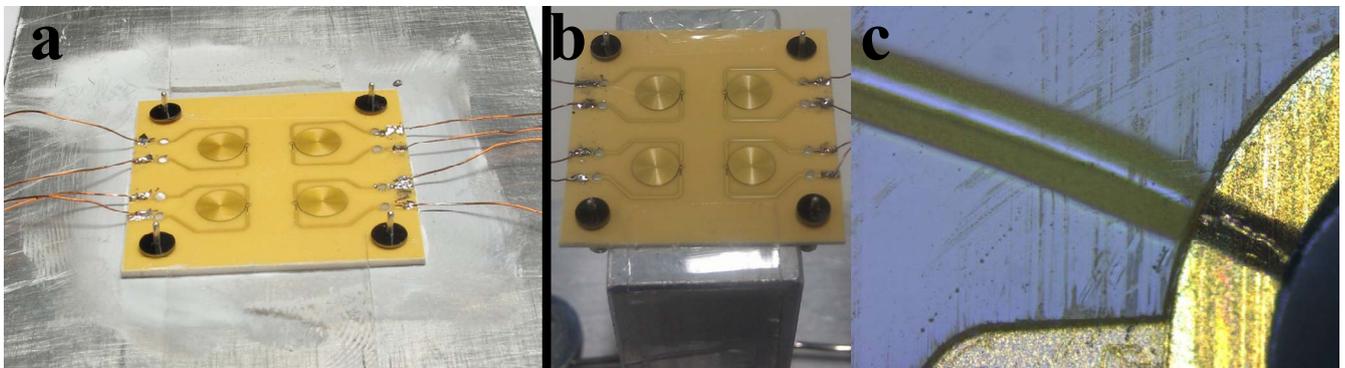


*Figure 7-8: A good and a bad heat sink. a) The heat sink covers the whole backside area of the coil substrate. b) The heat sink covers the backside only partially. c) The resulting uneven heat distribution led to the fracture of the substrate and coils.*

#### 7.1.2 Force measurements

In order to evaluate the forces a setup was built consisting of a cantilever with a known spring constant as shown in Figure 7-9. A magnet was attached to one end of the cantilever. The other end was fixed. The coil is placed under the magnet at a certain distance. As the current is increased the displacement of the cantilever is observed using an optical profiler; UBM microfocus profiler.

The results of the experiment for the coils and a cantilever with  $k = 42 \text{ N}\cdot\text{m}^{-1}$  are shown in Figure 7-10 for the unidirectional current coil and the spiral coil. The magnetic simulations of the force were shown in chapter 5.1.1.

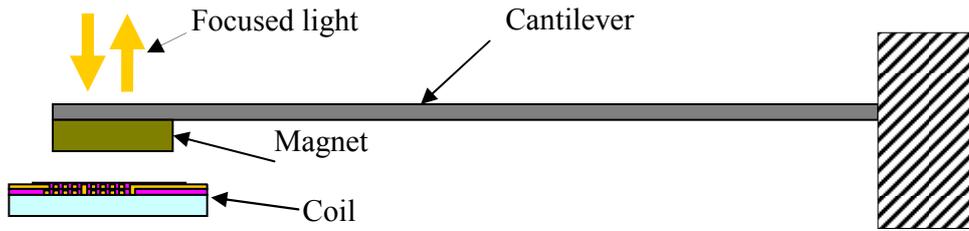


**Figure 7-9:** Built force-measurement setup consisting of a cantilever with a known spring constant with a magnet attached to one end of it. The other end is fixed. The coil is placed under the magnet at a certain distance. As the current is increased the displacement of the cantilever is observed using an optical profiler.

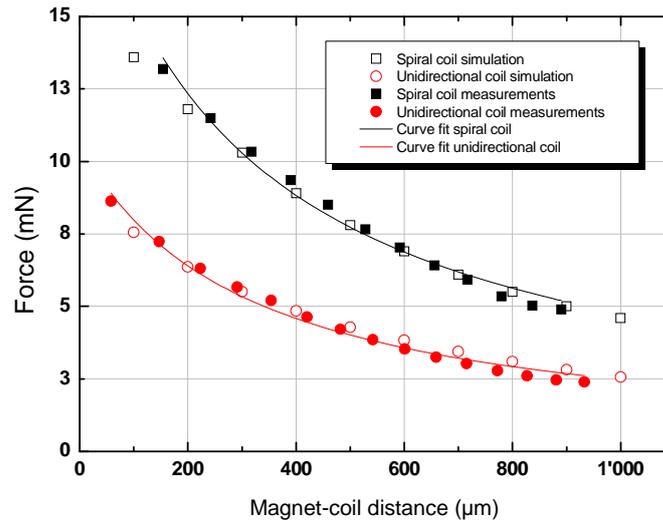


**Figure 7-10:** The resulting forces versus varying distances. The simulation results are also shown for comparison. The spiral coil configuration creates a higher force than the unidirectional coil which is in accordance to the simulation results. The curve fit of the measured forces are also shown that used the proposed empirical formula

A perfect match can be observed between simulations and the measurements in Figure 7-10 that confirm the force values used for mechanical simulations. Two curve fits are also shown in Figure 7-10 that will be discussed below.

### 7.1.2.1 Calculation of force

The simulation and measurement of the forces of the magnet-coil systems were shown in Figure 7-10. In order to be able to easily find the force of the magnet-coil system the following empirical formula was proposed for the force and it was used to curve fit the force profiles shown in Figure 7-10.

$$F = \frac{\alpha I}{\beta + z} \quad 1000\mu\text{m} > z > 100\mu\text{m} \quad \text{Eq. 7-5}$$

$I$  [A] is the injected current in amperes and  $z$  [m] is the distance between the magnet and coil in meters.  $\alpha$  and  $\beta$  are constants.  $\beta$  has the dimension of length  $L$  [m] and  $\alpha$  has the dimension  $L^2 * T$  (Tesla). Several different distance and current dependences can be proposed for the curve

shown in Figure 7-10. However the form represented in Eq. 7-5 was chosen because the curve fits show the lowest deviation in the values of  $\alpha$  and  $\beta$ .

The values of  $\alpha = 1.24 \times 10^{-5}$  and  $\beta = 3.03 \times 10^{-4}$  were acquired for the spiral coil and values of  $\alpha = 6.45 \times 10^{-6}$  and  $\beta = 3.04 \times 10^{-6}$  were acquired for the unidirectional current coil.  $\alpha$  is strongly length dependant. Therefore, the higher value of  $\alpha$  for the spiral coil shows that the effective length of the coil's wire under the magnet is longer for the spiral coil in comparison to the effective length of the wire under the magnet for the unidirectional current coil.

An important aspect of any system involving a spring and a nonlinear force is the snap-in effect. In short this effect makes the magnet snap into the coil when the gap reaches a small value. The snap-in occurs at different values for different initial gaps. It usually calculated to occur at values that are around one third of the initial distance [45]. In order to measure the snap-in distance of the coil and magnets the setup in Figure 7-9 was used. The magnet and spring were positioned at a certain distance from the coil. The current was continuously increased and the magnet approached the coil until snap-in occurred. The snap-in values for the data in Figure 7-11 are  $70\mu\text{m}$  and  $80\mu\text{m}$  for the  $300\mu\text{m}$  and  $400\mu\text{m}$  initial distances respectively. They are shown with black arrows in Figure 7-11.

In general these snap-in values are lower than the  $1/3$  of the total distance [45] and can even be considered somewhat independent of the total distance. The reason could lie in the fringing fields of coil and the magnet that are not considered in the theoretical calculations [45]. However the correct explanation of this phenomenon needs a complete analytical investigation which is out of the scope of this thesis.

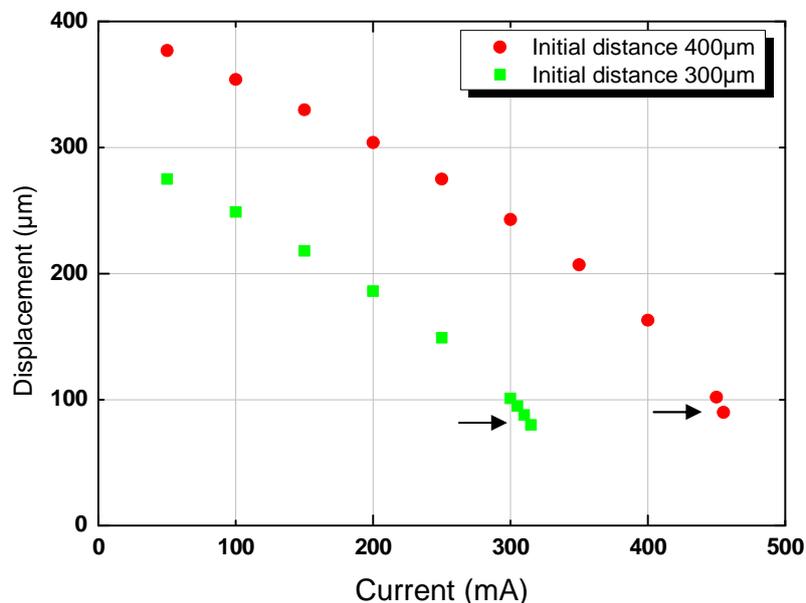


**Figure 7-11:** The results of the experiment for the spiral coil and a cantilever with  $k = 42 \text{ N.m}^{-1}$ . Three different initial values of the coil magnet gap ( $500\mu\text{m}$ ,  $400\mu\text{m}$ ,  $300\mu\text{m}$ ) are shown. The corresponding curve fits are shown in solid lines. The fits represent the numerical values very well. The snap-in point is shown with black arrows.

### 7.1.3 Comparison of coil designs

The two coils that had been fabricated were called the spiral coil and the unidirectional current coil. These two designs were compared for the amount of heat they generate and the ability to dissipate the generated heat in chapter 7.1.1, and most importantly their ability to produce force in chapter 7.1.2. It was shown that the spiral coil has half of the resistance of the unidirectional coil due to its geometry. Therefore it creates half of the heat created by the unidirectional coil.

The setup that was made for the measurement of the force between the magnets and the coils based on a cantilever with a known spring constant was shown in chapter 7.1.1. The results of the experiments were compared with the simulation results. It was shown that the spiral coil creates higher force than the unidirectional coil. This confirms the results of the simulations. According to these results the spiral coil has a lower resistance and therefore a lower operational temperature. It also creates a higher force. Therefore it was chosen as the design to be used in the magnetic actuation of the mirrors.

The current injection limit of the system was set to  $I = 500\text{mA}$  according to chapter 7.1.1. The coils are also very heat resistant and no electromigration could be observed in their long term operation. In summary the system can very well provide our required specifications.

### 7.1.4 Microfabrication

Several aspects of the microfabrication of the magnetically actuated mirror are shown here. As it was shown in chapter 6.1 the actuator wafer and the mirror wafer were bonded together. Later the silicon on top of the mirrors was etched to release the platform and the bonded mirror. There was a silicon dioxide layer to stop the DRIE etching. This layer protects the structures below the mirror from being etched. The fabricated mirrors demonstrated that this is possible even with very large openings if the bonded wafers are not significantly stressed. An example is shown in Figure 7-12. The round mirror is shown at the bottom of this figure. The spring is seen under the silicon dioxide layer that protected it during the DRIE etching.

The bonding process was another important part of the magnetic design. The alignment of the bonding process is a delicate procedure. The bow of the wafers and the applied pressure can result in misalignment of the two wafers. The metal bonding machine from SUSS Microtech AG, guarantees a misalignment lower than  $5\mu\text{m}$ . However this depends on the correct adjustment of the machine parameters. An extreme misalignment example is shown in Figure 7-12 and Figure 7-13. A perfect alignment put the edge of the round mirror above the edge of the square actuation platform; just before the spring. In general a misalignment of several ten of micrometers was present in one or two axes of the chips.

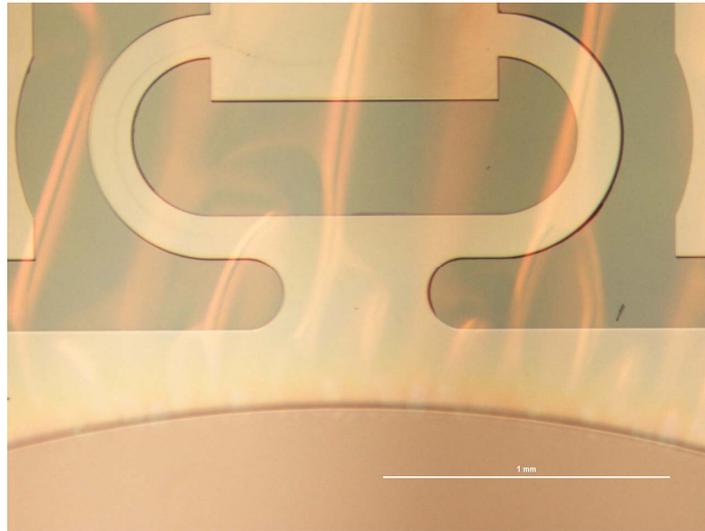


*Figure 7-12: SiO<sub>2</sub> layer that protects the structures below the mirror from being etched unwontedly. The round mirror is shown at the bottom. The spring is seen under the silicon dioxide layer that protected it during DRIE etching.*

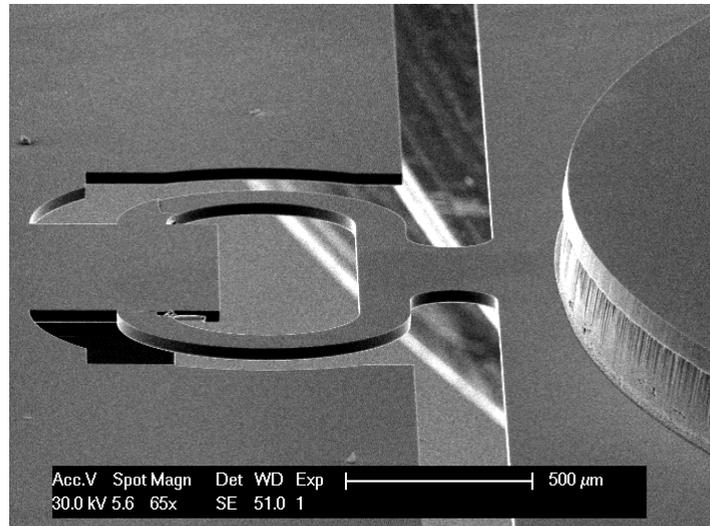


*Figure 7-13: An extreme misalignment example. A perfect alignment puts the edge of the round mirror above the edge of the square actuation platform, just before the spring. In general a misalignment of several ten of micrometers was present in one or two axes of the chips.*

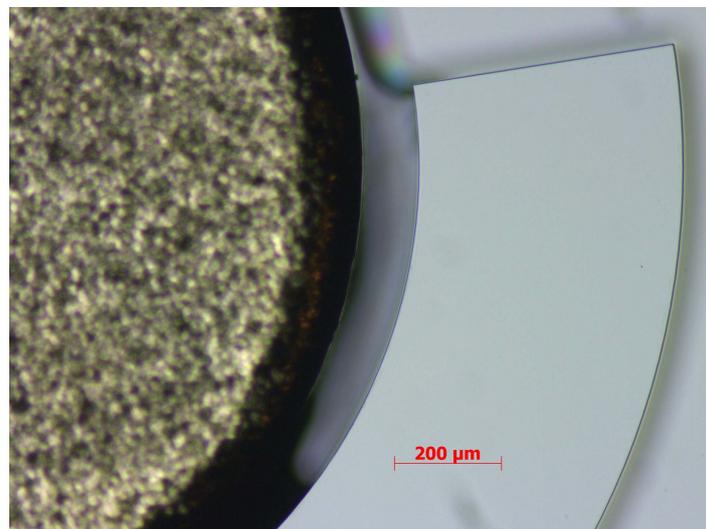


*Figure 7-14: Having too much glue could lead to misalignment of the magnet and the alignment structure as shown here. The glue does not let the magnet to be pushed to its place.*

Another major step in the magnetically actuated mirror is the assembly of the magnets on the moving platform. In this procedure some glue was put on the magnet. The magnet was then pushed towards the alignment structure on the back of the moving platform as shown in Figure 6-21 in section 6.6.1. However, since this procedure was done by hand the amount of glue could not be precisely controlled this led to having too much or too little glue on the magnet. Not having enough glue could lead to magnet detachment during operation. Having too much glue could lead to misalignment of the magnet and the alignment structure as shown in Figure 7-14. The glue does not let the magnet to be pushed to its place. A batch fabrication procedure for this step could increase the precision of this procedure. This point is important since the misaligned shifts the resonant frequencies of the mirror.

### 7.1.5 Resonant behavior and modes

The resonant frequencies and the mode shapes of the two magnetically actuated mirror systems (fast mirror and slow mirror) are presented below.

#### 7.1.5.1 Slow mirror

The resonant behavior of the slow magnetic mirror was measured using an impedance analyzer and a Laser Doppler Vibrometer (LDV). The LDV uses a laser beam that is directed at the surface of the mirror. It can measure the vibration amplitude and frequency of the mirror from the Doppler shift of the laser beam frequency. The setup is shown in Figure 7-15. The impedance-meter excites the mirror at different frequencies and reads the output of the LDV. The response of the mirror to a frequency sweep from 100 Hz to 300 Hz is shown in Figure 7-16. The response in red is measured in the ambient air pressure. There are three resonant peaks at 142 Hz, 186 Hz and 250 Hz which correspond to three different modes. The Q factor of the first peak is  $Q = 38$  which corresponds to a damping ratio of 0.01.

The experiment was repeated in a vacuum chamber. The pressure could be decreased to 0.05 mbar which is approximately 5 times more than the pressure in space. The result is shown in Figure 7-16 in black. The Q factor of the first peak in this case increases to  $Q = 63$  which corresponds to a damping ratio of 0.008. These results are summarised in Table 7-1

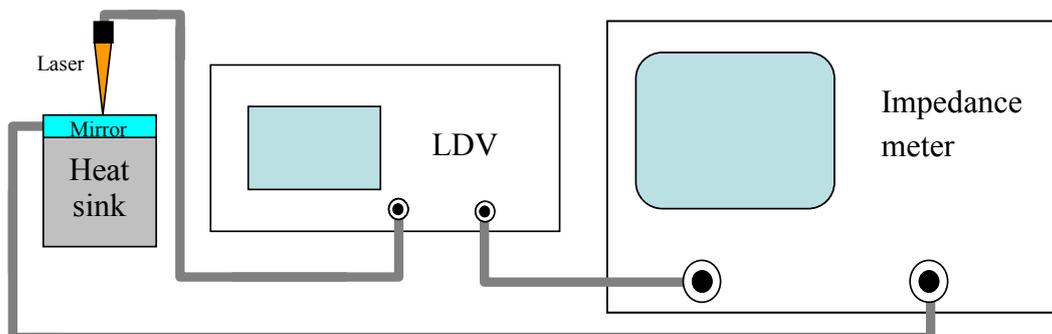


**Figure 7-15:** The resonant behavior of the system was measured using an impedance analyzer and a Laser Doppler Vibrometer (LDV). The impedance-meter excites the mirror at different frequencies and reads the output of the LDV.

*Table 7-1: resonant frequencies of the magnetic slow mirror*

| <b>Movement</b> | <b><i>Piston movement</i></b> | <b><i>Rotation around diagonal</i></b> | <b><i>Rotation around diagonal</i></b> |
|-----------------|-------------------------------|--|--|
| $f_r$ in air    | 142 Hz                        | 186 Hz                                 | 250 Hz                                 |
| $f_r$ in vacuum | 143 Hz                        | 187 Hz                                 | 253 Hz                                 |

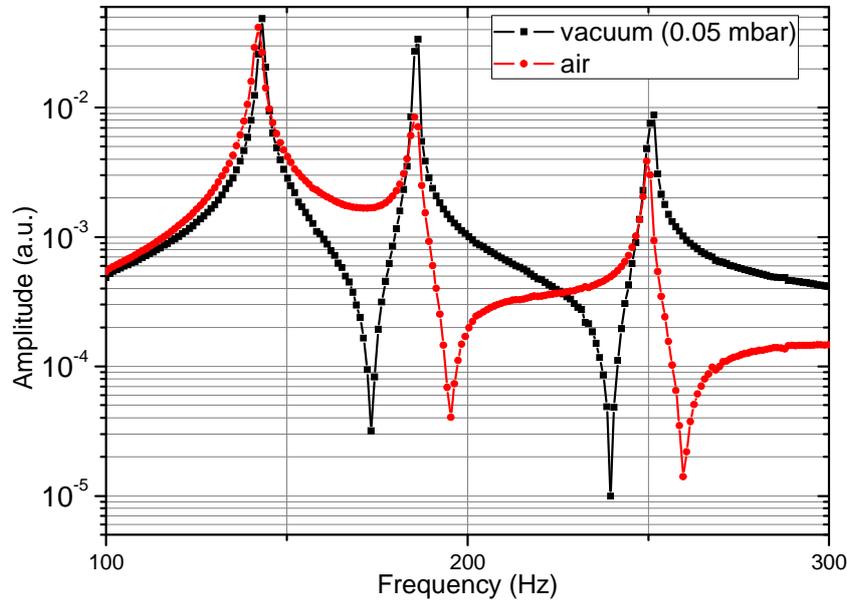


*Figure 7-16: The response of the mirror to a frequency sweep from 100 Hz to 300 Hz is shown for air in red and for vacuum in black. The vacuum pressure was  $P=0.05$  mbar. The  $Q$  factors in air and vacuum for the first peak (142 Hz) are  $Q = 38$  and  $Q = 63$  respectively.*

In order to find the mode shape of each of these 3 frequencies a different setup was used, as shown in Figure 7-17. In this setup an AC voltage source sends a sinusoidal signal with a certain frequency to the mirror and to an oscilloscope with two input channels. The signal that was sent to the oscilloscope was used as the reference for phase shift measurements. The signal sent to the mirror excites it at the desired frequency. On the other hand the LDV output is also sent to another channel of the oscilloscope. A Matlab program was used to read out the amplitude of the LDV response and calculate the amplitude of the oscillating mirror. It could also extract the phase shift of the mirror by comparing the sinusoidal waves on the two different channels of the oscilloscope. The laser of the LDV was mounted on a stage that could move on the X and Y directions. This stage was also controlled by the Matlab program. Therefore by scanning the laser on the mirror surface, the amplitude of the different parts could be read. Combining the amplitude and phase of the measurements gave us the modes of the 3 resonant frequencies. The first mode (142 Hz) is a piston movement. The second mode (186 Hz) and third modes (250 Hz), are modes that rotate around the two perpendicular diagonals of the actuation platform. These two last modes are shown in Figure 7-18 a & b.

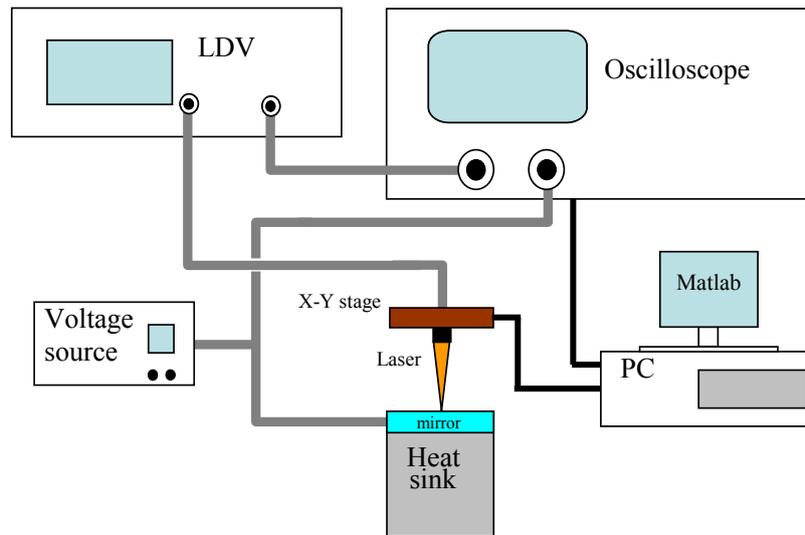


**Figure 7-17:** Setup that was used to find the mode shapes of the 3 resonant frequencies. An AC voltage source sends a sinusoidal signal with a certain frequency to the mirror and to an oscilloscope with two input channels. The LDV output is also sent to another channel of the oscilloscope. A Matlab program was used to read out the oscilloscope data and calculate the amplitude and phase shift of the oscillating mirror. It could also scan the laser light on the mirror surface.

The first mode corresponds well with the FEM simulation result that gives a resonant frequency of  $f_r^{simulation} = 114$  Hz for the piston mode. This is shown in chapter 5.1.2. The difference in the simulation and measurement should be due to the differences in the correct masses of the real and simulated geometries.

On the other hand the simulations show somewhat different resonant frequencies for the second and third modes. Simulations show that these two modes have the same resonant frequencies  $f_r^{simulation} = 202$  Hz. This is normal since the system is totally symmetrical in simulations. However, this contradicts the results of the measurements that show these two modes to have two different resonant frequencies (186 Hz and 250 Hz). The reason may be due to the fact that the assembled magnets and the mirror are not perfectly aligned. This leads to one side of the actuator to be heavier than the other side which in return changes the resonant frequencies of the two sides and. However, the mode shapes of the second and third resonant frequencies, shown in Figure 7-18 a & b, correspond well with the simulated mode shapes.

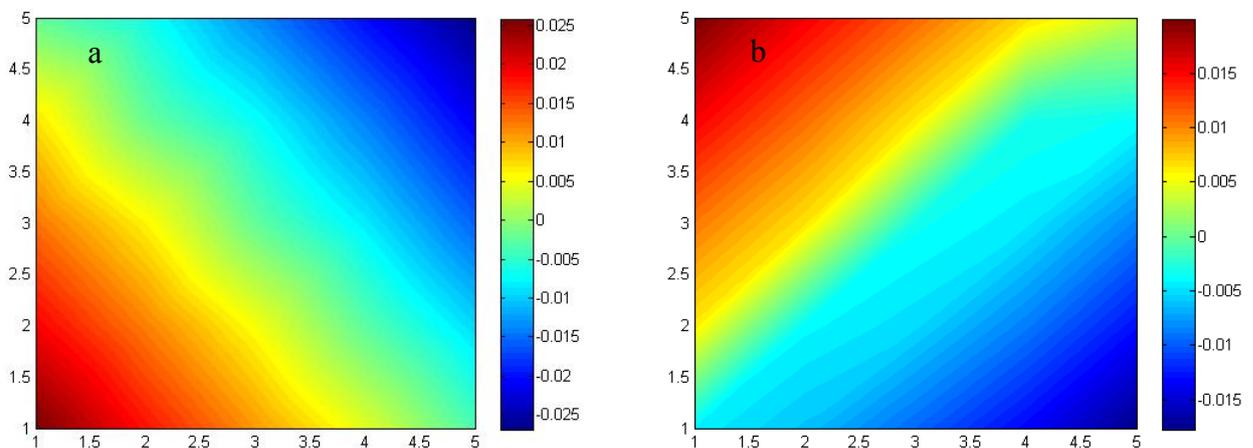


**Figure 7-18:** a) The second mode rotates around one of the diagonals of the mirror actuation platform at 186 Hz. b) The third mode rotates around the diagonal perpendicular to the first diagonal at 250 Hz.

### 7.1.5.2 Fast mirror

The resonant behavior of the fast magnetic mirror was measured using an impedance analyzer (LDV) as shown in Figure 7-15. The response of the mirror to a frequency sweep from 40 Hz to 1500 Hz is shown in Figure 7-16. The response in red is measured in the ambient air pressure. There are three resonant peaks at 774Hz, 872Hz and 1005 Hz which correspond to three different modes. The Q factor of the first peak is  $Q = 32$  which corresponds to a damping ratio of 0.02.

The experiment was repeated in a vacuum chamber. The pressure could be decreased to 0.05 mbar which is approximately 5 times more than the pressure in space. The result is shown in Figure 7-16 in black. The Q factor of the first peak in this case increases to  $Q = 110$  which corresponds to a damping ratio of 0.004. These results are summarised in Table 7-2.

In order to find the mode shape of each of these 3 frequencies the setup shown in Figure 7-17 was used. The first mode (774 Hz) is a piston movement. The second (872 Hz) and third modes (1005 Hz), are modes that rotate around the two perpendicular diagonals of the actuation platform. These two last modes are shown in Figure 7-20.

The first mode is 100 HZ lower than the resonant frequency shown in FEM simulations  $f_r^{simulation} = 878$  Hz for the piston mode. This is shown in chapter 5.1.2. The second mode has also a lower resonant frequency than the results of the FEM simulations  $f_r^{simulation} = 1005$ . However the third mode has a resonant frequency that corresponds to the Simulations  $f_r^{simulation} = 1011$ .

The reason may again be attributed to the fact that the assembled magnets and the mirror are not perfectly aligned. The mass of the bulk magnets could also be a contributing factor since they may vary from one to another. This could explain the general shift of the resonant frequencies to the lower values.

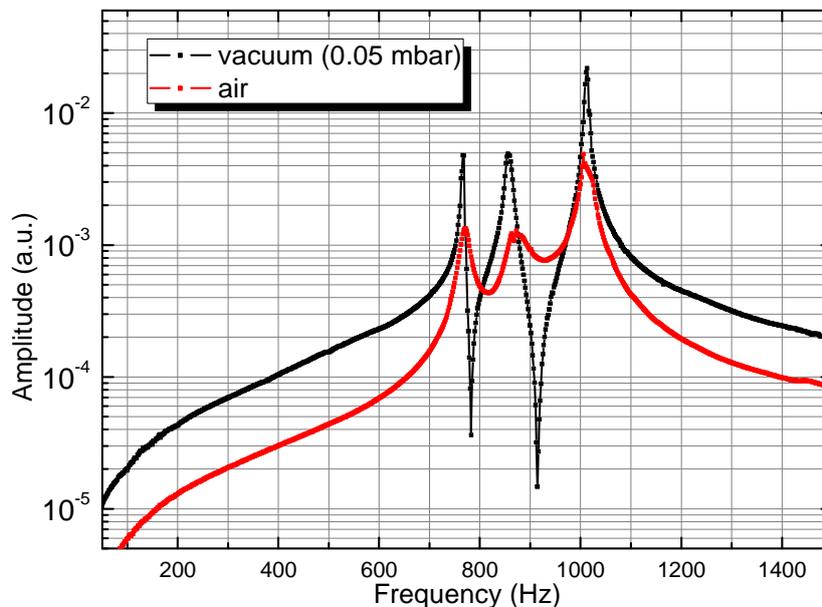


*Figure 7-19: The response of the mirror to a frequency sweep from 40 Hz to 1500 Hz is shown for air in red and for vacuum in black. The vacuum pressure was  $P=0.05$  mbar. The Q factors in air and vacuum for the first peak (770 Hz) are  $Q = 32$  and  $Q = 110$  respectively.*

Table 7-2: Resonant frequencies of the magnetic fast mirror

| Movement        | Piston movement | Rotation around diagonal | Rotation around diagonal |
|-----------------|-----------------|--------------------------|--------------------------|
| $f_r$ in air    | 774Hz           | 872Hz                    | 1005Hz                   |
| $f_r$ in vacuum | 770Hz           | 855Hz                    | 1012Hz                   |

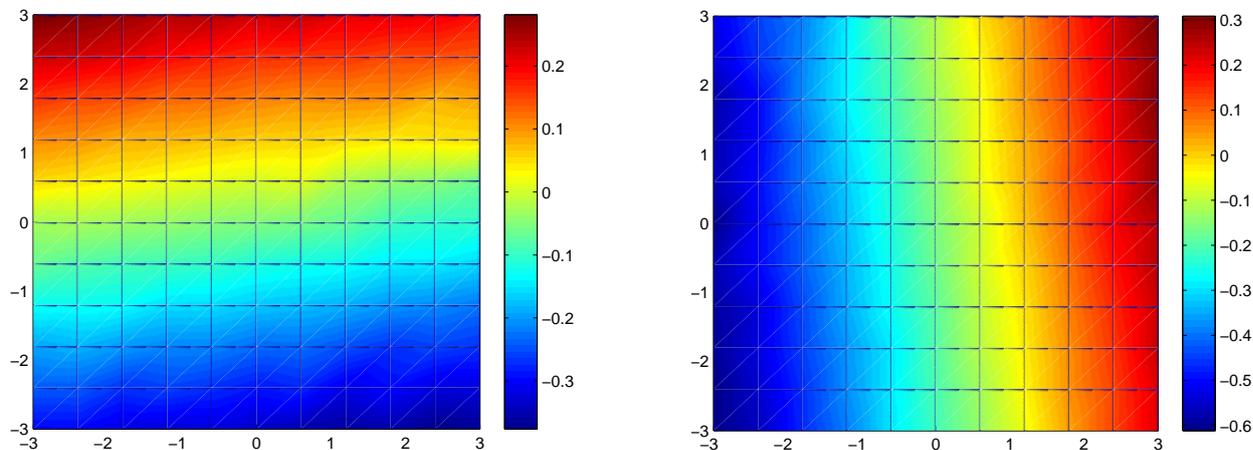


Figure 7-20: The second mode rotates nearly around a pair of the springs that face each other. b) The third mode rotates around the pair of springs that are perpendicular to the first pair as predicted by simulations.

### 7.1.6 Measurement of the static angular deflection

In order to measure the deflection, a setup was built using a beam splitter and a laser as shown in Figure 7-21. The laser beam was directed towards the mirror surface through the beam splitter. The reflected light was shone on a screen positioned at a known distance from the beam splitter. Therefore as the mirror deflects by  $\theta$  degrees the laser beam would deflect by  $2\theta$  degrees.

A maximum current of 500mA which is considered to be the safe limit can be injected to each coil as shown in 7.1.1. Two coils can be pushing and two pulling on the platform. The resulting rotation angles for the slow mirror are shown in Figure 7-22 for the X and Y directions as the current is increased. According to this graph the mirror can be mechanically deflected to  $\theta = 3.5^\circ$  degrees with a 350mA current injected in each coil. This result confirms that the mirror can be rotated to the desired angle. These results also show that the mirror is quite symmetrical and works within the specifications.

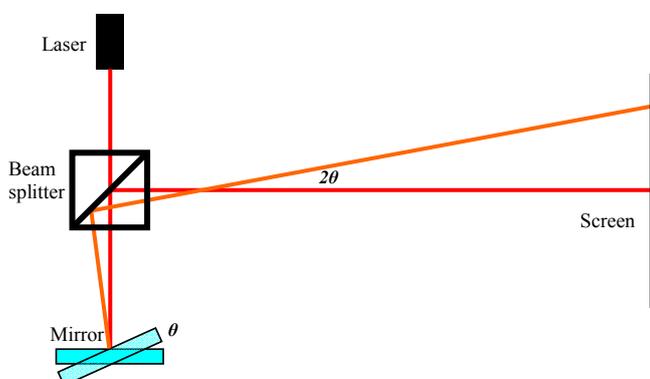
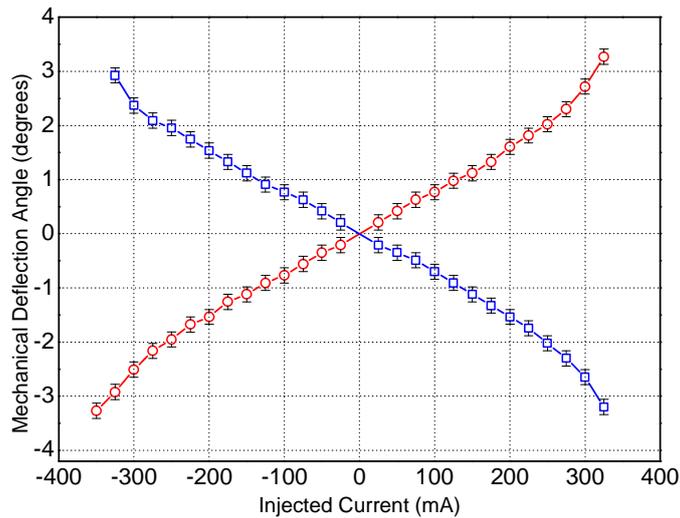
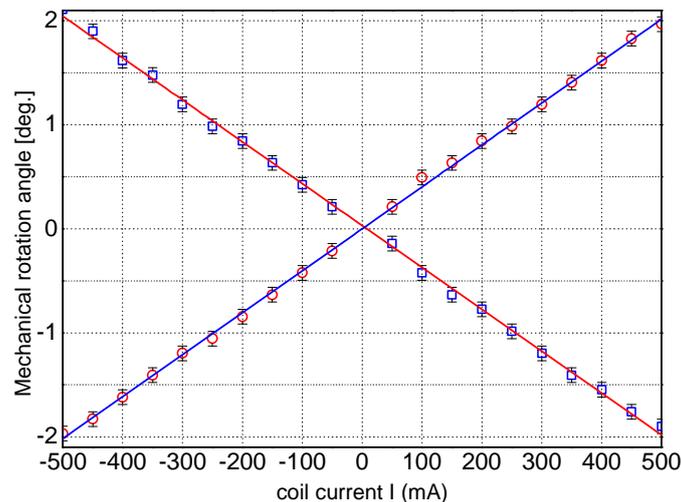


Figure 7-21: Setup for static angular deflection measurements of the mirror. It used a beam splitter and a laser. The laser beam was directed towards the mirror surface through the beam splitter. The reflected light was shone on a screen positioned at a known distance from the beam splitter. Therefore as the mirror deflects by  $\theta$  degrees the laser beam would deflect by  $2*\theta$  degrees.



**Figure 7-22:** The resulting rotation angles for the X and Y directions. According to this graph the mirror can be mechanically deflected to 3.5 degrees with a 350 mA current injected in each coil. These results show that the mirror works within the specifications and is quite symmetrical.

Another interesting result for the slow mirror is shown in Figure 7-23. If the distance between the coil and the magnet is increased, the force decreases with the inversed square law. This will cause the total deflection to drop unless the injected current is further increased. This is shown in Figure 7-23, where the coil-magnet distance is increased to  $850\mu\text{m}$ . Although the current was increased to 500mA the total deflection was only  $2^\circ$ . But the interesting result is that the force profile becomes quasi-linear as shown in Figure 7-23. The mirror deflects  $2^\circ$  with a current injection of  $I = 500\text{mA}$  in each coil. The reason for the quasi-linear behavior is due to the slower variation of the magnetic field as the coil-magnet distance is increased as shown in Figure 7-10.



**Figure 7-23:** If the distance between the coil and the magnet is increased to  $850\mu\text{m}$ , the total deflection drops due to the decrease of force by the inverse square law. But the force profile becomes quasi-linear (small non-linear variation). The mirror deflects  $2^\circ$  with a current injection of  $I = 500\text{mA}$  in each coil

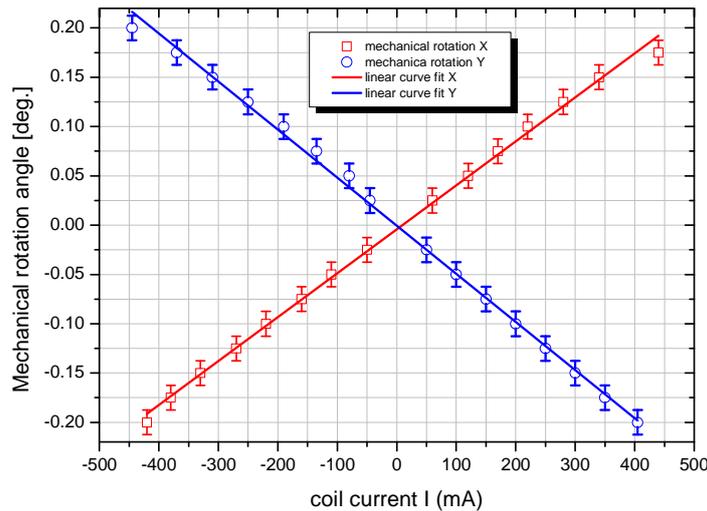


**Figure 7-24:** The rotation angle of the fast mirror is shown. The shown mirror has a quasi linear response to the applied current. It reaches the desired rotation of  $0.2^\circ$  and has a symmetrical response as can be seen from the linear fits of the measurements in X and Y directions.

The rotation angle of the fast mirror is shown in Figure 7-24. The shown mirror has a quasi linear response to the applied current like the results of the fast mirror shown in Figure 7-23. In both cases these quasi linear responses are due to the small total displacement of the magnets compared to the total distance between the coils and the magnets. The fast magnetic actuator also reaches the desired rotation of  $0.2^\circ$  and has a symmetrical response as can be seen from the linear fits of the measurements in X and Y directions.

### 7.1.7 Discussion

The electromagnetic actuator consists of several parts: the actuation platform, the mirror, the magnets and the coil. The fabrication of the actuation platform was shown to be a straight forward process. This led to a very reliable process-flow that produces homogeneous results.

The mirrors were bonded on top of the actuation platforms. The bonding process can have significant misalignment if the bonding tool parameters are not perfectly adjusted. The minimum misalignment in the machine that was used in our process is  $5\mu\text{m}$ . However this is a disadvantage that will be present in any process flow that uses bonding.

The assembly procedure of the magnets was done manually. This led to a somewhat uncontrolled positioning of the magnets on the platform backside.

The resonant frequencies and mode shapes of the systems were also investigated. They were found to be in good accordance with the simulations, although misalignments slightly shifted the resonant frequencies of the systems.

In summary both of the magnetic systems are easily fabricated and function according to the desired specification.

## 7.2 Mirror flatness characterization

In this chapter the effect of the bonding profile on the flatness of the mirrors will be discussed. As discussed before in chapter 6.1, the mirrors were made either by SOI wafer or by bulk silicon wafers the results are shown in the following and compared

### 7.2.1 Bonding profiles and their effect on SOI mirror curvature

The surface properties of the mirrors made with SOI wafers are shown here. The surface properties of the mirrors were measured after bonding with a WYKO optical profiler from VEECO. Four different typical results of the mirror curvature due to the bonding profile are shown in Figure 7-25. Figure 7-25a, is connected only with a dot at the centre. It should be mentioned that this mirror was chip-wise bonded with epoxy-resin glue (Araldite). Therefore further fabrication runs might show variations in the obtained values from this chip. Figure 7-25b shows a mirror that is bonded with 5 dots and no ring. Figure 7-25c shows a mirror bonded with 4 dots and a ring, and Figure 7-25d shows a mirror with 5 dots and a ring. This last mirror is deformed in the thinnest parts because the bonding process was done in vacuum. Since the bonding has hermetically sealed the mirror, the thin membrane has deformed under normal pressure. In order to avoid this kind of deformation, the ring should be separated to several unconnected parts to let air pressure. Figure 7-25c has also a bonding ring but it was not hermetically sealed due to misalignment during bonding. This means that a little opening is letting air in and out. Therefore no membrane deformation is produced. This mirror has an average flatness  $R_a = 207$  nm and a RMS flatness of  $R_q = 249$  nm. These values correspond to the mirror's average deformations.  $R_z$  and  $R_t$  show the largest and an average of 10 largest peak-to-valley heights.

Figure 7-25a & b do not have the outer bonding ring and give the best average deformations. While Figure 7-25a shows the best result, with  $R_a = 65$  nm and  $R_q = 81$  nm, it might not be the most reliable mirror for long term operation since it is hold in place with only one bonding dot. On the other hand Figure 7-25b is curved with  $R_a = 76$  nm and  $R_q = 91$  nm, which is nearly identical to the curvature of Figure 7-25a, but it could be a more reliable mirror for long term operations since it has 5 bonding dots.

These measurements show that bonding profiles that were more centralized produce flatter mirrors. However an important observation here is that Figure 7-25a & b have nearly identical curvatures. This curvature was thought to be the result of the intrinsic deformation of the SOI wafer due to stress. This was the reason why it was decided to use bulk silicon wafers to be able to compare the flatness with the SOI wafers as is discussed in the following.

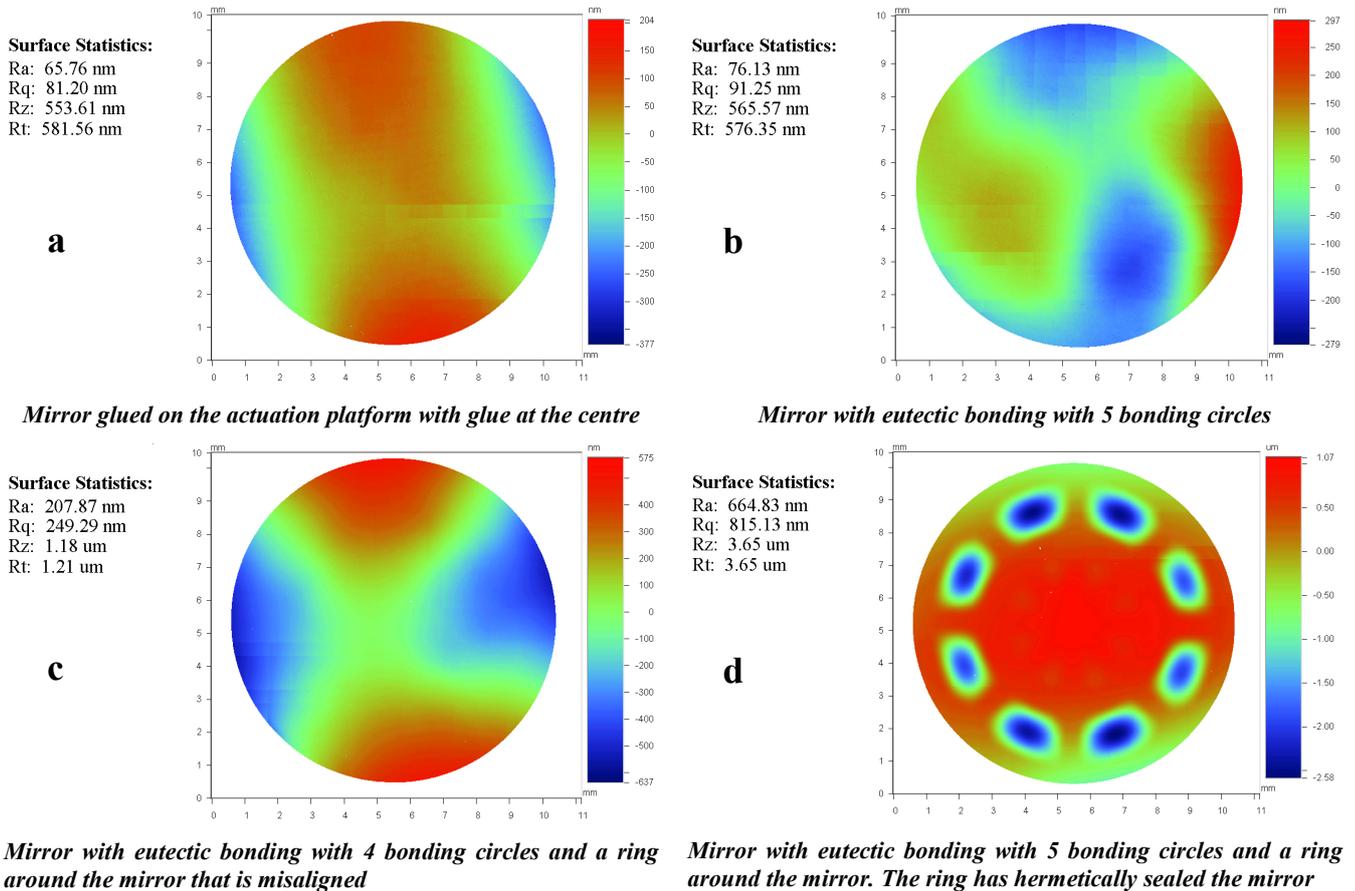
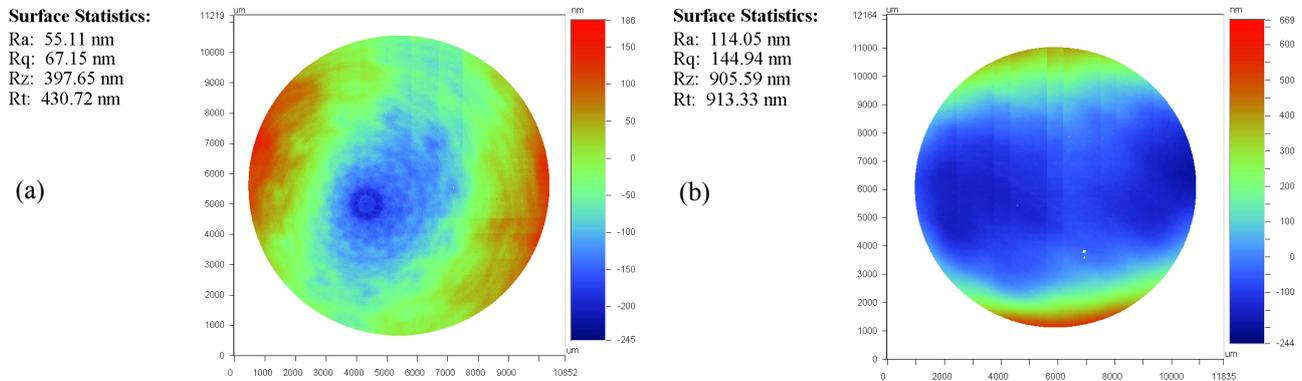


**Figure 7-25:** The surface properties of the mirrors were measured after bonding with a WYKO optical profiler from VEECO. Four different typical results of the mirror curvature due to the bonding profile are shown. The best results are from the mirrors that are connected closer to the centre (a and b).

### 7.2.2 Bonding profiles and their effect on bulk Silicon wafer mirror curvature

The surface properties of the mirrors made with the bulk silicon wafers are shown here. The surface properties of the mirrors were measured after bonding with a WYKO optical profiler from VEECO. Two different results of the mirror curvature due to the bonding profile are shown in Figure 7-26a & b. The mirror in Figure 7-26a, is connected with 1 dot at the center and 4 dots around the centre. It has an RMS curvature of  $R_q = 67\text{nm}$ . The mirror in Figure 7-26b, is connected with 4 dots around the center. It has an RMS curvature of  $R_q = 114\text{nm}$ . The mirror in Figure 7-26a, was formed from the center of the wafer while the mirror in Figure 7-26b was formed from the corner of the wafer. Although the mirror in Figure 7-26b has one dot less than the mirror in Figure 7-26a, it has a higher RMS curvature than the mirror in Figure 7-26a. The maximum and average peak-to-valley difference are shown with  $R_z$  and  $R_t$  respectively. These values are also higher for the mirror in Figure 7-26b and Figure 7-26a. The main reason should be linked to the different bows of the SOI wafer used for making the actuation platform and the bulk silicon wafer used for the mirror. In order to ensure contact of the two wafers during the bonding process the force was increased to flatten the two wafers. The stress induces varying deformation after the release of the mirror chips depending on their original position on the wafer. The circular aberration that can be seen on Figure 7-26a, could be the result of two much force on one of the bonding dots, while the other dots were under less force due to the stress gradient.

A comparison between Figure 7-25a and Figure 7-26b shows a slightly better mirror flatness quality for the mirror fabricated from the bulk silicon wafer. The peak to valley deformation is also slightly better. However no significant difference was observed to favor the Bulk silicon wafer over the SOI wafer. The fabrication process of the SOI wafer however, is simpler than the fabrication process of the bulk silicon wafer.



*Mirror bonded with five dots. One dot at center and 4 around it. Mirror bonded with 4 dots around the center of the mirror.*

**Figure 7-26:** The surface properties of the mirrors made with a bulk silicon wafer are shown for two different mirrors. a) The mirror is from the center of the wafer and has an RMS curvature of  $R_q = 67\text{nm}$ . b) The mirror is from the corner of the wafer and has an RMS curvature of  $R_q = 114\text{nm}$ . A comparison bulk and SOI wafers shows a slightly better mirror flatness quality for the mirror fabricated from the bulk silicon wafer.

### 7.3 Electrostatic actuator

The microfabrication of the electrostatically actuated mirror is characterized in the following. The resonant frequencies and the actuation modes were also investigated.

#### 7.3.1 Microfabrication

There were two delayed mask processes to fabricate the electrostatic actuation platform. The first delayed mask created the combs on the front side of the wafer and continues to etch them into the handle layer of the SOI wafer to create self aligned combs. The silicon on the backside of the combs was also etched to release the combs as discussed in chapter 6.5. From right to left, the ensemble of the moving platform, the combs, the trench that defines the electrode and the spring are seen in Figure 7-27.

Two backside close-ups of the released combs are shown in Figure 7-28. The combs on the left are the fixed combs and the combs on the right side are situated on the moving platform. The height difference is clearly seen. Figure 7-28b shows the notching effect of the DRIE on the right-side combs as the combs were etched from the front side. The roughness on the bottom of the combs on the left side is due to un-optimized DIRE process on the front side of the platform when the combs were being etched and not product of notching. The oxide layer discussed in chapter 6.5 provides complete protection for the combs as shown in Figure 7-29. This figure shows the backside before the combs on the right side are released with HF-VPE. All the trenches between the combs are completely closed with oxide except the opening between the combs and the spring.

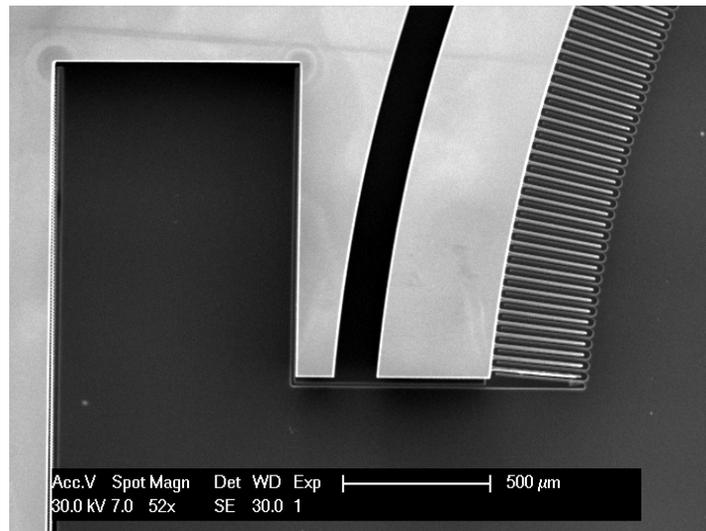


**Figure 7-27:** From right to left, the ensemble of the moving platform, the combs, the trench that defines the electrode and the spring are seen.

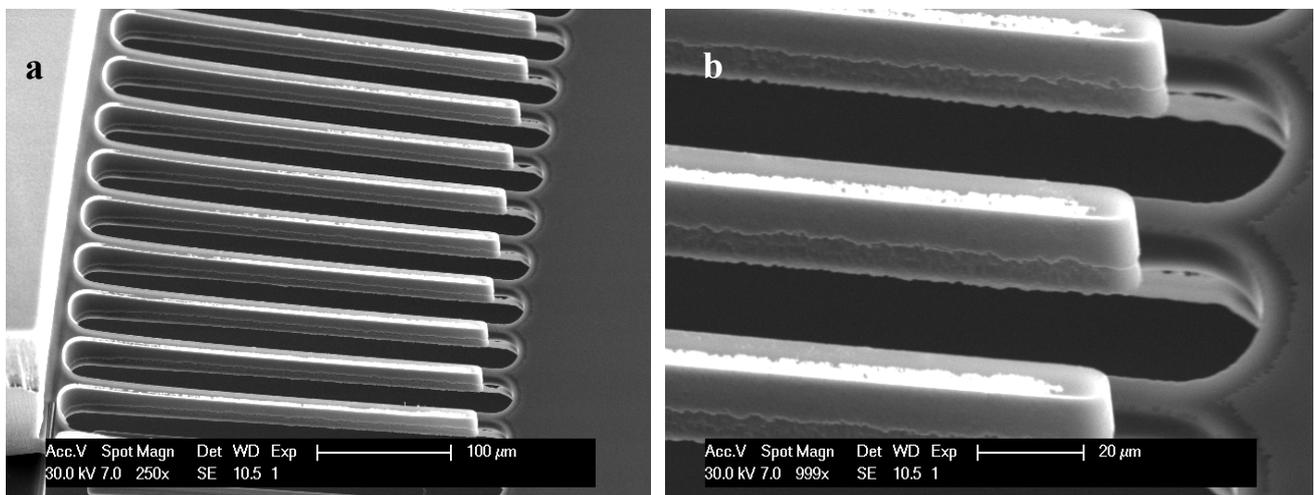


**Figure 7-28:** Two backside close-ups of the released combs are shown. The combs on the left are the fixed combs and the combs on the right side are situated on the moving platform. b) The combs on the right side are under-etched due to notching effect of the DRIE as the combs were etched from the front side. The roughness on the bottom of the combs on the left side is due to un-optimized DIRE process on the front side of the mirror

The silicon grasses that can be seen in Figure 7-29 is created by the DRIE process and are removed with Oxidation and during the HF-VPE step.

The gap between the combs is correlated with the force attainable from the system as discussed in section 4.3.2. The original gap between the combs was set to  $6\mu\text{m}$ . However, this gap was increased to  $8\mu\text{m}$  during processing on the topside of the actuator as shown in Figure 7-30a. The thickness of the combs has decreased from  $15\mu\text{m}$  to  $13\mu\text{m}$ . This was due to the thick AZ 9260 photoresist that was used and the Oxidation step shown in Figure 6-15. The thick photoresist was needed for the deep  $80\mu\text{m}$  DRIE of the combs. Since the DRIE process is not completely vertical the gap at the bottom after  $80\mu\text{m}$  of etching increased to more than  $9\mu\text{m}$  as shown in Figure 7-30b. the combs width has decreased to  $7.5\mu\text{m}$  at the bottom. Comparison of the thickness of the combs at the surface and the bottom shows a  $4^\circ$  deviation from vertical etching in the DRIE.

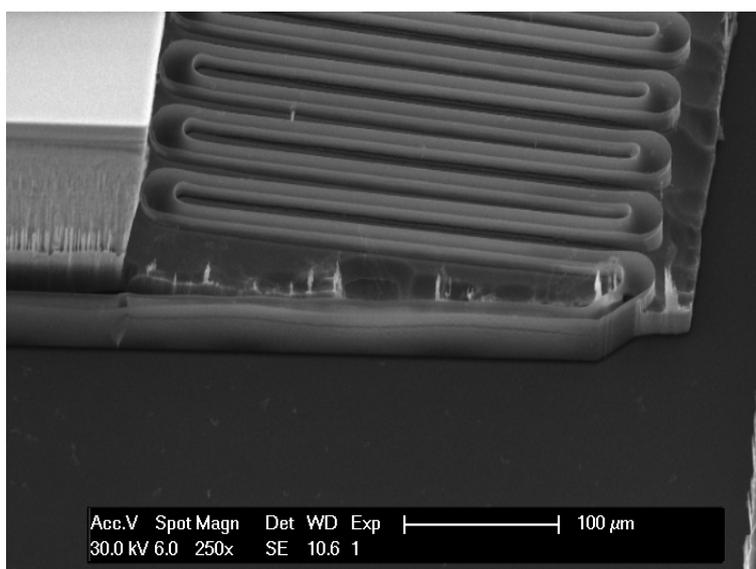


**Figure 7-29:** The oxide layer provides complete protection for the combs. This figure shows the backside before the combs on the right side are released with HF-VPE. All the trenches between the combs are completely closed with oxide except the opening between the combs and the spring. The silicon grasses that can be seen here were removed by an additional Oxidation and during HF-VPE.

In Figure 6-15 it was shown that the thickness of the springs had to be reduced in-order to achieve the correct spring constant. However the DRIE used for this step does not create a uniform surface as shown in Figure 7-31a. In addition the control of the thickness of the springs was also not completely precise. The step height and the roughness of the mirror are shown in Figure 7-31b. These measurements were done with an alpha stepper height profiler. According to this graph the springs are etched  $3\mu\text{m}$  more than the needed value of  $20\mu\text{m}$ . The embedded top-right small graph in Figure 7-31b shows a sample of the rough surface an average height difference of this sample is  $150\text{nm}$ . The maximum peak to valley height difference is around  $700\text{nm}$ . The height and the roughness of the mirror alter the spring constant of the springs.

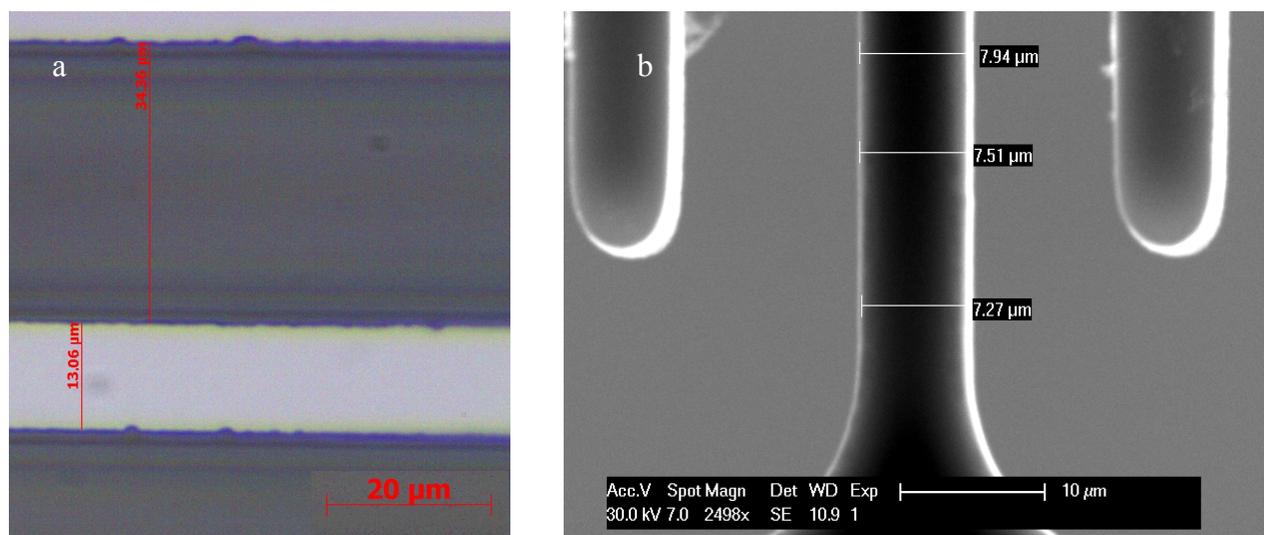


**Figure 7-30:** a) The original gap between the combs on the top of the actuator has increased from  $6\mu\text{m}$  to  $8\mu\text{m}$  during processing. The thickness of the combs has decreased from  $15\mu\text{m}$  to  $13\mu\text{m}$ . b) The gap at the bottom after  $80\mu\text{m}$  of etching increased to more than  $9\mu\text{m}$  and combs width decreased to  $7.5\mu\text{m}$ . This shows a  $4^\circ$  deviation from vertical etching in the DRIE process.

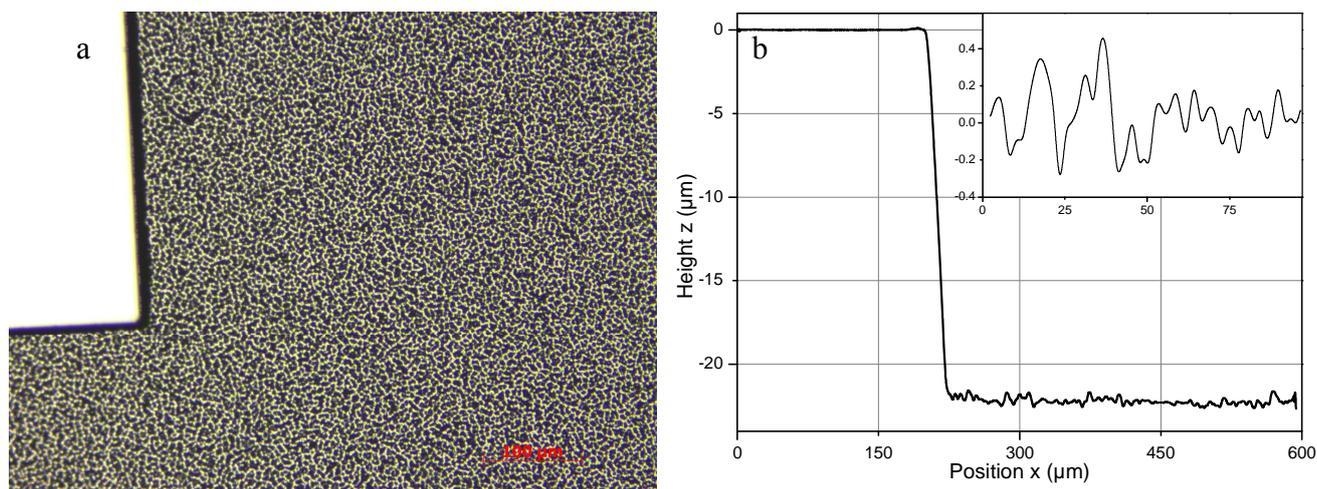


Figure 7-31: a) The rough surface of the spring after DRIE. b) The springs were thinned down  $23\mu\text{m}$  instead of  $20\mu\text{m}$ . the mean surface roughness of the sample shown on top-right side of the graph is  $150\text{nm}$ . The maximum peak to valley height is around  $700\text{nm}$ .

### 7.3.2 Resonant frequencies and mode shapes

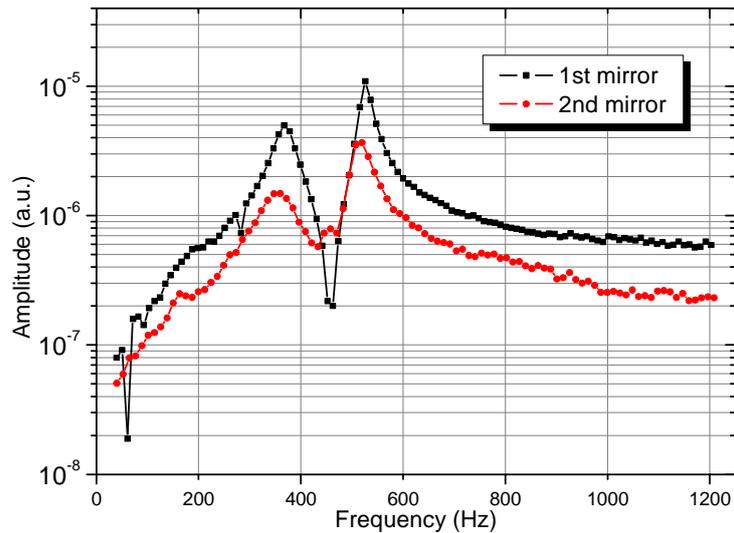
The resonant behavior of the system was again measured using an impedance analyzer and the LDV as shown in Figure 7-15. The response of two different actuators to a frequency sweep from 40 Hz to 1200 Hz is shown in Figure 7-32. There are two resonant peaks at 367Hz and 526Hz for the first mirror and 360Hz and 520Hz for the second mirror as summarized in Table 7-3.

The setup shown in Figure 7-17 was used to extract the mode shapes of the device. The first mode of the two mirrors shown in Figure 7-33a, corresponds with the piston movement as shown in chapter 5.2.2, Figure 5-15. The second mode shown in Figure 7-33b, is a rotation around one spring as shown in Figure 5-15. However according to these simulations there is a third rotation mode that should be close to the second mode. This mode was not seen in any of the systems.

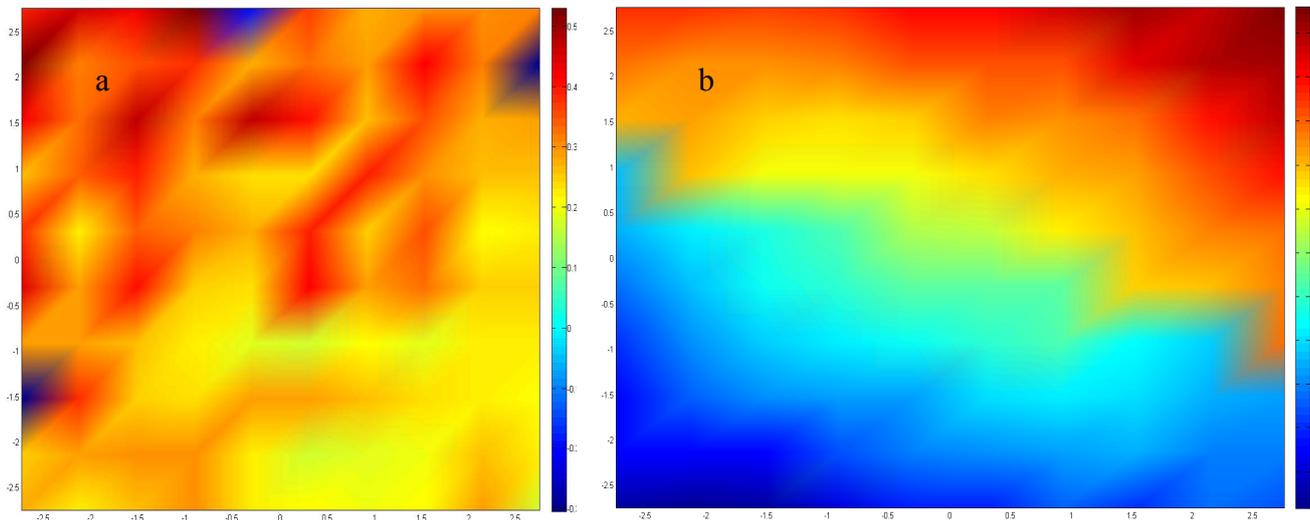
The observed two modes however are at much lower resonant frequencies than simulated resonant frequencies. This is partly due to the thinner springs of the device shown in Figure 7-31. The Q factors for the first and second mirrors are  $Q_1 = 6$  and  $Q_2 = 5$  respectively. These Q factors correspond to the damping ratios of 0.1 and 0.08 for the first and second mirror respectively

Table 7-3: Resonant frequencies of the first and second electrostatically actuated mirrors

|                              | <i>Piston movement</i> | <i>Rotation around one spring</i> |
|------------------------------|------------------------|-----------------------------------|
| <b>1<sup>st</sup> mirror</b> | 367 Hz                 | 526 Hz                            |
| <b>2<sup>nd</sup> mirror</b> | 360 Hz                 | 520 Hz                            |



*Figure 7-32: The response of two different actuators to a frequency sweep from 40 Hz to 1200 Hz is shown. There are two resonant peaks at 367 Hz and 526 Hz for the first mirror (shown in black) and 360 Hz and 520 Hz for the second mirror (shown in red).*



*Figure 7-33: a) The first mode corresponds with the piston movement of the mirror. b) The second mode corresponds with a rotation around one spring of the actuator.*

### 7.3.3 Discussion and comparison

The fabrication results and the actuation properties of the electrostatically actuated mirror were shown. The fabrication shows several challenges that include obtaining the correct gap between the combs and the appropriate thickness for the springs. These are technological challenges that are related to the clean-room equipments used; especially the DRIE. The minimum gap obtainable in our Facilities was set to be  $6\mu\text{m}$ . This value was further increased due to the thick photoresist that had to be used for the deep  $80\mu\text{m}$  etchings (1:13 aspect ratio). The non-vertical etching of the combs also resulted in further increase of the gap between the top and the bottom electrodes. This means that the total force of the combs will be lower than the desired value.

The springs were thinned down using DRIE. This process was not completely controllable and the springs were thinned down too much. This resulted in lower resonant frequencies than the expected

values. The DRIE that was used for this process created a very rough surface on the thinned springs that lead to further decrease of the resonant frequencies.

In general the microfabrication of the electrostatic actuator is more complicated than the electromagnetic actuator especially for diameters of several millimeters. As the mirror becomes larger, the combs get thicker in order to be able to rotate the system to the desired angle. Since the combs and the springs are made on the same layer, the combs had to be thinned down in order to have the right frequencies. This is not a very precise process as was shown in section 7.3.1.

On the other hand, the magnetic actuator has a separate actuation part from the springs. This provided us with more freedom and ease in design and fabrication, as shown in section 7.1.4, which in turn led to easier fabrication procedures for the magnetic design.

Therefore the characterization of these two types of actuators shows the advantage of the magnetic actuator in terms of fabrication and overall performance as shown in Table 7-4. However it should be noted that the proposed fabrication process for the electrostatic design was successful in creating completely self aligned vertical-comb actuators. Since the electrostatic actuator is scalable, this process is easily applicable to smaller devices. [112]

**Table 7-4: Comparison of the different actuators regarding their resonant frequencies,  $Q$  factor and static angular rotations. This table shows the overall advantage of the magnetic actuation scheme over the electrostatic actuation.**

|                                      | Resonant frequencies [Hz] |     |      | Actuation amplitude of first resonant freq. [a.u.] | Applied voltage/current | $Q$ factor | Static rotation [°] |
|--------------------------------------|---------------------------|-----|------|--|-------------------------|------------|---------------------|
| Magnetic slow mirror in air          | 142                       | 186 | 250  | $3 \cdot 10^{-3}$                                  | 20mA                    | 38         | $\pm 3.5^\circ$     |
| Magnetic slow mirror in vacuum       | 143                       | 187 | 253  | $4 \cdot 10^{-3}$                                  | 20mA                    | 63         | $\pm 3.5^\circ$     |
| Magnetic fast mirror in air          | 774                       | 872 | 1005 | $1.5 \cdot 10^{-3}$                                | 20mA                    | 32         | $\pm 0.2^\circ$     |
| Magnetic fast mirror in vacuum       | 770                       | 855 | 1012 | $5 \cdot 10^{-3}$                                  | 20mA                    | 110        | $\pm 0.2^\circ$     |
| 1 <sup>st</sup> Electrostatic mirror | 367                       | 526 | ---  | $1.5 \cdot 10^{-6}$                                | 30V                     | 6          | ---                 |
| 2 <sup>nd</sup> Electrostatic mirror | 360                       | 520 | ---  | $5 \cdot 10^{-5}$                                  | 30V                     | 5          | ---                 |

## 8 Summary and conclusion

This thesis describes the fabrication of a mirror system for satellite telecommunication based on three-1cm beam steering mirrors. It can be used for inter-satellite telecommunication and LIDAR applications. Two of these mirrors were electromagnetically actuated and one was electrostatically actuated. One of the electromagnetically actuated mirrors and the electrostatically actuated mirror were designed to have a maximum tilt angle of  $\theta = 0.2^\circ$  and resonant frequencies in the  $f_r = 1\text{kHz}$  range. These mirrors were called fast mirrors. The other magnetic actuator had a maximum tilt angle of  $\theta = 3.5^\circ$  and resonant frequencies in the  $f_r = 200\text{Hz}$  range. This mirror was called the slow mirror. One of the fast mirrors works in tandem with the slow mirror, to allow steering the light beam to the desired position.

This thesis is mainly investigating the ability of creating MEMS based technologies and mirrors that can be used in space exploration. The main motive for this interest was reducing the mass and the energy consumption of the device, and the general ability of implementing a mirror based on MEMS technology in space, and maintaining the highest mirror flatness possible. The mirrors used nowadays in space are usually bulky and have relatively high energy consumptions. They are based on conventional fabrication technologies that have proved their robustness and reliability. Their mirror sizes are several centimeters in diameter and they can provide high steering accuracy. Their resonant frequencies can range from a few Hertz to 2.5 kHz.

In this thesis we aimed at developing a compact microfabricated scanning mirror system of relatively large size (10 mm diameter) that have similar speeds and steering angular ranges in comparison with the conventional devices. The system was designed to have a very flat mirror surface, also be reliable and space compatible including a sound resistance to thermal effects, fatigue, and stiction between moving and stationary parts. More over it was frictionless, and to the extent possible, shock resistant.

The electrostatic and electromagnetic actuations are the two common non-contact actuations that are commonly used in MEMS devices. Both of these actuation methods were investigated in order to compare them with each other.

The electrostatic actuator has been in use for many years because of their easy integration in MEMS devices. Electromagnetic devices are more recently being integrated into MEMS devices and have exceptional potential in terms of forces they can create. Integration of soft magnetic materials in MEMS has been investigated by many different groups. These materials are easy to deposit in thin layers using electroplating methods, but their magnetic energy is limited and they can demagnetize easily. Integration and deposition of thin magnets for MEMS devices is an ongoing field. Their magnetic energy densities, although higher than soft magnets, has yet to reach the energy density of their bulk magnet counter parts. However, as this field progresses, better and stronger and totally integrated magnetic MEMS devices shall be anticipated in the future.

### Electromagnetically actuated mirror

In order to find the best magnetic actuation model many different magnetic actuators were studied and compared in order to find the best magnetic actuator that is compatible with our criteria and dimensions. An important factor in this investigation was the force to mass ratio of the moving system. The best magnetic actuation system was determined to be the moving magnet-stationary coil system that consists of 4 magnets positioned on four corners of a square moving platform. Four coils were positioned under the magnets to create the actuation force. In this thesis bulk fabricated magnets were used for actuation. This meant that the magnets had to be assembled on the actuation platform.

### Explanation of two mirror system

The reason why the system was separated to two mirrors became evident by examining the relation of the maximum achievable frequency and the maximum static tilt angle. If approximately defined, these two properties are inversely related. It was shown that by increasing the maximum tilt angle the resonant frequency will decrease and visa versa. In order to be able to have large steering angles and also be able to do fast steering the system was divided into two different mirrors, each responsible for one of these two tasks; one having a large steering angular range of  $\theta = 3.5^\circ$  and a resonant frequency of  $f_r = 200\text{Hz}$  and the other having a small steering angular range of  $\theta = 0.2^\circ$  and a resonant frequency of  $f_r = 1\text{kHz}$ .

### Electrostatically actuated mirror

The two main out of plain electrostatic actuation schemes are the parallel plate and vertical comb actuators. These designs were also studied and the vertical comb actuator was chosen as the fast mirror of the system. This decision was mainly based on the scalability of the vertical comb actuator. This would mean that if needed the proposed fabrication process could be used for smaller devices. It was shown that the electrostatic actuator can not have the large actuation ranges of a magnetic actuator. However, theoretically for an angular rotation of  $\theta = 0.2^\circ$  it can also have a resonant frequency of  $f_r = 1\text{kHz}$ .

Having established the basis, it was decided to fabricate two mirrors with  $f_r = 1\text{kHz}$ , one magnetic and one electrostatic in order to compare them. The slower mirror with  $f_r = 200\text{Hz}$  was made for electromagnetic actuation.

### Fabrication and characterization

The main steps in the fabrication of the system were the fabrication of the actuation platforms (electrostatic and electromagnetic) and the mirrors separately from two separate wafers. This allowed us to shape the mirrors to the desired form and simplified the fabrication of both the mirrors and the actuation platforms. The mirror wafer was then bonded to the desired actuation platform using eutectic bonding at wafer level. In total there were three components that needed to

be characterized and quantified; magnetic actuators, electrostatic actuator, and mirrors. The results and achievements of the characterization of the different parts are summarized below:

### 1- Mirrors

- a) Microfabrication: Mirrors were made out of SOI and bulk silicon wafers. The microfabrication of the mirrors is easier with the SOI wafer, although more expensive due to the high price of the SOI wafers.
- b) Bonding: the bonding of the mirror and the actuation platform wafers was done using eutectic bonding. The SOI wafers had lower stress after bonding due to the matching bow of the SOI wafer used for fabrication of the actuation platform and the SOI wafer used for microfabrication of the mirrors. This resulted in a higher yield for the SOI wafers than the bulk silicon wafer. However, the yield of the bonding process of the bulk silicon wafer could improve upon further iterations.
- c) Mirror flatness: The flatness of the mirrors made with SOI and bulk silicon wafers were compared. The best overall mirror RMS flatness value fabricated from SOI wafers was  $q_r=65$  nm. This value was slightly better for the mirror from bulk silicon wafers  $q_r=55$ . This corresponds to a flatness of  $\lambda/10$  for near infrared wavelengths.

### 2- Magnetic actuator platforms

- a) Microfabrication: The microfabrication of the magnetically actuated platform is very straightforward. The results of the microfabrication were very uniform and with an overall high yield.
- b) Assembly: Assembly of the magnets on the backside of the actuation platform is in general an easy task. However, the glue used for assembly can obstruct the correct positioning of the magnets. This leads to non-uniform mass distribution on the actuation platform. Automated or batch assembly of the magnets can greatly reduce the occurrence of misalignments.
- c) Coils: The coils used for actuation were fabricated by HighTec SA, Switzerland. Characterization of the coils showed that they can safely operate with current injections of up to 500mA. The temperature increase in the coils while in vacuum can be up to 100°C without any damage inflicted on the coils.
- d) Magnetic forces: The magnetic forces were in good agreement with the simulations and calculations.
- e) Resonant frequencies: The resonant frequencies and mode shapes of the two electromagnetic actuators were in good agreement with the simulations.
- f) Steering angle: The steering angle of both of the magnetic actuators were easily reached

### 3- Electrostatic actuator platform:

- a) Microfabrication: The microfabrication process of the electrostatic actuation platform was proven to be completely feasible. Due to the limitations in fabrication however, the desired comb gaps could not be reached. This hindered the ability of the device to create forces that were as high as expected. In general the microfabrication process needs to be further optimized.

- b) Resonant frequencies: The resonant frequencies of the electrostatic actuators were lower than expected mainly due to lower thickness of the springs. The springs could not be accurately thinned to the desired value due to the accuracy of the machines used.
- c) Steering angle: Due to the unoptimized fabrication process the electrostatic actuators could not be steered.

The fabrication process of the electrostatic actuator was done successfully, although further optimization is needed for making a completely functional device. However, having a functional process for creating self-aligned vertical comb actuators enables fabrication of smaller devices with the same process.

A comparison between the magnetic and electrostatic actuators shows that the magnetic actuator is in general much easier to fabricate and assemble for dimension around 10mm. Above all the process flow of the magnetic actuator is very simple and straight forward, resulting in high yield and uniformity.

The process flow of the electrostatic actuator is also very straightforward compared to many different vertical comb counterparts. However, it seems that the electrostatic vertical comb actuator is in general more suited for smaller devices.

A mirror RMS flatness of  $\lambda/10$  was obtained from the mirrors for near infrared wavelengths. The mirrors are in general curved and an average peak to valley as low as  $R_t = 430\text{nm}$  could be observed. These values are quite acceptable, although further optimization of the bonding procedure of the mirrors and the actuation platforms is still possible and could lead to fabrication of even flatter mirrors.

The devices fabricated in this thesis can be compared to the mirrors that are already used in space and MEMS devices of the same dimensions:

In general the mirror size of the devices used nowadays in space is larger than 10 mm. However, as discussed in the introduction, the beam size can easily be increased using additional optics (e.g. beam expanders), that can even be beneficial for the angular resolution of the system. However the main advantage of the devices developed in this project is their compactness and low mass, and the fact that these devices can also be used for rovers and for LIDAR applications.

The power consumption of the system is around 20W at its maximum. However this is mainly due to the choice of coils that are used that have very small thicknesses of  $7\mu\text{m}$ . If the thickness of these coils increases to  $50\mu\text{m}$ , as simulated in the theory chapter, the power consumption will reduce significantly to 4 W at its maximum.

The resonant frequencies and rotation angles of these devices are also in good competition with the large devices used nowadays in space.

A mirror that is very close in design to our 1cm magnetically actuated slow mirror is the TALP1000B sold by Texas Instruments. This design was shown in the state of the art. It has a rotation angle of  $\theta = 5^\circ$ , a resonant frequency of  $f_r = 130\text{Hz}$ , a mirror surface of  $A = 9\text{mm}^2$ , and a power consumption of 700mW. Our magnetically actuated slow mirror has a lower rotation angle

$\theta = 3.5^\circ$ , but a much larger mirror surface  $A = 80\text{mm}^2$  and has a higher resonant frequency  $f_r = 200\text{Hz}$  despite its larger mirror size.

Our mirrors, specially the magnetically actuated mirror, could meet the requirements of speed, angular rotation and mirror flatness. Theoretically, they also have very good heat dissipation properties. Although the designs were optimized to have high fracture thresholds, they are not capable of withstanding the shocks of a rocket launch. A simple solution to this challenge is to immerse the mirrors in paraffin that will sublime in the vacuum of space. As for operation failure, no failure was observed during the operation of the magnetically actuated mirrors even if coil to magnet snap-in occurred. The coils used in this project can be replaced with thicker ones. This will result in much lower energy consumption. However, even the coils tested here are capable of withstanding space conditions. No heat damage or electromigration was observed. In addition, these devices are not only usable for space telecommunication. As mentioned before, they can be used for LIDAR applications. They can even replace Galvo-mirrors since they have comparable mirror sizes. Although they have lower actuation angles than Galvo-mirrors, they can be considered as replacement to Galvo-mirrors in situations where the mirrors do not need high actuation angles but need to have lower consumption and to be compact.

In this thesis we have been able to successfully perform theoretical calculations, simulations, microfabrication and characterization of magnetically and electrostatically actuated mirrors. The steering devices fabricated with silicon in this thesis are on the edge of speeds and static angular deflections that is possible for their size. Very good mirror surface flatness of " $\lambda/10$ " was also obtained for the fabricated mirrors for near infrared wavelengths.



## 9 Outlook

Advancements in integration of magnetic materials into MEMS continue and will lead to general increase in performances of magnetic MEMS. Major increase in speeds of these systems however needs either more power consumption or further advancements in the energy density of magnetic materials. Further advancement in material properties “especially for the springs of the mechanical actuators” is also needed if much higher resonant frequencies and deflections are desired. However, the variety of the magnetic actuators gives them a great advantage in terms of compatibility and adaptability with different situations. Their scalability and higher forces can be much further exploited to increase the performance of many MEMS devices of smaller sizes, while being an excellent candidate for bigger ones. The main point that should be stated is that magnetic actuation promises very high performance reliability for both MEMS and MOEMS devices of various sizes.

Very good optical properties were found for the mirrors fabricated in this project. Their fabrication process which consisted of bonding the mirrors and the actuation platforms, at wafer level, facilitated the shaping and flattening of the mirrors to a great extent. This method provides a very reliable fabrication procedure and shows even further potential for ameliorating the optical properties of mirrors.



## References

1. Hoffmann, M. and et al., *Optical fibre switches based on full wafer silicon micromachining*. Journal of Micromechanics and Microengineering, 1999. **9**(2): p. 151.
2. Larry, J.H. *Digital Light Processing for high-brightness high-resolution applications*. 1997: SPIE.
3. Noell, W., et al., *Applications of SOI-based optical MEMS*. Selected Topics in Quantum Electronics, IEEE Journal of, 2002. **8**(1): p. 148-154.
4. Toshiyoshi, H. and H. Fujita, *Electrostatic micro torsion mirrors for an optical switch matrix*. Microelectromechanical Systems, Journal of, 1996. **5**(4): p. 231-237.
5. Waldis, S., et al., *Uniform tilt-angle micromirror array for multiobject spectroscopy*. Journal of Micro/Nanolithography, MEMS and MOEMS, 2008. **7**(2): p. 021014-11.
6. Adolph, P., W. Coppoolse, and J. Moerschell. *Development and test of a fine pointing assembly for optical intersatellite link communications*. 2002: SPIE.
7. Aoki, K., et al. *Wide and fine pointing mechanism with flexible supports for optical intersatellite communications*. 1999: SPIE.
8. Bailly, M. and E. Perez. *Pointing, acquisition, and tracking system of the European SILEX program: a major technological step for intersatellite optical communication*. 1991: SPIE.
9. Baister, G., et al., *The SOUT optical intersatellite communication terminal*. Optoelectronics, IEE Proceedings -, 1994. **141**(6): p. 345-355.
10. Chakraborty, P., K. Behdinan, and B. Tabarrok, *A TIP-TILT ADAPTIVE OPTICS SYSTEM FOR AMATEUR ASTRONOMERS AND OPTIMUM PLACEMENT OF ACTUATORS*. Journal of Sound and Vibration, 1999. **226**(1): p. 169-187.
11. Coppoolse, W., et al. *Dual-axis single-mirror mechanism for beam steering and stabilisation in optical inter satellite links*. in *Proceedings of the 10th European Space Mechanisms and Tribology Symposium*. 2003. San Sebastián, Spain.
12. Cossec, F.R., P. Doubrere, and E. Perez. *Simulation model and on-ground performances validation of the PAT system for the SILEX program*. 1991: SPIE.
13. Hafez, M., et al., *Design, simulations and experimental investigations of a compact single mirror tip/tilt laser scanner*. Mechatronics, 2000. **10**(7): p. 741-760.
14. He, N., et al., *Design and mechanism analysis of a novel type compact single mirror laser scanner*. Sensors and Actuators A: Physical, 2006. **125**(2): p. 482-485.
15. Henein, S., *Conception des guidages flexibles*. 1 ed. 2004: Presses polytechnique et universitaire romands.
16. Kim, W.-j., S. Verma, and H. Shakir, *Design and precision construction of novel magnetic-levitation-based multi-axis nanoscale positioning systems*. Precision Engineering, 2007. **31**(4): p. 337-350.
17. Loney, G.C., *Design of a small-aperture steering mirror for high bandwidth acquisition and tracking*. Optical Engineering, 1990. **29**(11): p. 1360-1365.
18. Nielsen, T.T. *Pointing, acquisition, and tracking system for the free-space laser communication system SILEX*. in *Free-Space Laser Communication Technologies VII*. 1995. San Jose, CA, USA: SPIE.
19. Sodnik, Z., B. Furch, and H. Lutz, *Optical Intersatellite Communication*. Selected Topics in Quantum Electronics, IEEE Journal of, 2010. **16**(5): p. 1051-1057.
20. Spanoudakis, P., et al. *Extremely high resolution tip-tilt-piston mirror mechanism for the VLT-NAOS field selector*. 2000: SPIE.
21. Suhonen, M. and et al., *Scanning micromechanical mirror for fine-pointing units of intersatellite optical links*. Smart Materials and Structures, 2001. **10**(6): p. 1204.
22. Man, K.F., *MEMS reliability for space applications by elimination of potential failure modes through testing and analysis*. SPIE, Micromachining and Microfabrication Meeting, 1999.
23. Ataman, C., et al., *A 2D MEMS Stage for Optical Applications*.

24. Helmbrecht, M.A., et al. *Micromirrors for Adaptive-Optics Arrays*. in *The 11th International Conference on Solid-State Sensors and Actuators*,. 2001. Munich, Germany.
25. Milanovic, V., G.A. Matus, and D.T. McCormick, *Gimbal-Less Monolithic Silicon Actuators for Tip-Tilt-Piston Micromirror Applications*. IEEE JOURNAL OF SELECTED TOPICS IN QUANTUM ELECTRONICS, 2004. **10**(3).
26. Miyajima, H., *Development of a MEMS electromagnetic optical scanner for a commercial laser scanning microscope*. Journal of Microlithography, Microfabrication, and Microsystems, 2004. **3**(2): p. 348-357.
27. Si-Hong, A. and K. Yong-Kweon, *Silicon scanning mirror of two DOF with compensation current routing*. Journal of Micromechanics and Microengineering, 2004(11): p. 1455.
28. Oliveira, L.C.M., et al., *A novel Si micromachined moving-coil induction actuated mm-sized resonant scanner*. Journal of Micromechanics and Microengineering, 2006(1): p. 165.
29. Dooyoung, H. and et al., *A self-aligned vertical comb-drive actuator on an SOI wafer for a 2D scanning micromirror*. Journal of Micromechanics and Microengineering, 2004. **14**(8): p. 1148.
30. Hsu, S., *Fabrication and characterization of a dynamically flat high resolution micro-scanner*. Journal of Optics A: Pure and Applied Optics, 2008. **10**(4): p. 044005.
31. Il Woong, J., U. Krishnamoorthy, and O. Solgaard, *High fill-factor two-axis gimbaled tip-tilt-piston micromirror array actuated by self-Aligned vertical electrostatic combdrives*. Microelectromechanical Systems, Journal of, 2006. **15**(3): p. 563-571.
32. Jeong, K.-H. and L.P. Lee, *A novel microfabrication of a self-aligned vertical comb drive on a single SOI wafer for optical MEMS applications*. Journal of Micromechanics and Microengineering, 2005. **15**(2): p. 277.
33. Kim, J., S. Park, and D.-I. Cho, *A novel electrostatic vertical actuator fabricated in one homogeneous silicon wafer using extended SBM technology*. Sensors and Actuators A: Physical, 2002. **97-98**: p. 653-658.
34. Kim, M., et al., *High fill-factor micromirror array using a self-aligned vertical comb drive actuator with two rotational axes*. Journal of Micromechanics and Microengineering, 2009(3): p. 035014.
35. Krishnamoorthy, U., L. Daesung, and O. Solgaard, *Self-aligned vertical electrostatic combdrives for micromirror actuation*. Microelectromechanical Systems, Journal of, 2003. **12**(4): p. 458-464.
36. Lee, D., et al., *Single-crystalline silicon micromirrors actuated by self-aligned vertical electrostatic combdrives with piston-motion and rotation capability*. Sensors and Actuators A: Physical, 2004. **114**(2-3): p. 423-428.
37. Oldsen, M., et al. *A novel fabrication technology for anti-reflex wafer-level vacuum packaged microscanning mirrors*. 2008: SPIE.
38. Oldsen, M., et al., *Waferlevel Vacuum Packaging: Essential for Microscanners in Mobile Applications*. ECS Transactions, 2008. **14**(1): p. 619-628.
39. Wu, M. and W. Fang, *Design and fabrication of MEMS devices using the integration of MUMPs, trench-refilled molding, DRIE and bulk silicon etching processes*. Journal of Micromechanics and Microengineering, 2005. **15**(3): p. 535.
40. Ilias, S., et al. *Large diameter dual-axis MEMS-based mirror for laser beam steering*. in *MOEMS and Miniaturized Systems X*. San Francisco, California, USA: SPIE.
41. Nam, S., et al., *A telescope for observation from space of extreme lightnings in the upper atmosphere*. Nuclear Instruments and Methods in Physics Research Section A: Accelerators, Spectrometers, Detectors and Associated Equipment, 2008. **588**(1-2): p. 197-200.
42. Cui, Z., et al., *Fabrication of micromirror-based magnetic sensor*. Journal of Physics: Conference Series, 2007: p. 012033.
43. Judy, J.W., R.S. Muller, and H.H. Zappe, *Magnetic microactuation of polysilicon flexure structures*. Microelectromechanical Systems, Journal of, 1995. **4**(4): p. 162-169.

44. Yalcinkaya, A.D., O. Ergeneman, and H. Urey, *Polymer magnetic scanners for bar code applications*. Sensors and Actuators A: Physical, 2007. **135**(1): p. 236-243.
45. Nemirovsky, Y., et al., *A Methodology and Model for the Pull-In Parameters of Magnetostatic Actuators*. MICROELECTROMECHANICAL SYSTEMS, 2005. **14**(6): p. 1253 -1264.
46. Jufer, M., *Électromécanique. Traité d'électricité*. Vol. 10. 2004: Presses polytechnique et universitaire romands.
47. Yalcinkaya, A.D., et al., *Two-axis electromagnetic microscanner for high resolution displays*. Microelectromechanical Systems, 2006. **15**(4): p. 786 - 794.
48. Makishi, W., Y. Kawai, and M. Esashi, *Magnetic Torque Driving 2D Micro Scanner with a Non-Resonant Large Scan Angle*. IEEJ Transactions on Sensors and Micromachines, 2009. **130**(4): p. 135-136.
49. Brunet, M. and et al., *Thick photoresist development for the fabrication of high aspect ratio magnetic coils*. Journal of Micromechanics and Microengineering, 2002. **12**(4): p. 444.
50. Jiang, A.Y.G., A.T. Ono, and A.M. Esashi, *High aspect ratio spiral microcoils fabricated by a silicon lost molding technique*. Journal of Micromechanics and Microengineering, 2006. **16**: p. 1057.
51. Chang, L. and Y.W. Yi, *Micromachined magnetic actuators using electroplated Permalloy*. Magnetics, IEEE Transactions on, 1999. **35**(3): p. 1976-1985.
52. Jang, Y.H. and Y.K. Kim, *Design, fabrication and characterization of an electromagnetically actuated addressable out-of-plane micromirror array for vertical optical source applications*. Journal of Micromechanics and Microengineering, 2003(6): p. 853.
53. Judy, J.W. and R.S. Muller, *Magnetic microactuation of torsional polysilicon structures*. Sensors and Actuators A, 1995. **1**: p. 332-335.
54. Judy, J.W. and R.S. Muller, *Magnetically actuated, addressable microstructures*. Microelectromechanical Systems, Journal of, 1997. **6**(3): p. 249-256.
55. Osborn, J.A., *Demagnetizing Factors of the General Ellipsoid*. Physical Review, 1945. **67**(11-12): p. 351.
56. Yun-Ho, J. and K. Yong-Kweon, *Design, fabrication and characterization of an electromagnetically actuated addressable out-of-plane micromirror array for vertical optical source applications*. Journal of Micromechanics and Microengineering, 2003. **13**(6): p. 853.
57. Arda, D.Y., U. Hakan, and H. Sven, *NiFe Plated Biaxial MEMS Scanner for 2-D Imaging*. Photonics Technology Letters, IEEE, 2007. **19**(5): p. 330-332.
58. Isikman, S.O. and H. Urey, *Dynamic Modeling of Magnetic Film Actuators*. Lasers and Electro-Optics Society, 2007. LEOS 2007. The 20th Annual Meeting of the IEEE, 2007: p. 912-913.
59. Arnold, D.P. and W. Naigang, *Permanent Magnets for MEMS*. Microelectromechanical Systems, Journal of, 2009. **18**(6): p. 1255-1266.
60. Nakano, M., et al., *Anisotropic properties in Fe--Pt thick film magnets*. Journal of Applied Physics, 2009. **105**(7): p. 07A732.
61. HAFEZ, M., *Compact fast-steering tip/tilt laser scanner for high power material processing applications in IMT*. 2000, EPFL.
62. Cougat, O., *Micro-actionneurs électromagnétiques (MAGMAS)*. 2002: Hermes Science. 338.
63. Cugat, O., J. Delamare, and G. Reyne, *Magnetic micro-actuators and systems (MAGMAS)*. Magnetics, IEEE Transactions on, 2003. **39**(6): p. 3607-3612.
64. Griffiths, D.J., *Introduction to Electrodynamics*. 3rd ed. 1999: Prentice Hall 576.
65. Boyer, T.H., *The force on a magnetic dipole*. American Journal of Physics, 1988. **56**(8): p. 688-692.

66. de Bhailçs, D., et al., *Modelling and analysis of a magnetic microactuator*. Sensors and Actuators A: Physical, 2000. **81**(1-3): p. 285-289.
67. Kruusing, A., *Optimizing magnetization orientation of permanent magnets for maximal gradient force*. Journal of Magnetism and Magnetic Materials, 2001. **234**(3): p. 545-555.
68. Feustel, A., O. Krusemark, and J. Müller, *Numerical simulation and optimization of planar electromagnetic actuators*. Sensors and Actuators A: Physical, 1998. **70**(3): p. 276-282.
69. Kruusing, A., *Actuators with permanent magnets having variable in space orientation of magnetization*. Sensors and Actuators A: Physical, 2002. **101**(1-2): p. 168-174.
70. Reitz, R.J., *Foundations of Electromagnetic Theory*. 2009: Pearson Education.
71. Brauer, J.R., *Magnetic Actuators and Sensors*. 2006: Wiley-IEEE Press.
72. Jack, W.J., *Batch-Fabricated Ferromagnetic Microactuators with Silicon Flexures*. 1996, University of California, Berkeley.
73. Jiles, D., *magnetism and magnetic materials*. 2nd ed. 1998: Taylor & Francis.
74. Peirs, J., D. Reynaerts, and H. Van Brussel. *Scale effects and thermal considerations for micro-actuators*. in *Robotics and Automation, 1998. Proceedings. 1998 IEEE International Conference on*. 1998.
75. Trimmer, W. and R. Jebens. *Actuators for micro robots*. in *Robotics and Automation, 1989. Proceedings., 1989 IEEE International Conference on*. 1989.
76. Dennison, E. *On-Axis Field of a Finite Solenoid*. 2004; This formula uses the formula for the field due to a thin shell solenoid, integrated over a range of radii to obtain the magnetic field at any point on the axis of a finite solenoid. ]. Available from: <http://www.netdenizen.com/emagnetttest/solenoids/?solenoid>.
77. Danilov, V.I. and M. Ianovici, *Magnetic field of thick finite dc solenoids*. Nuclear Instruments and Methods, 1971. **94**(3): p. 541-550.
78. Labinac, V., N. Erceg, and D. Kotnik-Karuza, *Magnetic field of a cylindrical coil*. American Journal of Physics, 2006. **74**(7): p. 621-627.
79. Degani, O., et al., *Pull-in study of an electrostatic torsion microactuator*. Microelectromechanical Systems, Journal of, 1998. **7**(4): p. 373-379.
80. Farson, D.F. and et al., *Electrical discharges between platinum nanoprobe tips and gold films at nanometre gap lengths*. Nanotechnology, 2006. **17**(1): p. 132.
81. Germer, L.H., *Electrical Breakdown between Close Electrodes in Air*. Vol. 30. 1959: AIP. 46-51.
82. Hourdakis, E., B.J. Simonds, and N.M. Zimmerman, *Submicron gap capacitor for measurement of breakdown voltage in air*. 2006, AIP. p. 034702.
83. Slade, P.G. and E.D. Taylor, *Electrical breakdown in atmospheric air between closely spaced (0.2  $\mu\text{m}$ -40  $\mu\text{m}$ ) electrical contacts*. Components and Packaging Technologies, IEEE Transactions on, 2002. **25**(3): p. 390-396.
84. Judy, J.W., *Microelectromechanical systems (MEMS): fabrication, design and applications*. Smart Materials and Structures, 2001(6): p. 1115.
85. Torres, J.M. and R.S. Dhariwal, *Electric field breakdown at micrometre separations*. Nanotechnology, 1999. **10**(1): p. 102.
86. R.S.Dhariwal, J.-M.Torres, and M.P.Y. Desmulliez, *Electric field breakdown at micrometre separations in air and nitrogen at atmospheric pressure*. IEE Proceedings online, 2000.
87. Takahito, O. and et al., *Micro-discharge and electric breakdown in a micro-gap*. Journal of Micromechanics and Microengineering, 2000. **10**(3): p. 445.
88. Wibbeler, J., G. Pfeifer, and M. Hietschold, *Parasitic charging of dielectric surfaces in capacitive microelectromechanical systems (MEMS)*. Sensors and Actuators A: Physical, 1998. **71**(1-2): p. 74-80.
89. Calmes, S., S. Schweizer, and P. Renaud. *Resonating large-angle and low-consumption micromachined optical scanner*. 1998: SPIE.
90. Lei, W., et al., *A Tip-Tilt-Piston Micromirror Array for Optical Phased Array Applications*. Microelectromechanical Systems, Journal of. **19**(6): p. 1450-1461.

91. Young, W.C., *Roark's Formulas for Stress & Strain, 6th edition*. 6 ed. 1989: McGraw-Hill.
92. Chu, P.B., et al., *Design and nonlinear servo control of MEMS mirrors and their performance in a large port-count optical switch*. *Microelectromechanical Systems, Journal of*, 2005. **14**(2): p. 261-273.
93. Mitsui, T., Y. Takahashi, and Y. Watanabe, *A 2-axis optical scanner driven nonresonantly by electromagnetic force for OCT imaging*. *Journal of Micromechanics and Microengineering*, 2006(11): p. 2482.
94. Tsuboi, O., et al., *A ROTATIONAL COMB-DRIVEN MICROMIRROR WITH A LARGE DEFLECTION ANGLE AND LOW DRIVE VOLTAGE*. *The Fifteenth IEEE International Conference on Micro Electro Mechanical Systems*, 2002: p. 532 - 535.
95. Caglar, A. and U. Hakan, *Modeling and characterization of comb-actuated resonant microscanners*. *Journal of Micromechanics and Microengineering*, 2006(1): p. 9.
96. Lee, J.H., et al., *Bonding of silicon scanning mirror having vertical comb fingers*. *Journal of Micromechanics and Microengineering*, 2002(5): p. 644.
97. Krishnamoorthy, U., et al., *Dual-mode micromirrors for optical phased array applications*. *Sensors and Actuators A: Physical*, 2002. **97-98**: p. 21-26.
98. Overstolz, T., *Tunable Optical Microsystems featuring Vertical Electrostatic Comb Drives*, in *Institute of Microtechnology*. 2007, University of Neuchatel.
99. Schonhardt, S., et al., *Combdrive Configuration for an Electromagnetic Reluctance Actuator*. *Microelectromechanical Systems*, 2008. **17**(5): p. 1164-1171.
100. Wheeler, H.A., *Simple Inductance Formulas for Radio Coils*. *Proceedings of the Institute of Radio Engineers*, 1928. **16**(10): p. 1398-1400.
101. Ahn, C.H. and M.G. Allen, *A planar micromachined spiral inductor for integrated magnetic microactuator applications*. *Journal of Micromechanics and Microengineering*, 1993. **3**(2): p. 37.
102. Mohan, S.S., et al., *Simple accurate expressions for planar spiral inductances*. *Solid-State Circuits, IEEE Journal of*, 1999. **34**(10): p. 1419-1424.
103. Zhao, J., *A new calculation for designing multilayer planar spiral inductors*. *EDN*, 2010.
104. Merzaghi, S., P. Meyer, and Y. Perriard. *Development of Planar Microcoils for an Electromagnetic Linear Actuator Fabricated in Batch-Type Wafer Technology*. in *Industry Applications Society Annual Meeting, 2008. IAS '08. IEEE*. 2008.
105. Cugat, O., et al., *Novel magnetic micro-actuators and systems (MAGMAS) using permanent magnets*. *Sensors and Actuators A: Physical*, 2006. **129**(1-2): p. 265-269.
106. Overstolz, T., et al. *Compact And Stress-Released Piston Tip-Tilt Mirror*. in *Micro Electro Mechanical Systems, 2006. MEMS 2006 Istanbul. 19th IEEE International Conference on*. 2006.
107. Sunghoon, K., V. Milanovic, and L.P. Lee, *Vertical combdrive based 2-D gimbaled micromirrors with large static rotation by backside island isolation*. *Selected Topics in Quantum Electronics, IEEE Journal of*, 2004. **10**(3): p. 498-504.
108. Yeh, J.L.A., C.Y. Hui, and N.C. Tien, *Electrostatic model for an asymmetric combdrive*. *Microelectromechanical Systems, Journal of*, 2000. **9**(1): p. 126-135.
109. Schuster, C.E., M.G. Vangel, and H.A. Schafft, *Improved estimation of the resistivity of pure copper and electrical determination of thin copper film dimensions*. *Microelectronics Reliability*, 2001. **41**(2): p. 239-252.
110. Rao, V.V.R.N., S. Mohan, and P.J. Reddy, *Electrical resistivity, TCR and thermoelectric power of annealed thin copper films*. *Journal of Physics D: Applied Physics*, 1976(1): p. 89.
111. Lloyd, J.R., *Black's law revisited--Nucleation and growth in electromigration failure*. *Microelectronics Reliability*. **47**(9-11): p. 1468-1472.
112. Moulin, J., et al., *High current densities in copper microcoils: influence of substrate on failure mode*. *Microsystem Technologies*, 2007. **13**(11): p. 1553-1558.



## Aknowledgments

I would like to thank Professor Nico de Rooij for giving me the opportunity to work in his group, where the team spirit and freedom in all aspects of research are the driving force for realization of novel ideas.

I would like to thank Dr. Wilfried Noell my advisor who is always ready to help and discuss and from whom I have learnt a lot and for all the support he has given me during my work in the MOEMS group at SAMLAB. I appreciate a lot the generosity, the support and the long discussions we had in the evenings despite the lack of time.

I also thank Dr. Benedikt Guldemann from the European Space Agency (ESA) for initiating this project. I wish to acknowledge the partial funding of this project by ESA.

My first year in the SAMLAB group started with working under the supervision of Professor Urs Staufer. I thank him a lot for giving me the opportunity of working with him. During this time I also worked with Teru Akiyama and Friedjof Heuck, Kaspar Suter, Daniel Parrat, Raphaël Imer and Sebastian Gautsch. I will always remember their team spirit and all the productive discussions and the many enjoyable moments we had together.

I would like to thank all my colleagues of the MOEMS group; Roland Bitterli, Fabio Jutzi, Stefan Weber, Nicolas Golay, Michael Canonica, Jonathan Masson, but especially Çağlar Ataman, Sébastien Lani and Yves Pétremand for all the fruitful discussions and all the instructions that helped in the advancement of this project.

I also thank the other members of SAMLAB, Alexandra, Danick, Peter, Sara, Jérôme, David, Blaise, Andres, Aon, Philip, Francisco, Rokhaya, Yexian, Frederic, Olivier, Rahel, Jason, Luca, Franz. I reserve a special thank for Karine Frossard that was always ready to answer all my recurring administrative questions.

I also would like to thank all the staff of the CSEM cleanroom, where most of the fabrication was done. They are always helpful and patient and this work would be unimaginable without their collaboration. I would like to thank especially Edith Milot, Claudio Novelli, Sylviane Pochon, Lorant Guilot, Stephan Ischer, Giovanni Bergonzi, Rémy Fournier and Piere-Andre Clerc.

I would like to thank Mireille Leboeuf and Massoud Dadras for all the help and training they provided for the SEM and AFM equipment and measurements. I should also thank Massoud for his praying eyes catching the non-scaled, but most importantly for being the guiding light in the dark underground mazes of science.

In general, all the abovementioned names are acknowledged for the many pleasant “happy hours” passed together.

I thank my family and especially my parents for their love, patience and unconditional support during all of these years, while a very special thank goes to my aunt Soussan who apart from being generally splendid also helped me a lot during my dissertation journey.



# Curriculum vitae

## Dara (Zaman) Bayat

Date of birth: April 24th, 1979

Place of birth: Tehran, Iran

E-mail: [dara.bayat@gmail.com](mailto:dara.bayat@gmail.com)

## Education

Doctoral school (PhD Research) of Ecole polytechnique Fédérale de Lausanne (EPFL) Microsystems and electronics program **2006-2011**

University of Neuchâtel, Institute of Micro and Nano technology **2004-2006**  
Master of Micro and Nano Technology

Azad university of Tehran, Science and Research Campus **2003-2004**  
First year of Master of Theoretical Physics

Azad university of Tehran, Science and Research Campus **1997-2003**  
Bachelor of applied physics

## Experience

*Research and development of microfabricated mirror systems for inter-satellite telecommunications using electromagnetic and electrostatic actuation schemes.* **2006-2011**  
Research assistant and PhD student at Sensors, Actuators and Microsystems Laboratory, EPFL (Prof. Nico de Rooij; under supervision of Dr. Wilfried Noell)

*Research and development on Behavior of the tuning-fork AFM probes.* **2006-2007**  
Scientific assistant at Sensors, Actuators and Microsystems Laboratory, University of Neuchatel (Prof. Nico de Rooij; under supervision of Prof. Urs Staufer)

*Study of the high frequency response of quantum dot lasers.* **2005-2006**  
Master thesis on Quantum Dot (QD) group at EPFL (Prof. A. Fiore) **(6 months)**

*Qualification of an AFM for Martian exploration.* **Semester project**  
University of Neuchâtel, Institute of Micro and Nano technology **2004-2005**  
**(3 months)**

*High reflective substrates for “nip” solar cells, Photovoltaic and thin-film electronics.* University of Neuchâtel, Institute of Micro and Nano technology **Semester project**  
**2004-2005**  
**(3 months)**

## Technical skills

### Extensive clean-room experience

Different microfabrication techniques: such as thin film deposition, photolithography, etching, bonding technology and Packaging

|                                   |  |
|-----------------------------------|--|
| <b>Characterization Equipment</b> | 3D interferometer Microscopes for MEMS characterization, Optical Profiler, Scanning Electron Microscope, network analyzers, Optical setups |
| <b>Scientific Programming</b>     | Matlab, Mathematica, Expert, MAXWELL, Coventor, COMSOL   |
| <b>Operating systems</b>          | Linux, Windows   |

## Languages

|                |   |
|----------------|---|
| <b>English</b> | Writing, reading, speaking: fluently                |
| <b>French</b>  | Writing (intermediate), reading, speaking: fluently |
| <b>German</b>  | Writing, reading, speaking: beginner                |
| <b>Persian</b> | Mother language                                     |

## Awards

Student scientific Omega Award of 2006: Study of the high frequency response of quantum dot lasers. Master thesis in Quantum Dot (QD) group at EPFL.

## Publications and conferences

Bayat, D., T. Akiyama, et al. "Dynamic behavior of the tuning fork AFM probe" *Microelectronic Engineering* 85(5-6): 1018-1021, 2008

Bayat, D., et al. "Large electrostatically and electromagnetically actuated mirror system for space applications" *Optical MEMS and Nanophotonics (OPT MEMS)*, Aug. 2010

Dara Bayat; Caglar Ataman; Benedikt Guldimann; Sébastien Lani; Wilfried Noell; Nico de Rooij "Microfabricated mirrors for space applications" *Proceedings Paper SPIE, Photonics West*, San-Francisco Feb. 2011

Lani, S., et al., "3D Assembly Using Au-Si Eutectic and Au-Au Thermocompression Wafer Level Bonding for M(O)EMS Device Fabrication". *ECS Transactions*. 33(4): p. 37-46.

Ataman, C.; Lani, S.; Noell, W.; Jutzi, F.; Bayat, D.; de Rooij, N.; "Fabrication and characterization of 3D integrated 2 DOF Micromirror Arrays for excessive thermal loads", *2011 IEEE 24th International Conference on Micro Electro Mechanical Systems* pp.684-687, 23-27 Jan. 2011

Wilfried Noell; Dara Bayat; Caglar Ataman; Benedikt Guldimann; Sébastien Lani; Nico de Rooij "Hybrid Microfabricated Mirrors For Space Applications" *International Conference on Space Optics, ICSO*, Oct. 2010

Wilfried Noell; Dara Bayat; Caglar Ataman; Benedikt Guldimann; Sébastien Lani; Nico de Rooij "Hybrid Microfabricated Mirrors For Space Applications" *7th ESA Round-Table on MNT for Space Applications*, Sept. 2010